UNIVERSITY OF SOUTHAMPTON

FACULTY OF ENGINEERING SCIENCE AND MATHEMATICS
School of Engineering Sciences

Modelling of a Microfluidic Ultrasonic Particle Separator

by
Rosemary June Townsend

Thesis for the degree of Doctor of Philosophy

February 2006

UNIVERSITY OF SOUTHAMPTON

ABSTRACT

FACULTY OF ENGINEERING, SCIENCE AND MATHEMATICS

SCHOOL OF ENGINEERING SCIENCES

Doctor of Philosophy

MODELLING OF A MICROFLUIDIC ULTRASONIC PARTICLE SEPARATOR

by Rosemary June Townsend

Particles within an ultrasonic standing wave experience an acoustic force causing the particles to move to certain positions within the acoustic field. This phenomenon can be used to manipulate particles and so provides a means to separate, concentrate or trap particles, cells or spores. The work described is applied to a micro-engineered flow-through device for processing small samples and incorporates a fluid filled chamber of depth typically between 100 and 200μm, and therefore approaches microfluidic dimensions. The successful design and subsequent performance of such devices rely on the predictability of particle trajectories which are influenced predominantly by acoustic and fluid flow fields. Therefore, the majority of this research seeks an understanding of the nature of these fields and, in turn, reliable simulation of particle trajectories.

Computational fluid dynamics (CFD) modelling is used to develop a robust 2-dimensional model of the device's microchannels and is used to predict the presence of eddy regions, associated with the etch fabrication techniques, which are likely to disrupt the separation process. Based on a geometric study, simulations and subsequent test results on a fabricated device have revealed geometric modifications which minimise these eddy flows and promote the existence of laminar flow within the main channel of the device.

Finite element analysis (FEA) provides a method to investigate the 2-dimensional characteristics of the acoustic field and reveals variations in acoustic pressure across the width of the device, giving rise to lateral radiation forces frequently reported in similar ultrasonic devices. This work investigates acoustic enclosure modes in 2 or 3-dimensions as a possible cause of these lateral variations, with modelled results matching well with experiment.

A particle force model has also been developed which predicts the motion of particles through the device, and by which concentration and separation performance may be calculated. This tool is used to investigate acoustic design, operating conditions and separation performance for both the micro-engineered device and a device based on a quarter-wavelength, providing valuable insight into various trends observed.

The novelty in this work is the application of macro-scale numerical techniques to micro-engineered ultrasonic particle manipulators and the execution of an extensive analysis of the design and operation of such devices. These analyses have demonstrated, and therefore have explained, various phenomena associated with the fluid and acoustic fields, and how they influence particle separation performance. The development of similar devices can be aided by the use of the numerical simulation methods featured throughout this thesis.

Contents

List of Figures

List of Tables

Author's Declaration

I, **Rosemary June Townsend** declare that the thesis entitled

Modelling of a Microfluidic Ultrasonic Particle Separator

and the work presented in it are my own. I confirm that:

- this work was done wholly or mainly while in candidature for a research degree at this University;
- where any part of this thesis has previously been submitted for a degree or any other qualification at this University or any other institution, this has been clearly stated;
- where I have consulted the published work of others, this is always clearly attributed;
- where I have quoted from the work of others, the source is always given. With the exception of such quotations, this thesis is entirely my own work;
- I have acknowledged all main sources of help;
- where the thesis is based on work done by myself jointly with others, I have made clear exactly what was done by others and what I have contributed myself;
- parts of this work have been published as:

  1. Harris et al. *Ultrasonics* (2004)
  2. Townsend et al. *Ultrasonics* (2004)
  3. Hill et al. *Proceedings of the Institute of Acoustics.* (2004)
  4. Townsend et al. *Sensors and Actuators B: Chemical.* (2005)
  5. Harris et al. *Sensors and Actuators B: Chemical.* (2005)
  6. Martin et al. *Biosensors and Bioelectronics.* (2005)

Signed:

Date:

Acknowledgements

Firstly, I would like to acknowledge the financial support from EPSRC, dstl, Porvair (Microfiltrex), the Royal Academy of Engineering and the University, allowing this research to be conducted.

I would also like to acknowledge the many people who have given me technical guidance including Dr. Ken Thomas, Prof. Robert Wood, and also those involved in USWNet including Dr. Jeremy Hawkes and Prof. Terry Coakley with whom there has been much collaboration. I would like to thank Neil White and Steve Beeby for their support and involvement in the project, especially for the fabrication of experimental devices, and also to Jiexiong Ding for his valuable work in the lab. Also, the support given by Nick Harris is greatly appreciated, always ready to give helpful advice and a much needed pep talk. Similar thanks extend to Martyn Hill for his helpful ideas, explanations, patience, support, the list is endless! You are an excellent supervisor.

My parents and the rest of the Townsend and Boltryk families also had an important role to play in supporting me through the harder times and always being available to offer their love and support.

A very special thanks goes to Peter for his understanding, putting up with me, his unwavering support, and his (and the dog's) continued affection.

List of Abbreviations

Abbreviation	Description
CFD	Computational Fluid Dynamics
cMUT	Capacitative micromachined ultrasonic transducer
FEA	Finite Element Analysis
MEMS	Micro Electro-Mechanical System
μTAS	Micro Total Analysis System

List of Symbols

Symbol	Description
A	Area
C	Particle concentration
C_0	Static capacitance
C_D	Drag coefficient
C_m	Mechanical capacitance
c	Sound velocity, particle concentration
c_f	Fluid sound velocity
c_p	Particle sound velocity
D_h	Hydraulic diameter
d	Diameter, characteristic dimension
d_p	Particle diameter
$\langle \bar{E}_{kin} \rangle$	Time averaged acoustic kinetic energy density
$\langle \bar{E}_{pot} \rangle$	Time averaged acoustic potential energy density
F_{ac}	Radiation force
F_{ac}^0	Radiation force amplitude
F_B	Buoyancy force
F_D	Drag force
F_L	Lift force
f	Friction factor, frequency
g	Gravitational field constant
h	Channel depth
k	Wave number
L	Channel length, layer thickness
L_e	Entrance length
L_m	Mechanical inductance
m	Particle mass
N	Avogadro's number
P	Perimeter
p	Acoustic pressure
Q	Flow rate
R	Particle radius
R_0	Universal gas constant
R_m	Mechanical resistance
Re	Reynolds number
Re_p	Particle Reynolds number
Re_t	Transitional Reynolds number

Symbol	Description
S	Area
T	Temperature
t	Time
U	Fluid velocity
U_0	Free stream fluid velocity
u	Particle x velocity
u	Acoustic particle velocity
u_0	Amplitude of acoustic particle velocity
$\bar{u}_s$	Mean (streaming) slip velocity
V	Particle volume
V_c	Settling velocity
V_{in}	Input voltage
V_{M1}	Transition velocity of a suspension
V_t	Transducer voltage
v	Particle y velocity
w	Channel width
Y	Channel depth
Z	Impedance
Z_{m0}	Mechanical input impedance
Z_{mL}	Terminating material impedance
Δ	Boundary layer thickness
δ	Boundary layer thickness
$\langle\bar{\epsilon}\rangle$	Time averaged acoustic energy density
λ	Wavelength
μ	Dynamic viscosity
ν	Kinematic viscosity
ρ	Density
ρ_0	Undisturbed material density
ρ_f	Fluid density
ρ_p	Particle density
ϕ	Acoustic contrast factor
ϕ^G	Gradient of radiation force potential
ω	Angular frequency ($2\pi f$)

Chapter 1

Introduction

1.1 General

Particles within an ultrasonic standing wave experience a radiation force. This radiation force depends on the acoustic field pattern and causes particles to move towards the acoustic pressure nodes or anti-nodes. For second phase particles within a fluid suspension, the acoustic radiation force offers a method to manipulate particles, moving particles to various positions, fractionating particles or causing them to converge thus increasing their concentration. Such a technique, therefore, has applications in the processing of biological samples containing cells or spores; for example, a concentrate would increase the sensitivity of any subsequent tests. The simple structural design also permits simplification and miniaturisation of laboratory processes; miniature systems which incorporate such processing and sensor stages are termed Micro Total Analysis Systems (μTAS) or "lab-on-a-chip".

This thesis describes the numerical simulation of various aspects of particle manipulation, but is centred around a micro-engineered ultrasonic separator, the operation of which relies on acoustic radiation forces. The device processes a sample of a fluid/particle mix by passing it through a half wavelength ultrasonic standing wave contained within a fluid chamber, causing the particles to congregate on the nodal plane along the centre of the chamber. By controlling the respective flow rates through two outlets it is possible to pass the particle concentrated stream through one, leaving clarified fluid to pass through the other. Therefore, this device operates primarily as a clarifier and is designed to demonstrate the potential of acoustic separation within a micro-engineered device and is an example of a micro electro-mechanical system (MEMS).

The efficiency of separation is dependent on various factors including the operating conditions and geometric design of the micro-engineered device as these influence the fluid dynamics, acoustic field and particle motion within the device. Numerical modelling is used to investigate these factors, building on previous modelling work which concentrated on the 1-dimensional acoustic aspect of the device. The numerical modelling work includes development of a CFD model, an acoustic FEA model and particle force model, by which the fluid dynamics, the 2-dimensional acoustic field and particle motion within the device may be simulated respectively. In turn, these enable the degree of separation or clarification to be quantified.

Simulations also predict, and thus explain, various acoustic and fluid phenomena which have an impact on separation performance. Further to this, simulations have been used for the appropriate redesign of geometry to discourage fluid flow phenomena which is detrimental to separation performance.

Several devices have been fabricated from which experimental results have contributed to validation of the various models mentioned above. Geometry revisions recommended through the use of CFD have been incorporated into fabricated devices, yielding positive results and demonstrating the potential use of simulation tools.

1.2 Background

Observations of acoustic forces on particles in a standing wave causing particle accumulation and fractionation were first recorded in the late 1800s [1] and the phenomenon has since been investigated as a means to separate particles from a carrying fluid. Various methods have been patented, including methods which use a drifting standing wave to transport particles to another part of the device.

By contrast, the University of Southampton has investigated a ‘flow-through’ type of separator, where a fluid stream is continually processed through a ‘stationary’ standing wave, the position of multiple outlets enabling the particle concentrate to be separated from clean fluid regions. Initial experiments investigating this method of separation used flow rates of between 8 to 20 l/hr and have shown that a useful level of particle separation can be achieved [2, 3].

It is intended to develop this method on a much smaller scale to produce a separator capable of processing millilitre samples. Researchers at Cardiff University have designed and tested a device fabricated from stainless steel, capable of separating yeast and polystyrene particles at a flow rate

of 0.1ml/s [4]. Researchers at the University of Southampton are developing a similar device [5], but by using micro-engineering fabrication techniques it may be incorporated into microfludic systems encompassing similar devices.

1.3 Structure

The separator device is novel in terms of how it combines micro-engineering technology with an ultrasonic phenomenon, therefore chapter 2, containing much of the literature review, concentrates on these two aspects. The chapter then concludes with the application of this technology within other devices relying on ultrasonics and within the microfluidic ultrasonic separator about which this work is centred, and also summarises the modelling techniques used in relation with these devices. As this thesis draws on a range of techniques and areas of research some literature is not included in this chapter, but instead incorporated into the following chapters where its relevance can be clearly shown.

Chapters 3 and 4 study the fluid and acoustic characteristics, respectively, within the microfluidic ultrasonic separator, which both influence the trajectory of particles through the device and therefore will ultimately determine the success of the device to separate or concentrate. These chapters also describe the CFD and FEA modelling mentioned above. Chapter 5 describes the development of the numerical simulation of particle trajectories and concentration which makes assumptions about and uses simplifications of the fluid and acoustic fields, put into context by the two preceding chapters. In chapter 6, the thesis culminates in analysis and test of separator devices, comparing the model described in chapter 5 with experimental performance of the devices.

1.4 Research Contributions

This thesis presents the methods employed to predict both the behaviour of particles and fluid within the channels of the Southampton micro-engineered separator and a related device. The simulation approaches have been validated against experimental results taken from fabricated devices and are shown to be valuable tools to determine and evaluate modifications.

CFD simulations have described the flow patterns generated by passing fluid through anisotropically etched structures, but improvements to the flow pattern have been simulated and shown experimentally, whilst bound by the limited geometric variations offered by the KOH etch process.

The flow efficient design of fluid networks approaching microfluidic scale had been shown to be possible using a commercial CFD program and has wider implications regarding the design of microfluidic networks.

FEA of the 2-dimensional acoustic field has predicted the presence of lateral radiation forces, assisting in their explanation and describing the relative influence of materials and geometry. The effects of lateral radiation forces have been observed in similar ultrasonic devices and suggests that FEA has a role in diagnosing acoustic phenomena observed in other resonators.

To predict the movement and concentration of particles, a numerical model is developed. This predicts the particle concentration throughout the processing chamber and is able to describe discontinuities such as at the edge of the particle stream and wall concentration. This simulation method demonstrates the combined influence of the acoustic and fluid flow fields on particle distribution, which becomes more significant when the acoustic wavelength is comparable to the chamber depth and a parabolic laminar flow profile exists. Separation performance is also predicted using this simulation method describing the influence of various operating parameters, validated experimentally. This simulation approach has potential application in the design of other field-assisted particle manipulators where the spatial control of particle concentration is vital to the successful operation of the device.

Chapter 2

Introduction to Separator Development

The development of the microfluidic ultrasonic separator relies on two main topics: micro-engineering fabrication techniques which determine the geometric design and fluid flow regime, and the acoustic radiation force which gives rise to particle convergence and ultimately separation. The first three sections within this chapter review literature broadly concerned with these areas, therefore introducing the basic principles of the design and operation before introducing the separator device itself. The microfluidic ultrasonic separator and related devices are then discussed in sections 2.4 and 2.5 which present the various ways in which the acoustic radiation force has been employed and the simulation methods used to predict the characteristics of operation.

2.1 MEMS Technology

Micro Electro-Mechanical Systems (MEMS) is the term used for micron scaled devices which incorporate both electrical and mechanical parts, typically on a common silicon substrate. Due to the scale of these systems the fabrication technology is specialised, referred to as micro-engineering, and principally using etched wafers to build the bulk of the device structure. Other than their size, the layered construction make MEMS devices very distinctive. The ultrasonic separator is a MEMS device: it incorporates fluid microchannels, a piezoelectric transducer and is fabricated using micro-engineering techniques. By appreciating the technologies associated with MEMS it is possible to recognize limitations in design in terms of the ultrasonic separation device geometry, manufacture, operation and integration into a system composed of similar devices.

2.1.1 Micromachining

MEMS devices are typically fabricated using micromachining techniques where material is added to or etched from a suitable substrate. Bulk micromachining methods are used to fabricate the main structure of the ultrasonic separator involving the etching and bonding of wafers, frequently used for fabricating MEMS devices. Other fabrication techniques not used here have been developed, capable of producing more complex structures and devices.

Silicon is the most common substrate material, although other materials include glass, ceramics, plastics and other single crystal materials. Injection moulding of PMMA (acrylic) for use in micro-engineered devices has also been demonstrated [6]. However, within the ultrasonic separator Pyrex and silicon wafers are used, and therefore, only the fabrication methods relevant to these materials are described further.

Bulk Micromachining

Bulk micromachining describes the technique where geometry is formed by selectively removing material from wafers by etching [7, 8, 9]. To control the etch pattern a photoresist layer is applied to the substrate, which, after exposure, is developed to remove either the exposed or unexposed areas of resist, depending on the substances used. The remaining resist creates a mask on the surface of the silicon and is used to control the subsequent silicon etch process.

Wet Etching: Wet etching processes involve the application of a chemical solution, causing exposed substrate to dissolve. As with a silicon substrate, the etchant can act either isotropically, where material is removed equally in all directions, or anisotropically, such as that achieved using potassium hydroxide (KOH), where the etchant shows a preference to certain crystal planes [7, 8, 10, 11]. With KOH etching of single crystal silicon (diamond cubic structure [12]), (111) crystal planes etch significantly slower than the other crystal planes. Therefore, for silicon wafers of $\langle 100 \rangle$ orientation, KOH etching produces trapezoidal geometries with surface set at 54.74°, corresponding to (111) planes. Due to its reliance on the crystalline structure, anisotropic etching can produce predictable geometry and a good surface finish, although the range of geometries possible is limited.

Figure 2.1(a) illustrates the use of a mask in controlling the etch pattern upon a silicon wafer and figures 2.1(b) and (c) show the result of using isotropic and anisotropic etchants, respectively. It

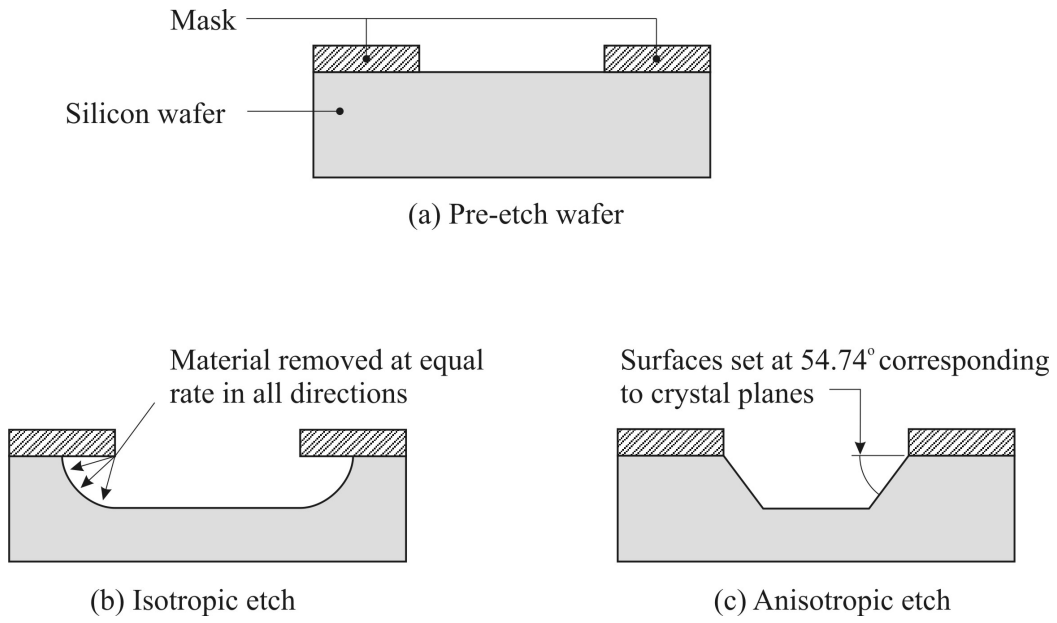

Figure 2.1: The etching process showing a) the etch mask, b) the etched geometry resulting from an isotropic etch and c) the angular geometry resulting from an anisotropic etchant.

can be seen that the isotropic etch undercuts the etch mask and produces curved sides to the etch depression, with the etch time typically determining the etch depth. With the anisotropic etch the resulting trapezoidal trench can be clearly seen and, unlike the isotropic etch, does not undercut the mask.

Dry Etching: Other etch techniques include dry etching [8, 9, 13]. For example, *reactive ion etching* uses a combination of chemical etching and ion bombardment to physically etch away material and break down molecular bonds. The resulting plasma causes highly directional etching and creates a geometry of nearly 90^{o} angles to the substrate surface. A related technique is *Deep Reactive Ion etching*, which uses a cycle of plasma and sidewall protection which is able to etch 100's of microns deep into the silicon. *Deep Cryogenic etching* also produces vertical sidewalls, but without the scalloped surfaces produced by the Deep Reactive ion etch technique. Generally these dry etching techniques are more expensive and complex than wet isotropic and anisotropic etch techniques which are used for the fabrication of the separator.

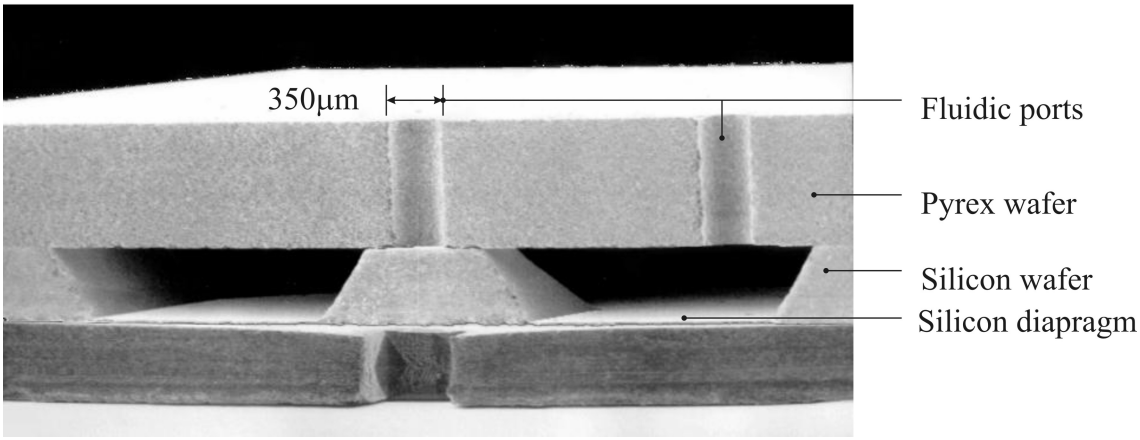

Figure 2.2: Cross-section of a micro-engineered microvalve (Nguyen et al. [14]).

Bonding: It is possible to create a device that contains complex internal geometry by building the structure from several etched wafers. Depending on the wafer materials involved, bonding of multiple wafers can be achieved, either using fusion bonding for silicon to silicon where components in intimate contact with each other are heated to $>1000^{o}$C producing an atomic bond, or anodic bonding for silicon to glass, which uses an electric field [7, 8]. Figure 2.2 shows an example of a layered structure, typical of many MEMS devices, and also shows an anisotropically etched silicon layer. The image taken is of the cross-section of a microvalve incorporated into a micro dosing system [14, 15] and uses an electrostatic actuated silicon diaphragm to control movement of fluid through the two fluidic ports.

Surface Micromachining

Surface micromachining, where the wafer is not necessarily etched, involves layers of various materials being deposited onto the substrate, for which Bustillo et al. [16] present an excellent overview. Such layers can include conducting, insulating materials and sacrificial layers onto which further layers may be added, some of which, for example, may be deposited using chemical-vapour-deposition. To introduce the basic process, figure 2.3 illustrates the deposition and patterning of a sacrificial layer (figure 2.3(a) and (b)) followed by similar deposition and patterning of a polysilicon structural layer (figure 2.3(c) and (d)). Any etched windows through the sacrificial layer create anchor points for the structural layer. Finally, acid removal of the sacrificial layer leaves the structural material intact and, depending on the process and etch patterns of the

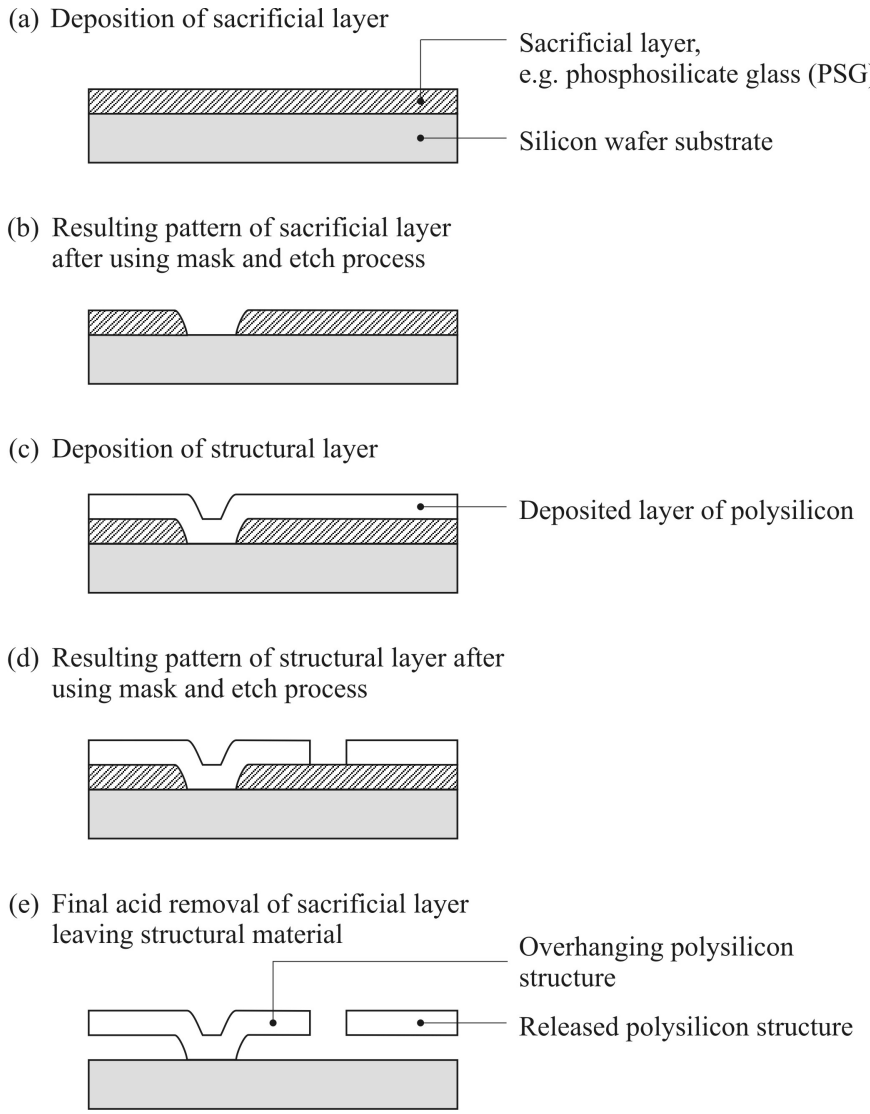

Figure 2.3: Schematics showing the production of structural overhangs and released structures using a basic surface-micromachining process.

various layers, produces overhangs or released structures as depicted in figure 2.3(e).

The use of sacrificial layers is applied to the manufacture of micro gears and similar freestanding components, as the sacrificial layer allows release of the surface micromachined or moulded structure from the base wafer. The fabrication of free-standing components and hinges makes it possible to rotate structures out of plane, creating 3-dimensional devices.

One application of surface micromachining is the fabrication of capacitative micromachined ultrasonic tranducers (cMUT's). For an example see the work developed by Stanford University [17, 18] where the use of cMUT's as an alternative to piezoelectric transducers is studied. This

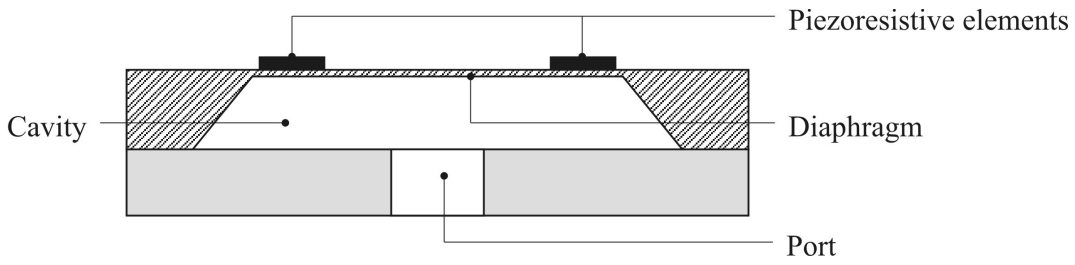

Figure 2.4: Basic MEMS pressure sensor construction.

uses surface micromachining techniques and sacrificial layers to create a diaphragm suspended over the surface of a silicon substrate and separated by a small gap; an electrode is then deposited onto the diaphragm. A voltage applied between the diaphragm electrode and wafer substrate causes electrostatic movement of the diaphragm, the excitation of which generates a sound wave. Jin et al. describe in detail the various stages involved in the fabrication of such a transducer [18].

2.1.2 MEMS Devices

Basic Device Types

As previously mentioned these devices incorporate both electrical and mechanical elements into a single device or system. A basic example of a MEMS device is a pressure sensor and typically consists of a diaphragm formed by etching [19]. This diaphragm will deflect with pressure which is sensed by, for example, piezoresistive elements deposited at certain locations on the diaphragm. Figure 2.4 shows the typical construction.

A variety of other mechanical structures and electrical sensing or actuation techniques may be incorporated into MEMS devices. For example, sensors may include a suspended mass or resonant beam structure, the deflection or resonant frequency of which, respectively, is influenced by the parameter to be measured. Depending on the mechanical structure used, the deflection or resonant frequency is then sensed by a piezoresistor, capacitor or photodetector [19, 10]. Other devices include accelerometers, micro-motors, tweezers, optical components, gyroscopes, switches and microfluidic devices.

Advantages of MEMS devices

Micromachining techniques and the ability to integrate both mechanical and electrical aspects of a device allow the creation of complex yet small MEMS devices, typically cheaper than more bulky conventional devices which are built from discrete components [9]. Indeed, MEMS fabrication has adopted already well established techniques from the IC industry. This has reduced micromachining development costs, increased device reliability and enabled the use of batch production, contributing again to reduce costs [19].

Due to low costs, some devices have the advantage of being disposable. For example, micro pressure sensors used in the medical industry can avoid the processes of cleaning and sterilisation after each use, ultimately one advantage associated with an ultrasonic separator. Bryzek & Petersen [7] mention the importance of reduced fabrication costs.

Applications

MEMS sensors have wide applications, being used for automotive applications, notably micro-engineered accelerometers in airbag systems and tyre pressure sensors, aero and medical industries. More specialised devices such as tweezers and micro-motors have applications in microsurgery and bioresearch, for example in performing surgery and manipulating tissue samples [20].

2.2 Microfluidics

Microfluidics is a subdivision of MEMS technology where micro-engineering techniques are used to create fluidic circuits used in the processing of small fluid samples. Fluid channels are typically of the order of microns to hundreds of microns and, due to the scale, the fluid flow characteristics within a microfluidic device may differ from large macroscale flow systems. In this section, the flow through channels of a similar scale to those found in the ultrasonic separator are discussed and appropriate simulation methods considered. Various microfluidic devices are also introduced, describing their principle of operation and their applications.

2.2.1 Flow Theory

Laminar Flow

When investigating fluid flow, the type of flow is typically determined by the Reynolds number which represents the relative significance of inertial and viscous forces and indicates either turbulent or laminar flow, respectively. For example, a Reynolds number up to 2300 for closed ducts indicates that viscous forces dominate and that the flow is laminar. Reynolds number is defined below [21]:

$$\mathrm{Re} = \frac{\rho v d}{\mu}, \tag{2.1}$$

where ρ is the fluid density and μ is the fluid viscosity. Also, v is the characteristic velocity and d is the characteristic length, usually average velocity and pipe diameter, respectively, for flow through a circular duct.

However, for non-circular ducts the characteristic length will typically be made equal to the hydraulic diameter, D_h:

$$D_h = \frac{4A}{P}, \tag{2.2}$$

where A is the cross-sectional area and P is the wetted perimeter. Applying this to the main channel of the ultrasonic separator which has a width of 5mm and channel depths between 0.175 and 0.250mm, we calculate D_h = 0.338 to 0.476mm. Based on a flow rate of 0.1ml/s, as used by Hawkes & Coakley [4] and applied to the estimate of the mean flow velocity, Re ≈ 38 which lies comfortably in the laminar region.

Once the condition of laminar flow is established, the velocity profile, $u(y)$, for fully developed laminar pressure driven (Poiseuille) flow can be predicted theoretically, which for flow between parallel plates is described by the following equation [22]:

$$U(y) = -\frac{1}{2\mu}\frac{\mathrm{d}}{\mathrm{d}x}(p + \rho g z)(Yy - y^2), \tag{2.3}$$

$$\text{or} \quad U(y) = \frac{6\bar{U}}{Y^2}(Yy - y^2), \tag{2.4}$$

where Y is the channel depth, $\bar{U}$ is the mean flow velocity, μ is the fluid viscosity, ρ is the fluid density, p is pressure and z is a measure of the plate inclination, where these parameters are illustrated in figure 2.5.

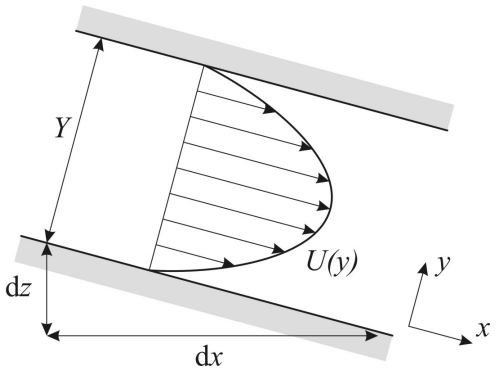

Figure 2.5: Fully developed flow between parallel plates.

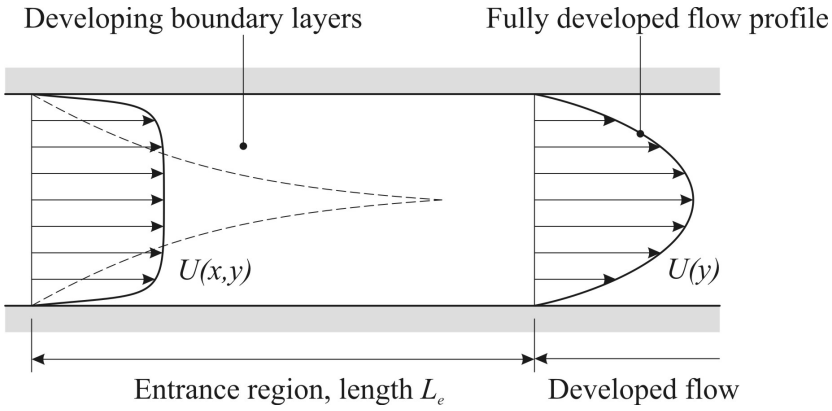

Figure 2.6: Entrance region of a duct inlet.

As fluid either enters a duct or moves past a discontinuity in the geometry such that the flow becomes disturbed or approximates a uniform velocity profile, boundary layers will begin to develop over the wall area where shear forces dominate, but as the flow moves further downstream these boundary layers eventually fill the entire cross-section of the duct. After a certain distance, known as the entrance length, the flow becomes fully developed laminar flow and can be described by equation (2.4), remaining constant as a function of x along the channel. Figure 2.6 illustrates this boundary layer growth downstream of an inlet.

The entrance length, L_e, for flow between parallel plates as shown in the figure is described by the following equation, adapted from Cebeci & Bradshaw [23], so that the characteristic lengths for d

and Re are both taken to be the channel depth:

$$\frac{L_e}{d} \approx 0.05\mathrm{Re}, \tag{2.5}$$

This gives $L_e = 0.18$ to 0.25mm based on the channel heights and flow rate given earlier, and is therefore the order of $\sim d$, which for a channel of length 14mm, typical of the main channel within the ultrasonic separator, represents no more than $\sim 2\%$ of the total channel length. However, even for creeping or very low Reynolds number flows the entrance length does not tend to zero. For example, in circular ducts the minimum entrance length is 0.6 diameters.

Transition from laminar to turbulent flow is typically taken to occur at Re = 2300 for circular closed ducts. However, Gravesen et al. [24] report that this is not always a valid assessment for flow through microchannels where the entrance length equals or exceeds the length of the device. At seemingly low Reynolds numbers the flow will be dominated by entrance type flow and therefore cannot be described by simple analytical laminar flow expressions. Considering this, the transitional Reynolds number Re_t below which developed laminar flow exists in the channel is given below for closed ducts:

$$\mathrm{Re}_t \approx 30\frac{L}{D_h} \tag{2.6}$$

For example, taking hydraulic diameter, $D_h = 0.338$mm, and length of the device, $L \approx 14$mm taken as the distance between the inlet and first outlet (see section 2.5.1 for device dimensions), this results in $\mathrm{Re}_t \approx 1240$ and therefore a maximum flow rate $Q \approx 3.2$ml/s. This is significantly larger than the flow rate of 0.1ml/s used in the Cardiff separator device suggesting, therefore, that during typical operation of similar devices the flow rate will be low enough to assume that laminar flow exists. (Some simulation work reports coefficients smaller than 0.05 as used in equation (2.5) [25, 26]. This further supports the assumption that fully developed laminar flow dominates the flow characteristics of the device.)

Although the velocity profile for flow between parallel plates has been quoted, the main channel of the ultrasonic separator has a width to height ratio $w/d \geq 20$. It is conceivable that the small height of the channel dominates the fluid flow, although the extent to which the sides of the channel influence the flow profile is not obvious. Desmet et al. [27] investigate the flow through high aspect-ratio channels, characteristic of micro-engineered fluid devices, and bring together analytical descriptions of flow. These analytical expressions indicate that across the width w of a high aspect channel, where $w > d$, the flow is characterised by narrow boundary layers either side

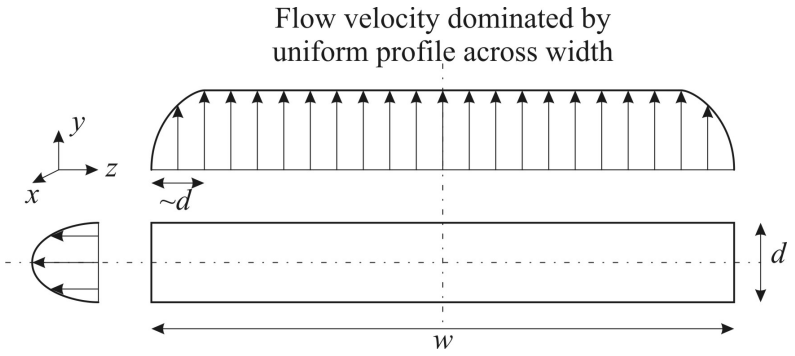

Figure 2.7: Schematic of flow profiles through a duct of rectangular cross-section, with fluid flowing in the x direction. Velocity profiles across the width and depth of the channel illustrated.

of a wide uniform flow velocity, dominating the channel flow as illustrated in figure 2.7. These boundary layers extend $\sim d$ into the flow. For a channel width of 5mm this suggests that the flow will be dominated by a uniform flow profile, unvarying across the width of the device. Within the wide uniform flow region, and from the equations presented by Desmet et al., there is negligible difference between the mean flow velocity and that for flow between parallel plates, therefore it would be reasonable to apply the parabolic flow profile described by equation (2.4).

It is recognised that acoustic streaming may disrupt the parabolic laminar flow profile, however, the presence of streaming depends on the acoustic design of the device and is explained in section 2.3.2.

Flow Phenomena Associated With Microchannels

Surface tension effects should not be a problem for fluid filled devices; however, if gas bubbles are present in the device surface tension effects can cause problems with the removal of the bubbles. Gravesen et al. [24] explain that to move a bubble obstruction a pressure drop related to the reciprocal of the channel dimension is required and so becomes significant for channels of a only few microns. Such surface tension effects therefore have implications on experimental work, although only during initial priming of a device and expelling any air. Addition of detergents reduces surface tension effects [21] and so may alleviate problems with bubble obstruction. Surface tension also gives rise to capillarity where a liquid is drawn along a small diameter duct [21, 28]. This occurs for liquids which wet a surface, where the contact angle between the liquid and surface is

acute. Where the working fluid is typically water, capillary action conveniently assists the filling of microfluidic devices, as the fluid is naturally drawn through the device without any pumping mechanism or applied pressure drop.

In the preceding pages the velocity profile (equation (2.4)) between parallel plates and within high aspect ratio micro-fabricated channels is assumed to have a no-slip condition. This is where the fluid velocity at the walls of the channel reduces to zero. For increasingly small scale channels, the continuum assumption of a fluid begins to break down and the behaviour of the individual fluid molecules becomes significant. When considering the flow of fluid at the molecular scale, the fluid molecules will skip along the surface of the channel and the no-slip assumption will not be valid when this molecular movement becomes significant compared to the flow characteristics. Gad-el-Hak [29] discusses this thoroughly and mentions the use of an *apparent* viscosity with no-slip theory which compensates for boundary slip. The slip condition and the breakdown of the continuum assumption with regard to the numerical modelling of fluid flow is mentioned in the following pages, in section 2.2.2. The continuum assumption also breaks down for high shear flows; however, Nguyen & Wereley [28] give an example at the limit of this assumption – the flow of liquid argon between parallel plates separated by 1μm and the flow drawn by the movement of one of the plates at 10^6m/s – demonstrating that most microfluidic flows can be considered as continuous as flow velocities will be several orders of magnitude smaller than this limiting case.

Influence of Suspended Particles

The discussion above is applicable to Newtonian fluids, such as water which for a given temperature have a constant viscosity, μ. However, some fluids do not exhibit constant viscosity with fluid shear stress and are termed non-Newtonian [21]. Fluids containing a particle suspension may exhibit non-Newtonian behaviour [30] and include blood, the characteristics of which Chang et al. [31] simulate for flow through microchannels.

Acoustic manipulation processes are frequently applied to the processing of low concentration samples where Newtonian behaviour can be assumed. Depending on the particles used, higher particle concentrations may sooner influence the acoustic characteristics of the fluid sample rather than the fluid flow properties. Indeed, tests investigating the feasibility of acoustic separation applied to acoustically hard sand particles have concluded that particle concentrations above 1% by weight decrease separation efficiency and separation is difficult to achieve above 5% by weight [32]. Conversely, separation of blood ($\sim 50\%$ cell concentration) has been demonstrated [33] and

although the acoustic efficiency of the process is unclear, the acoustic properties of the blood cells do not contrast significantly with the blood plasma, resulting in little distortion of the acoustic field. Therefore, the presence of a high concentration of cells is not a limiting factor in this application. It can be assumed that with the low concentrations ($< 1\%$ by wt.) processed by the ultrasonic separator, it is reasonable to assume that both the carrier fluid's Newtonian and acoustic properties predominate.

Sedimentation of particles could be possible, forming a thin layer of particles on the bottom surface of the fluid chamber. This is because particles held within a fluid carrier are subject to both buoyancy forces and drag forces, therefore, for particle densities greater than that of the fluid, in stationary flow these particle forces result in sedimentation. For fluid flow through ducts, Govier & Aziz [34] describe transition velocities which determine the degree to which a suspension is maintained by the fluid flow rate. For example, V_{M1} is the velocity above which a symmetrical (homogenous) suspension is maintained. Below this velocity gravitational effects become more significant and sediment forms as velocity decreases further. One expression given for V_{M1} is shown below, for a duct diameter d and fluid of density ρ and viscosity μ:

$$V_{M1} = 294 V_c \left(\frac{V_c d \rho}{\mu} \right)^{1/7}, \tag{2.7}$$

and where $V_c = \frac{g(\rho_p - \rho) d_p^2}{18\mu}$ is the terminal settling velocity of a particle of diameter d_p and density ρ. For typical values for water, 1μm diameter latex particles of density 1050kg/m^3 and duct of hydraulic diameter 0.338 to 0.476mm (as above), the transition velocity $V_{M1} \sim 1.5\mu$m/s. This equates to a flow rate of $Q \sim 0.002\mu$l/s which is significantly smaller than the flow rates used for the purposes of this thesis, therefore the particle suspension can be assumed symmetrical and that a sediment will not form.

2.2.2 Simulation of Microchannel Flow

Whilst much research has been undertaken to understand the characteristics of gaseous flows through microchannels (see Gad-el-Hak [29] for a general review), there appears to be limited conclusive literature discussing liquid flows. Recent studies exist which aim to determine the scale at which liquid flow ceases to be described by macro-scale or classical flow theory and the Navier-Stokes set of governing equations, which also form the basis for CFD (examples of these studies include Pfahler et al. [35], Mala & Li [36] and Peng & Peterson [37]). Judy et al. [38] and

Gad-el-Hak [20] both present an overview of such investigations which study a range of microscale channels and cross-sectional shapes, and compare experimentally measured pressure drops with values calculated using macroscale flow theory. These investigations are typically concerned with the experimental measurement of $f\mathrm{Re}$, a function of the friction factor and Reynolds number, or more commonly termed Poiseuille number. Measured values can then be compared to the value used in macroscale theory; for example, for flow between parallel plates $f\mathrm{Re} = 24$. A difference between the measured and theoretical value therefore indicates deviation from macroscale theory and the Navier-Stokes equations.

Judy et al. note that in the literature deviations from macroscale flow theory have generally been observed to occur for hydraulic diameters below 100μm, but also that more obvious changes are observed for channel sizes of the order $\sim 1\mu$m. Conclusive arguments are limited as the experimental uncertainty is often significant enough to disguise any deviation from macroscale theory should it exist.

Papautsky et al. [39] describe a model based on micropolar fluid theory which models the influence of local fluid particle motion on the flow and includes effects such as fluid rotation and wall effects which the Navier-Stokes equations do not consider. The modelled results match experimental data much more accurately, although, in the study at the Reynolds number and flow rate appropriate for the purposes of this thesis, the more traditional Navier-Stokes equations are considered to be sufficiently accurate.

Computational modelling has been applied to simulate microchannel flow, both for laminar [40, 41, 42] and turbulent flows [43] in microchannels. Commercial numerical packages based on the Navier-Stokes equations have been applied to the analysis of fluid flow in microfluidic systems; for example, aspects of fluid flow through injector systems incorporating channels of dimensions $200\mu m$ [44, 40] and micromixer channels down to dimensions of $70\mu m$ [43] have been simulated. Van Akkers et al. [40] describe in detail the application of the commercial package Flow3D/CFX, whilst Koch et al. [45] links this software to the finite element package ANSYS to model a micro-machined valve. Software developments by ANSYS Inc. have now created a package for multi-physics systems, developed with MEMS technology in mind and capable of simultaneous simulation of solids, fluids and various other fields and mediums [46].

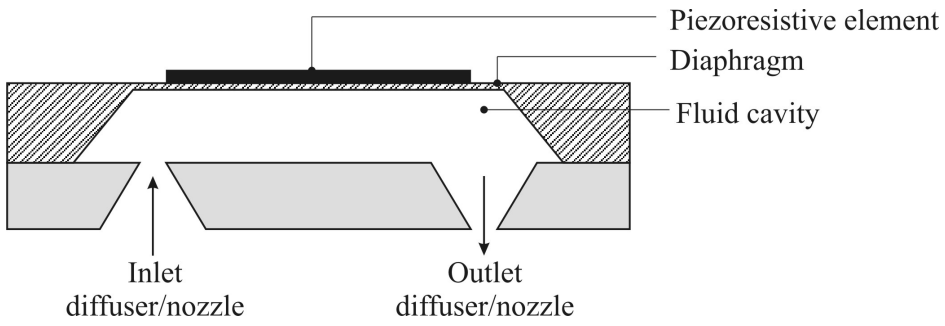

Figure 2.8: Schematic of micropump relying on diffuser/nozzle flow rectification.

2.2.3 Microfluidic Devices

Microfluidics is a sub division of MEMS which consists of devices designed for fluid flow. An important application for such devices is in "miniaturised total chemical analysis systems" (μTAS) or "lab-on-a-chip" devices. Such devices incorporate a variety of integrated fluidic components, including valves, pumps and nozzles, which can be fabricated together on a single substrate. The principal components are described below:

Microfluidic Components

Valves: Micro-valves generally rely on a diaphragm or flap opening and closing against a duct face, using piezoelectric (such as that demonstrated by Koch et al. [45, 47]), electromagnetic, thermopneumatic or other actuation methods compatible with the micron scale of the device. Although not preventing negative fluid flow, diffuser/nozzle ducts can be used to encourage positive fluid flow with the advantage of having no moving parts and zero power consumption, relying on the different fluid losses incurred when orientated as a diffuser or nozzle; i.e. for the same pressure drop, the nozzle will permit a greater flow rate than orientated as a diffuser. Figure 2.8 illustrates a pair of such ducts within a pump system, rectifying the flow [28].

Pumps: There are two principal mechanical methods employed to pump liquid through microchannels, namely actuation of a plug along a channel and actuation of a diaphragm [48]. The former method uses either a liquid metal or bubble plug actuated by electrodes and an array of heaters, respectively. In the case of the bubble plug the heaters also serve to form the bubble. With

the diaphragm method, the diaphragm is actuated by a piezoelectric layer, the motion of which causes variations in the internal volume of the device and therefore fluid displacement. A pair of one-way valves ensures positive fluid displacement; these are either etched flap valves or diffuser ducts (see figure 2.8). Another method to ensure positive fluid displacement demonstrated by Husband et al. [49] is to use a series of diaphragms which operate peristaltically. Non-mechanical pumps also exists for certain fluids, for example, taking advantage of electrostatic forces [50].

Injectors: Injectors are pumps which deliver droplets using the growth of a bubble to isolate a discrete volume of liquid and force it through a nozzle [51]. Again, a heater is used to control the formation of the bubble.

Flow sensors: An important component in Microfluidic systems is a flow sensor. Examples of how the devices operate include measuring the transit time of a heat pulse and sensing the pressure drop across a restriction [51]. Nguyen presents a good introduction to the variety of sensing techniques available [52].

Mixers: In Microfluidic applications laminar flow is dominant; therefore mixing, for the purposes of say drug delivery and chemical tests, generally relies on diffusion processes [53, 54]. However, micromixing has been realised on a microscale using turbulent flow induced by the use of jets, increasing the efficiency of mixing [43].

Reaction Chambers: Reaction chambers realised on a microfluidic scale have applications in polymerase chain reaction (PCR) DNA analysis systems. In such systems, the microfluidic chip will include microchannels and heaters which facilitate controlled reactions between DNA samples and reagents. DNA analysis relies on multiple reactions, therefore a chip incorporating multiple reaction chambers and complete fluid handling, e.g. pumps, is desirable [55, 56].

Silicon Micro Turbines: Although unlikely to be incorporated into a μTAS device, micro-scaled gas turbine engines have been created, and are an interesting concept. These can produce 10-50W of electrical power and have rotation speeds of $\sim$1.2x10^6rpm, such examples developed by the Massachusetts Institute of Technology [57, 58]. As for conventional turbines, micromachined turbines include bearings, compressor, turbine and combustion chamber elements and potentially have applications in powering portable equipment and in space vehicle propulsion systems.

Applications of Microfluidic Devices: Injectors are found in commercial inkjet printer heads and have been considered for use in biomedical and chemical handling for the accurate dispensing of substances [20]. However, applications for microfluidic devices become far more diverse when a selection of devices can be integrated, so that a fluid sample can be prepared and processed by a single device (μTAS). For example, medical applications, including drug delivery systems, may incorporate micropumps, valves, micromixers and sensors on a single chip. This is also the aim with DNA analysis systems [55, 56], chemical and biochemical detectors, where processing of clinical samples or bacterial agents through a micromachined device may be achieved quickly and require only small samples. An introduction to μTAS devices is given in the following subsection.

Micro Total Analysis Systems (μTAS)

With the development of microfluidic components, analysis systems composed of a series of such component devices fabricated on a single chip becomes feasible. Manz et al. [59] gave an early review of such a concept, miniaturising total analysis systems (TAS) in order to improve the performance of the process, for example, in environmental monitoring. They explain that the reduction of length scales reduces the transport times, the consumption of liquid samples and reagent, and also increases the speed of sample processing.

More recent reviews [60, 61] clearly associate μTAS with micro-fabricated microfluidic devices. Auroux et al. [61] describe how various microfluidic processing stages such as injectors and mixers have been applied to sample processing, especially in biochemical analysis, referring to a vast number of publications. For example, the analysis of DNA within microfluidic devices has been investigated by Bu et al. [56] describing the development of a chip for DNA amplification, a device which is portable and provides rapid analysis when compared to the conventional macro-scale equivalent. This particular device incorporates a micropump, reaction chambers and various sensors, demonstrating their integration into the single chip.

Reyes et al. [60] discuss the development of micro-fabricated devices with reference to μTAS and also how the integration of various devices or processing stages may be achieved, and several types of fluid interconnections are mentioned, including the use of capillary tubing between micro-fabricated system components. Schabmueller [62] describes how wafers may be stacked in order to incorporate multiple fluid processing and operation stages, and this was demonstrated with the fabrication of a chemical reaction system incorporating pump, mixing and sensor components on a single chip. This avoids additional fabrication steps which would otherwise be required to

fabricate individual devices and to form fluid connections between these devices. It also avoids introducing excessive dead volume as the entire fluid network consists of etched micro-channels.

Certainly, the growing interest in μTAS fuels the development of microfluidic devices and research into microfluidic flow, the development of individual microfluidic components providing more possibilities and solutions for μTAS devices.

2.3 Acoustic Separation and Associated Phenomena

2.3.1 Acoustic Radiation Forces

A particle within an acoustic field experiences an acoustic radiation force, which is a non-linear second order effect. Gol'dberg [63] explains that a particle within an acoustically oscillating fluid medium does not necessarily oscillate as one with the medium. Relative movement between the particle and surrounding fluid results in scattering of the acoustic wave and momentum transfer between the fluid and particle. The momentum transfer equates to a force experienced by the particle and is referred to as the acoustic radiation force.

This phenomenon was first recorded by Kundt & Lehmann [1] in the 1870s and recently the scientific community has found new impetus to apply the phenomenon to particle manipulation processes. For example, it is acoustic radiation forces which are used to concentrate particles within the ultrasonic microfluidic separator described later in this chapter.

King [64] derived an expression for the acoustic radiation force acting on incompressible spheres within a plane wave, then Yosioka & Kawasima [65] extended this for compressible spheres. It was shown theoretically that the radiation force acting on a sphere of radius R due to a plane travelling wave, wave number k (where $k = 2\pi/\lambda$) is dependent on $(kR)^4$, which for $R \ll \lambda$ is very small [63] (Gröschl [66] presents a similar argument). However, in a standing wave the force is instead dependent on a kR term and therefore becomes significantly larger. The practical use of radiation forces is therefore limited to standing waves and resonant fields.

For particles suspended within a fluid carrier and in a standing wave propagating in the y direction, the radiation force F_{ac} acts in the y direction and is also a function of the y position. It is quoted by Gröschl [66] and others in a form similar to the following:

$$\begin{aligned} \langle F_{ac}(y)\rangle &= {F_{ac}}^0 sin(2ky), \\ \text{where } {F_{ac}}^0 &= \frac{4}{3}\pi\langle\bar{\varepsilon}\rangle kR^3\phi. \end{aligned} \tag{2.8}$$

In the above equation $\langle\bar{\varepsilon}\rangle$ is the time averaged energy density which can also be expressed as a function of the acoustic pressure amplitude. k is the wave number and ϕ is the acoustic contrast factor, defined as:

$$\phi = \frac{5\rho_p - 2\rho_f}{2\rho_p + \rho_f} - \frac{{c_f}^2\rho_f}{{c_p}^2\rho_p}. \tag{2.9}$$

where ρ_p and ρ_f are the particle and fluid densities, and c_p and c_f represent speed of sound for the particle and fluid mediums.

Gor'kov [67] derived an expression for the radiation force acting on a particle in an arbitrary field. The following is taken from Gröschl [66]:

$$\langle F_{ac}(x,y,z)\rangle = -\nabla\langle\phi^G(x,y,z)\rangle, \tag{2.10}$$

$$\text{where } \langle\phi^G(x,y,z)\rangle = -V\left[\frac{3(\rho_p-\rho_f)}{2\rho_p+\rho_f}\langle\bar{E}_{kin}\rangle - \left(1-\frac{{c_f}^2\rho_f}{{c_p}^2\rho_p}\right)\langle\bar{E}_{pot}\rangle\right] \tag{2.11}$$

where V is particle volume, $\langle\bar{E}_{kin}\rangle$ and $\langle\bar{E}_{pot}\rangle$ are the time averaged kinetic and potential energies at a point in the field and ϕ^G is the gradient of radiation force potential. These equations are generally true in the case of $kR \ll 1$ [63].

Referring to equation (2.11), if the velocity and pressure fields are known it is possible to derive the time averaged kinetic and potential acoustic energy densities. For a progressive wave the time averaged force $\langle F_{ac}\rangle$ tends to zero, as the gradients of both the time averaged pressure and velocity fields are small, therefore leading to negligible displacement of particles. In contrast, in a plane standing wave the expression simplifies to equation (2.8) (part of this derivation is given by Yasuda [68]) and is a 1-dimensional description of the radiation force with a rigid boundary existing at $y = 0$.

To understand the physical influence of the radiation force on particles, figure 2.9 illustrates the spatial relationship between the acoustic pressure field of a standing wave and radiation force, shown over a distance of $\lambda/2$. It can be seen from the diagram and equation (2.8) that the radiation force varies at twice the spatial frequency of the acoustic wave and can also act in a positive or negative y direction.

Figure 2.9 illustrates the case for $\phi > 0$, typical for solid particles, where the radiation force causes particles to converge towards the nearest pressure node which are sites of low potential energy, the force also being a function of position in the wave. For example, particles positioned in region A experience a downward force, away from the pressure anti-node and towards the pressure node, at which point the force reduces to 0 and, assuming no other disturbances to the particles, they come to rest. Particles in region B however experience an upward force, again away from the anti-node and towards the pressure node. In this system, particles are repelled from the anti-nodes and attracted to the nodes where the particles agglomerate.

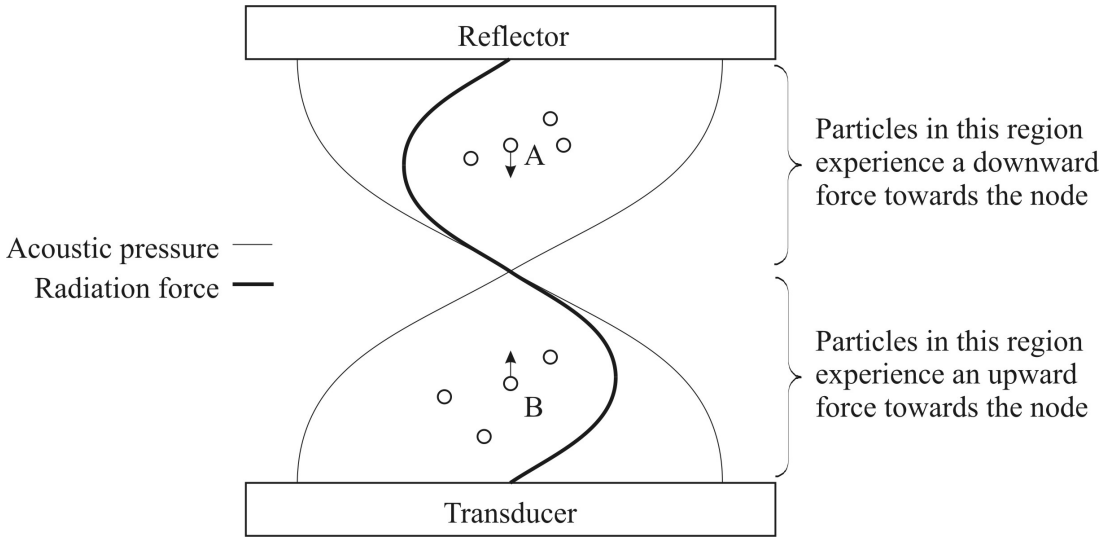

Figure 2.9: Acoustic force in a standing wave.

Conversely, for particles where $\phi < 0$ such as for benzene liquid phase droplets in water [69], equation (2.8) shows that these particles are instead drawn to the pressure anti-node. A more complex case arises for gas bubbles which although typically $\phi < 0$ in their equilibrium state, move to either the pressure node or anti-node depending on bubble size [70, 71]. This is associated with the bubble itself resonating and the resulting periodic change of the gas density. For the application with which this thesis is concerned, solid particles are used resulting typically in $\phi > 0$ and movement towards the pressure nodes.

Measurement of Acoustic Radiation Force

Generally, literature investigating acoustic radiation force experimentally have demonstrated a good level of agreement with the theory presented here [72, 73]. However, some discrepancies with the theory have been discussed, for example, by Yasuda & Kamakura [74] who observed that for particles of diameter less than 5μm, the linear dependence of the acoustic force on the volume, V, of a particle begins to fail. This discrepancy was explained by considering the existence of a shell around the particle increasing the apparent radius of a particle, R', one possible cause being a viscous fluid boundary layer. The thickness of the boundary layer, δ, based on Yasuda and Kamakura's paper, can be calculated as follows:

$$\delta = \sqrt{\frac{2\mu}{\rho_f \omega}} \tag{2.12}$$

Based on this proposed explanation, for an operating frequency of approximately 3MHz ($\omega = 2\pi f$) and fluid parameters based on those of water, the boundary layer thickness of a particle is $\sim 0.3\mu$m, where the apparent radius $R' = R + \delta$. This example translates to a 50% increase in radiation force for a $2\mu m$ particle, down to a 9% increase for a $10\mu m$ radius particle. However, this hypothesis does not consider streaming flows which are commented on in section 2.3.2, and which provide another explanation for the behaviour of small particles.

Secondary Radiation Force

Particles within an acoustic field experience forces other than the primary acoustic radiation force. The primary radiation force as previously discussed is a result of the interaction between the oscillating fluid and scattering from particles, however, a particle can also be influenced by the scattered field from a neighbouring particle [66, 75]. The radiation force resulting from these particle interactions is known as Bjerknes force or secondary radiation force (although in the literature this is occasional used as a collective term to describe lateral acoustic forces resulting from both particle-fluid and particle-particle interactions). The magnitude of the particle interaction force is a function of the acoustic velocity and pressure profiles, such that particles aligned with the direction of sound propagation will experience a repulsive force whilst those aligned normal to sound propagation experience an attractive force.

The force is also a function of the reciprocal of particle spacing and therefore becomes negligible for a low concentration suspension where particle spacing is large. However, as particles begin to agglomerate onto a plane due to the primary radiation force reducing particle spacing, the secondary radiation forces increase. This means that for particles gathered at the pressure node, they are also forced together laterally by Bjerknes forces into clusters or as a membrane on the nodal plane. As these secondary radiation forces are still small relative to the primary radiation force, it takes a significant time to form particle clusters. Therefore secondary radiation forces have been disregarded in some analyses of flow-through devices where particles are exposed to the acoustic field for a short, finite length of time just sufficient to move particles to the nodal planes, or where particle concentration is low [76].

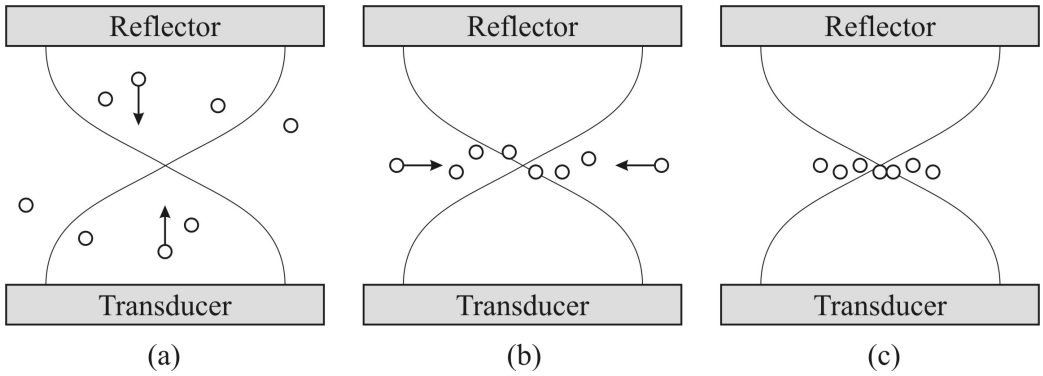

Figure 2.10: Lateral radiation forces acting on particles.

Lateral Radiation Forces

The preceding pages have illustrated the effect of acoustic radiation force in terms of a simple acoustic field giving rise to an axial radiation force, aligned in the direction of the acoustic propagation. However, in practical systems lateral variations in the acoustic field typically occur and give rise to lateral radiation forces [66, 77].

To demonstrate the movement of particles under these forces, figure 2.10(a) illustrates the motion of particles within a standing wave, initially subjected to the axial primary radiation force. For a positive value of ${F_{ac}}^0$ the particles are forced towards the pressure node until they lie in the nodal plane depicted in (b). Similarly, variations in the acoustic field within the nodal plane create a radiation force potential, ϕ^G, which creates a radiation force as described by equation (2.11) [78]. This force is perpendicular to the axis of the sound wave and, depending on the nature of the acoustic field, moves particles towards a single point (c) or into striations as observed during preliminary experiments with the ultrasonic separator. The source of these lateral variations are due to, for example, the cavity boundaries and divergence of the wave [66].

Schram [78] comments that depending on the geometry of the resonating system and acoustic beam, lateral radiation force could be comparable to the axial component. Various experimental investigations have been undertaken to measure or characterise lateral radiation force [77, 79, 80, 81]. For example, Whitworth & Coakley observe the lateral movement of particles within a cylindrical cavity with results comparing well with the analytical description of the acoustic field. Woodside et al. [80] measure lateral forces within a rectangular resonator and compare this

with the axial radiation force, revealing 100-fold difference between the axial and smaller lateral forces. With a similar system, Woodside et al. [81] also measure the amplitude of displacement of the reflector and transducer surfaces and link lateral variations in displacement amplitude to the lateral movement of particles within the device, with the resonant patterns on the reflector surface explained in terms of acoustic shear waves. More recently, Lilliehorn et al. [82] use the near-field interference pattern of an acoustic field to give rise to lateral variations and high lateral forces to trap particles in 3 dimensions.

In summary, lateral radiation forces are shown in the literature to be caused by non-uniformities in the acoustic field which themselves may be generated by a variety of resonant effects, including the fluid cavity boundary and geometry, near-field interference and boundary shear-waves. Depending on the design of the resonator and cause of the lateral variations, lateral radiation forces may become comparable to the axial component of radiation force.

2.3.2 Acoustic Streaming

Acoustic streaming describes the bulk motion of fluid caused by an acoustic field. These flows are caused by attenuation of the acoustic field where acoustic energy is dissipated into the fluid in the form of momentum. As discussed by Lighthill [83], attenuation occurs either in the bulk of the fluid or due to the presence of a solid boundary, each leading to different forms of streaming flows (see also [84, 85]).

Acoustic streaming is discussed as it potentially influences the operation of the ultrasonic separator. If significant, any fluid currents generated by the acoustic streaming may influence the movement of particles relative to the acoustic node, as observed in other devices [86, 87, 88].

Streaming in an unbounded system

This is typically large scale streaming where the attenuation of sound as it passes through a medium creates a radiation pressure gradient creating a fluid motion away from the acoustic source. Zarembo [89] refers to this type of streaming as Eckart streaming, although this phenomena is also termed “quartz wind” or “sonic wind”. Depending on the nature of the acoustic source and power transmitted, the streaming can develop into a turbulent jet [83].

Streaming in bounded systems

Schlichting Streaming: Attenuation of the acoustic energy also occurs with the presence of solid surfaces such as solid obstacles or system boundaries. Due to the attenuation caused by a solid surface, streaming forces are created in the region immediately adjacent to the surface, creating flow within a boundary layer, often referred to as Schlichting streaming. For example, a wave propagating through a channel will induce streaming along the walls of the channel.

Rayleigh Streaming: In the special case of a standing wave the streaming velocities are greater than those for a progressive wave and create vortices within the boundary layer. The streaming flow adjacent to the main body of fluid is known as the mean slip velocity, $\bar{u}_s$, which always flows towards the velocity nodes and induces vortex flows in the main body of the fluid. These Rayleigh streaming vortices are typically $\lambda/4$ deep and are positioned between the nodal planes of the standing wave. Figure 2.11(a) illustrates the pattern of Rayleigh streaming vortices which are observed in a simple rectangular cavity showing both the Schlichting boundary layer vortices and the larger vortices which they induce. Rayleigh [90] provided much of the theoretical work describing the occurrence of this phenomenon between two planes, particularly the vortices that accompany the boundary layer streaming. In narrow channels where the calculated boundary layer streaming thickness approaches the same order of magnitude as the channel width, the boundary layer streaming will suddenly dominate, disguising any Rayleigh type streaming which would have been predicted by the original theory [91].

Figure 2.11(b) represents the same pattern of streaming flow as (a), but transposed to a high aspect ratio channel such as the ultrasonic separator where the height of the channel is $\lambda/2$ and, indeed, Rayeigh type streaming flows have been observed in micro-scale high aspect ratio devices such as those investigated by Spengler et al. [88].

Significance of streaming velocity

Streaming will influence acoustic particle manipulation processes as the streaming flow imparts a drag force on particles, which is significant if of the same order as radiation forces. To determine the magnitude of the streaming velocity and therefore the significance of the flow, slip velocity can be calculated for Rayleigh streaming and is defined as the relative tangential velocity between

(a) Rayleigh streaming in simple rectangular cavity

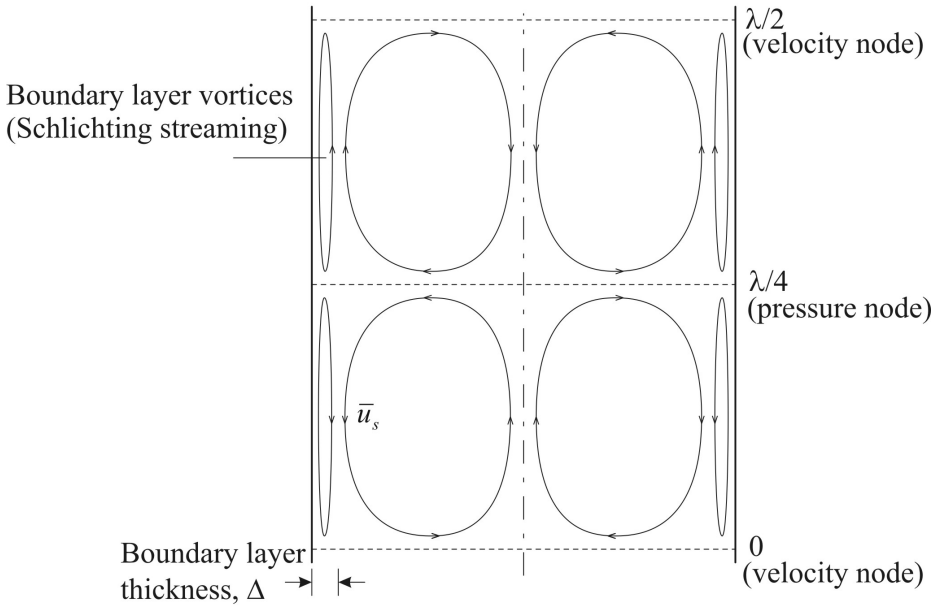

(b) Rayleigh streaming in a high aspect ratio, λ/2 deep cavity

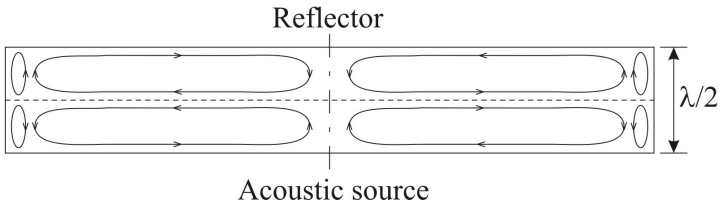

Figure 2.11: Rayleigh streaming in (a) a simple long rectangular cavity and (b) a high aspect cavity such as the ultrasonic separator where streaming pattern assumed to be consistent with (a) and classic Rayleigh streaming flows (not to scale, boundary layer thickness estimated to be of the order of 1μm or less).

the wall and streaming motion immediately beyond the boundary layer [83, 89, 90], quantified as follows:

$$\bar{u}_s = -\frac{3}{8}\frac{{u_0}^2}{c}\sin(2ky). \tag{2.13}$$

It can be seen that the slip velocity depends on acoustic particle velocity amplitude u_0 which in turn depends on the strength of the acoustic field chosen for the particular application. As the acoustic energy increases, the streaming velocity as well as the radiation force also increase, complicating the relative significance of each effect. However, using the acoustic impedance transfer model of Hill et al. [2] (see section 2.5.2) and entering typical operating conditions, the acoustic velocity amplitude is of the order 1.2m/s, from which the maximum value of $\bar{u}_s$ is 0.36mm/s.

Similarly, the boundary layer thickness as given by Zarembo [89] is:

$$\Delta = 1.9\left(\frac{2\mu}{\rho\omega}\right)^{1/2}, \tag{2.14}$$

which for a frequency of ∼3MHz results in a boundary layer thickness of $\Delta = 0.6\mu$m.

The Cardiff device [4] operates using 0.1ml/s of fluid flow through the main channel and, based on the fluid channel geometry of the Southampton device, this corresponds to a mean flow velocity of 80mm/s. This is large compared to the maximum streaming slip velocity of 0.36mm/s, calculated above. However, this streaming velocity calculation assumes that the acoustic source extends the width of the channel and is pistonic, which is not necessarily true in the practical system. Therefore, in the absence of a more accurate approach, equations (2.13) and (2.14) are considered approximations only when calculating the scale of acoustic streaming. In summary, although Rayleigh type streaming may be present in the high aspect ratio ultrasonic separator chamber, it is likely to be characterised by a low slip velocity having a minimal influence on particles and, besides, may not conform to the ideal Rayleigh patterns illustrated. Therefore, it is deemed more appropriate to consider Rayleigh streaming qualitatively for the purposes of this thesis.

Streaming flows are also generated in the vicinity of particles as losses are induced by the walls of a particle. Danilov & Mironov [92] present a useful analysis of the relative significance of the drag force induced by this localised streaming and the acoustic radiation force, which when coupled are termed the total mean force on a particle. In their analysis they define the viscous wave penetration depth where ν is kinematic viscosity,

$$\delta = \sqrt{\frac{2\nu}{\omega}}. \tag{2.15}$$

By considering the relative magnitude of δ and particle radius R, the contributions of the radiation and streaming drag forces to the total mean force are determined, concluding that in a plane standing wave for $\delta \ll R$ streaming is negligible and the mean force can be described by Gor'kov's equation (2.11) for radiation force. However, for $\delta \geq R$, streaming becomes increasingly significant and drag dominates the total mean force experienced by a sphere or particle. Applying equation (2.15) to water at 3MHz results in $\delta = 0.3\mu$m, therefore in order to avoid considering streaming flows, particles of radius $R \gg 0.3\mu$m must be used.

Equation (2.15) is identical to the boundary layer depth used by Yasuda & Kamakura [74]. Although the theory presented by Danilov & Mironov is more comprehensive, the observations of Yasuda & Kamakura do record a divergence from equation (2.11) for decreasing particle sizes and this suggests that streaming may in part explain their observations. Related to these boundary layer losses, Gröschl [66] summarises the work by various authors describing analytically the effect of viscosity on radiation force (for example see Doinikov [93]). The conclusions drawn from this source are consistent with the Danilov & Mironov analysis presented here and equation (2.15).

2.4 Applications and Simulation of Radiation Forces

Due to the ability to control the movement of particles, acoustic radiation forces have been applied to the manipulation of particles including filtration and fractionation processes. This section gives a brief introduction to particle processing based on established processes as well as alternative techniques, examples of which are devices encompassing acoustic radiation force phenomena. Further to this, a more thorough description is given regarding the various devices which exploit acoustic radiation forces and principle of their operation. The various modelling techniques used to describe and predict the performance of these acoustic devices are of great relevance and are also described.

2.4.1 Overview of Particle Processing

A brief introduction to established particle processing techniques, predominantly separation, is given below, (for examples on established techniques see books by Belter et al. [94] and Svarovsky [95]) and can be grouped into one of two principles: filtration or sedimentation [96] where most methods can be operated as a continuous or batch process. Further to this is the aggregation of particles using an externally applied field, such techniques also extending to more refined particle manipulation strategies.

Filtration

Filtration methods use a permeable medium through which the fluid phase passes depositing the solid phase either on the surface (cake) or within the filter medium (deep bed). Therefore, this method is controlled by the relative sizes of the suspended particles and filter pores. One of the main disadvantages associated with filters is the reduction in flow rate as the cake layer builds up. This can be avoided in some applications by directing the flow parallel to the filter membrane so that the surface is constantly swept by the flow and is essentially self cleaning.

Sedimentation and Aggregation

Sedimentation relies on the difference between the specific gravities of the solid and liquid phases, such as in the simple case of a settling tank. Whilst the rate of separation can be increased as with a centrifuge, the control of the process is limited by the properties of each phase. To assist the

process, another constituent which separates more readily than the suspended particles and to which the particles attach can be introduced. Flotation is one example, where the solid phase particles attach themselves to gas bubbles introduced into the suspension [97]. These bubbles are then transported to the surface where the particles are collected.

Field-Assisted Aggregation and Manipulation

In the more general case of sedimentation or aggregation, solids held in suspension can be collected by taking advantage of the difference between other properties of the solid and liquid phases, rather than relying on gravitational effects alone. Examples include magnetic separation, electrophoresis and acoustic aggregation which are all field assisted methods and are typically non-invasive techniques.

Karumanchi et al. [98] review such aggregation methods with an emphasis on biotechnology. For example, magnetic separation is one of the principal methods discussed by Karumanchi et al. and relies either on particles (or cells) being inherently magnetic or by introducing a magnetic constituent to which the particle or cell can become attached, similar to flotation techniques. Application of a magnetic field is then used to separate the magnetic particles aiming to either create an aggregate or separate from other particles or cells less magnetically active. Similarly, electrophoresis is related to the magnetic technique, but instead relies on particles having an electric charge allowing particle movement to be controlled by an electric field.

Dielectrophoresis is another particle manipulation technique, but is distinctly different to electrophoresis in that it does not rely on the charge of a particle, instead relying on the ability of a particle to be polarised relative to the surrounding electrolyte. When a non-uniform electric field is applied, the dielectric properties of the particle cause it to experience a force, either towards the point of higher or lower electric field, depending on the relative permittivities of the electrolyte and particle media.

In general, these methods find a range of applications, including food and water processing. In biotechnology these methods have been realised on a microfluidic scale and are effective for separation between different molecule/cell types (fractionation) as well as between phases, electrophoresis notably finding applications in DNA analysis [28], and dielectrophoresis used in medical diagnostics [99].

2.4.2 Review of Ultrasonic Devices

This section describes the range of devices which rely on acoustic radiation forces. These devices accomplish various tasks including the separation, fractionation or manipulation of particles or bubbles. Acoustic streaming has also been exploited in some devices and is also mentioned.

Devices Using Radiation Forces

In the simple case acoustic radiation forces can be used in a batch mode to concentrate particles or cells which then sediment under gravity. Examples include the clarification of blood plasma by Cousins et al. [33] who use a tubular transducer system where a radial standing wave is set up in a vertically orientated tube containing the blood sample. As blood cells begin to concentrate along the centre of the tube at the pressure node, the cell clusters fall as sediment and after $\sim$6 minutes of irradiation produced plasma of 99.7% clearance, approaching that possible using a centrifuge. A similar but commercially available system is the BioSep system of AppliSens [100, 101] designed to process large volumes of cell culture of up to 200litres/day as reported by Gorenflo et al. [102].

Other devices used to operate a continuous separation process, but without relying on sedimentation, have been fabricated and include flow-through devices in which a particle suspension is continuously fed into the device and processed. 'h'-shaped devices are an example of flow-through devices, as reported by Bohm et al. [103], Benes et al. [104] and Hill & Wood [3]. The typical configuration is shown in figure 2.12 and demonstrates that as particles enter the chamber they become held within acoustic nodal planes adjacent to the lower wall, the multiple number of nodes indicating that the height of the channel is significantly greater than the acoustic wavelength. Fluid is drawn through two (or more) outlets with one outlet aligned with the inlet (lower outlet) and another offset (upper outlet). The fluid motion passing through the outlets gives rise to fluid drag forces acting on the particles, the flow through the lower outlet associated with drag acting predominantly parallel to the transducer and perpendicular to acoustic radiation forces, the upper outlet associated with both parallel and axially aligned drag forces. The acoustic radiation forces balance the axially acting drag forces and so the particles are prevented from being drawn through the upper outlet creating clarified flow. However, drag forces acting parallel to the transducer are not resisted and so particles are drawn along the nodal planes and through the lower outlet, allowing a particle concentrate to be formed.

Another method to allow continuous operation was used by Tolt & Feke [69] who used frequency

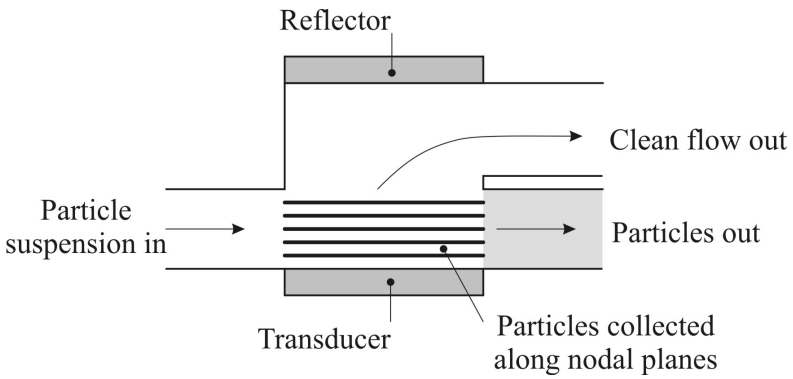

Figure 2.12: Operation of flow-through h-shaped particle separator (Hill & Wood 2000).

sweeping, where varying the acoustic frequency over a small range and using a saw-tooth function caused movement of the nodal planes in the direction of acoustic propagation. Therefore, particles could be continuously fed into the chamber and then carried by an acoustic node to an outlet. A schematic of this process is shown in figure 2.13 illustrating the movement of particles towards one end of the chamber leaving clarified fluid to be extracted at the other end. It also shows that transducers are positioned at both ends of the chamber, one to drive the acoustic field and the other as a reflector which can be used to monitor the resonance via an oscilloscope.

More recent studies have used small scale devices, typically involving chamber depths of 100's of microns. This scale is applied to the generation of half or quarter-wavelength fluid resonance modes and is suitable for rapid processing of small samples and possible integration with developing μTAS technology. For example, within a half-wavelength device tested by Hawkes & Coakley [4] particles are concentrated along the centre of the processing chamber. Outlets are positioned such that they extract different regions of the fluid, these regions corresponding to the subsequent particle stream and clear fluid streams. The device studied within this thesis is based on a similar operating principle, although its design, operation and fabrication is explained more fully in section 2.5.

As well as separation/clarification of particles/fluid, fractionation of different particle types is possible as demonstrated by Gupta et al. [105]. Here, two particle types, polystyrene and low-density polyethylene with similar densities were used which, due to the difference in their compressibility, had positive and negative acoustic contrast factors ϕ respectively within a carrier fluid of a certain wt% water to glycerol and so could be driven to different parts of the standing wave. Within a

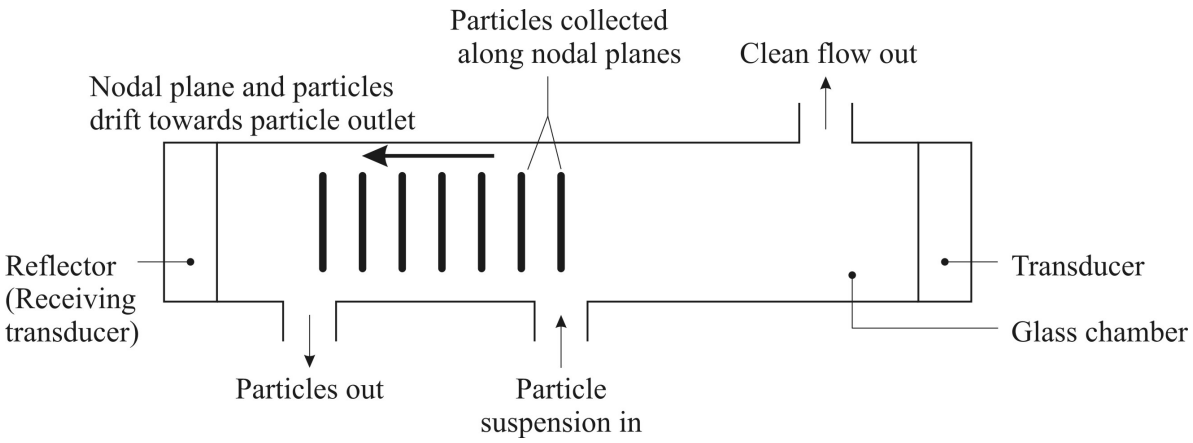

Figure 2.13: Collection of particles using acoustic radiation force and frequency sweeping (Tolt & Feke 1993).

half-wavelength device, this resulted in one type of particle collecting at the centre of the chamber (pressure nodal plane) and the other type moving to the top and bottom walls of the chamber (anti-nodal planes). Subsequent separation of the particles was then possible using flow splitters to extract specific portions of the fluid. Similarly, separation of lipid particles from blood cells (erythrocytes) has been demonstrated by Petersson et al. [106]. This relies on the lipids having a negative acoustic contrast factor and moving away from the erythrocytes which have a positive value. This application is relevant to the cleansing and recycling of blood during surgery.

Fractionation has also been demonstrated by Johnson & Feke [107] by exploiting variation in particle acoustic contrasts, but relies on each particle type experiencing a different force magnitude, influencing speed of response to the acoustic field. Different particle types move through the acoustic field at different rates and become fractionated across the chamber depth. Application of fluid flow orthogonal to the acoustic field can then carry the particles to an array of outlets. A more complicated technique is described by Mandralis et al. [108] demonstrated using polystyrene particles, but once the particles are fractionated *across* the chamber, introduction of a laminar flow profile can carry particles at different speeds and spreads the particles out along the *length* of the chamber. Ultimately, particles of zero contrast are carried to one end of the chamber and graded along the chamber length through to high contrast particles carried to the other end of the chamber. To enable fractionation, such devices require the use of half or quarter-wavelength sized chambers containing only one pressure node.

The feasibility of acoustic radiation force assisted separation with biological samples has been conclusively demonstrated; for example, Pui et al. [109] aggregated mammalian cells and Gaida et al. [110] investigated the acoustic fractionation of viable and non-viable cells. A range of other biological applications have been discussed by Coakley et al. [111]. In general, cell viability is not affected during sound irradiation, i.e. cells are not significantly damaged.

Lateral radiation forces have also been used in the 2-dimensional trapping of particles. Spengler & Coakley [112] and Morgan et al. [113] used the primary radiation force first to move particles to a nodal plane, then to form clusters on the plane due to lateral radiation forces strong enough to withstand fluid flow and associated fluid drag forces. Trapping of particles has also been demonstrated using lateral forces arising from near-field interference patterns of the acoustic field [82].

Gupta & Feke [114, 115] investigate the trapping of particles against a fluid flow, but aided by the presence of a porous mesh. Although the pores are larger than the particles which are captured, the particles have a tendency to become trapped due to a number of mechanisms brought about by the acoustic field. For example, secondary radiation forces are believed to act between the mesh fibres and particles causing the particles to adhere to the mesh fibres or at least become obstructed by the fibres and preventing the particles being flushed through by the fluid. Wang et al. [116] test this trapping approach on mammalian cells, allowing cells to be collected and separating them from the effluent stream and other smaller unwanted products.

Whilst all of the above deal with the manipulation of solid particles, liquid phase and gas phase particles can also be controlled using radiation forces. For example, Abe et al. [117] could control the motion of bubbles within a standing wave, moving the bubbles to acoustic pressure nodes.

Devices Using Quarter-wavelength ($\lambda/4$) Fields

So far, the devices described have used fluid chambers no smaller than $\lambda/2$, relying on at least one pressure node for particle handling. Many early devices used multiple nodal planes such as that by Tolt & Feke [69] and Hill & Wood [3], although a progression towards the processing of small sample volumes and micro-fabrication make the use of smaller chamber depths more appropriate and of the order of the acoustic wavelength. Although challenging to design, quarter-wavelength devices have been tested where a pressure node will be positioned near or beyond the fluid chamber surface. Figure 2.14 illustrates the effect that a quarter-wavelength mode has on particles, showing that (a) particles are moved to the pressure node when the node is positioned

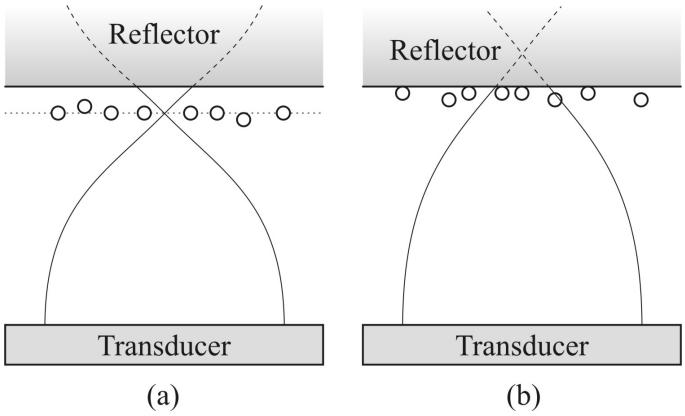

Figure 2.14: Particle movement in quarter-wavelength fluid chambers where (a) the node is positioned within the fluid layer and (b) the node is positioned within the reflector layer.

within the fluid chamber, and (b) particles move towards the node but push up against the chamber wall when the node is positioned just beyond the surface and in, say, the reflector layer.

Hawkes et al. [118] have designed and tested a quarter-wavelength device which has the pressure node positioned beyond a glass reflector surface such that particles are forced up against this surface. A 200-fold increase in capture along the glass surface was measured after applying the acoustic field and would have applications in biosensing, increasing speed and sensitivity of bio-detection. A similar device is investigated later in this thesis [119].

Devices Using Acoustic Streaming

Although microfluidic devices offer a range of particle and fluid processing techniques, the scale of these devices ensures that the flow is inherently laminar in nature and mixing is dominated by diffusion processes. However, as described earlier in section 2.3.2, losses within an acoustic field create fluid movement. These streaming flows have been used in ultrasonic devices to successfully enhance mixing of liquid phases as described by Suri et al. [120] in cylindrical containers of diameters 50 and 100mm using frequencies of the order of 1MHz, and also by Yaralioglu et al. [121] using a micro-fabricated device and extremely high frequency devices (450MHz). Medical applications exist, for example diagnosis of fluid filled cysts has been studied using ultrasound to induce acoustic streaming in fluid regions and detecting the resulting fluid movement [122].

Streaming has also been observed to disrupt particle manipulation processes in devices relying on

acoustic radiation forces. Studies by Kuznetsova & Coakley [87] and Spengler et al. [88] have shown that in a standing wave streaming effects on particles are significant. Although the primary radiation force is large and can transport particles onto nodal planes, particles were seen to move within these planes as they are subject to both lateral radiation forces and streaming. For smaller particles, streaming flow dominated the particle movement and so has obvious implications on particle trapping devices which rely on lateral radiation forces to concentrate particles [112].

2.4.3 Review of Simulation Techniques

Design of the devices mentioned above typically involved simulation of the acoustic system, or the fluid flow and particle movement in order to investigate the influence of various parameters. A summary of the simulation techniques reported in the literature is given in this section and is a useful introduction to some of the modelling approaches used throughout this thesis. Fluid simulation has previously been considered in section 2.2.2, therefore, to cover the remaining aspects relevant to the ultrasonic microfluidic separator, acoustic and particle simulation are considered here.

Acoustic Simulation

In order to predict the magnitude of the acoustic radiation force the resonant behaviour of the acoustic device must be considered. Basic calculations can be used to specify an approximate fluid layer thickness and operating frequency, i.e. for a half-wavelength chamber $f = c/2h$, but this approach does not consider the influence of the remaining device structure and how that alters the resonant frequency. A more complex treatment is required for the layered system and one which predicts the effect of material and geometric parameters on the acoustic field and, in turn, the radiation force.

For a layered resonator and for the 1-dimensional case, Nowotny et al. [123, 124] describe a transfer matrix approach which determines boundary values for each layer of the resonator by solving differential equations in matrix form. Once boundary values, such as displacement and mechanical stress, are determined the acoustic field properties within a selected layer can be calculated. This second stage is processed in a similar manner to the first by dividing the thickness into multiple layers and again solving for boundary values for each layer. This ultimately enables the input conditions of the transducer to be related to the acoustic field within the fluid layer. A general

description of the approach is given by Gröschl [66] and it has been applied successfully to the analysis of devices by Benes et al. [76] and Hawkes et al. [125].

An alternative approach is to consider the acoustic impedance of the device. The acoustic impedances of each layer combine to give the total impedance of the device which acts as a load upon the transducer and, using an equivalent circuit, can be used to model the frequency response of the device. Using the total impedance of the device and the properties of the transducer, it is possible to calculate the forces exerted at each layer boundary from which acoustic pressure and velocity fields may be determined. A more comprehensive description of this approach is given in section 2.5.2 as acoustic design of the microfluidic ultrasonic separator is developed with this simulation. This model is used by Hill [126] to investigate the influence of various parameters on the acoustic characteristics of a layered resonator and the radiation force acting on a particle. The model also aids the selection of layer thicknesses to design for certain resonant modes and nodal positions.

Lilliehorn et al. [82] are interested in the simulation of the near-field acoustic interference patterns and the lateral radiation forces that are generated on a particle. Their model is based on simulation techniques used to describe interference in optical systems (see Wu et al. [127, 128]) and compares well with experimental observation, thus appearing a suitable method for the analysis of analogous acoustic systems.

Particle Simulations

To assess the design and performance of acoustic manipulation devices, the movement of particles within such devices can be modelled in order to predict the level of separation or fractionation achievable. Simulation of particle behaviour is typically achieved by considering the forces experienced by particles.

Particle trajectories can be calculated using a balance of particle forces and using simple numerical integration to simulate the deflection of a particle as it moves through the fluid chamber. Hawkes et al. [4] and others [117, 129, 130] simulate particle trajectories to assess the efficiency of separation or fractionation processes and, where these processes involve the division of flow to extract a specific portion of the flow, it is typical to model the trajectory of the particle which marks the point of this division. For example, figure 2.15(a) illustrates a half-wavelength system where particles are converging to the centre plane and moving downstream towards a splitter. Simulation

of a particle found at the edge of this particle stream can be used to specify appropriate operating conditions to ensure that the entire particle stream passes one side of the splitter and that complete clearance is obtained on the other side of the splitter. Alternatively, by modelling the particle which coincides with the splitter and calculating its original location at the inlet, it is possible to determine the separation efficiency and outlet particle concentrations based on a knowledge of the inlet concentration profile (figure 2.15(b)). This latter approach has been used by Johnson & Feke [107] and Gupta et al. [105] to assess fractionation processes. The simulation approaches reported in the literature typically include only the primary acoustic radiation, fluid drag and gravitational forces. Lateral radiation, secondary radiation and other interparticle forces are neglected due to their apparently low magnitudes.

Higashitiani [72] uses a derivation based on the conservation of mass to express particle concentration within an acoustic standing wave as a function of time. Analytical expressions are given for the case of initial sound irradiation where the acoustic forces dominate, and also for the case a sufficient time later when diffusion processes dominate. This method does not consider or determine particle trajectories, a distinct difference compared to other approaches considered in this section, and therefore can be considered a Eulerian approach as opposed to Lagrangian. An example of these two approaches is seen in a general treatment of particle/fluid simulation by Durst et al. [131] where their Lagrangian approach considers forces experienced by second phase particles, whereas the Eulerian approach treats the particle phase as a continuum and continuum equations, similar to those used for a fluid, are used. The Eulerian approach is suitable for most cases, although the Lagrangian approach provides information on particle trajectories and can handle multiple particle types.

Analytical expressions of the acoustic radiation force have been coded into CFD simulations (Benes et al. [104]) and has also been accompanied by expressions describing Rayleigh streaming flows by Holwill [132]. This can be useful to determine particle trajectories within more complex flow fields, for example, where the flow profile within the acoustic field changes. The application of complex computational methods to simple laminar flow systems is impractical due to the disproportionate processing power required.

(a) Particle trajectory used to predict capture of entire particle stream

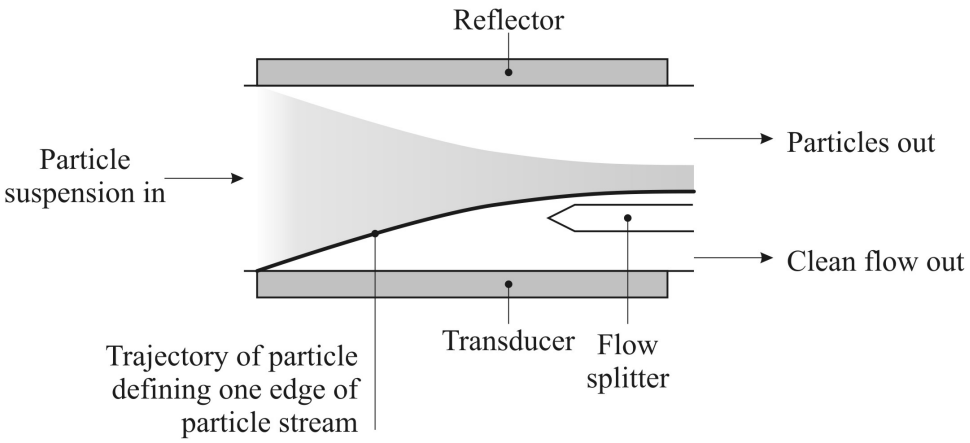

(b) Particle trajectory used to predict separation efficiency where particle stream divided between outlets

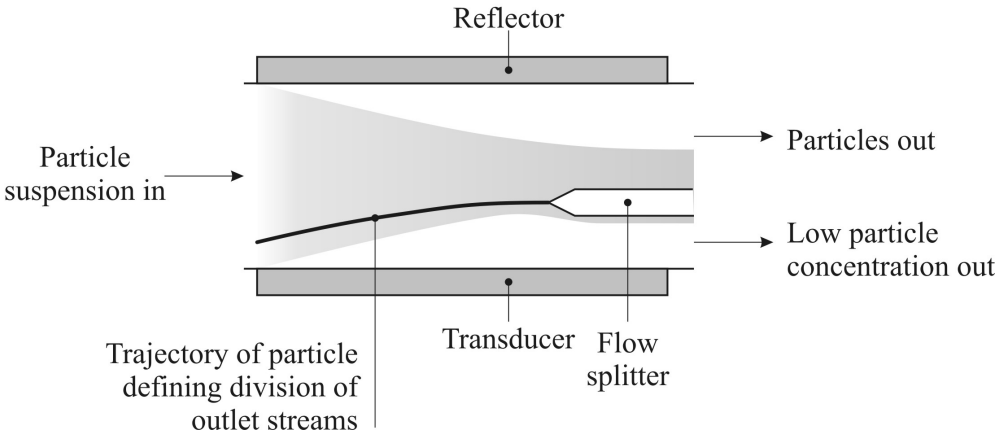

Figure 2.15: Particle trajectories used to determine separation and fractionation efficiency.

2.5 Introduction to the Ultrasonic Microfluidic Separator

The simulation work described in this thesis has been carried out alongside the fabrication and test of an ultrasonic separator, guiding the work and providing essential experimental data. The ultrasonic separator device in question has been developed at the University of Southampton and takes advantage of the university micro-machining facilities to realise the device on a microfluidic scale, and therefore provide the potential for integration within microfluidic systems. The separator is designed to operate using a half-wavelength resonance and to separate particles held in a fluid suspension. Acoustic radiation forces drive particles to a plane within the processing chamber, and controlled extraction of various portions of the resulting flow aim to separate clear fluid from particle concentrated fluid. This section describes the fabrication and principle of operation, which is followed by a description of the acoustic modelling developed for use as a design tool and to understand the acoustic characteristics of such a resonator. A significant portion of this thesis is developed from this acoustic modelling and thereby builds a series of complimentary design tools.

2.5.1 Construction

The design and operation of the separator is related to the laminar flow separator device described by Hawkes et al. [4] in terms of the scale and operation of the device. The laminar flow separator was constructed from metal plates forming the reflector and acoustic matching layer, and encasing the fluid chamber. The operational frequency was approximately 3MHz and so to produce a half-wavelength standing wave the fluid chamber had a depth of 250μm. The microfluidic separator described here is on a similar scale, but uses materials such as silicon and Pyrex suitable for micro-machining processes and therefore results in different acoustic characteristics, although the fluid chamber was initially designed with the same fluid depth of 250μm.

The construction of the microfluidic separator is illustrated in figure 2.16 and shows the arrangement of the piezoelectric (PZT) transducer, silicon matching layer and the Pyrex reflector layer. The fluid chamber is created by isotropically etching into the Pyrex producing curved walls inside the chamber. This also means that the Pyrex wafer thickness used in the fabrication always equals the combined depth of the fluid and reflector layers. The Pyrex layer also allows observation of the particle suspension during operation and the condition of the fluid chamber. The silicon layer is etched to include three fluid ducts, with the characteristic angular geometry resulting from the anisotropic etch process clearly seen. Once etched, the Pyrex and silicon layers are bonded

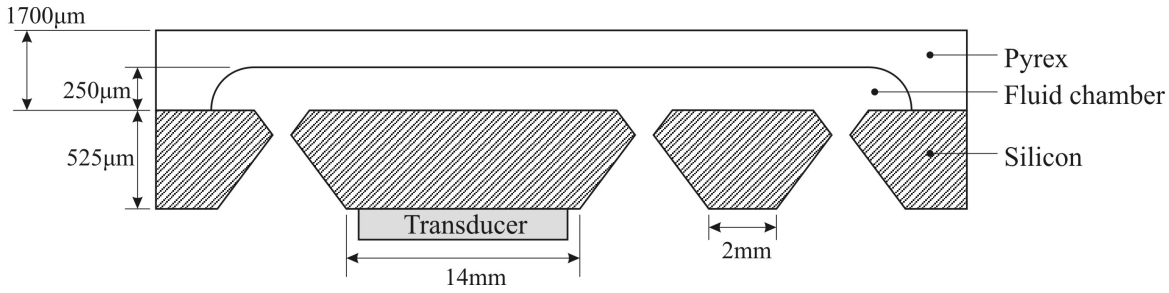

Figure 2.16: Cross-section of the ultrasonic microfluidic separator (not to scale).

anodically.

Typical dimensions are indicated in figure 2.16 although the fluid chamber depth, and therefore the reflector layer depth, have changed during the study. Also note that the fluid chamber has a high length-to-height ratio typically greater than 50:1. The width of the chamber and ducts (not indicated in the diagram) are approximately 5mm, which results in a width-to-height ratio of at least 20:1.

2.5.2 Operation

The separator is a flow-through device within which a fluid sample can be continuously fed through the inlet duct. Figure 2.17 shows the flow path of the sample up through the inlet duct and into the main chamber of the device. Within this area the transducer is used to generate a half-wavelength standing wave across the chamber and perpendicular to the direction of flow. As particles move through this field they are deflected in the y direction by the acoustic radiation forces acting on them and move towards the node of the standing wave positioned along the centre of the chamber. Simultaneously, the particles are subject to fluid drag forces which transport them along the chamber towards the outlets. For separation to be possible the particles must have formed into a narrow stream, as indicated in the diagram towards the end of the acoustic field (light grey shaded area). As the flow within the device is laminar this particle stream remains intact and can be extracted through either outlet. The diagram indicates the case when the flow rate through outlet 2 is greater than outlet 1 and therefore particles are extracted through outlet 2. Clarified fluid is extracted through the other outlet.

When using a half-wavelength resonance and this duct configuration, the outlet through which

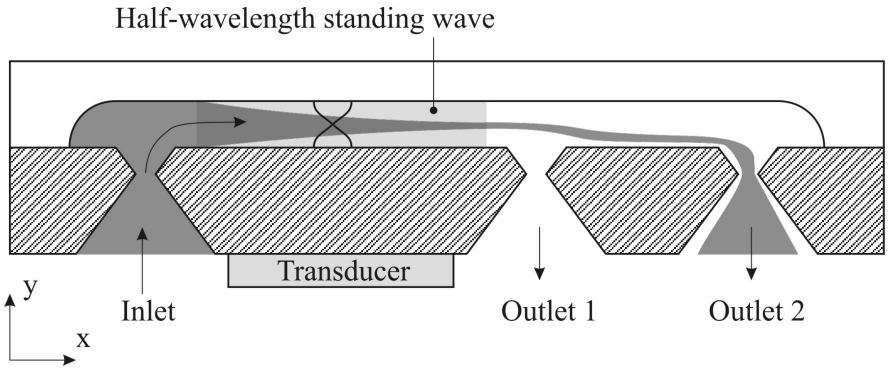

Figure 2.17: Operation of the ultrasonic microfluidic separator.

the particle stream is extracted must have a flow rate at least half that of the total, or inlet, flow rate. This means that the maximum concentration achievable is only a 2-fold increase, the device therefore acting more effectively as a clarifier.

Acoustic Simulation

To predict the nature of the acoustic field within the separator device an acoustic impedance transfer model is used. This model is described by Hill & Wood [3] and Hill et al. [2] and was originally used to describe an h-shaped device. The approach considers the total acoustic impedance of the layered device which can then be related to the transducer using an equivalent electrical impedance.

Figure 2.18 illustrates a basic acoustic system and properties of the media. The input mechanical impedance of the acoustic system, Z_{m0}, where a plane wave is propagating through a material with properties density ρ_0, speed of sound c, area S, and thickness L, and with the cavity terminated with a material of impedance Z_{mL}, is calculated as follows [133]:

$$Z_{m0} = \rho_0 c S \left(\frac{Z_{mL} + j\rho_0 c S \tan kL}{\rho_0 c S + j Z_{mL} \tan kL} \right), \tag{2.16}$$

where k is the wave number.

When simulating the separator the impedance, Z_{m0}, seen by the transducer is ultimately required and depends on the properties of the glue, silicon, fluid and reflector layers. Therefore, it is necessary to calculate the input impedance of each successive layer. For example, equation (2.16)

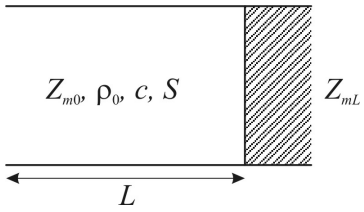

Figure 2.18: Acoustic Properties associated with a closed cavity.

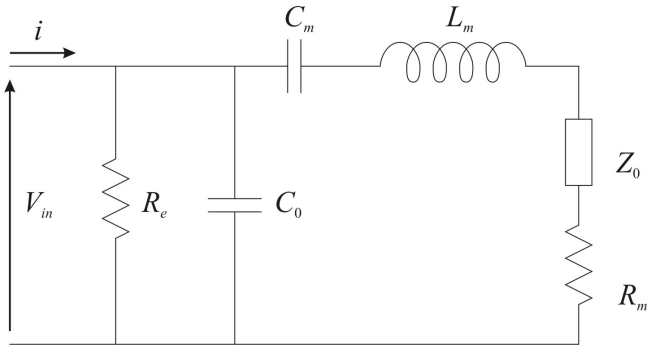

Figure 2.19: Equivalent circuit of separator.

is first used to calculate the impedance from the reflector layer where Z_{mL} is simply the impedance of the surrounding air. The resulting value of Z_{m0} now describes the termination impedance, Z_{mL}, when looking through the fluid layer. This calculation is repeated until the transducer layer is reached.

The resulting value of Z_{m0} as seen from the transducer now describes the total mechanical impedance of the device and is represented by an equivalent electrical impedance Z_0. In order to model the resonant behaviour of the device and related electrical characteristics, an equivalent circuit is considered as shown in figure 2.19 where R_e represents the electrical losses, C_0 is the static capacitance of the transducer and C_m, L_m and R_m are the equivalent mechanical capacitance, inductance and resistance, respectively. Further, to determine the nature of the acoustic field within the cell, the mechanical impedance is used to calculate the forces generated at layer boundaries, which in turn are used to describe the variation in the acoustic pressure and velocity fields. This transfer model is described in more detail by Hill et al. [2].

The equivalent circuit is modelled within MATLAB and typically used to simulate the frequency

response. This can be compared to the measured frequency response of a device and used to fine-tune parameters. It can also be used in a predictive capacity to determine the resonant frequencies of the device.

To model the acoustic behaviour within the device, the force exerted by the transducer can be calculated and is proportional to the voltage applied across the transducer. As the wave propagates through the devices it in turn generates a force between each layer of the device. These forces can then be used to determine the acoustic pressure p and velocity u fields within each layer, as a function of y in a direction perpendicular to the transducer and layer boundaries. Although the model does not simulate variations in the field along its length or across the width, it provides a 1-dimensional description of the most dominate component.

As can be seen from equation (2.11) the radiation force depends on the kinetic and potential energy. Kinsler et al. [133] give these energies as functions of the acoustic pressure and velocity and are time and position dependent. Here, the time averaged expressions are shown, where ρ_0 is the undisturbed fluid density and u and p are time averaged acoustic velocity and pressure fields:

$$\langle \bar{E}_{kin}(y) \rangle = \frac{1}{4}\rho_0 u(y)^2, \tag{2.17}$$

$$\langle \bar{E}_{pot}(y) \rangle = \frac{1}{4}\frac{p(y)^2}{\rho_0 c^2}. \tag{2.18}$$

MATLAB is again used to determine these values and by substituting them into equation (2.11) the radiation force as a function of y can be calculated. The resulting data describes the spatial variation of radiation force, an example of which is shown schematically in figure 2.9.

2.6 Conclusions

2.6.1 Flow Through Microfluidic Channels

The development of μTAS technologies highlight the importance of realising fluid and particle processes on a micro-scale in order to be incorporated into these analysis systems. Although many other fabrication routes are available, the microfluidic ultrasonic separator is fabricated using the bulk micro-machining approach providing a method to batch fabricate many devices. Wet anisotropic etching is used for the silicon layer, but creates angular geometry which limits the

geometric design of fluid channels, although it does create smooth surfaces which limit fluid friction losses. The fluid flow field dominates the motion of particles, therefore the influence that the angular etched duct geometries has on flow streamlines, and therefore particle trajectories, is of some interest and should be investigated.

Although well within the laminar flow region the flow within the etched ducts of the device cannot be simulated analytically as for the main channel, therefore a computational approach is required for these duct regions. It is understood from the literature that flows can be modelled with reasonable accuracy using commercial CFD codes down to hydraulic diameters of the order of 100μm. Conversely, the main fluid channel of the separator device is suitably long and wide such that the classical description of flow between parallel plates can be applied as well as the entrance region being short ($< 2\%$ of the channel length), becoming negligible for the low flow rates used in experimental tests of the separator device. It is assumed that the low concentration of particles ($< 1\%$ by wt.) will produce a negligible effect on the behaviour of the fluid requiring only the fluid to be considered in the both the CFD model and analytical treatment.

Surface tension effects and capillarity will influence experimental work on the separator. This should only affect the initial priming of the device channels and experimental procedures need to be adopted which flush the device and eliminate trapped air bubbles.

2.6.2 Acoustic Field/Particle Interaction

Acoustic field-assisted devices have the advantage over other field-assisted techniques in that they rely on acoustic properties inherent in any particle suspension. Many acoustic devices have been designed and tested for the processing of particle suspensions, although the separator device discussed as part of this thesis is one of the few to be fabricated using micro-engineering techniques. The various devices described demonstrate the application of acoustic fields to the separation, fractionation and trapping of particles with a significant number applied to bio-sample processing.

The effect of acoustic radiation forces is well documented and has been applied to the manipulation of particles and cells. Of the forces experienced by a particle in an acoustic field, the primary (or axial) radiation force is considered to be of most significance, although streaming becomes more important for sub-micron diameter particles. Secondary radiation forces are negligible for low concentration suspensions and short residence time processes such as for flow-through devices. Geometric features and boundaries within a resonator are one possible source of variations

within the acoustic field and associated lateral radiation forces. The magnitude of these lateral forces may be large enough to significantly influence the movement of particles and, depending on the function of a particle manipulator, may be either beneficial or detrimental to the process and therefore be an important consideration in some resonator designs.

Acoustic streaming flows have been observed in other acoustic particle manipulation devices and suggest the presence of Rayleigh type streaming. The exact nature of the flow field generated is not clear for high aspect ratio chambers and therefore without specialising in this area it would be imprudent to attempt to predict the nature of streaming flows within the separator device, although it is important to recognise Rayleigh streaming when interpreting experimental results. Other types of streaming have been considered including localised streaming around the particle which is estimated to be negligible for micron-scale particles.

2.6.3 Simulation of Particle Manipulation Processes

Particle trajectory models have frequently been used for the simulation of acoustic particle manipulation devices and typically involve solving particle equations of motion. A complex simulation of the acoustic field can usually be avoided and equation (2.8) is employed with the placing of acoustic nodes on, say, a boundary. However, the use of a more accurate simulation of the acoustic field in fluid chamber depths $\leq \lambda/2$ and in micro-scale devices is important as the other layers of the device significantly influence the acoustic behaviour. For example, the acoustic impedance transfer model described in section 2.5.2 simulates the layered device and supplies numerical data describing the acoustic field and radiation force. This model is not limited to the resonant case, but can simulate the acoustic field over a range of frequencies. As the acoustic design of the microfluidic ultrasonic separator has been developed using this model, it is appropriate to adopt the model code for the purposes of this thesis when simulating particle behaviour within the separator device.

Chapter 3

Development of Fluid Channel Geometry

3.1 Introduction

As well as the acoustic field, the fluid flow field has a major influence on the particle trajectories through the separator and, therefore, the particle separation efficiency. To predict the movement of particles the flow patterns must be known and be stable over a range of flow rates, and it is the role of this chapter to investigate this computationally.

Brief summaries of laminar flow theory and fluid modelling approaches were presented in the previous chapter, investigating the scale at which the Navier-Stokes equations and macroscale fluid flow theory was applicable, and concluded that simulation of the separator using a macroscale CFD code was a valid approach. These summaries are frequently referred to in following sections with regard to the development of a suitable 2-dimensional CFD model to represent the separator geometry and fluid flow. Section 3.4 then describes the application of this model in simulating the separator fluid channels and reveals eddy regions detrimental to the separation process that were also visualised experimentally. Eddy formation can distort particle trajectories and influences sedimentation formed on the channel walls, in turn strongly influencing the performance of the device.

The flow patterns within the device are influenced by the fluid flow rate and the channel geometry, therefore these parameters may be modified to improve various aspects of the flow. However, the fluid flow rate is an important parameter (together with the acoustic radiation force) to control

the rate at which particles agglomerate. Therefore, when improving the flow pattern and to avoid compromising the particle agglomeration rate, it is preferential to modify only the geometry. Once a study to improve the flow pattern has been completed (as a result of geometric modifications), it should be ensured that the results stand for a range of flow rates. Adjustment to the flow rate will then be reserved for optimisation of particle agglomeration rate, and will not alter the flow pattern significantly.

Similar devices have been fabricated from steel and glass [4, 125], however for this technique to be realized on a microfluidic scale etched silicon and Pyrex are being used. This has potential advantages of batch production and easy incorporation into microfluidic systems containing micropumps etc. which handle only very small sample volumes. However, the nature of micro-engineering fabrication techniques restricts the geometric design of the microchannels and in this case geometric modifications are limited by basic wet etch fabrication methods. This geometric study is presented in section 3.5 describing the influence of the geometric design of the device on pressure losses and eddy formation and aiding the selection of a geometry which suppresses eddy formation.

3.2 Microchannel Geometry

3.2.1 Separator Construction and Geometry

The micro-machined separator device consists of a 525μm thick silicon wafer and 1700μm Pyrex wafer, etched and then joined using anodic bonding. Fluid enters and leaves the device via ducts etched into the silicon. The duct geometries currently used in the separator consist of either single or double sided anisotropically etched ducts that lead to an isotropically etched channel within the Pyrex, and across which the acoustic standing wave is set up. Figure 3.1 illustrates the typical wafer geometry incorporating either single or double etched ducts.

Isotropic and anisotropic etchants are used for the Pyrex and silicon wafers respectively, where the anisotropic etch produces predictable angular geometries where the etch process is effectively halted at the (111) crystal planes, forming angles of 54.74^o. Alternative methods of creating the ducts, such as deep ion etching, exist and although such methods may provide more geometric variations this study reveals a satisfactory solution based simply on wet etching techniques.

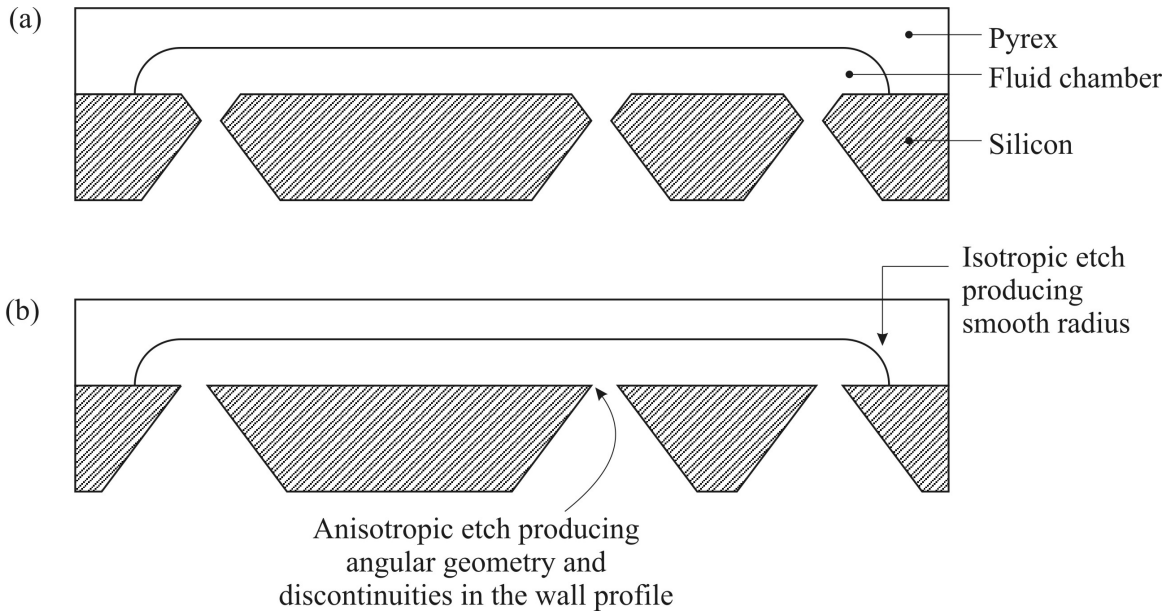

Figure 3.1: Silicon etched duct geometries used in original microfluidic ultrasonic separator design incorporating (a) double etched ducts or (b) single etched ducts (not to scale).

3.2.2 Influence of Geometry on Separator Performance

Anisotropically etched geometry is dictated by the orientation of the wafer crystal planes and so produces angular wall geometry and discontinuities in the wall profile. Such discontinuities cause fluid flow to separate from the channel wall giving rise to fluid boundary layer separation, in which the direction of flow is reversed at the wall [22, 21] and a flow vortex results. To avoid confusion between such *flow separation* and *particle separation* which is discussed in later chapters, boundary layer separation flow patterns will be referred to as *eddy regions*.

An example of eddy flow formation is shown in figure 3.2 where a step in the wall geometry creates a sudden expansion, and an associated eddy flow within the stagnant region of the step. When compared to the bulk flow, the eddy region typically has a low flow velocity and is reversed at the wall. This can occur in flows of low Reynolds number in the laminar regime and is therefore not a turbulent effect.

With regard to eddy flows being present within the ultrasonic separator during operation, the formation of eddies presents a condition where particle movement cannot easily be predicted. For example, particles are manipulated by the acoustic field within the main channel, but the presence

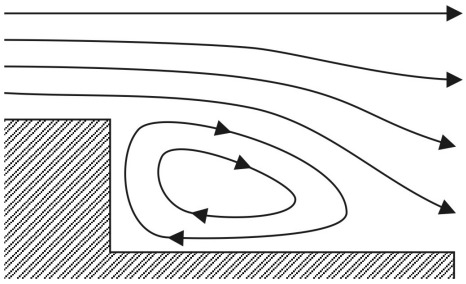

Figure 3.2: Formation of an eddy region downstream of a step.

of an eddy in this region will distort the laminar flow field and also particle trajectories, which in turn influences the separation efficiency of the device. Additionally, the degree to which particles become trapped within eddies is unknown, but presents doubts over the ability to successfully flush clean the device should it be required to process subsequent fluid samples.

The following sections develop a model to investigate the exact nature of these eddy flows within the separator device and then uses this model to identify channel geometry which limits the formation of these eddies.

3.3 Development of the CFD Model

3.3.1 Approach to CFD Study

In order to study the influence that the microchannel geometry has on the development of eddies, a study based on numerical simulation of the fluid flow was undertaken. The CFD computer package used is CFX5 and is a general purpose and commercially available program. This software enables a variety of possible geometries to be modelled over a range of flow rates and provides comprehensive visualisation of the flow, useful for direct comparison with experimental observations, but also valuable where observation of the flow is not possible. CFD is used here in preference to more basic fluid theory due to the complexity of the fluid channels, although basic theoretical flow profiles are used to validate computational results.

The aspect ratio w/d of the fluid channels is typically greater than 20, therefore to reduce the size of the model and computation time, 2-d models are considered for simulation of the fluid flow through various parts of the device. As the concentration of yeast particles used in experiment is

low enough to assume negligible effect on the fluid dynamics, the CFD simulations are further simplified by modelling only the fluid flow and exclude the influence of solid phase particles.

Before applying CFD to study the effects of specific fluid flow parameters it is necessary to establish a degree of confidence with a basic CFD model by studying its performance. The following study involves optimising the model by increasing the accuracy of the solution and reducing the processing time. However, there is often a conflict: it is necessary to increase the processing time if a more accurate solution is required. To progress, acceptable levels of accuracy and computational time must be chosen appropriate for the problem being simulated. These two aspects are influenced by various CFD modelling parameters including geometry and mesh characteristics introduced below. Following this, the approach to optimising the model for accuracy involves running CFD simulations of the flow domain and studying the change in results when model parameters are altered, specifically the mesh size. Once the appropriate level of each model parameter is established, these can be applied to a final CFD model for use investigating the influence of boundary conditions, fluid characteristics and small changes in domain geometry of the separator.

The CFD simulations consider only the micro-channels of the device and so the flow domain consists of the ducts etched through the silicon and the main channel etched into the Pyrex. No modelling of the manifold block onto which the device is mounted is included.

3.3.2 Overview of CFD Parameters

Within the CFX package, certain user input parameters are key to improving the level of accuracy of flow solutions. There are also parameters held within the output file which are indicative of the solution accuracy. Those most appropriate to this work are introduced below.

Input (Pre-processor)

Geometry: Naturally, the choice of geometry is dependent on the fluid problem being analysed although to avoid excessive processing times, whilst giving more scope for increased accuracy, it is often necessary to reduce the size of the model. This involves modelling only part of the fluid domain; for example, symmetry planes can be used to describe the 2-dimensional aspect of a fluid problem. This is explored in more detail in section 3.3.3. Also, if the characteristics of the flow are known at any point between the inlet and outlet boundaries, the geometry can be divided into two separate models as boundary conditions would be known.

Fluid Model: As opposed to basic fluid characteristics, for example, density and viscosity, the user defines the fluid model to be used, either laminar or turbulent. With the turbulence regime several models exist which include the $k-\epsilon$ model. For simulations of the separator device it is always ensured that the laminar model is applicable by limiting Re.

Mesh: Mesh parameters are available which control the general size of each element and any mesh refinement which the software then uses to generate a mesh structure. If enabled by the user, mesh adaption allows mesh refinement of certain elements to occur during processing if large variations in flow parameters are observed in those locations. This results in a more accurate solution and allows more rapid convergence of the solution once an appropriate level of refinement is achieved. A simulation within this section typically involves the use of between 10,000 and 30,000 nodes.

Boundary Conditions: The boundary conditions applied to a model depend again on the fluid problem being analysed, although the position of the boundary (for example, an inlet or outlet) can be controlled. One specific example of where relocation of the boundary is necessary is where eddy regions lie near or across the boundary, which causes large errors in the solution and problems converging to a solution during processing. In this situation it is advised that the boundary is moved 10 diameters downstream of the eddy region [134].

Processing Control: In CFX the residual target parameter controls when to cease processing and accept the solution. A smaller residual target results in a more accurate solution.

Output (Post-processor)

Residual: This parameter is indicative of accuracy and is repeatedly calculated during processing, essentially measuring the variation of the solution between each iteration, which for a converging solution will tend to zero. The solution is considered to have converged when the calculated residual equals or is less than that of the user defined residual target.

Imbalance: Imbalance of momentum and mass is calculated at the end of the processing phase and is a measure of conservation across all boundaries.

Errors

Mesh error: The software is unable to mesh the flow domain when the user specifies certain combinations of geometry and mesh values. Due to the sensitivity of the algorithms used

to create the mesh, small changes in mesh parameters can eventually prove successful, although this process can be time consuming.

Non-convergence: This can either be divergence or oscillation (cycles of convergence and divergence). In the case of the former, small and apparently insignificant changes in the boundary conditions can solve the problem. With oscillation, a change in the CFD time step parameter is necessary.

3.3.3 Optimisation of the Model

The parameters above are used to help optimise the model and ensure that the solution is independent of the mesh characteristics. For the simulation of the ultrasonic separator at low Reynolds numbers there will be regions of fully developed flow so, to assess the solution, the velocity profile determined by the CFD package in these regions is compared to the theoretical profile according to equation (2.4). A measurement of the CFD velocity error is therefore possible, quantifying the validity of the CFD results. The theoretical entrance length (equation (2.5)) is also used as a comparison for the CFD results.

Z-Axis Mesh Study

When creating a 2-dimensional model in CFX the program still requires a third dimension and must be at least one element thick. Figure 3.3 illustrates a pair of symmetry planes separated by a distance Z containing the 2-d model. The symmetry planes preclude wall friction and simulate flow between infinitely wide parallel plates (variables constant in z-axis), therefore the flow solution should be independent of Z and the mesh size/density in the z-direction.

To confirm that the solution is independent of the z characteristics of the mesh a simple CFD model is used and is of a simple parallel plate channel 8mm long, 100μm deep and with a domain thickness, Z, ranging from 10 to 80μm. The mean inlet velocity applied at the inlet plane is 0.2m/s. A series of simulations are processed for a range of Z values and with the elements "stretched", so that the model remains only one element thick, i.e. the element size in the z-direction is equal to Z and the number of elements across the width, $n = 1$.

Figure 3.4(a) shows the velocity profiles extracted from the simulations and compares these to the theoretical velocity profile according to equation (2.4). The velocity variation between each CFD simulation is not discernible, implying that the width of the domain does not have a significant

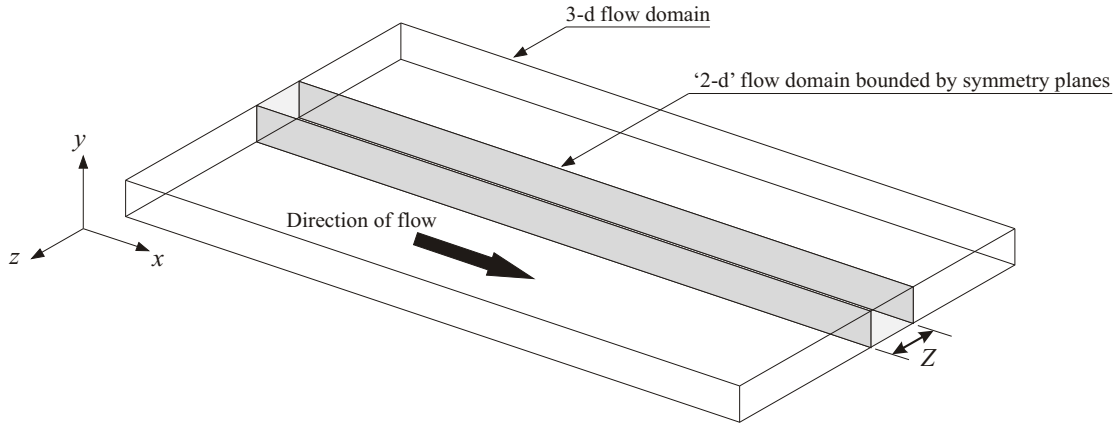

Figure 3.3: Position of symmetry planes for 2-d modelling.

influence on the CFD results. A difference can be seen between the CFD results and the theoretical velocity profile, although this error will be tackled later.

To reduce processing time the flow domain volume (or rather number of elements) needs to be minimised. Therefore, a thickness of one element in the z-axis is optimum. Again, a series of simulations are used to test that this does not influence the solution, where in each simulation a different number of elements is used across the domain width. Each element is 10μm wide, so for example, a domain thickness $Z = 40\mu$m comprises of $n = 4$ elements across the width.

Figure 3.4(b) again shows that there is indistinguishable difference between the CFD results, suggesting that the solution is independent of the number of elements between symmetry planes. Therefore it is concluded that the use of one element between symmetry planes and of an arbitrary width is suitable for 2-d modelling.

For a channel 100μm deep and with mean inlet velocity 0.2m/s, the theoretical entry length is 0.12mm (equation (2.5)), after which point the flow is fully developed and velocity will not change as a function of x. Figure 3.5 shows the maximum, centre line velocity as the flow progresses down the channel, where fully developed flow is indicated by the velocity reaching a steady value (~ 0.3m/s). This occurs at approximately 0.10mm along the channel, agreeing with the theoretical value for $\mathrm{Re} = 20$ and confirms that at this stage the 2-d simulation gives a reasonable representation of flow between parallel plates.

3.3.4 Mesh Dependence Study

Generally, mesh refinement increases the accuracy of the result although, to make the analysis practical, there is a limit to the refinement necessary or else excessive computation time results.

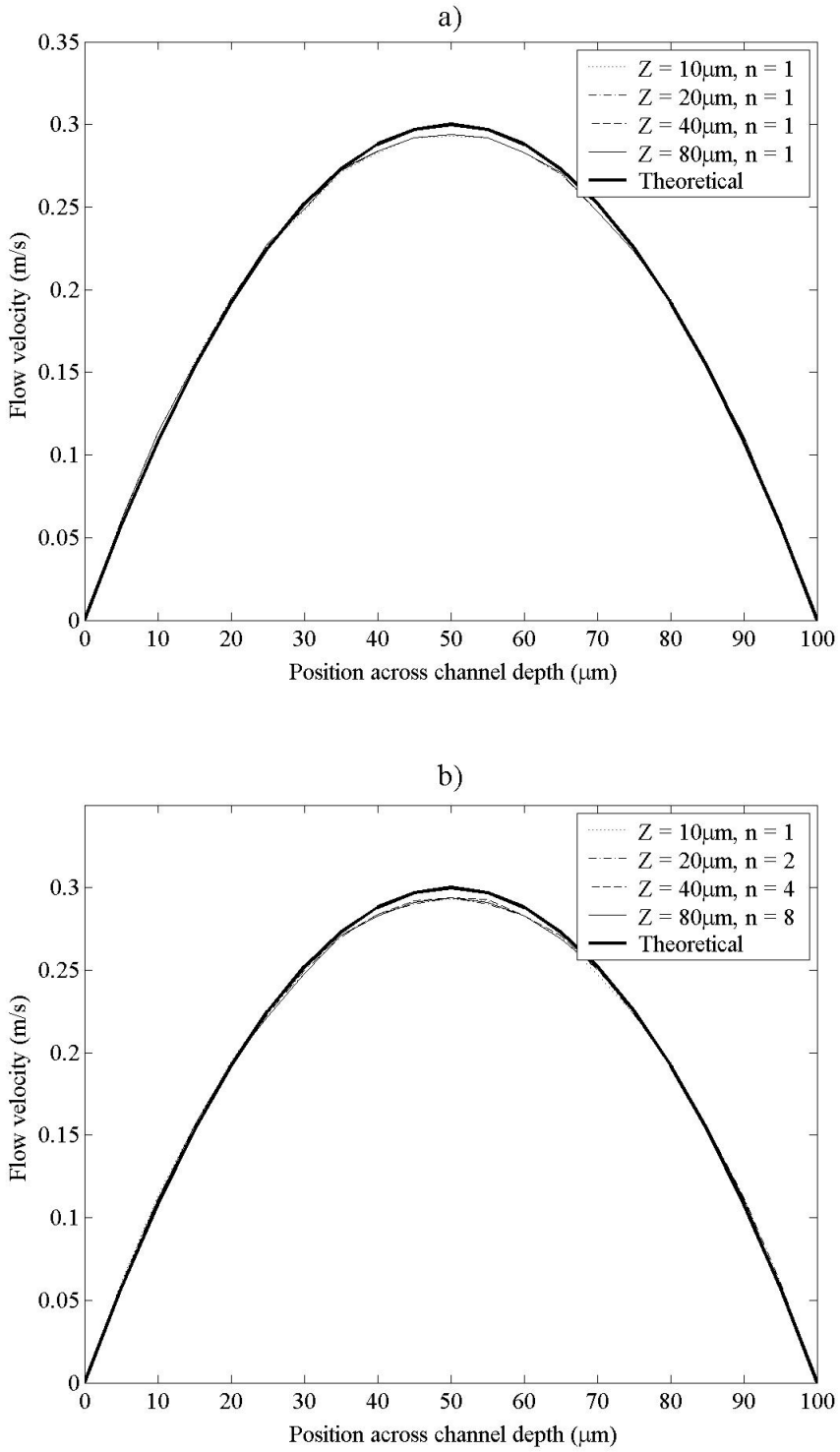

Figure 3.4: Comparison of flow profiles using (a) one element in z-axis and (b) multiple elements in z-axis.

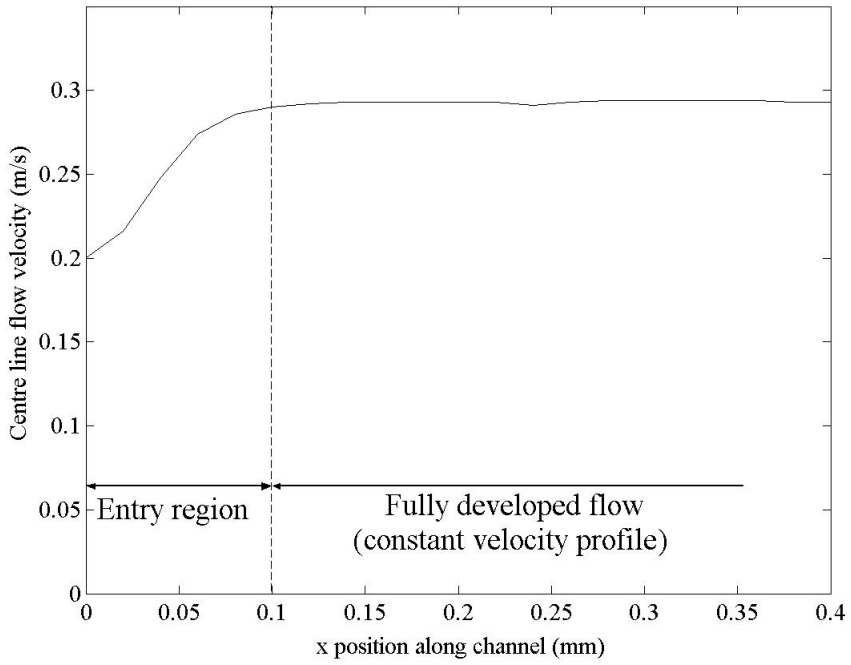

Figure 3.5: Development of flow in main channel (maximum, centre line velocity shown).

To help determine a reasonable level of mesh density in the $x - y$ plane, a mesh dependence study is used which involves modelling the same flow domain geometry, but adjusting the mesh at each stage, for example, halving the element size between simulations. With a second order model, the log of error plotted against the log of a measure of mesh size should reveal an approximately linear relationship; as mesh refinement is doubled, error is halved.

For the mesh dependence study parts of the flow domain may be removed and so the investigation involves modelling three sections of the silicon/Pyrex part of the device. As shown in section 2.2.1 the entry length of the flow in the main channel is small and therefore fully developed flow dominates in that part of the device. This suggests that there is little to benefit from modelling the entire volume of the main channel as no change in the velocity profile will be seen. It is therefore reasonable to reduce the flow domain which also reduces computation time. The shaded regions in figure 3.6 show the remaining areas to be used in the study. Part of the main channel will still be modelled in order to contribute to the mesh dependence study.

To measure the error in each simulation, velocity flow profiles in fully developed regions are again compared with the theoretical parabolic flow profile (equation (2.4)). In regions where the flow is not fully developed, particularly through the ducts, the flow profile cannot be calculated

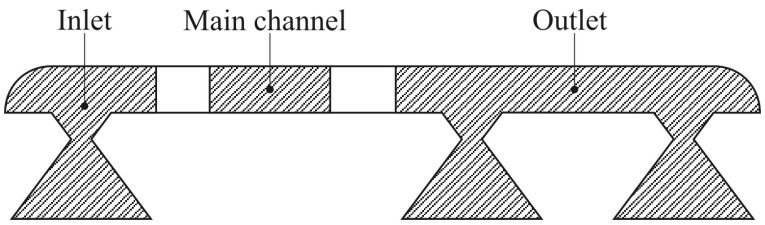

Figure 3.6: Sections of the device to be used for mesh dependence study.

theoretically. These regions are analysed by measuring the change in velocity between subsequent simulations with the solution appearing to converge as the mesh is refined.

Velocity profiles from the simulation of the inlet duct and averaged over small regions near the outlet plane, are shown in figure 3.7 with the theoretical flow profile. This shows a degree of convergence to the theoretical velocity profile as the mesh is refined, therefore error is being reduced and tending to zero. Figure 3.8 quantifies the average magnitude of error for the results shown above and plots the percentage errors against the general element size defining the mesh to give an approximate indication of the effect of element size. The results from other regions in each section of the device all show similar results, consistently showing that a general element size of 12μm results in an average error less than 1% when compared to the classical solution.

3.3.5 Mesh Refinement

Where velocity or pressure gradients are large, accuracy of the solution deteriorates for a given element size. These larger gradients typically exist near boundaries (walls) and geometric features where pressure losses may exist and are also associated with eddy formation.

To retain accuracy in such regions it is necessary to reduce the element size. In CFX this can be achieved by using wall refinement, although the user must judge the level of refinement for various parts of the flow domain. Here it is considered more efficient to use “mesh adaption” which selectively refines elements during processing of the solution, where large gradients are calculated to exist and so does not rely on the user’s judgement. *Mesh adaption* is used throughout subsequent modelling of the device.

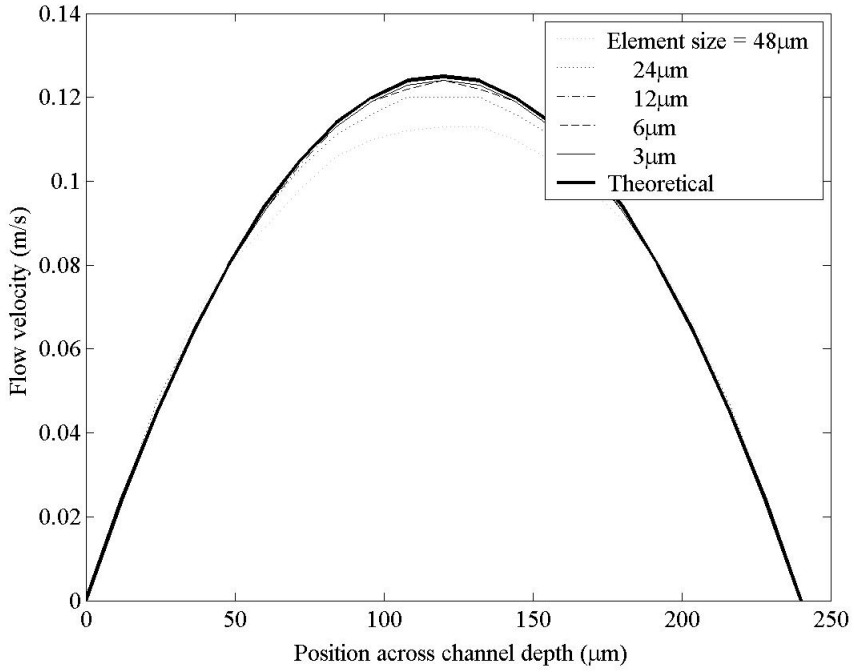

Figure 3.7: Flow profiles in fully developed regions.

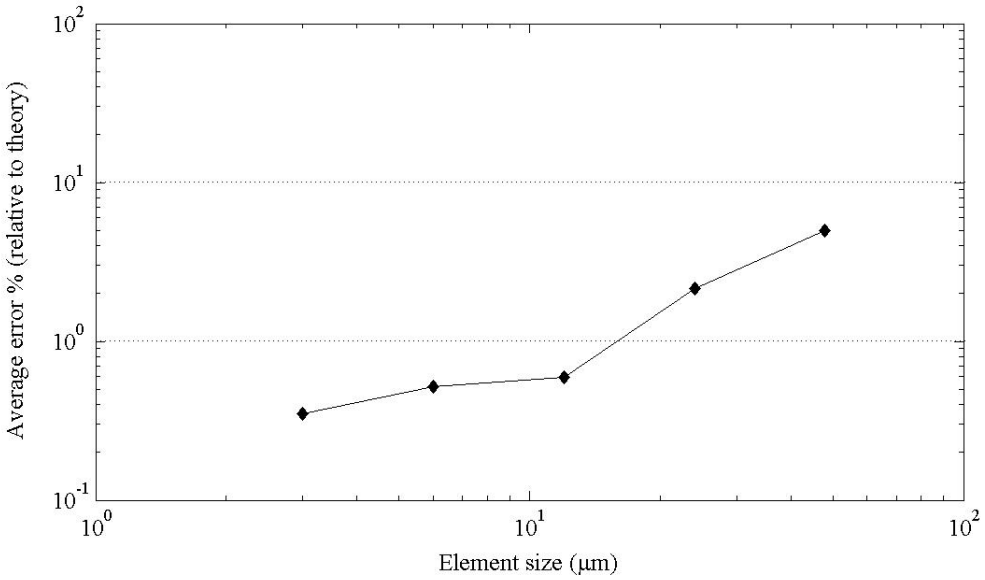

Figure 3.8: Plot of log error against log of element size.

3.3.6 Conclusion

Results show that for a 2-d model of the separation device a z thickness of one element can be used, minimising element number and therefore processing time. Also, if parameters including thickness and z-axis stretch need fine adjustment to avoid mesh errors, this can be done without affecting the accuracy of the result.

For CFD simulations at this scale the mesh dependence study indicates that a general element size of 12μm is used, as this results in an average error of less than 1% when compared to the classical parabolic velocity profile for laminar flow. *Mesh adaption*, an automated process within the CFD package, is available for selective refining of the mesh during the computation, avoiding the need to apply a computationally expensive general wall refinement, and refines the mesh in regions exhibiting a high velocity or pressure gradient which usually occur adjacent to wall boundaries and at geometric discontinuities. Figure 3.9(a) shows the typical mesh pattern with the basic 12μm element size applied to the mesh algorithm and (b) with further mesh refinement.

3.4 Study of Eddy Flow within Original Device

3.4.1 Simulation of Fluid Flow

By modelling the device using typical operational flow conditions it is possible to simulate eddy flow phenomena detrimental to the performance of the device and determine their approximate location. Here the minimum flow velocity is based on the Cardiff device at 0.1ml/s flow rate and pressure at both the outlets set to atmospheric pressure (zero differential pressure).

Simulation of Inlet Flow

With the current device geometry, CFD results (figure 3.10) show that above a flow rate of 0.1ml/s an eddy region develops immediately downstream of the inlet and becomes more significant at increasing flow rates. There is also an eddy region at the end of the main channel, contained within the curved isotropic etch profile created in the Pyrex layer. This eddy is associated with the alignment tolerances between the silicon and Pyrex layers which determine the position at which the inlet duct joins the main channel.

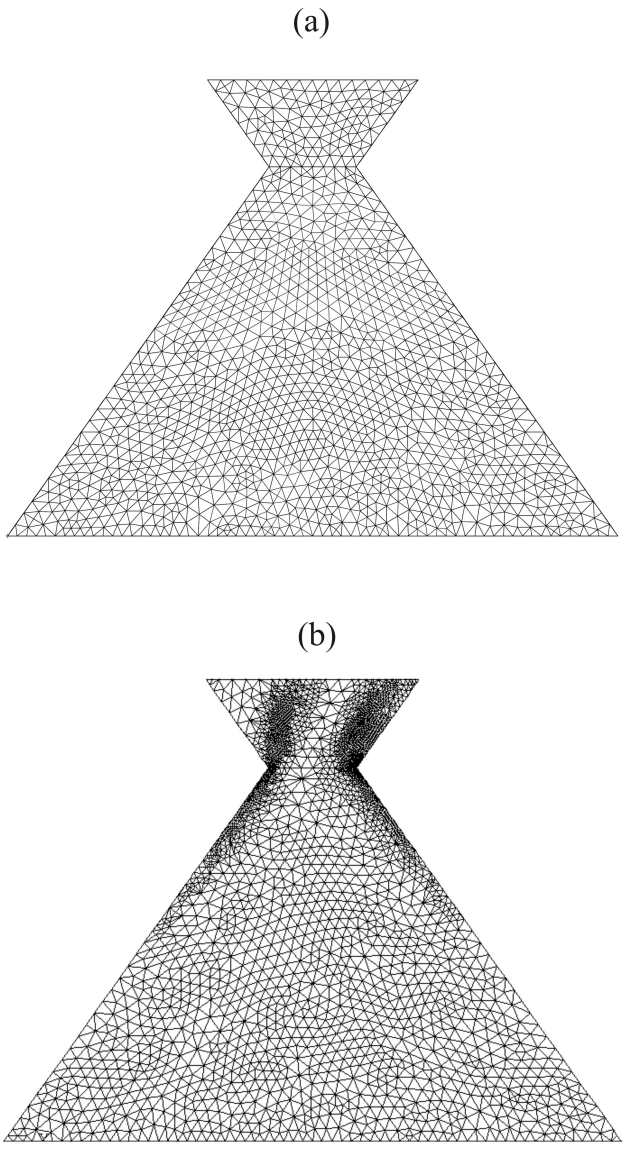

Figure 3.9: Typical mesh pattern for (a) unstructured mesh and (b) unstructured mesh with *mesh adaption*.

(a) flow rate 0.1ml/s

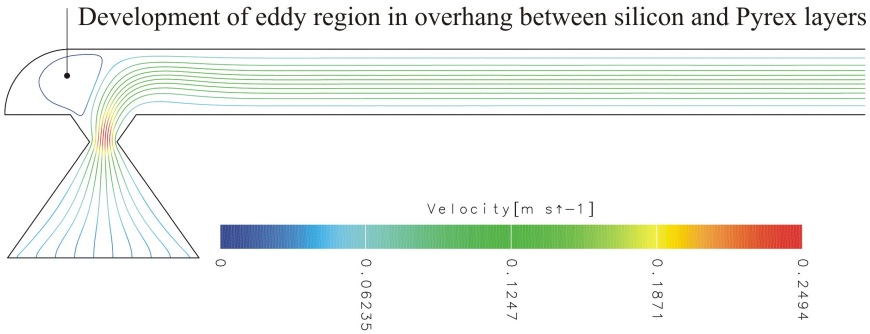

(b) flow rate 0.3ml/s

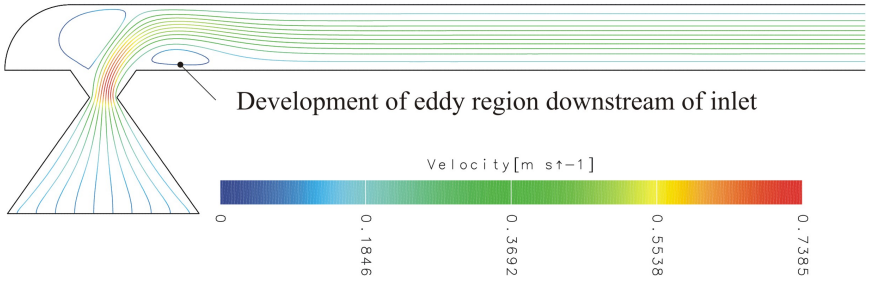

(c) flow rate 0.5ml/s

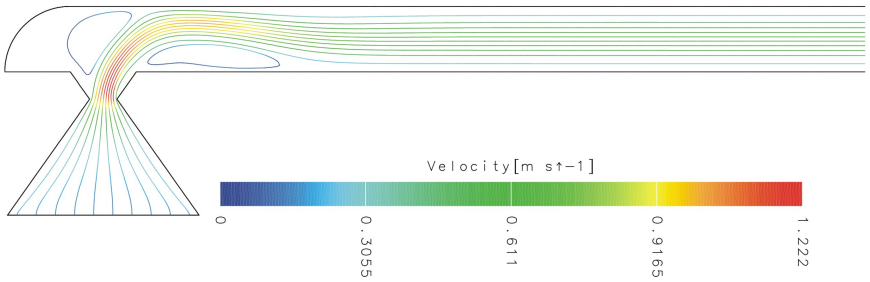

Figure 3.10: Locations of eddy regions downstream of inlet.

Simulation of Outlet Flow

Figure 3.11 shows the location and size of the eddy regions opposite outlet 1 and in the overhang near outlet 2 at various flow rates in the outlet end of the device. Note that in these simulations of the outlet ducts the large eddy regions in the diverging section of both ducts cross the outlet boundaries of the simulation. This may not be an accurate description of the flow field in these areas where ideally, as good CFD practice recommends, an extension of 10 diameters of the flow domain is used downstream of suspected eddy flows.

No CFD analyses described here consider the influence of transient flow so it is unknown what influence fluid pressure pulses, such as those produced by pumping, would have on the fluid flow and therefore separation efficiency of the device.

Together with that for the inlet region, sites within the device susceptible to eddy flow formation have been identified and are presented in figure 3.12. It is then possible to concentrate on these regions when investigating geometry modifications.

3.4.2 Experimentally Observed Flow Patterns

An initial batch of microengineered cells has been produced to investigate the ultrasonic separation capabilities of a micro-engineered device and contains devices of the two different duct geometry designs shown in figure 3.1. These devices were also used to validate the CFD model by measuring and comparing the size of the eddy region downstream of the inlet duct. The eddy region in question is illustrated in figure 3.10 and is chosen as it can be observed in the fabricated devices. Most of the other eddy regions illustrated in the diagram are either obscured or are difficult to observe and so can not be easily investigated experimentally. The experimental results taken from the fabricated devices were extracted by studying the movement of particles under the influence of the flow field only (it has been assumed that particles have little influence on the fluid dynamics and are neutrally buoyant). This is achieved by pumping a mixture of water and a low concentration of yeast particles through the device at a known flow rate, and using a Motic DMB3 digital biological microscope to record images looking down through the device Pyrex layer. The extent of the regions may be clearly seen in real-time, although figure 3.13 shows a still image where the recirculating eddy flow is discernible from the laminar stream striations. CFD results are collected by modelling the inlet region of both duct designs and using streamline plots to determine the extent of the eddy region from the leading edge of the main channel.

(a) flow rate 0.1ml/s

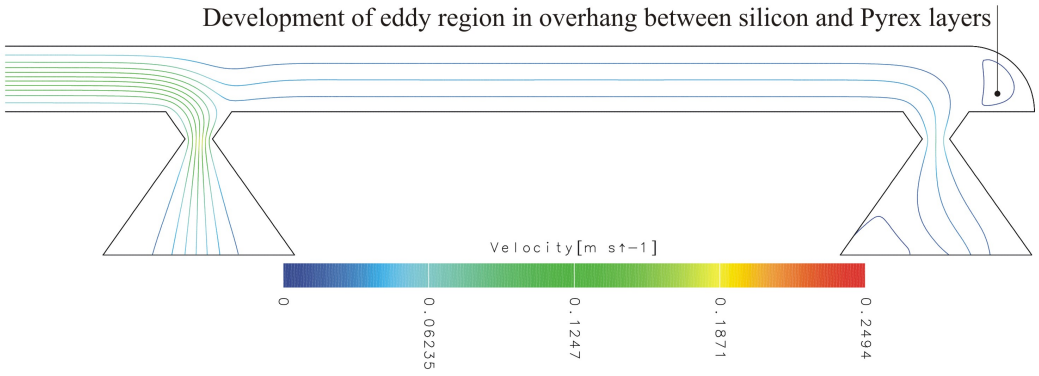

(b) flow rate 0.3ml/s

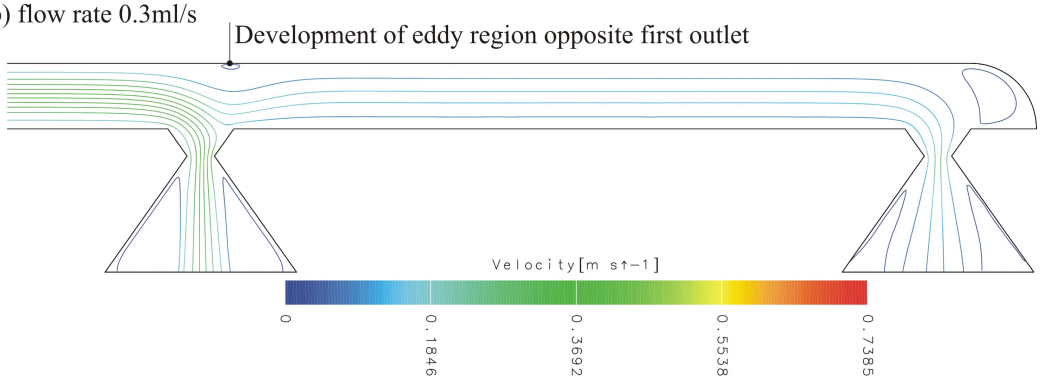

(c) flow rate 0.5ml/s

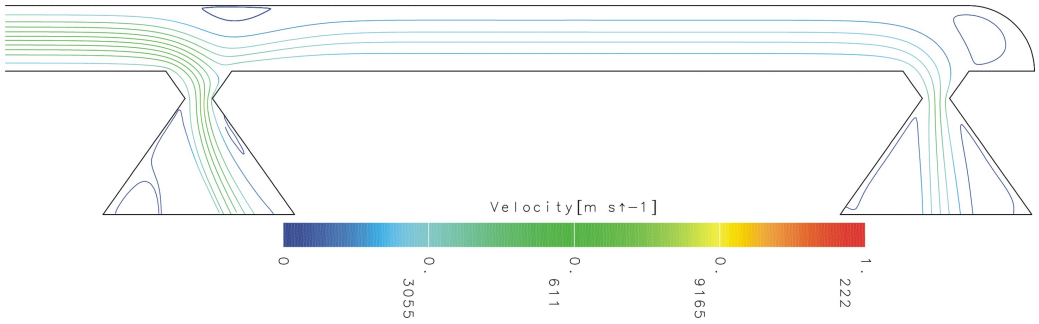

Figure 3.11: Locations of eddy regions adjacent to outlet ducts.

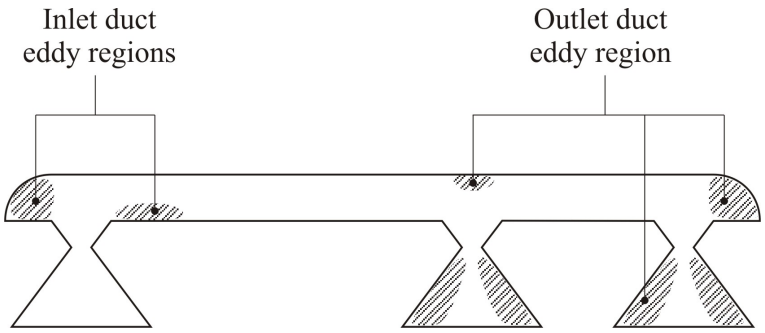

Figure 3.12: Locations within separator device associated with potential eddy flow formation.

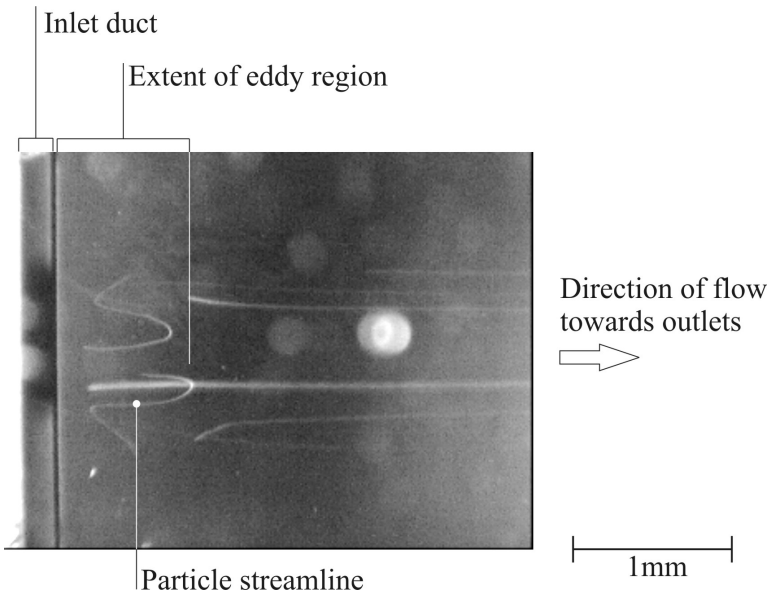

Figure 3.13: Photograph of observable eddy region downstream of inlet duct and looking down through Pyrex layer of device.

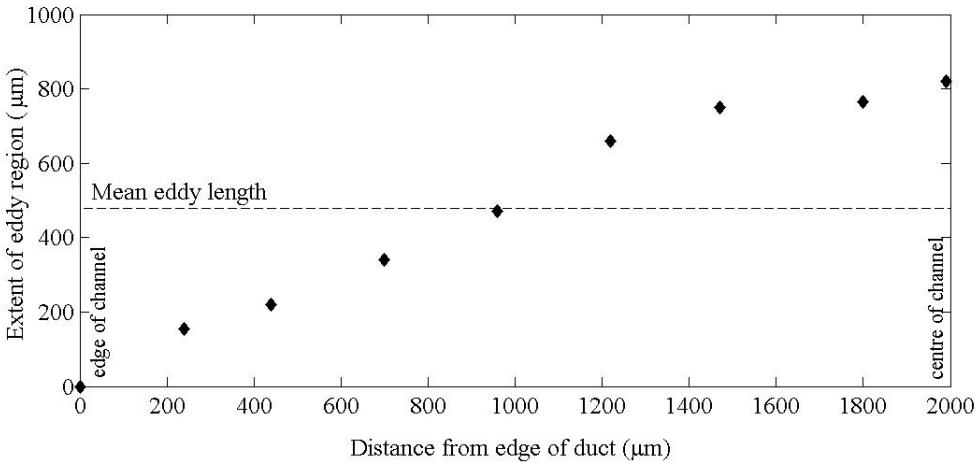

Figure 3.14: Experimentally observed variation in eddy size across inlet duct region.

It has been observed that the flow velocity through the inlet duct is not uniform across the width of the device and is caused by the manifold geometry beneath the device which issues a narrow jet of fluid towards the centre of the inlet. This causes the size of the associated eddy to vary across the width which is demonstrated in the plot shown in figure 3.14, the data for which is measured experimentally. It can be seen that near the side of the channel the eddy region is small and corresponds to a lower flow velocity, whereas towards the centre of the channel the jet emanating from the manifold creates a larger flow velocity and therefore longer eddy region. At flow rates between 0.1ml/s to 0.3ml/s the mean eddy size (calculated by numerically integrating the experimental data in the figure) is on average approximately 0.5 times that of the maximum (centre) eddy length and is indicated on the plot. Therefore, to simplify the experimental work, the maximum eddy size only has been measured and adjusted by a factor of 0.5 to take into account the non-uniform flow and to record a mean eddy length.

3.4.3 Validity of Model

In figure 3.15 the size of the eddy region for both simulated and modelled data is plotted as a function of flow rate and demonstrates that eddy size is strongly related to the fluid flow rate. An initial inspection shows that the CFD results underestimate the length of the eddy region, however they both show that the double-etched geometry produces a slightly smaller eddy region compared to the single etch geometry up to a flow rate of 0.5ml/s. The difference between experimental and CFD results can be explained by the following: a) in general the exact conditions at the inlet boundary of the CFD model are unknown although a parabolic profile has been assumed; b) pulses produced by the peristaltic pumps have been observed to cause fluctuations in the flow rate and therefore variations in the eddy size, although it has not been possible to quantify these variations; c) as demonstrated in figure 3.14, the flow through the device is not uniform across its width and suggests that a more computationally expensive 3-d CFD would be more appropriate; d) a build-up of particles can reduce the duct size and encourages more significant flow separation and a larger eddy, although the device was flushed frequently during experimental work. It is also noted that for the simulated data at the higher flow rates, the length of the eddy region for the double etched duct exceeds that of the single etch duct. Further CFD studies at these higher flow rates may be able to determine whether this is a genuine result of increased Re or due to errors in CFD model.

In general this exercise demonstrates that a 2-d CFD model provides a valuable method to predict the location and scale of eddy formation within microfluidic channels. This has been applied

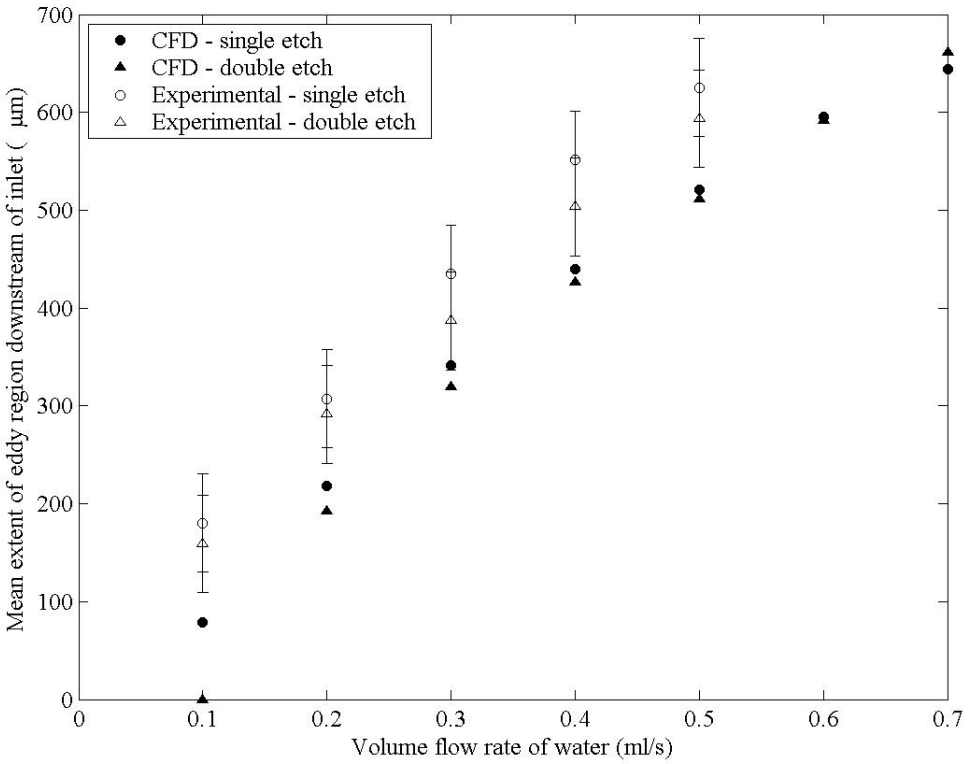

Figure 3.15: Eddy region size (downstream of inlet duct) as predicted by CFD compared to that recorded in experiment.

to ducts incorporating a minimum dimension of 160μm, where this measurement is taken from the 'waist' of the double etched ducts. However, by extending the complexity of the simulation to include transient and 3-dimensional aspects of the flow, it is anticipated that a more accurate representation of the flow can be generated, should this be required.

3.5 Geometric Study

3.5.1 Introduction

The geometric study aims to improve the duct design by restricting the onset of eddies and reducing pressure drops. As eddy regions are typically caused by discontinuities found in the duct geometry, an initial visual inspection can be used to identify these features. The visual inspection covers a range of possible geometries created by the anisotropic etch process. This approach serves to reduce the problem to a few geometric designs which are then each investigated more thoroughly within CFD simulations.

3.5.2 Qualitative Study

Eddy regions occur when the flow becomes separated from the wall. Within a fluid network this occurs in areas where the cross-section changes, such as in diffusive channels and at discontinuities and sharp edges in the wall geometry. For example, an anisotropic etch such as the single-etched duct inherently creates a diffusive duct with an inclusive angle of 70^o, based on the etch angle relative to the perpendicular $(90^o - 54.74^o = 35.26^o)$. This can result in significant losses if compared to the optimum angle of 6 to 7^o for turbulent flow and given by fluid mechanics text books [21]. Also, the separator device is formed from multiple wafer layers and misalignment between these can introduce sharp edges and sudden expansions or reductions in the fluid channel size. For example, where a single-etched duct acts as a convergent channel (inlet duct in figure 3.1(b)) as the fluid enters the main channel the fluid is subject to an extreme expansion, although no eddy is necessarily induced in the duct itself.

For the reasons discussed above the study concentrates on double-etched ducts and, in order to efficiently cover a range of possible duct geometries, a parametric approach is used. This analysis assumes an anisotropic wet silicon etch such as KOH, where figure 3.16 illustrates the parameters used to describe the resulting etched duct geometry with the direction of flow either way through

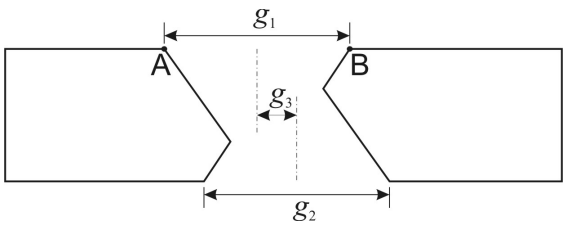

Figure 3.16: Parameters used to describe anisotropic etch geometry.

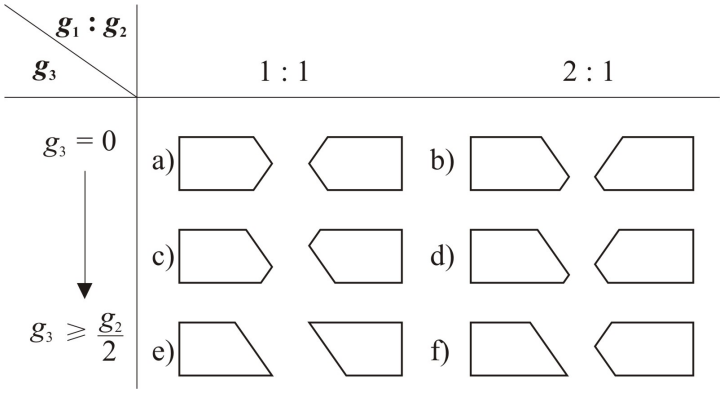

Figure 3.17: Range of anisotropically etched ducts considered in study

the duct. Parameters g_1 and g_2 describe the width of the top and bottom etch masks and subsequent etched areas, whereas g_3 describes the distance between the centrelines of the top and bottom etch areas, effectively representing their offset and the degree to which the duct is skewed.

For the purposes of the geometric study it has been assumed that the inlet and outlet 2 ducts are positioned at the extreme ends of the main channel, i.e. there are no redundant areas at the ends of the main channel. This is designed to discourage eddy formation either end of the main channel such as that demonstrated in figure 3.10 near the inlet duct. However, this assumes a fabrication method such that high accuracy is applied both to the alignment of the Pyrex upon the silicon layer and to the isotropic etching of the Pyrex which determines the length of the main channel.

By classifying the geometry in terms of the parameters g_1, g_2 and g_3, figure 3.17 illustrates the basic geometry groups used for the study. Again, fluid flows either way through the duct with the main channel flow passing either from the left or right.

Considering the selection of geometries displayed in figure 3.17, a discontinuity cannot be avoided where fluid passes to the main channel and beyond the silicon layer (points A or B indicated in figure 3.16). However, only the geometry type shown in figure 3.17(e) is unlikely to encourage eddy formation within the duct area itself; all other geometries contain discontinuities and a divergent element. It is therefore this parallel sided duct geometry which shall be investigated further.

3.5.3 CFD Study

Simple inspection has eliminated geometries which have a significant expansion or contraction. However, more insight is gained from CFD simulations investigating dimensions and the robustness of the flow pattern to small inaccuracies in dimensions and mask alignment. This is achieved by completing a series of simulations of the flow through both the inlet and outlet ducts, investigating the influence of dimensions g_1 (where $g_2 = g_1$) and also the influence of small etch mask inaccuracies which create the geometry illustrated in figure 3.17(f). The key observations are as follows and are based on CFD simulations using a flow rate of 0.5ml/s:

Duct width

Over a complete series of simulations, an optimum design is observed when subsequent sections of the flow path remain constant or gradually reduce in cross-sectional size, replicating the effect of a convergent duct and ensuring that flow remains adhered to the wall. An example of this is shown in figure 3.18 which demonstrates that, as the width of the parallel sided inlet duct is increased and becomes larger than the preceding channel section, an eddy region is created and expands. Note that this is only of significant advantage in the inlet region of the separator device as only the inlet duct leads to the relatively narrow main channel.

Error/offset in masks

Any errors or offset in the double sided alignment process used to align the etch masks on either side of the silicon wafer will potentially introduce a discontinuity. Such discontinuities generally encourage an eddy, the eddy size being related to the magnitude of the error/offset. Figure 3.19 depicting the outlet 2 duct shows one example of this where an eddy region forms within the area created by the curved isotropic etch profile within the Pyrex layer and the chamfer within the anisotropically etched silicon duct. However, the flow through outlet 1 is not influenced by the

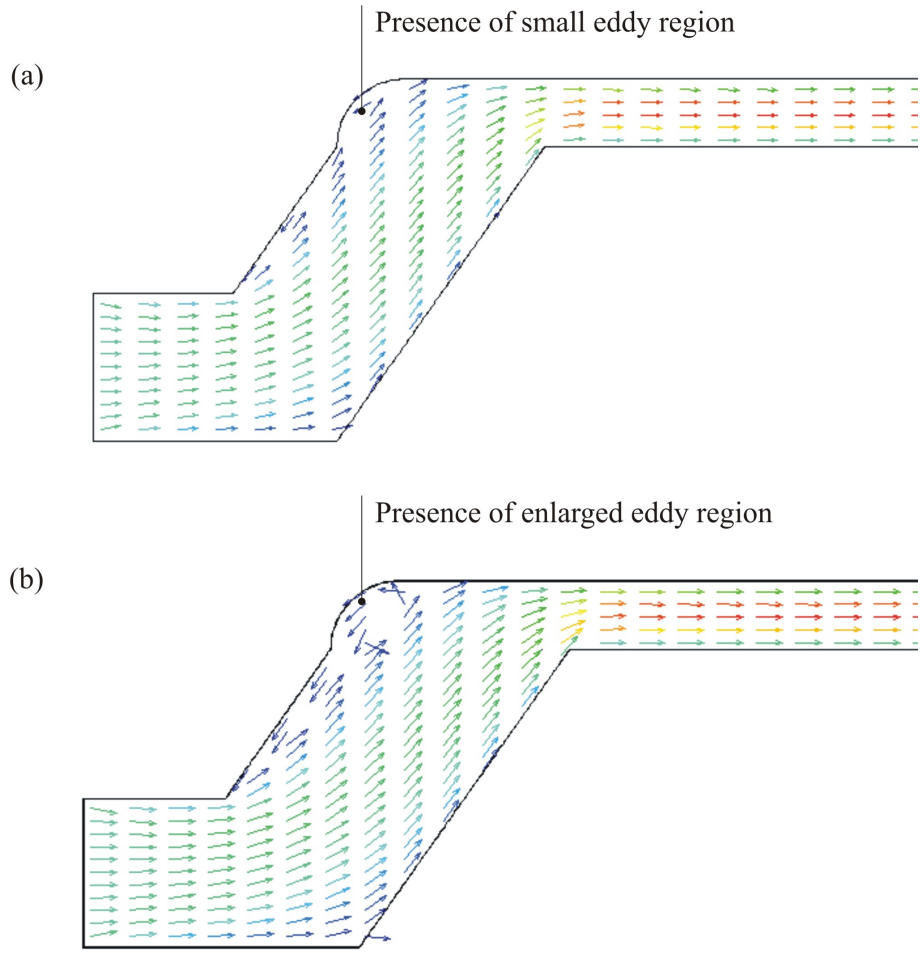

Figure 3.18: Influence of duct width on inlet duct flow pattern for a) minimum duct width and b) a 150μm increase in width.

Pyrex etch profile and is less sensitive to double sided alignment inaccuracies. Figure 3.20 shows that an eddy only forms within the main channel above the duct at a high degree of alignment inaccuracy where a large chamfer is present in the duct. This is unlikely to occur since the double sided alignment process is typically accurate to +/- $5\mu m$.

The eddy regions in the outlet ducts themselves and downstream of the main channel can be seen in figures 3.19 and 3.20 to be large, but importantly do not encroach on the flow within the main channel. Also, by not including more of the downstream geometry the accuracy of the simulation within the eddy regions is limited, therefore no conclusions will be drawn from this part of the simulation.

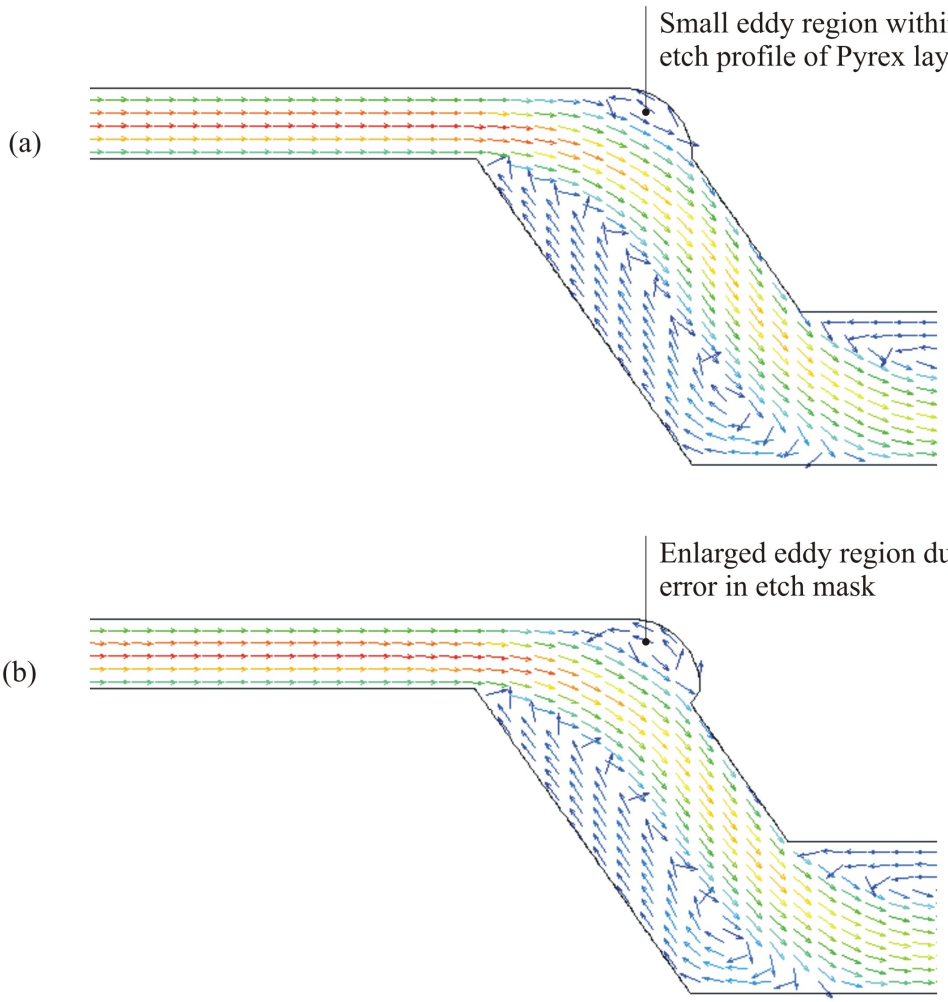

Figure 3.19: Influence of error/offset in etch mask on outlet 2 flow pattern for a) no offset and b) top etch increased by 50μm.

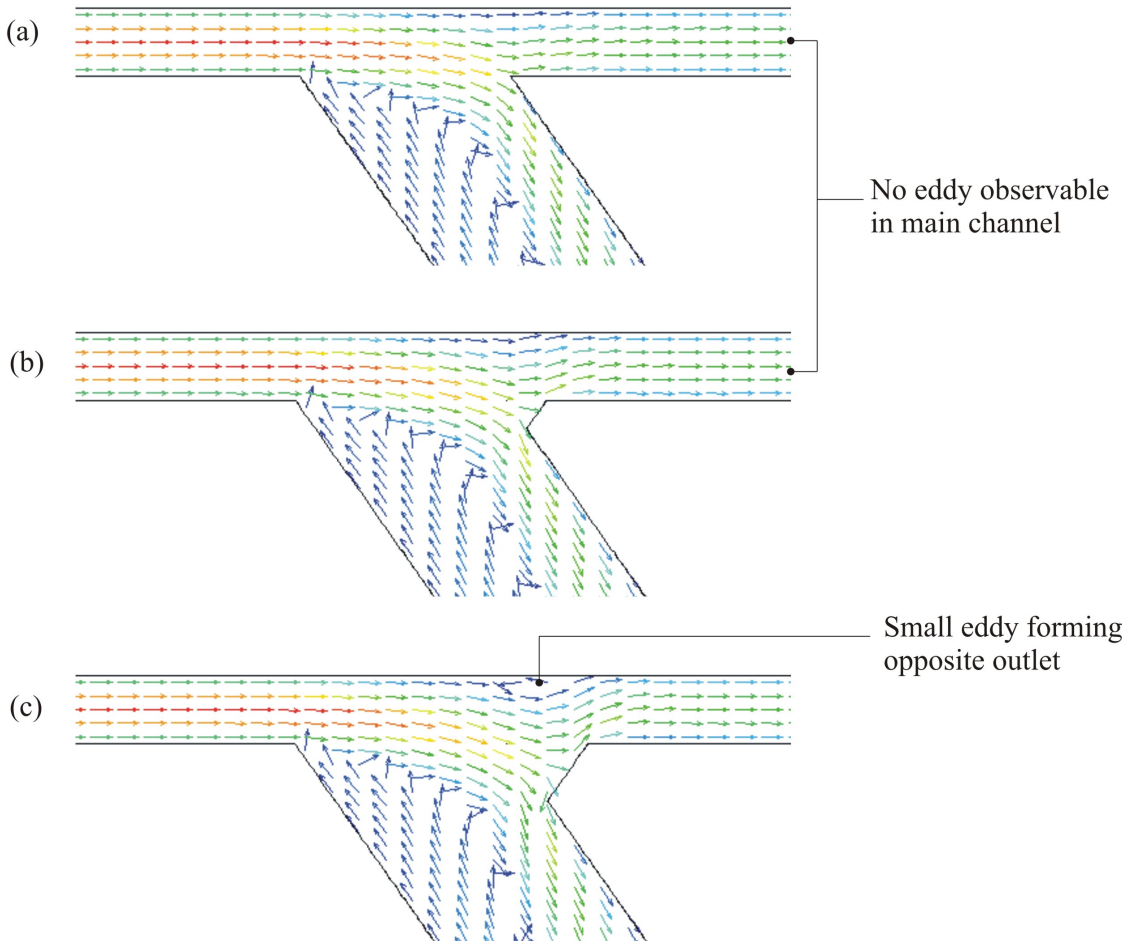

Figure 3.20: Influence of error/offset in etch mask on outlet 1 flow pattern for a) no offset, b) top etch increased by 50μm and c) top etch increased by 100μm.

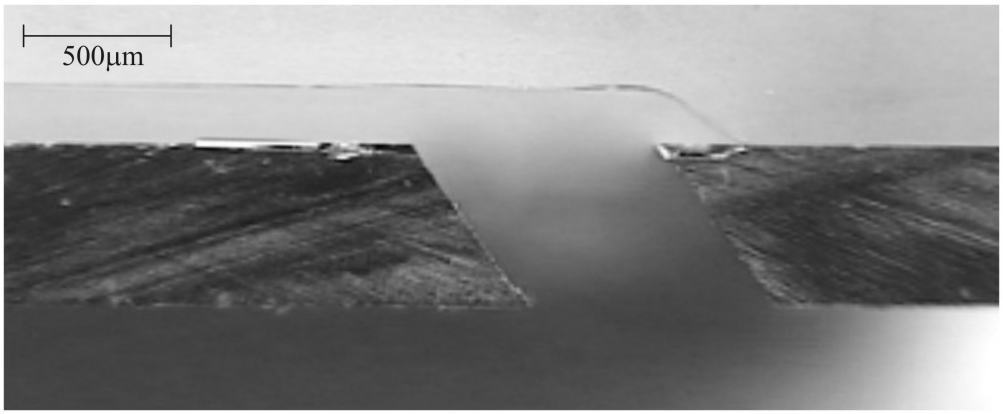

Figure 3.21: Cross-section of outlet 2 duct incorporating revised geometry.

3.5.4 Experimental Flow Tests of Modified Geometry

Parallel ducts have been used within a new batch of devices from which figure 3.21 shows an example of the outlet 2 region and is taken from a cross-sectioned device. The potential chamfering of the duct edges produced by errors in alignment has not occurred. However, the alignment of the Pyrex and silicon wafers, which was performed by eye, means that the outlet duct is not aligned exactly with the end of the main channel. The use of an optically aligned anodic bonder would produce more satisfactory results by reducing this overhang.

The device has been tested using the same method described in section 3.4.2 and no eddy downstream of the inlet is observed up to flows of 0.6ml/s, beyond which the flow pattern is difficult to discern. This level of eddy suppression is significant when compared to the results recorded in figure 3.15 for the original, more angular geometry where eddies downstream of the inlet exist at a much lower flow rate of 0.1ml/s and possibly below this value. The only drawback of the parallel duct is the imposition of a minimum channel width which is based upon the silicon wafer thickness.

Figure 3.22 shows the pressure distribution in both the double-etched and parallel sided inlet duct geometry, where the large pressure drops seen within the double-etched geometry are not observed within the new parallel geometry where the pressure contours are much more widely and evenly spaced. It is accepted that eddy formation and, possibly, pressure losses are still likely to be significant within the outlet ducts, although more careful design of the downstream fluid network would be beneficial.

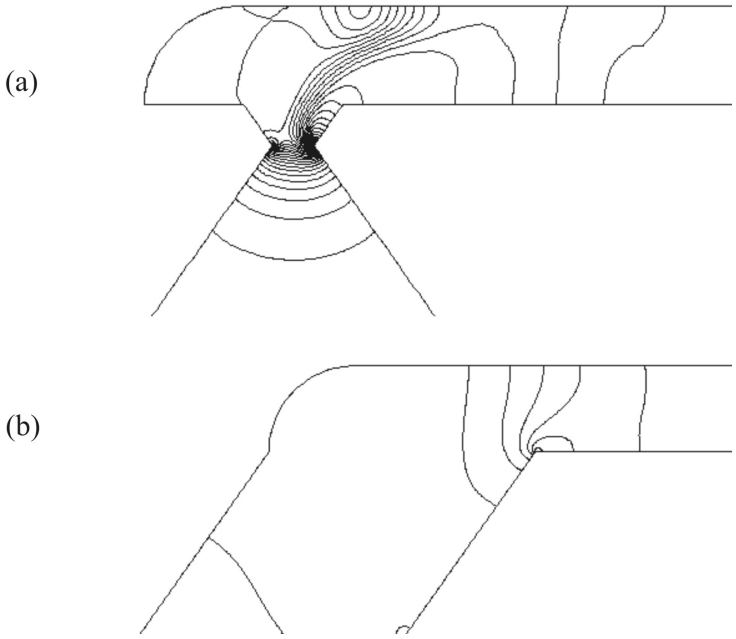

Figure 3.22: Pressure profile in a) original double etched inlet duct geometry and b) parallel etched inlet duct geometry.

3.6 3-Dimensional Assessment of Outlet Region

Within the main fluid chamber it has been assumed that the particle separation effect due to the acoustic radiation force is less efficient towards the side walls. The isotropic etch process used in the fabrication of the Pyrex creates curved side walls, as well as the curved walls either end of the main channel, as illustrated repeatedly throughout this chapter. Because of this, outlet 1 has been designed not to extend across the full width of the chamber, but is smaller than the width of outlet 2, approximately 4mm compared to 5mm wide. This means that any fluid towards the side walls which is not effectively processed is not drawn through outlet 1, which would reduce the clearance and separation efficiency. However, this potentially invalidates the 2-d flow assumption as lateral (z direction) flows are potentially created within the outlet duct region. This section presents a brief investigation into the effect of dissimilar outlet ducts and mentions the implications on simulating the particle movement and separation process discussed in chapters 5 and 6.

A coarse 3-d model has been used which, although it has not been optimised for accuracy, is chosen to involve only a relatively short processing time and give a general indication of the flow behaviour. The model includes the outlet region of the main channel and uses a symmetry plane

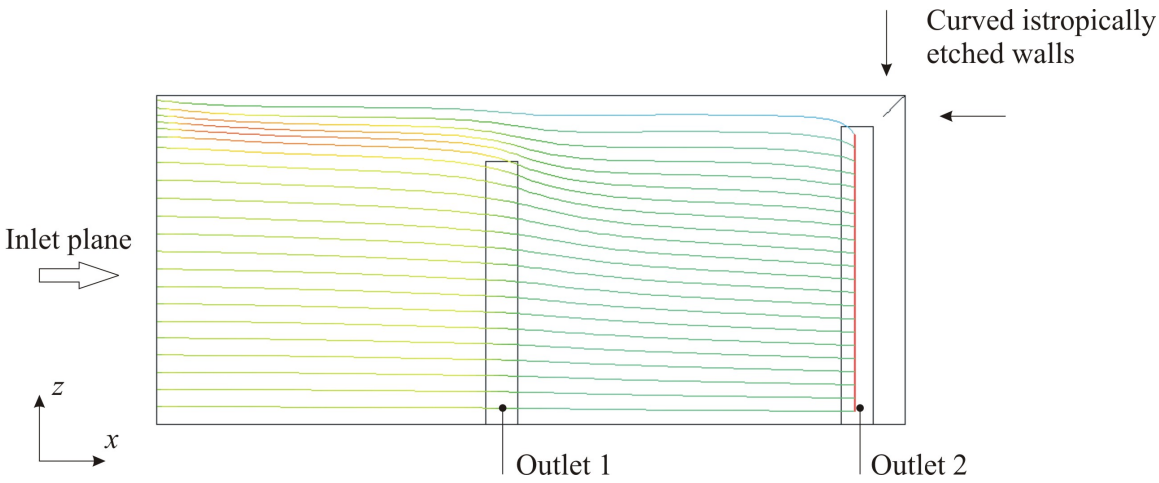

Figure 3.23: 3-d CFD simulation of outlet region looking down through Pyrex layer and illustrating streamlines of fluid passing through outlet 2.

so that only half the flow domain needs to be modelled. To simplify the model further, the outlet duct geometry is not included, but instead is replaced by simple outlet planes to which flow rate boundary conditions are applied.

Using the 3-d model, figure 3.23 illustrates the flow pattern when looking down through the Pyrex layer, with the example based on a total flow rate of 0.1ml/s with 60% of the flow passing through outlet 1 and 40% through outlet 2. To simulate this, mass flow rate boundary conditions are applied to the inlet and outlet 2, with zero gauge pressure applied to outlet 1. The figure shows a set of streamlines for fluid destined for outlet 2, where it can be seen the fluid across the full width of the channel is drawn. However, the streamlines show that there is a z component of velocity and that towards the top of the fluid domain beyond the extent of outlet1 the streamlines are more bunched, suggesting that a significant proportion of the fluid drawn through outlet 2 originates from the wall region.

To illustrate this more clearly figure 3.24 indicates how the fluid, as seen at the inlet plane in the main channel of figure 3.23, becomes divided on reaching the outlet ducts. The plot is orientated such that the fluid would pass perpendicular to the paper with the x and y axes corresponding to the positions across the width and depth of the channel, respectively. The dark grey area indicates the region of fluid which ultimately passes through outlet 2, whereas the light grey area represents the fluid passing through outlet 1. If a 2-d flow field is assumed the division of fluid would be uniform

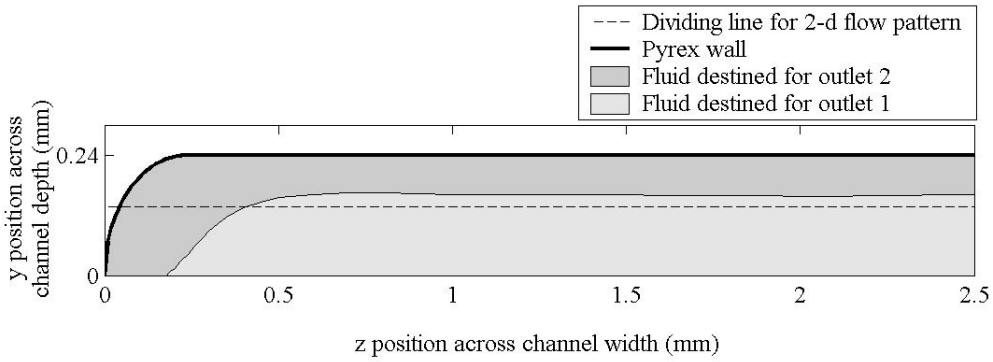

Figure 3.24: Division of fluid between outlet 1 and outlet 2 and corresponding position within main channel. Both 3-dimensional and 2-dimensional flow systems considered.

across the width of the channel, i.e. flow through outlet 1 comprises of a region of fluid located between the silicon face and up to a certain depth within the channel indicated by the dashed line, the position of which depends on the proportions of fluid being drawn from each outlet. However, this line does not coincide with the division indicated by the two shaded areas. Instead the 3-d aspects of the fluid flow mean that all fluid within the side wall region flows through the wider outlet 2, and is compensated by a greater proportion of the fluid in the centre (and inline with outlet 1) being drawn through outlet 1. This has implications on the approach used to predict particle separation, as particles which would normally be considered to pass through outlet 2 using a 2-d model may in fact pass through outlet 1 if a 3-d flow system were to be considered.

To determine accurately the position of flow division in the 3-d system, a significantly more refined CFD simulation would be required and solutions generated over a range of flow rates and outlet 1 to outlet 2 flow proportions. Due to the significant computational time required, the simple 2-d flow field is assumed when determining particle separation efficiencies in later chapters, with the

implications of this assumption being discussed.

3.7 Conclusions

It has been shown that significant improvements in the microchannel geometry can be achieved even with the limited geometry potential of the wet etch process, which for silicon geometry is restricted by an anisotropic etch. CFD and experimental results demonstrate that this has been most successful in the main channel of the device where highly laminar flow is required for predictable operation of the device in manipulating particles. In one case problematic eddy formation has been eliminated within a range of flow rates at least 6 times larger than that for the original geometry. Significant improvement can be made by eliminating duct shapes associated with eddy losses such as divergent ducts and geometries.

The principal advantage of the elimination of eddy flows for devices employed in the processing of fluid/particle samples is in the reduction of sedimentation and therefore contamination of subsequent samples. Crevices associated with eddy region sites are locations where particles typically lodge and are therefore detrimental to the operation of reusable (as opposed to disposable) devices which require flushing to remove contaminants. In this study eddy flows within the duct regions have been investigated and limited by the use of parallel sided ducts.

By modifying the geometry to reduce the eddy region size, adverse pressure gradients contributing to the eddy formation are also reduced and minimise the total pressure drop across the microfluidic device. This translates to a reduction in the total power required to pump fluid through the system; a benefit to μTAS devices. In general these benefits may be found in low power microfluidic devices such as micro-pumps, where etched ducts are used to carry fluid to different planes within a fluid circuit of layered wafer structures and resistance offered by the fluid system needs to be minimised. Further work is required to improve aspects of the outlet ducts where the flow field is highly dependent upon the downstream fluid network.

The assumption that the flow field is 2-dimensional in nature has been investigated within the outlet region of the device where the geometry of the outlet duct create lateral flow components. This geometry invalidates the 2-d assumption which implies that uniform regions of fluid are extracted through either outlet. The flow pattern has been shown to be more complex and has implications when predicting particle separation which is discussed in chapter 6.

Chapter 4

Lateral Acoustic Fields in the Separator

4.1 Introduction

The operation of the separator relies on the acoustic radiation force experienced by a particle and its ability to move particles to the nodal plane(s). The acoustic design of the device is therefore paramount to successful separation. Due to the layered nature of the design, the layer thickness y dimensions are relatively small compared to the length and width (x and z dimensions), therefore, when driving the device at frequencies which excite a thickness resonance the acoustic characteristics through the y-axis predominate. The design of the separator therefore relies on the y-axis acoustic characteristics which are predicted using the 1-d model described in section 2.5.2.

However, lateral forces acting perpendicular to the axis of propagation (x-z plane) have frequently been reported and it is generally appreciated that such forces can significantly influence the movement of particles. The primary axial radiation force induces particles to move parallel to the direction of acoustic propagation, whereas lateral forces are aligned perpendicular in the x and z directions of the device. During device operation particles are observed to form into striated patterns (figure 4.1) which suggests the existence of lateral forces and, as the patterns vary with frequency, also suggests that the forces can be attributed to the acoustic field. In figure 4.1(a) with the fluid flow condition, any acoustic forces in the x direction are negligible compared to the fluid drag force and so the effect of the acoustic force acting in the z direction can be observed easily, revealing striations. However, in figure 4.1(b) with a no flow condition, x direction forces are also observed and become more significant at the end of the transducer (right-hand side of image), again indicating that these forces are acoustically generated.

It can also be seen in (b) that, as the lateral radiation forces cause particles to move into closer proximity to each other than would be attributed to the primary radiation force alone, particle clumping is induced where inter-particle forces become more significant. Although inter-particle forces themselves are not studied in this thesis it is appreciated that such forces contribute to the forming of particle aggregates which can disrupt the separation process as the aggregate does not necessarily have the same characteristics as the individual particles, e.g. the aggregate may sediment out of the suspension or block and disrupt the movement of the fluid. The forming of aggregates in this application is therefore not considered desirable, but in part can be controlled by reducing the strength of lateral forces.

In this chapter the nature and cause of lateral radiation forces are investigated to understand and predict their occurrence and magnitude. This is achieved by investigating the acoustic field computationally to understand better the nature of the lateral forces and factors which influence their magnitude, and in particular to determine the significance of the lateral force relative to the primary axial radiation force. This study therefore also demonstrates the use of FEA as a tool for the acoustic design of the device.

4.2 Development of 2-Dimensional Acoustic Model

4.2.1 Acoustic Simulation Techniques

The acoustic impedance transfer model (section 2.5.2) considers the 1-dimensional acoustic field and therefore only the axial (y-axis) radiation force. To extend the simulation work to consider 2-dimensions, the use of finite element analysis (FEA) is examined, consistent with the computational approaches used throughout this work. For this FEA work the ANSYS computer package is used.

Other than that described in section 2.4.3, the literature has revealed little which is directly relevant to the simulation of acoustic fields within MEMS and similar scale systems, and certainly not to the extent reported for the simulation of fluid. The small amount of literature which is available uses established equations and techniques when simulating micro-scale ultrasonic devices with no special treatment reported to take into account the scale of the systems. Also, there is scant literature concerning FEA acoustic computational simulation which implies a reasonable level of confidence in this established technique.

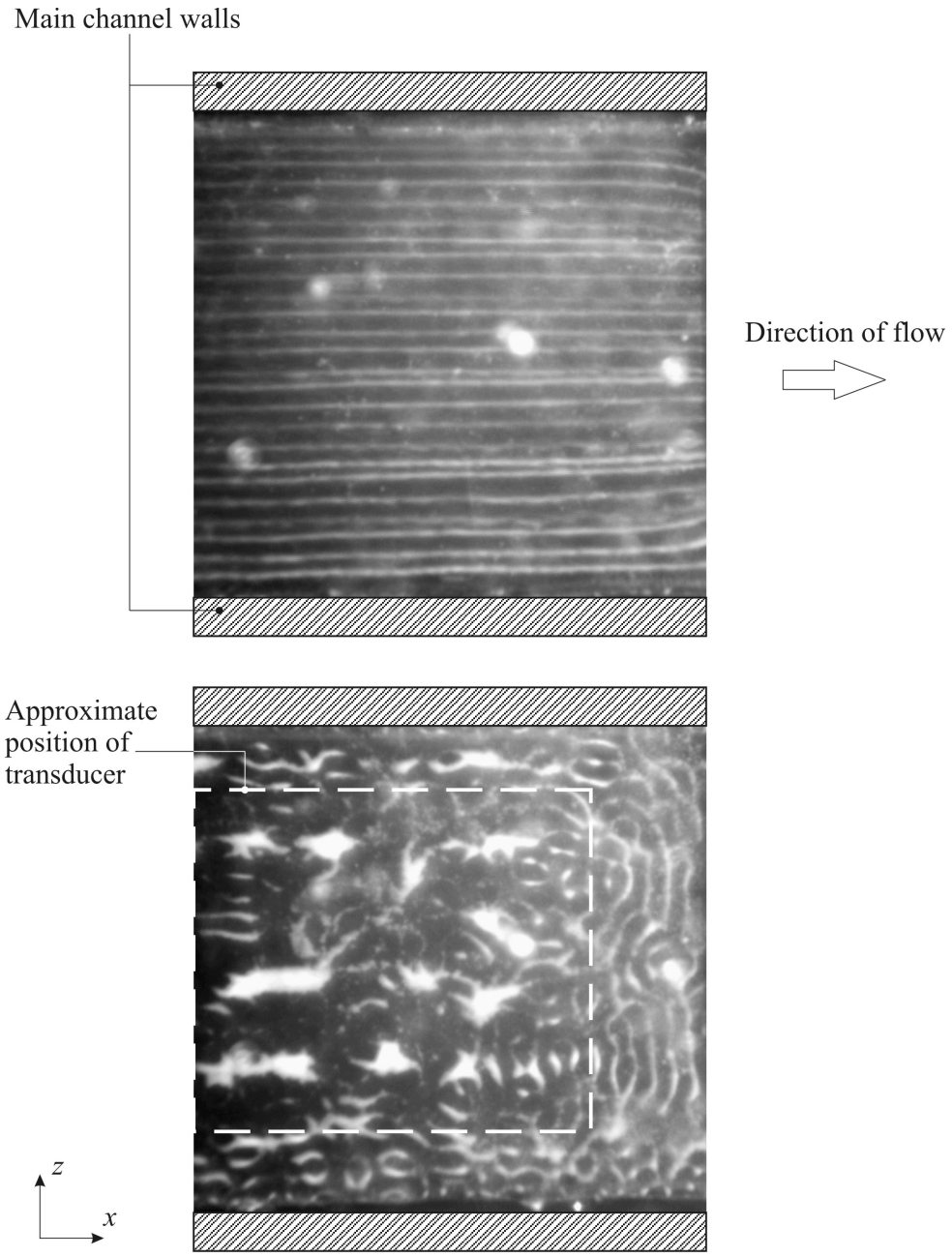

Figure 4.1: Image taken during operation of cell at a frequency of 3.4MHz and showing striation patterns (a) with fluid flow and (b) with no fluid flow.

It is certainly not proposed that the 2-d simulation described here replaces the 1-d model used to determine the critical dimensions and material properties of a design. At this stage, the 2-d model is presented as a more qualitative tool and is not used in subsequent simulation of particle movement which is reserved for the 1-d model.

4.2.2 Construction and Processing of Model

The approach to developing a suitable FEA model is similar to that used for the CFD model in chapter 3, therefore only the specific differences when processing the acoustic simulation are described here. One important difference is the orientation of the 2-d plane; in the fluid CFD simulation the model described the x-y plane and neglected the z-axis, across width, direction as it was assumed that the x-y flow field was significantly more important. With the acoustic field, it can be seen in figure 4.1(a) that during operation, other than the stronger y-axis primary axial force, the lateral forces acting in the z direction are of most interest as these form the striated patterns, therefore suggesting acoustic simulation of the y-z plane.

Pre-processor

The finite element analysis investigation uses plane acoustic fluid elements, requiring the input of acoustic property values including density, sonic velocity and absorption coefficient at boundaries. The acoustic fluid elements are used for both the fluid and solid phase layers of the separator; although solid elements are available giving similar modal results, they are not as convenient for submission and extraction of acoustic parameters within solid phase regions. Also, use of fluid elements does not support the analysis of structural modes, therefore analysis results only include acoustic enclosure modes.

Using the 2-d plane elements and appropriate boundary conditions, it is possible to approximate the 1-d as well as the 2-d case. Figure 4.2(a) illustrates schematically the use of a single pressure release surface and a horizontally constrained one element wide model to simulate the acoustic field in the fluid and reflector (Pyrex) layers. In this case the field varies only in the y direction and is effectively a 1-d simulation. Figure 4.2(b) simulates the 2-d aspect of the fluid and reflector layers where the reflector layer is seen to encase the fluid region. Pressure release boundaries exist on the top and side of the reflector and to simplify the simulation only half the structure is modelled, facilitated by the use of a symmetry plane on the left side.

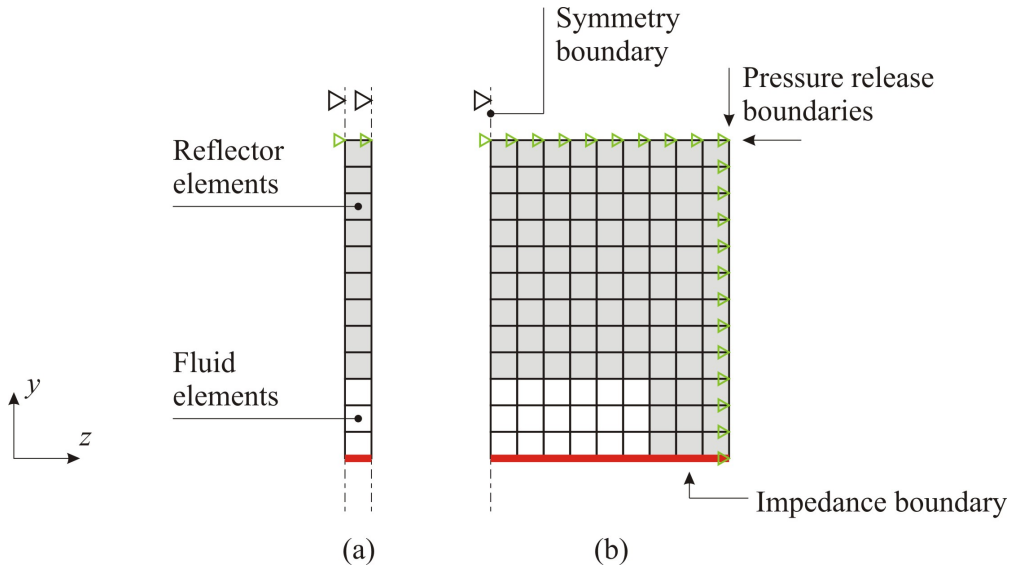

Figure 4.2: Schematics of (a) 1-dimensional and (b) 2-dimensional models indicating the fluid and reflector elements and boundary conditions. Boundary conditions applied include zero displacement boundaries (▷), pressure release boundaries (▷) and impedance boundaries (-).

Although the FEA software is capable of simulating all the layers included in the separator design, only the reflector and fluid layers are included in the current study. Once a degree of confidence is established with this level of modelling, subsequent work may include simulation of the silicon matching layer, glue and transducer, but is beyond the remit of this thesis.

Solution Phase

Both modal and harmonic analyses can be completed on the model, giving the response to modal frequencies or a chosen frequency, respectively. For harmonic analyses, the applied pressure at the vibrating surface may be input as a complex number, indicating a phase difference between the acoustic pressure and velocity fields, and allows for losses in the media. The modal analyses are used to identify the resonant behaviour of the layers and are used throughout this study.

Post-processor

In the output listings of the ANSYS package the modal analysis gives a real component of the acoustic pressure field. However, the harmonic analysis gives real and imaginary components of

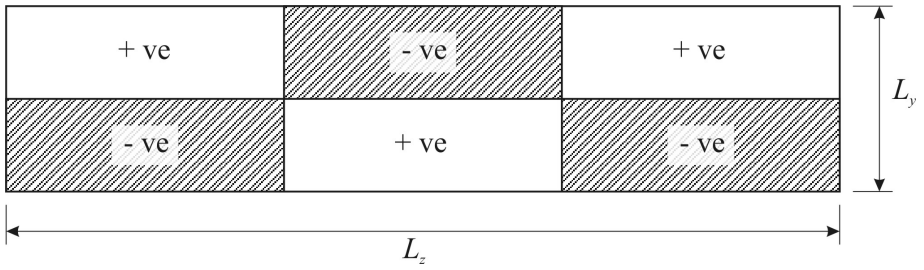

Figure 4.3: Example of mode shape pressure maxima and minima in a rectangular cavity for $m = 2$ and $n = 3$.

pressure and particle velocity and so can be used to determine the acoustic radiation force. Also, vector y and z quantities are given as separate components corresponding directly to axial and lateral radiation force components.

4.2.3 2-Dimensional Fields in Rectangular Enclosures

To investigate the accuracy of the model a 2-dimensional resonant pattern is simulated. A simple rectangular waveguide is used as the basic resonant characteristics can be determined analytically. Kinsler et al. [133] give an expression for the resonant frequencies of a rectangular waveguide,

$$f = \frac{c}{2}\sqrt{\left\langle \frac{l}{L_x} \right\rangle^2 + \left\langle \frac{m}{L_y} \right\rangle^2 + \left\langle \frac{n}{L_z} \right\rangle^2}, \tag{4.1}$$

where the various dimensions of the waveguide are given by L_x, L_y and L_z with relative mode orders of l, m and n. If the x dimension is assumed large compared to the other dimensions, equation (4.1) is reduced to a 2-d description of the y-z plane. As an example, a mode pattern resulting from $m = 2$ and $n = 3$ is shown in figure 4.3 which indicates regions of acoustic pressure maxima and minima. For the reflector layer, based on a thickness of 1525μm, device external width of 6.8mm and $c = 5430$m/s for Pyrex, this mode shape would occur at a frequency of 3.76MHz.

The same geometry is simulated in the FEA model and comprises simply of a 2-d rectangular structure with pressure release boundaries on all sides. A modal analysis then identifies various resonant frequencies and the associated mode shape. The mode shape described in figure 4.3 has

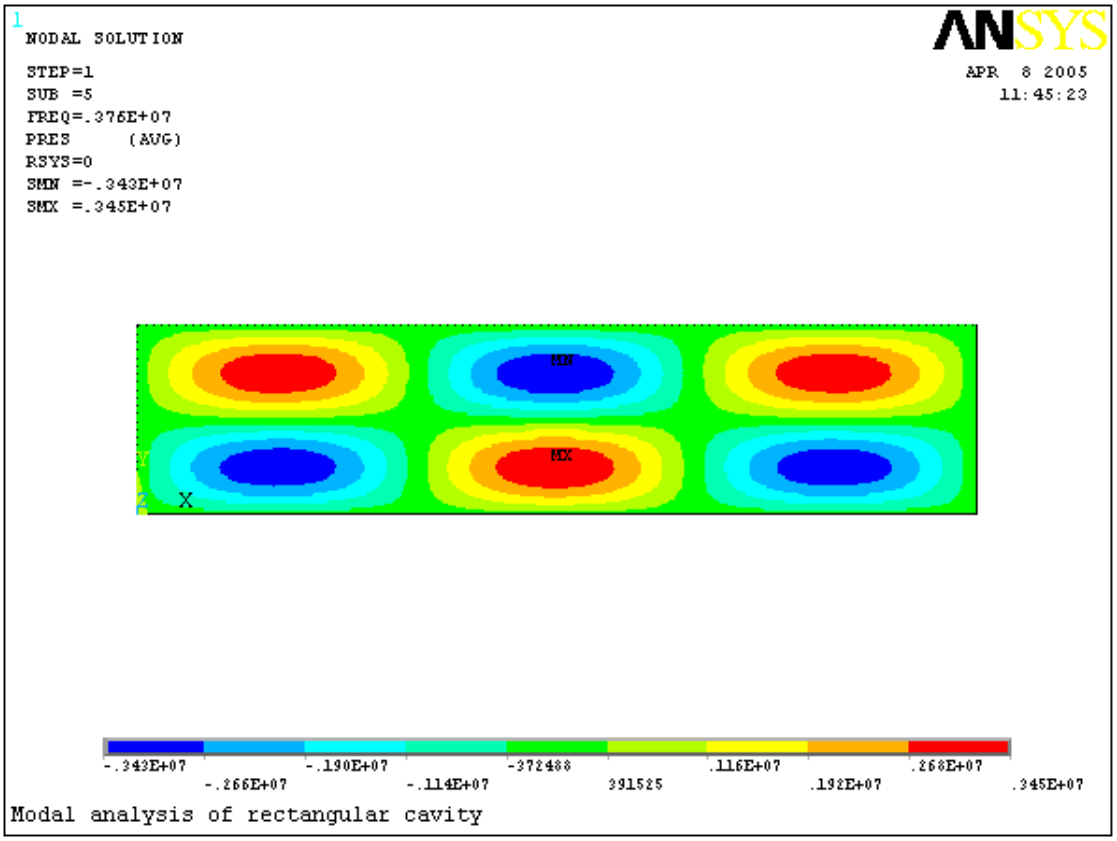

Figure 4.4: Modelled example of resonance in a rectangular cavity.

been modelled and is shown in figure 4.4. The analytically calculated and modelled frequencies are in agreement, providing confidence in the FEA approach used.

It can be seen in figure 4.4 that 2-dimensional resonant fields are characterised by acoustic pressure variations occurring in both directions. In the fluid filled cavity it is expected that similar 2-d enclosure modes give rise to pressure gradients and, therefore, acoustic forces in the lateral z direction as well as the y direction, as initially intended for particle manipulation. Further, it can be imagined that all 3 dimensions would be subject to similar modes. Whilst the mode shape and resonant frequency in a simple rectangular cavity can be determined analytically, the geometry and therefore the mode shapes in layered ultrasonic devices is more complex and cannot be solved analytically, supporting the use of computational approaches such as FEA. The following subsections now progress with an FEA model and attempt to simulate the layered structure of the

device both in 1-d and 2-d.

4.2.4 Comparison with 1-Dimensional Simulation

As the FEA model agrees well with the analytically determined frequencies of a simple 2-d cavity resonance, the fluid and reflector layer of the separator device are now modelled. A modal analysis of the basic structure seen in figure 4.2(a) is used to determine the 1-d resonant frequencies of the layers and is compared to the frequencies calculated by the 1-d MATLAB model. The MATLAB model is reduced to include only the fluid and reflector layers, to maintain similarity between the two models. The two models predict slightly different resonant frequencies, for example, the FEA model predicts two resonant frequencies of 3.37MHz and 4.35MHz compared to 3.46MHz and 4.33MHz for the MATLAB model, differing by up to 3%. This difference may be attributed to the different methods used to describe losses in the respective ANSYS and MATLAB models.

Figure 4.5 illustrates the resonant pressure fields predicted by each model and uses an arbitrary acoustic particle velocity boundary condition of 0.002m/s at the boundary between the matching layer and fluid layer. The resonant frequencies chosen correspond to modes 3 and 4 reported in Hill et al. [126] which are both approximately half-wavelength fluid layer modes.

Referring to figure 4.5 it can be seen that the lower frequency mode results in a node positioned slightly above the centre line of the fluid layer as the fluid depth $h < \lambda/2$ and the depth of the reflector layer is approximately equal to λ. There is a poor comparison between the two models regarding the magnitude of the pressure field in the reflector layer which may be due to the small difference in the frequencies predicted and acoustic losses, although the mode shapes compare well. For the higher frequency mode both the mode shape and pressure amplitude compare well, showing that the reflector and fluid layers are $\frac{5}{4}\lambda$ and $\frac{1}{2}\lambda$ respectively with a nodal plane existing along the centre plane of the fluid channel.

4.2.5 Comparison with Experimental Observations

The FEA model above is extended to describe the fluid and reflector layers in 2-d and uses the model structure represented in figure 4.2(b) with pressure constraints applied to the external surfaces only. The simulation is based on the measured width of the Pyrex layer (external width) of 6.8mm and design width of the fluid of 5mm. The curved side walls created by the isotropic etch are also included in the model. This model can be compared to experimental observations such

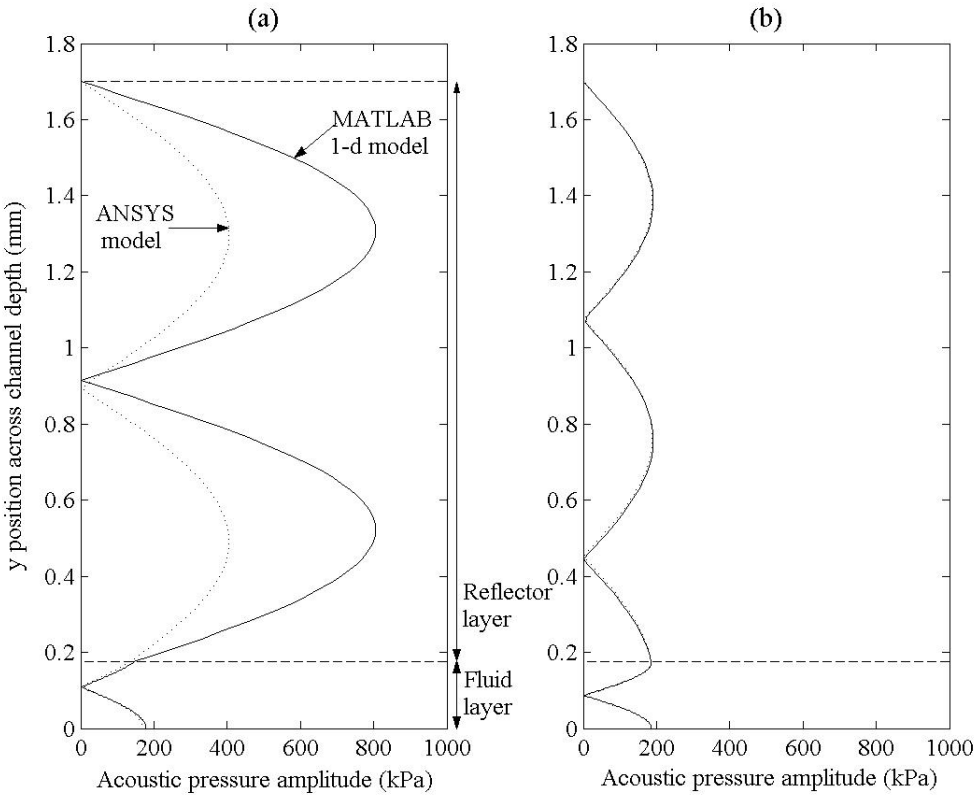

Figure 4.5: Comparison between the acoustic pressure fields predicted by the FEA and MATLAB models for resonant frequencies of a) 3.37MHz and 3.46MHz for the respective models and b) 4.35MHz and 4.33MHz and based on an acoustic particle velocity of 0.002m/s at the fluid plane.

as that pictured in figure 4.1(a) and aims to validate the model and demonstrate the source of the striated patterns.

The two modes identified in the previous subsection are investigated as these are the modes used in operation of the separator. However, the resonant frequencies and behaviour of the 2-d modelled system are different to the 1-d system as additional boundary conditions and geometry are used in the simulations. As well as these two axial half-wavelength modes, the FEA model also identifies many other, predominantly lateral modes, although are not investigated here.

Figure 4.6 shows the results of a modal analysis of the reflector and fluid layers and describes the pressure field within the system. It can be seen that in (a) a standing wave of order approximately $m = 2$ and $n = 1$ is present in the reflector layer, which is predominantly a through thickness resonance resembling the pressure profile in figure 4.5(a). The field pattern within the fluid layer is much more complex and is highly non-uniform, showing acoustic 'hot spots' at regular positions across the channel width. These hot spots suggest that particles will move to a series of lateral positions across the fluid chamber with an approximate spacing of 0.25mm. The experimentally observed striations are spaced at approximately 0.21mm apart which is comparable to the modelled results, the discrepancy possibly due to inaccuracies in the fluid channel dimensions used in the simulation.

The higher frequency mode shown in figure 4.6(b) shows a more complex pattern than expected within the reflector layer which is likely to be caused by the axial resonance coinciding with a lateral resonance producing a 2-d pattern. However, the pattern within the fluid layer is more uniform and, although some lateral variation still exists at this frequency, the nodal plane (green contour) can be seen to run along the centre plane of the fluid layer as predicted by the 1-d simulations.

Lateral variations in the fluid layer acoustic field cause a variation in the axial strength of the radiation force and therefore obvious implications on the particle separation efficiency. Also the lateral variations themselves are accompanied by lateral radiation forces which may induce particle agglomeration, allowing short range inter-particle forces to cause particles to cluster further. Although this may enhance particle separation as the radiation force is proportional to particle volume (equation (2.11)), sedimentation of particle clumps has been observed and is detrimental to successful separation.

By investigating the harmonic response of the fluid/Pyrex system to an applied pressure, it would be possible to extract acoustic pressure and velocity data used to determine the radiation force acting on a particle within the fluid layer. However, it is felt that a quantitative assessment of

(a)

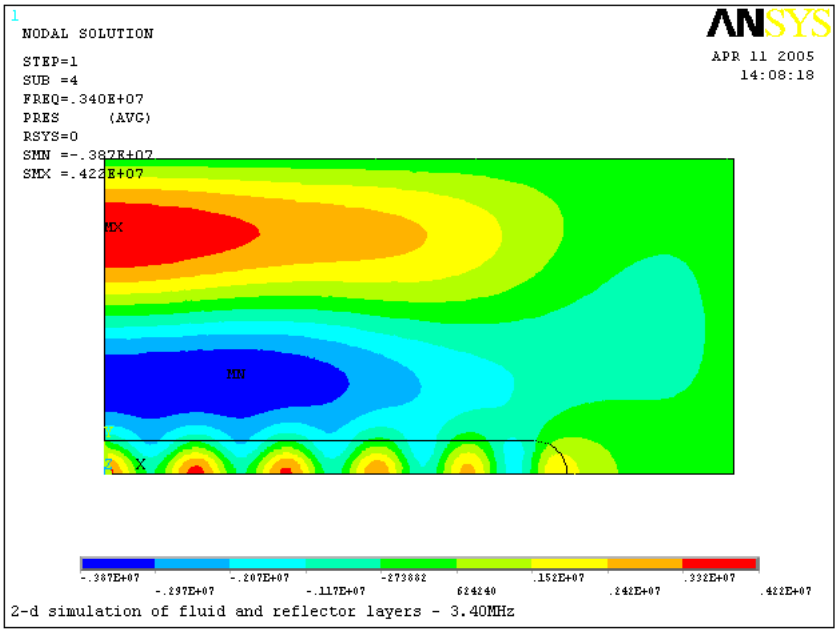

(b)

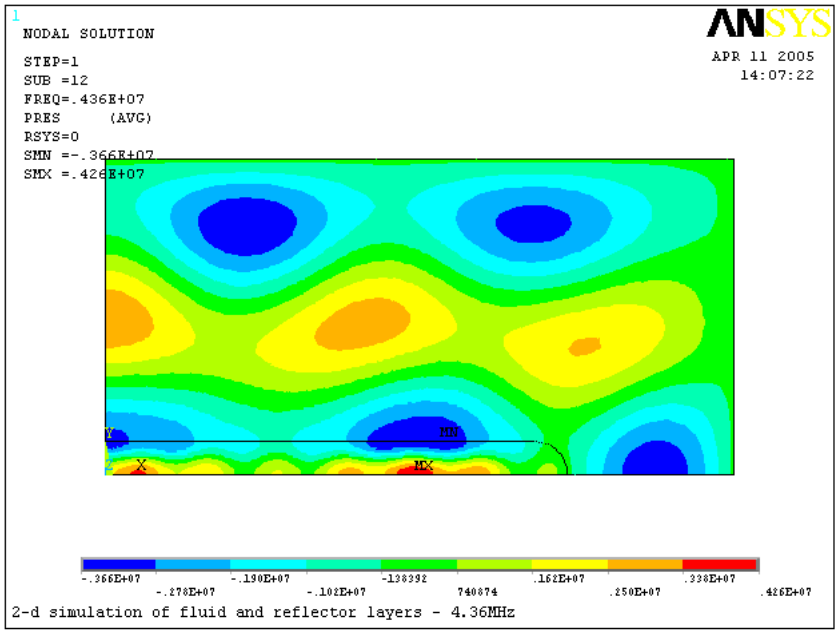

Figure 4.6: 2-d mode shapes given by modal analysis of fluid and reflector layers for a) 3.40MHz and b) 4.36MHz.

the radiation force would be misleading as the simulation is highly sensitive to lateral dimensions (investigated further in the following section), and also the nature of the applied vibration is not accurately described without extending the model to include the silicon and transducer layers.

Instead, the modal analysis can provide a qualitative assessment of the significance of lateral modes and variations in the acoustic field. The radiation force acting on a particle held within the fluid layer is in part related to the gradient of the acoustic potential energy density (equation (2.11)), in turn related to the square of the acoustic pressure, and defines the magnitude and direction of the force. Therefore, a particle will follow the route of maximum gradient and to regions of low pressure amplitude (green contours). Using the pressure data given in the modal analyses upon which figure 4.6 is based, the lateral gradient of potential energy density is up to approximately 85% and 39% of the more dominant axial gradient for the 3.40MHz and 4.36MHz modes respectively, measured in the central region of the fluid layer near the plane of symmetry.

These values are significant regarding the movement of particles within the fluid and resulting separation and, although it is not intending to use these values in separation predictions, it does present a case for further investigation into lateral fields.

4.3 FEA Study of Material and Geometry

It has been shown that the presence of lateral modes are a likely cause of lateral variations in the acoustic field and the formation of particle striations during operation. This section investigates the influence of selected parameters on the acoustic field within the fluid layer using similar FEA models describing the fluid and reflector layers and has been limited to the lateral design of the fluid side-walls. The axial geometry and material properties are not altered as these are more integral to the operation of the device. This study provides recommendations for the design of similar devices and demonstrates the use of FEA.

4.3.1 Influence of Side-wall Width

Referring to figure 4.4 and equation (4.1), the pressure release boundaries on all sides of the cavity have a bearing on the mode shape and resonant frequency. Therefore, it is reasonable to assume that at the same frequency (3.76MHz), but applying a more complex set of boundary conditions, would influence the resonance characteristics of the cavity and mode pattern. Applying this to

the separator device, it is conceivable that the side wall of the fluid chamber influences the lateral mode shape seen in the fluid layer, but by maintaining the y characteristics, the dominant through-thickness resonance should remain relatively unaffected. Therefore, the FEA model is used to demonstrate the influence of the side-wall thickness upon the lateral mode.

The side-walls of the experimental devices are defined by the width of the bonded Pyrex/silicon region, estimated to be approximately 0.9mm wide. The simulations in figure 4.7 describe the influence of this side-wall width whilst maintaining a fluid channel width of 5mm, where a modal analysis is again used to predict the mode shape when the through-thickness resonant frequencies are excited.

For mode 1 at ~ 3.4MHz shown in figure 4.7, it can be seen that as the thickness of the side-wall is decreased from 1.0mm to 0.2mm, the distinctive lateral variations lose definition and the field becomes more uniform across the width. This could be the reduced acoustic impedance of the wall for the smaller side-wall widths as well as the increasingly better match between the fluid and reflector layer widths such that there is a reduction in acoustic pressure at the fluid chamber/side-wall boundary.

For mode 2 at ~ 4.4MHz also shown in figure 4.7, a similar trend can be seen although the mode shape in (a) reveals more lateral variations within the reflector layer than the fluid layer. Even so, a more uniform field is predicted for small side-wall widths, with (c) revealing no discernible lateral periodic variations in the fluid. Generally this suggests that by reducing the side-wall width, particles passing within the fluid layer will move towards a more well defined nodal plane across the fluid layer width, rather than moving to acoustic hot spots and forming striations.

For the small side-wall widths it has previously been mentioned that the acoustic pressure is low at the fluid chamber/side-wall boundary, close to the pressure release boundary on the external surface of the reflector layer. Within the fluid layer the acoustic pressure increases in magnitude from this boundary towards the centre of the fluid layer (from right to left). Correspondingly, the magnitude of the axial (y) acoustic radiation force increases to a maximum at the centre, therefore a particle will converge towards the nodal plane at a greater rate within the centre of the fluid layer.

Generally, as the side-wall is reduced in width and the impedance seen by the fluid layer at the lateral edges reduces, the acoustic field in both the reflector and fluid layers becomes more uniform. With a more uniform field within the fluid layer it is anticipated that lateral forces will become insignificant and striations are unlikely to form. For the development of the separator device it has not been possible to experimentally test the effect that side-wall width has on lateral forces

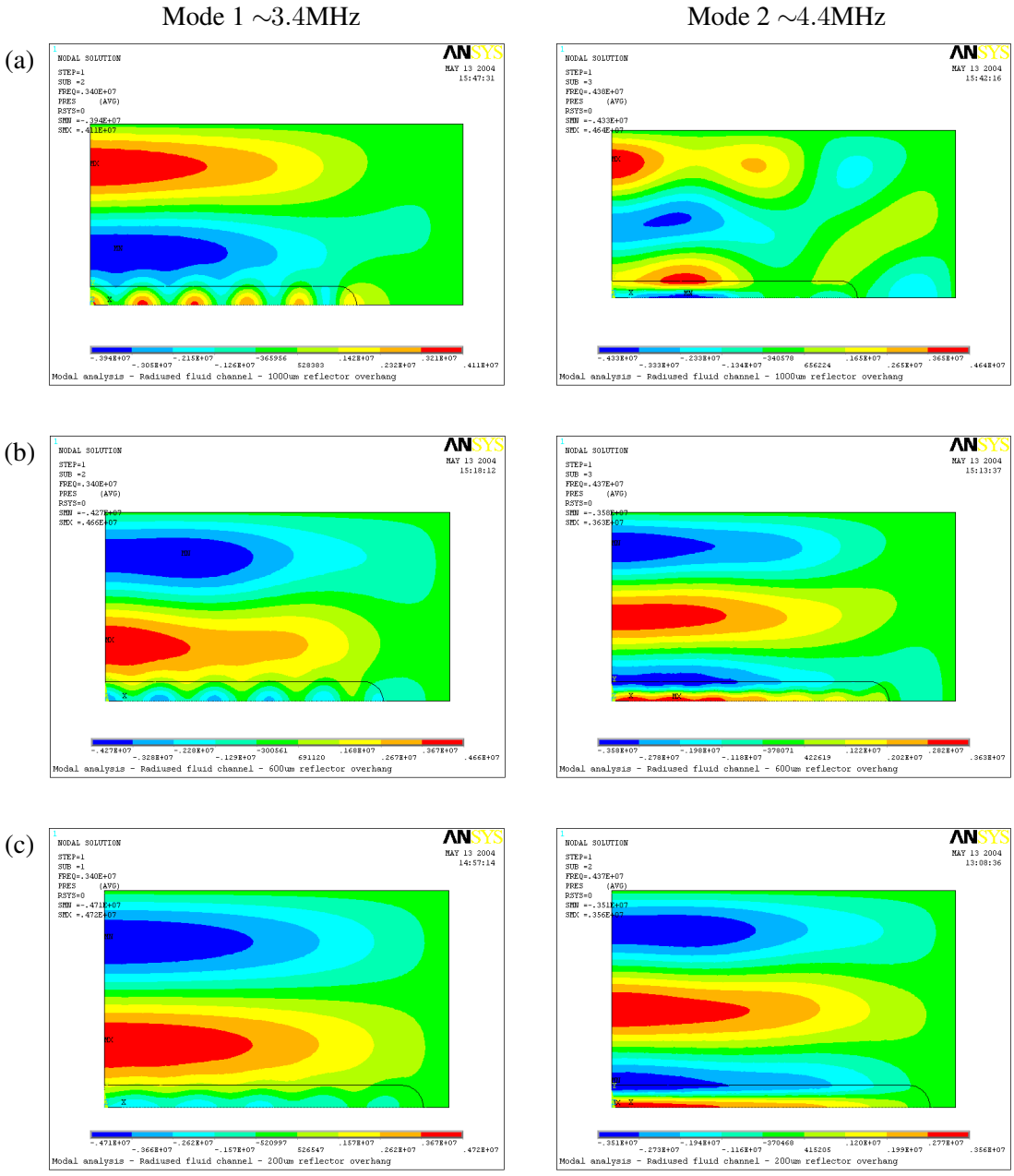

Figure 4.7: Influence of side-wall width on mode shape within separator for side-walls of a) 1mm, b) 0.6mm and c) 0.2mm.

and therefore experimental validation of this work is not possible. However, assuming that side-wall width does have a significant influence on the lateral field pattern, it may be possible to tune existing devices by the removal of wall material which presents interesting future work.

4.3.2 Influence of Side-wall Material

The separator device relies on the etch depth of the Pyrex reflector layer to define the fluid layer thickness. However, the quarter-wavelength device used by Martin et al. [119] and discussed in section 6.3 uses a separate spacer to position the reflector layer relative to the matching layer. The spacer does not serve to seal the fluid chamber, therefore an elastomer seal is used, for example, Sylgard 182 silicone elastomer which has properties $\rho = 1050\text{kg/m}^3$ and $c = 1027\text{m/s}$ [135]. Striations are not readily observed in this device, the movement of particles suggesting that the axial acoustic field is dominant with only a smooth lateral variation reducing to a minimum near the fluid chamber walls. Hawkes et al. [118] use a similar construction and, although in this case there is clearly lateral movement of spores on reaching the nodal plane (reflector surface), the axial field still appears to dominate.

The presence of the acoustically damping seal may assist in the prevention of acoustic hot-spots and associated particle striations, therefore in the FEA model of the separator device, the Pyrex side-walls are replaced with a separate structure with Sylgard 182 properties to investigate the influence of the side-wall material on lateral variations in the acoustic field.

Figure 4.8 illustrates the mode shapes for the through-thickness resonant frequencies, but replacing the 0.9mm wide Pyrex side-walls in figure 4.6 with rectangular cross-section elastomer region. With mode 1 a significant difference between the fluid layer mode shapes of figures 4.6(a) and 4.8(a) can be seen. The latter, using the elastomer side-wall, does not predict the presence of acoustic hot spots across the width of the fluid layer and, although the contours suggest a small degree of variability in the acoustic field, it is significantly more uniform.

For mode 2, comparing figures 4.6(b) and 4.8(b) there is no significant difference between the acoustic field patterns within the fluid layers. In both figures the acoustic field varies across the width of the fluid showing periodic regions of high acoustic pressure (red contours), although the axial y field gradient still dominates the smaller lateral z gradient. Instead, the presence of the elastomer material has a greater influence on the reflector layer, reducing the magnitude of the acoustic pressure towards the right-hand edge of the Pyrex, above the elastomer seal and adjacent to the external pressure release boundary.

(a) Mode 1 ∼3.4MHz

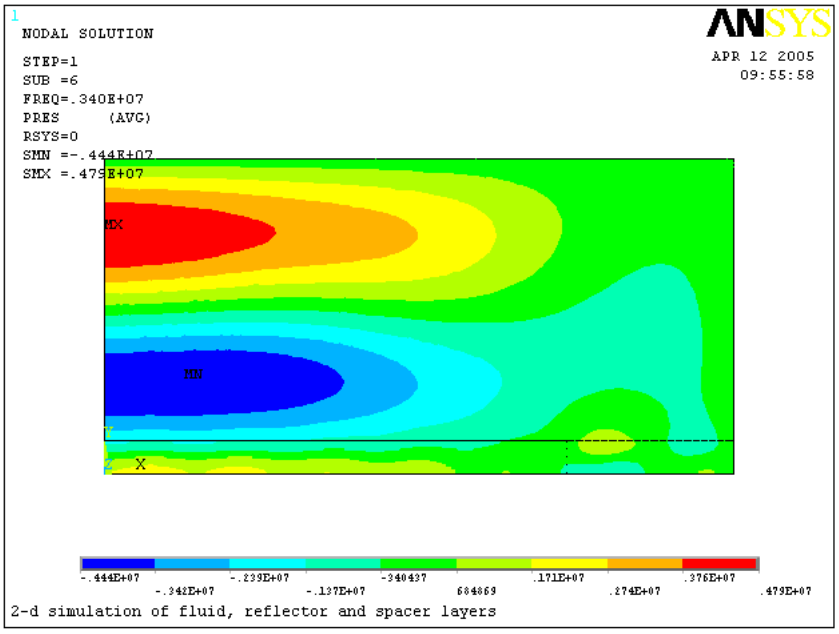

(b) Mode 2 ∼4.4MHz

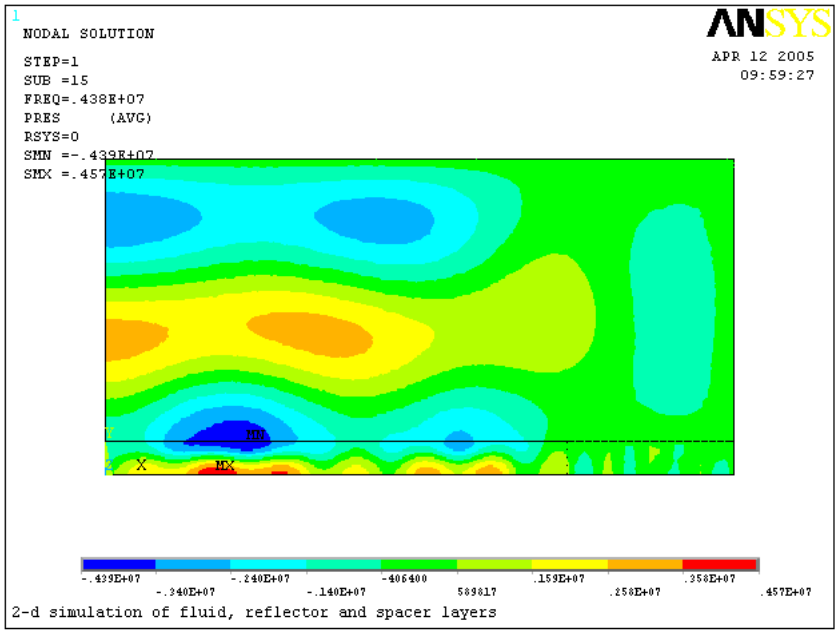

Figure 4.8: Influence of silicone elastomer spacer side-wall on mode shape within separator for both modal frequencies.

It is also observed that for both modes shown in (a) and (b), the elastomer region appears to exhibit its own enclosure mode. For example, in (a) a quadrant pattern can be discerned, although the pressure amplitude is low compared to the field within the reflector and fluid region.

In general, it is shown that the use of alternative materials may aid in reducing lateral variations in the fluid layer acoustic field, in this case using an elastomer material to form the walls of the fluid layer. It is noted that the acoustic properties of the elastomer material are more closely matched to the fluid (in this case water) as compared with the Pyrex material of the reflector which significantly alters the impedance boundary conditions seen at the sides of the fluid layer. However, the materials are not matched such that all through-thickness modes will exhibit a more uniform acoustic field along the lateral direction, as demonstrated by mode 2 at ~ 4.4mHz, therefore the use of an alternative material does not present a universal solution to lateral modes.

4.4 Conclusions

In acoustic resonator devices used for the manipulation of particles, lateral variations in the acoustic field are known to exist and give rise to lateral acoustic radiation forces. Depending on the design of the device these lateral forces may be insignificant, although in the separator device investigated the forces are large enough to form striations as particles are drawn laterally towards positions of low acoustic pressure and potential energy. Although acoustic interference and structural modes can give rise to lateral variations, acoustic enclosure modes as a cause are instead investigated.

The mode shapes within the fluid and reflector layers have been simulated using a FEA simulation, using modal analyses to identify the characteristics of the field at two through-thickness resonant frequencies. These simulations reveal lateral variations in the acoustic field within the fluid layer and acoustic hot spots of high acoustic pressure amplitude causing high lateral pressure field gradients in the fluid. Using the modal analyses it is possible to estimate the relative magnitudes of the axial and lateral radiation forces by measuring the y and z components of the pressure field gradient. This demonstrates that when enclosure modes are excited, high lateral pressure gradients create lateral forces which are of the same order as the axial component of force, significantly influencing particle trajectories. To validate the FEA simulation, the spacings of the experimentally observed particle striations are compared with that of the acoustic field variations predicted by the FEA simulation and show a reasonable level of consistency.

Further simulations are then used to investigate the influence that the fluid chamber side-wall has

on the lateral field. It is shown that the width of the Pyrex etched side-wall significantly influences the occurrence of lateral modes, where reducing the width of the side-wall reduces the lateral variations in the field and therefore associated lateral acoustic radiation forces. The influence of the side-wall material is also investigated briefly and suggests that acoustically softer materials may introduce more favourable boundary conditions which discourage strong lateral modes.

Currently, these FEA simulations are simplified such that they simulate only two layers of the devices and therefore it is accepted that the solutions they present are approximations. Consequently, there is not yet enough confidence in the simulations in order to predict the magnitude of the lateral acoustic forces and particle trajectories. Also, it is known from experimental observation that forces exist in all 3 dimensions, demanding a more complex 3-d simulation to predict accurately the behaviour of a particle.

Even so, this study demonstrates that enclosure modes are a likely cause of the formation of particle striations in the separator device and that FEA is a useful tool to predict the presence of these modes and approximate the modal pattern. Further and more extensive experimental validation would be valuable to more fully understand the influence of the lateral geometry and materials used in the separator device construction and additional simulation work to predict more accurately the magnitude of lateral forces.

Chapter 5

Simulation of Particle Motion

5.1 Introduction

As discussed previously, the combination of forces experienced by a particle determines whether it will move towards the acoustic nodal plane at a great enough rate for separation or capture to occur. Based on these forces, a simulation of particles as they pass through the acoustic and fluid fields, and the resulting trajectories, make it possible to predict the performance of an ultrasonic manipulator device and investigate the influence of a variety of parameters upon particle distributions. In this chapter, such simulation methods are developed and are then used in a predictive capacity in chapter 6. Academic research into acoustic manipulation is occasionally accompanied by analytical or numerical simulations describing the particle trajectories in order to predict concentration or separation efficiency as described more fully in section 2.4.3, although here more detailed numerical simulation of the device and acoustic field is used, thus making it possible to simulate the influence of a greater number of parameters upon particle movement, and adopting fewer assumptions.

A numerical model used to determine particle trajectories is described, where the approach involves considering forces exerted on a particle as it passes through the acoustic field. Solving these forces numerically gives a set of coordinate points describing the path taken by the particle in a given time interval. To calculate the acoustic radiation force, the simulation incorporates the acoustic transfer model introduced in section 2.5.2, and so is not limited to the simple case where the standing wave velocity nodes are positioned on the boundaries of the fluid cavity (equation (2.8)).

A visual inspection of particle trajectories can suggest whether complete clearance or capture has been achieved, but cannot give the degree achievable, e.g. the decrease in concentration or the percentage of particles captured on the chamber wall. More appropriately, by tracking multiple particles or considering the conservation of particles and treating them as a continuum, the concentration profile across the fluid channel can be calculated. The numerical approaches are described and simple cases are compared to analytical solutions. Concentration profiles are then used to determine predictions for outlet concentrations, the approach for which is described.

Although the latter numerical approaches to predict concentration profiles begin to resemble basic forms of numerical fluid simulation, it is considered unnecessary to combine particle simulations with computational fluid dynamics code when simulating the applications considered in chapter 6. As demonstrated in chapter 3, microfluidic flow is dominated by viscous forces, therefore, in a simple geometry typical of microfluidics a predictable laminar flow profile can be assumed to exist and does not require a computationally expensive solution. In the case of more complex flow, CFD data can be generated independently for low particle concentrations where the presence of particles has negligible influence on the fluid dynamics. The CFD data generated can be used in subsequent analyses such as that described in this chapter. A similar approach can also be considered to provide 2 or 3-dimensional data describing the acoustic field. However, the process of incorporating such data is time consuming and the work in chapters 3 and 4 has not aimed to provide accurate descriptions of the fluid and acoustic fields in 2 or 3 dimensions, therefore both the fluid and acoustic fields are here described in 1 dimension only (y direction).

5.2 Movement of Suspended Particles

The forces acting on an object determine its motion, therefore in order to predict the behaviour of particles in suspension passing through an acoustic field, the particle forces need to be quantified. This section describes the main forces and how they are used to calculate particle trajectories.

5.2.1 Particle Forces

The principal forces acting on particles held within a fluid suspension include i) gravitational (buoyancy) forces F_B, ii) fluid drag forces F_D, and iii) acoustic radiation forces F_{ac} when an acoustic field is present. An acoustic field may also give rise to streaming flows within the fluid (section 2.3.2) influencing the fluid drag forces, although this phenomenon is not considered within

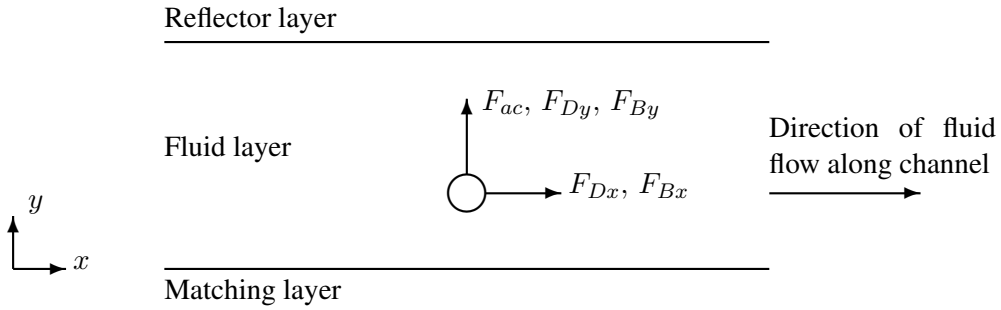

Figure 5.1: Principal components of force acting on a particle and orientation of axes x and y within fluid cavity.

the following work as streaming flows are considered insignificant. These three forces are now described in more detail where the x and y directions relate to directions parallel and perpendicular to the channel walls, respectively, as indicated in figure 5.1.

Gravitational Force

Due to a difference in density between the carrier fluid and a particle, $\rho_f - \rho_p$, a particle of radius R will experience a gravitational force F_B either up or down relative to earth (positive force up) [21] and described below for x and y components, where θ is the inclination of the main channel relative to the horizontal.

$$F_{Bx} = \frac{4}{3}\pi R^3 g(\rho_f - \rho_p)\sin\theta \tag{5.1}$$

$$F_{By} = \frac{4}{3}\pi R^3 g(\rho_f - \rho_p)\cos\theta \tag{5.2}$$

Drag Force

The drag force, F_D, on an object of cross-sectional area A within a fluid of density ρ_f and free stream velocity of U_0, is described by the following equation:

$$F_D = \frac{1}{2}C_D\rho_f U_0^2 A. \tag{5.3}$$

The drag coefficient, C_D, is determined by considering a series of regimes, dependent on particle Reynold's number, $\mathrm{Re}_p = 2R\rho_f U_0/\mu$ [21]:

$$\begin{aligned}
&\textit{Stokes flow}: && \mathrm{Re}_p < 0.2, && C_D = \frac{24}{\mathrm{Re}_p} \\
&\textit{Allen flow}: && 0.2 < \mathrm{Re}_p < 500, && C_D = \frac{18.5}{\mathrm{Re}_p^{0.6}} \\
&\textit{Newton flow}: && 500 < \mathrm{Re}_p < 10^5, && C_D = 0.44
\end{aligned}$$

Stokes flow describes the condition of steady flow around a sphere where viscous flow dominates, whereas with the increase of Re_p flow separates from the surface of the sphere at which point drag terms for Allen and Newton flows apply. It can be seen that both the drag force and the Reynold's number, from which the drag coefficient C_D has been defined, are dependent on the free stream velocity or, more accurately, the relative velocity between the fluid and particle. The fluid flow through the main channel of a microfluidic ultrasonic manipulator is assumed similar to that seen between parallel plates, as the depth of the channel is very small compared to the width and dominates the characteristics of the flow profile, as concluded in chapter 3. For flow between parallel plates, the velocity profile is described by equation (2.4) where h is the channel depth:

$$U_x = \frac{6\bar{U}_x}{h^2}(hy - y^2), \tag{5.4}$$

where the maximum flow velocity occurs along the centre of the channel, $y = h/2$, so it follows that $U_{x_{max}} = \frac{3}{2}\bar{U}_x$.

Optimum flow rates for the ultrasonic separator are considered to be small and in the region of less than 0.1ml/s ($\bar{U}_x = 0.083$m/s), corresponding to a maximum fluid velocity of 0.125m/s. The resulting Reynold's number for a 1μm diameter particle which is stationary relative to the flow is therefore $\mathrm{Re}_p = 0.125$ and so is described by the Stokes flow regime. In practice and due to the low inertia of the particles, the relative velocity, U_0, between the particle and fluid flow in the x direction is negligible and small in the y direction, therefore it is assumed that the Stokes flow regime is applicable for the simulation of most micron scaled particles. Here the particle velocity has components $\dot{x}$ and $\dot{y}$.

By describing the drag coefficient C_D using the Stokes flow regime, the drag force from equation 5.3 in both x and y directions becomes:

$$\begin{aligned} F_{Dx} &= 6\mu\pi R(U_x - \dot{x}) \\ &= 6\mu\pi R(\frac{6\bar{U}_x}{h^2}(hy - y^2) - \dot{x}) \qquad \text{for a parabolic flow profile,} \end{aligned} \tag{5.5}$$

$$\begin{aligned} F_{Dy} &= 6\mu\pi R(U_y - \dot{y}) \\ &= -6\mu\pi R\dot{y} \qquad \text{where } U_y = 0. \end{aligned} \tag{5.6}$$

The latter condition of $U_y = 0$ assumes that there is no bulk flow moving in a direction perpendicular to the walls, as in the case where acoustic streaming is taken to be negligible.

Acoustic Radiation Force

The time averaged acoustic radiation force is described below (equations (2.10) and (2.11)):

$$\begin{aligned} \langle F_{ac}(x,y,z)\rangle &= -\nabla\langle\phi^G(x,y,z)\rangle \\ \text{where} \qquad \langle\phi^G(x,y,z)\rangle &= -V\left[\frac{3(\rho_p - \rho_f)}{2\rho_p + \rho_f}\langle\bar{E}_{kin}\rangle - \left(1 - \frac{c_f^2\rho_f}{c_p^2\rho_p}\right)\langle\bar{E}_{pot}\rangle\right]. \end{aligned}$$

To calculate the time averaged kinetic and potential energy densities, $\langle\bar{E}_{kin}\rangle$ and $\langle\bar{E}_{pot}\rangle$, the acoustic impedance transfer model described in section 2.5.2 is used. These parameters help determine the variation in acoustic pressure and velocity through the fluid layer, and are also used to calculate energy density. This approach takes into account the layered nature of the ultrasonic device and its influence on the acoustic field and resonant frequency. This method also allows the acoustic radiation force to be calculated over a range of frequencies and is not limited to the resonant case.

Other Forces

Forces other than those described above also act on particles, but are not considered in subsequent simulation of particle trajectories or concentration. Such forces or processes are briefly discussed below.

Diffusion: Brownian motion and diffusion of particles within a suspension is caused by molecular movement of the liquid. The resulting mean displacement of a particle λ is given by,

$$\lambda = \sqrt{t}.\sqrt{\frac{R_0 T}{N}\frac{1}{3\pi\mu R}}, \tag{5.7}$$

where t, R_0, T and N are time, universal gas constant, temperature and Avogadro's number respectively [136]. For example, for a device with a channel height of 250μm, length 8.5mm and width 5mm and operating at a flow rate of 0.01ml/s (resident time of 1s), the mean displacement of a 1μm diameter particle is approximately 1μm, and at 0.001ml/s (resident time of 10s) is 3μm. This is negligible compared to the deflection caused by the acoustic radiation force, therefore diffusion is not considered within any further numerical treatment. However, it is recognised that in quarter-wave devices where particles are deflected towards the slower fluid velocity regions near the channel wall, the residence time within the acoustic field for a particle typically becomes much greater, in which case diffusion processes may create small discrepancies between measured and predicted results.

Lateral forces: Within the main channel forces will also be acting in the z direction across the width of the channel. These lateral forces will originate from acoustic streaming, fluid flow due to the 3-dimensional nature of the channel geometry and lateral radiation forces. Of these, only the lateral radiation forces significantly influence the particle trajectories within the main channel and before the outlet region as observed in experiment, and these have been discussed separately in section 2.3.1. The fluid streamlines and therefore particle trajectories within the outlet region typically have a z component as the width of the first outlet is less than the channel width, as investigated in section 3.6. However, the more simple case described in 2 dimensions is assumed, where the height at which the two outlet flows split does not vary with z (see section 5.3.4). The implications of this assumption are discussed in chapter 6.

Lift forces: Fluid lift force will act on a particle within a flowing medium where a velocity gradient exists. The particle will tend to move to the region of higher fluid velocity which, in the case of the particle separator, will be along the centre of the chamber and coincide with the acoustic node for a half-wavelength resonance. The Saffman lift force acting on a particle and perpendicular to the direction of flow is given below where $K = 6.46$ [137]:

$$F_L \sim K\mu u \left(\frac{\mathrm{d}u}{\mathrm{d}y}\right)^{1/2} \frac{R^2}{\nu^{1/2}} \tag{5.8}$$

From this equation it is possible to estimate the order of displacement expected as a result of lift. Based on the same parameters employed above for the analysis of diffusion, the mean deflection of a 1μm particle within a flow of 0.01ml/s is approximately 16μm towards the centre plane and for 0.001ml/s reduces to a deflection of 5μm and therefore will have a small influence on particle separation within microfluidic separator device. The omission of lift forces when predicting particle trajectories and resulting performance of the separator will tend to underestimate the performance as the lift force will assist the separation process in a half-wavelength system. However, the opposite may apply to quarter-wavelength devices which involve the movement of particles towards the fluid chamber boundary away from the high velocity region of the fluid.

These forces, which although are not included in the development of the particle model described in the following sections, will be considered in the discussion sections in chapter 6.

5.2.2 Particle Trajectories

Particle trajectories are calculated by summing particle forces and solving the expression in terms of x and y. The equations of motion of a particle can be written:

$$\sum F_x = m\ddot{x} \qquad \Rightarrow \qquad \ddot{x} = \frac{F_{Dx} + F_{Bx}}{m}$$

$$\sum F_y = m\ddot{y} \qquad \Rightarrow \qquad \ddot{y} = \frac{F_{ac} + F_{Dy} + F_{By}}{m}$$

These equations are solved numerically based on a set of initial conditions for x, y, $\dot{x}$ and $\dot{y}$, and a complete set of system equations, as follows:

$$\frac{\mathrm{d}x}{\mathrm{d}t} = \dot{x}, \qquad \frac{\mathrm{d}^2x}{\mathrm{d}t^2} = \frac{F_{Dx}(y,\dot{x}) + F_{Bx}}{m},$$

$$\frac{\mathrm{d}y}{\mathrm{d}t} = \dot{y}, \qquad \frac{\mathrm{d}^2y}{\mathrm{d}t^2} = \frac{F_{ac}(y) + F_{Dy}(\dot{y}) + F_{By}}{m}.$$

This system of equations is conveniently solved using a MATLAB ordinary differential equation (ODE) solver which is based on numerical differentiation equations, and returns an array containing a series of time increments with the associated particle coordinates and velocity data, x, y, $\dot{x}$

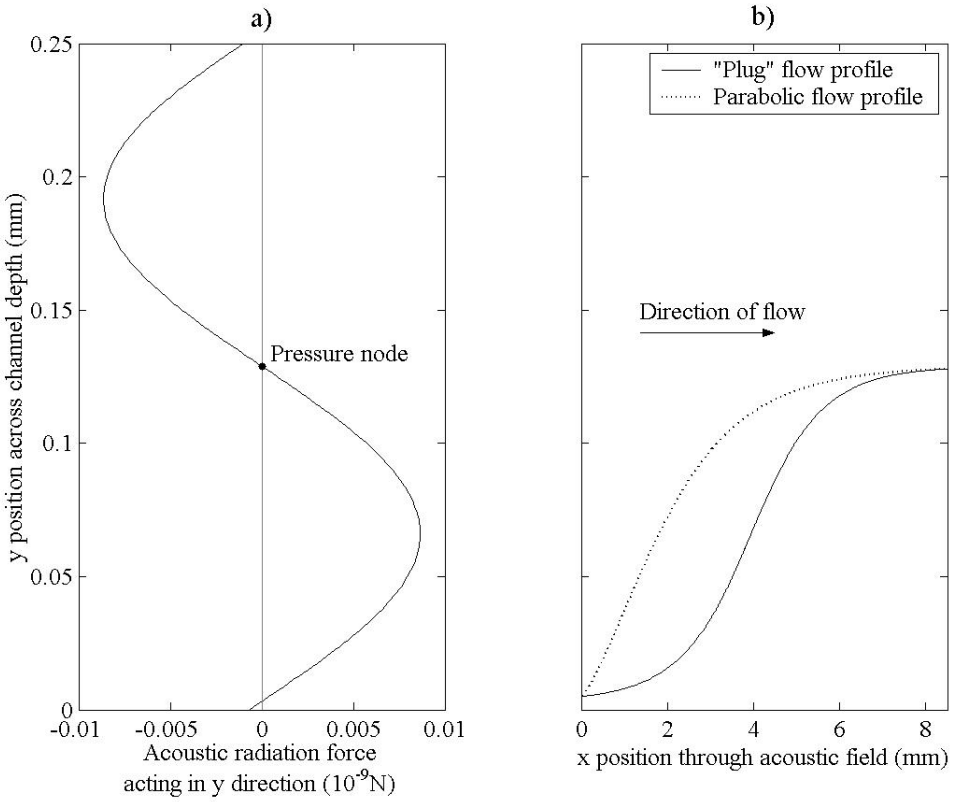

Figure 5.2: Example of a half-wavelength acoustic resonance illustrating a) the force profile across the channel depth and b) the resulting particle trajectories for both 'plug' and parabolic flow profiles. The channel considered is of height 250μm, width 5mm and field length 8.5mm with a fluid flow rate of 0.03ml/s.

and $\dot{y}$. A plot of the x and y coordinates as they vary with time illustrates the particle trajectory, examples of which are shown in figure 5.2.

Here two particles have been modelled, with the radiation force, F_{ac}, taken at the half wave resonant frequency, i.e. $\lambda \approx 2h$. It can be seen in figure 5.2a that the radiation force is not necessarily symmetrical about the centre line of the channel; there is one pressure anti-node within the fluid layer near the lower wall of the channel ($y = 0$) below which particles would be forced towards the wall. In the simple case (equation (2.8)) the pressure anti-nodes are positioned on the walls of the fluid channel, although this is not necessarily the case for resonance in a multiple layered system.

The particle trajectories are shown in conjunction with the acoustic radiation force (figure 5.2b) and also illustrate the influence of the laminar parabolic flow profile by comparing it with the particle trajectory for 'plug' flow (uniform fluid velocity profile where $U_x = \bar{U}_x$). The rate of convergence towards the node is not influenced by the longitudinal (x) flow profile, illustrated

if position y was plotted as a function of time. However, for the parabolic profile the low flow velocity at the wall causes the particles to begin converging at a position further upstream in x as compared to plug flow, and vice versa in high flow velocity regions such as along the centre of the channel. This demonstrates the significant influence the flow profile has on the particle trajectory and therefore the implication on design and resulting efficiency of the device, discussed more thoroughly in chapter 6.

5.3 Concentration of Particles

The concentration of particles can be calculated either by considering a series of individual particles or the particles as a continuum, i.e. simulating particle trajectories and calculating the change in particle spacing using the resulting coordinate data, or by applying conservation rules to the particle flow rate, respectively. Either method has advantages and disadvantages associated with it which are discussed below, together with a description of the technique.

The purpose of determining particle distribution is to predict the concentration at the outlet end of the channel and this location is consistently referred to using the index M. In all examples presented, a uniform concentration at the inlet is assumed and plotted concentration data is always taken as a ratio of the inlet concentration, e.g. c_M/c_0.

5.3.1 Concentration based on particle trajectories

In this section, concentration is calculated numerically by considering the change in y separation between adjacent particles, the trajectories of which have been determined using the ODE solver described above.

Within a small region the particle flow rate per unit depth is a product of the depth of the region, Δy, the x velocity, $\dot{x}$, and concentration c. Referring to figure 5.3 and considering a pair of particles, n and $n+1$, moving along their respective trajectories, the particle flow rates at the beginning of their trajectories is equal to that at end of their trajectories, assuming steady state conditions where no particles build up over time within the area depicted. This gives the following where c and $\dot{x}$ values are taken at the mid-point between the particles.

$$c_0(y_{0,n+1} - y_{0,n})\dot{x}_0 = c_M(y_{M,n+1} - y_{M,n})\dot{x}_M. \tag{5.9}$$

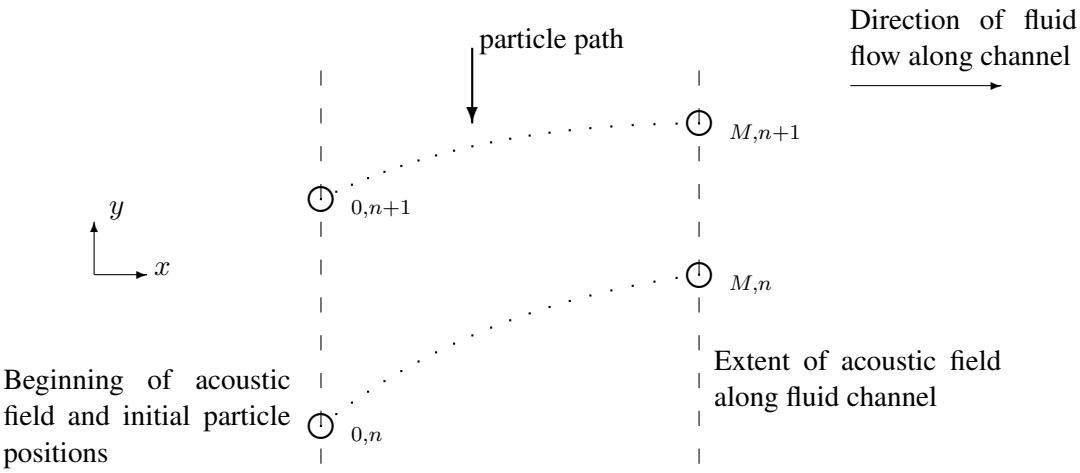

Figure 5.3: Nomenclature for particles moving along the channel and following trajectories (dotted lines) where the index M indicates the extent of the acoustic field and n refers to each particle modelled.

Rearranging gives the concentration at the extent of the acoustic field and is based on particle position and velocity:

$$c_M = c_0 \left(\frac{y_{0,n+1} - y_{0,n}}{y_{M,n+1} - y_{M,n}} \right) . \left(\frac{\dot{x}_0}{\dot{x}_M} \right) \tag{5.10}$$

Determining the trajectories for a series of particles supplies associated y-coordinate positions and longitudinal velocity terms, $\dot{x}_0$ and $\dot{x}_M$.

Figure 5.4(a) illustrates an example of an acoustic radiation force profile created by a half wavelength resonance. This is accompanied by a simulation of a series of particles as they pass through the acoustic field, where figure 5.4(b) illustrates their predicted trajectories. These trajectories are seen to converge to a plane positioned approximately along the centre of the channel and figure 5.4(c) shows the resulting concentration profile (dotted line) using the method described above. As expected, the concentration at the centre of the channel has increased and falls away towards zero towards the walls.

However, each dot represents the concentration determined from a pair of particle trajectories, therefore data is limited by the number of particles simulated and the concentration of data within any area is proportional to the particle concentration. This distribution of data can be seen in the figure, for example, within regions from where particles are repelled few data points exist, providing little information about that region. More data is available if particles are converging

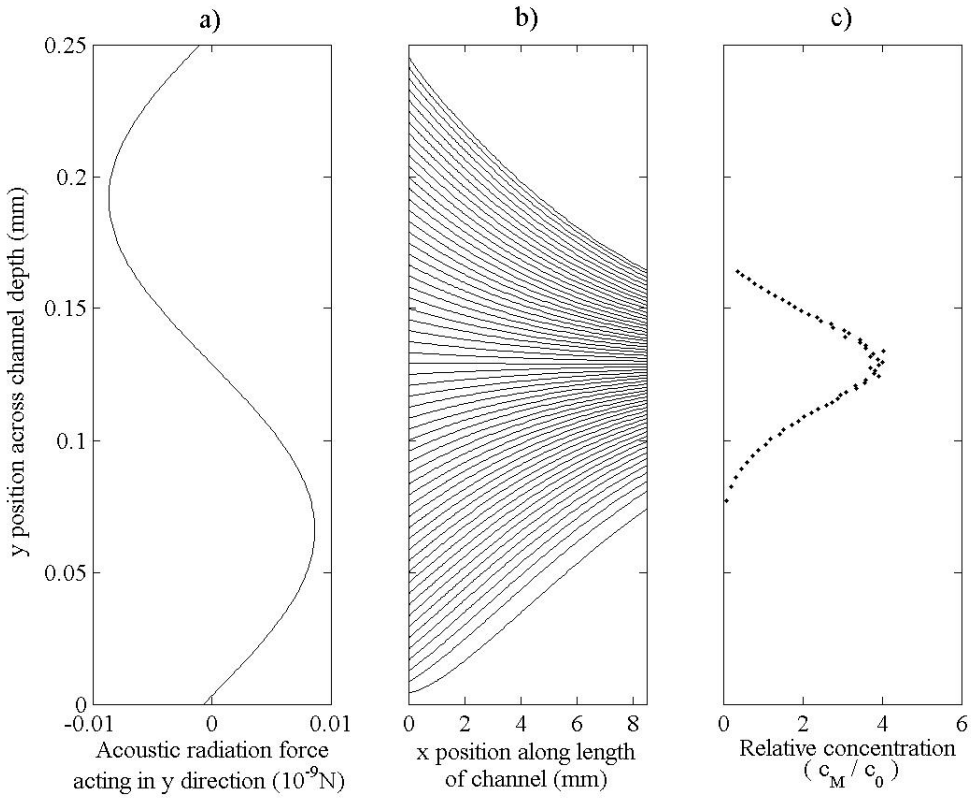

Figure 5.4: Example of a) a half-wavelength acoustic radiation force profile, b) the resulting particle trajectories through the field and along the channel and c) the particle concentration at a distance 8.5mm from the inlet plane calculated using particle trajectory coordinate data (dotted line). The channel considered is of height 250μm, width 5mm and field length 8.5mm with a fluid flow rate of 0.12ml/s.

or more particles are simulated, however in this case the concentration data may become irregular due to errors within the numerical solution of the trajectories, as can be seen in the figure at the centre of the channel in the high concentration region.

5.3.2 Concentration based on conservation of particle flow

An alternative approach is to consider the particles as a continuum within the carrier fluid. Remaining with the concept of conservation of particle flow, we begin with the basic continuity equation for a fluid [138, 139] where the density ρ is analogous to the concentration of particles and the velocity field vector is V,

$$\frac{\partial \rho}{\partial t} + \mathrm{div}(\rho V) = 0. \tag{5.11}$$

Assuming a well mixed sample the concentration of particles delivered through the inlet of the ultrasonic device is constant, therefore, after a short time the distribution of particles within the main channel is a function of x and y only and a steady state condition is reached where $\frac{\partial \rho}{\partial t} = 0$. Expanding equation (5.11) where velocity V has x and y components u and v, also replacing ρ with particle concentration c gives,

$$c\frac{\partial u}{\partial x} + u\frac{\partial c}{\partial x} + c\frac{\partial v}{\partial y} + v\frac{\partial c}{\partial y} = 0. \tag{5.12}$$

This is an *Eulerian* approach [131, 139] as there is no consideration of the particle trajectories in the solution.

Regular Grid

Equation (5.12) can be solved numerically, first by reducing the channel to a 2-dimensional grid, as illustrated in figure 5.5, and then replacing the partial derivatives with finite difference equations as shown:

$$\begin{aligned} \frac{\partial u}{\partial x} &= 0, & \frac{\partial v}{\partial y} &= \frac{v_{m,n+1} - v_{m,n-1}}{2\Delta y}, \\ \frac{\partial c}{\partial x} &= \frac{c_{m+1,n} - c_{m,n}}{\Delta x}, & \frac{\partial c}{\partial y} &= \frac{c_{m,n+1} - c_{m,n-1}}{2\Delta y}. \end{aligned}$$

Here, it has been considered reasonable to apply forward differences in the x direction and central differences in the y direction. As the difference between the x-direction velocity u of a particle and the laminar flow profile is negligible, u can be described by equation (5.4), for which u is constant along the length of the channel and so the partial derivative with respect to x is zero. Also, the y-direction velocity v of a particle can be derived from the forces acting on the particle [74] such that,

$$v = \frac{F_{ac} + F_{By}}{6\pi\mu R}(1 - \exp(\frac{-6\pi\mu R}{m'}t)). \tag{5.13}$$

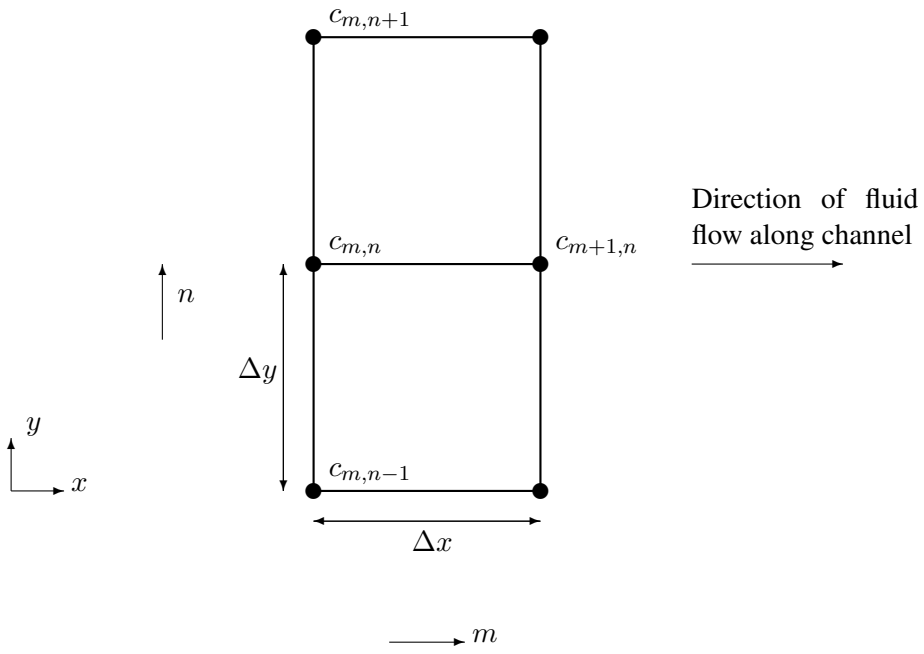

Figure 5.5: Nomenclature and grid used in the numerical solution of particle concentration where suspended particles are considered as a continuum. Index m and n refer to the x and y grid positions.

As the profile of F_{ac} across the channel is known numerically from the acoustic impedance transfer model, it is straightforward to apply this to the above equation. As the particle mass is small the inertial term in the above equation is also small. Therefore, after removing the inertial term and including a buoyancy term the particle velocity can be described numerically as,

$$v_{m,n} = \frac{F_{ac_{m,n}} + F_{By}}{6\pi\mu R}. \tag{5.14}$$

Substituting the difference equations into equation (5.12) and rearranging gives,

$$c_{m+1,n} = c_{m,n}\left(1 - \frac{\Delta x}{2\Delta y}\frac{(v_{m,n+1} - v_{m,n-1})}{u_{m,n}}\right) - \frac{\Delta x}{2\Delta y}\frac{v_{m,n}}{u_{m,n}}(c_{m,n+1} - c_{m,n-1}). \tag{5.15}$$

To solve for concentration, the inlet condition of $c_{0,n} = 1$ for all n is applied to equation (5.15) and, by marching through x, successive values $c_{1,n}$, $c_{2,n}$, $c_{3,n}$ etc. can be determined until the outlet region is reached. Equation (5.15) is an *explicit* scheme as it relies on known upstream values.

Various other schemes can be written based on alternative finite difference equations used to describe each partial differential term. These may include downstream, unknown values of c, making the computation *implicit*. However, these approaches are either inherently unstable and will never

produce a reliable solution, or conditionally stable making the implementation of these schemes troublesome [139]. Also, stability conditions are related to the spacing of grid points, so typically involves grid refinement in the direction in which the computation progresses (x-direction). This is not desirable for high aspect-ratio geometry such as that found in microfluidic devices, increasing computation time significantly.

Hybrid Method

An adaptation of the approach described above is to consider the particles moving through an alternative grid structure by which particle trajectories are also taken into account. In justification, Ames [139] notes that the schemes discussed above are not tailored to solving fixed time (or steady state) problems in 2-dimensional space, but instead a *hybrid* approach is required using alternative grid points and interpolation.

Referring to figure 5.6, particles pass through the volume defined by ABCD in through AB and out through CD. The bounds AC and BD have no particles crossing them and so by definition must describe particle trajectories, unlike the grid described in figure 5.5. The following conditions are stated:

$$\text{Particle flow in AB} = u\,c\,\mathrm{d}y \tag{5.16}$$

$$\text{Particle flow out CD} = \left(u + \frac{\partial u}{\partial x}\mathrm{d}x\right)\left(c + \frac{\partial c}{\partial x}\mathrm{d}x\right)\left(1 + \frac{\mathrm{d}x}{u}\frac{\partial v}{\partial y}\right)\mathrm{d}y \tag{5.17}$$

Due to the high length to height ratio of the channel, the trajectory through that channel will typically have a small y component compared to x, therefore the expressions for velocity and concentration are simplified by excluding any partial y derivatives.

As a steady state condition is being simulated, equations (5.16) and (5.17) are equal and can be simplified to the following where second order terms are taken to be negligible and as before $\frac{\partial u}{\partial x} = 0$:

$$u\frac{\partial c}{\partial x} + c\frac{\partial v}{\partial y} = 0. \tag{5.18}$$

This equation is a reduced version of equation (5.12) and, in a similar manner, can be described numerically by replacing the partial differential terms using difference equations whilst retaining the same indexing:

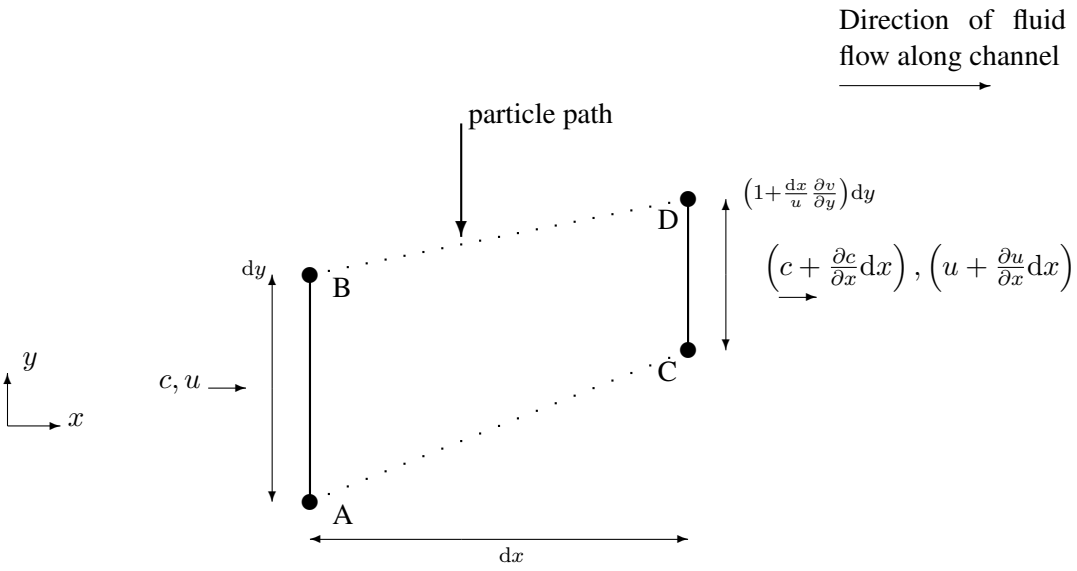

Figure 5.6: Representation of fluid system used to derive hybrid numerical solution of particle concentration where suspended particles are considered as a continuum.

$$c_{m+1,n} = c_{m,n}\left(1 - \frac{\Delta x}{2\Delta y}\frac{(v_{m,n+1} - v_{m,n-1})}{u_{m,n}}\right). \tag{5.19}$$

This method treats the particles as a continuum, but the grid used is not regular, instead reflecting the particle trajectories so index n now refers to a particle path. In order to provide a more even distribution of data after each step of Δx, the data can be interpolated from the new particle y positions back to the original y positions, where particle y displacement is $\frac{v_{m,n}}{u_{m,n}}\Delta x$. This conveniently makes the bracketed term in equation (5.19) constant for all steps.

Regarding particle movement at the wall, it is uncertain as to whether particles forced towards the wall will adhere to or roll along the wall making concentration predictions in that region misleading. Also, where a particle moves away from the wall a discontinuity in concentration is formed as towards the edge of the particle stream the concentration will suddenly reduce to zero. This discontinuity is more obvious in figure 5.9, which is discussed in the next section. To account for both cases the wall concentration is made equal to zero. Although this effectively removes wall particles from the calculated concentration profile, they can be accounted for by calculating the difference between the initial and final particle flow rates, assuming steady state conditions and that particle flow rate is conserved, and has been used in chapter 6.

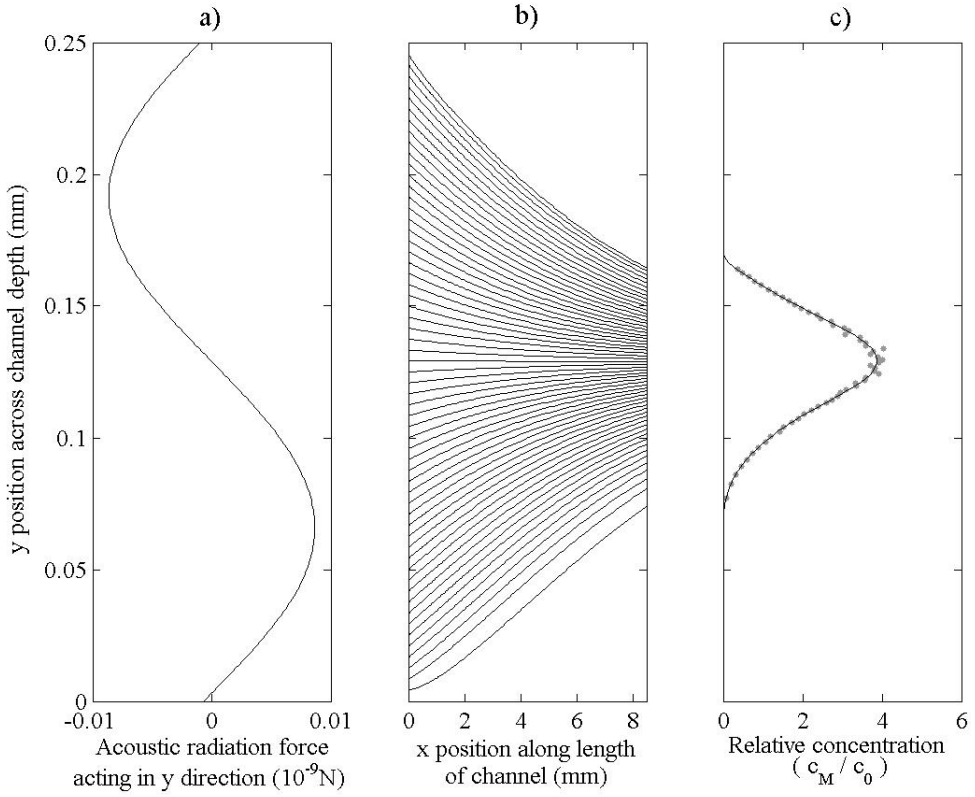

Figure 5.7: Example of a) a half-wavelength acoustic radiation force profile, b) the resulting particle trajectories through the field and along the channel and c) the particle concentration at a distance 8.5mm from the inlet plane calculated using the hybrid method (solid line) and also based on particle trajectory coordinate data (grey dotted line). The channel considered is of height 250μm, width 5mm and field length 8.5mm with a fluid flow rate of 0.12ml/s.

The same operating conditions and parameters used in figure 5.4 are repeated and figure 5.7(c) shows the resulting concentration calculated using the numerical approach based on the hybrid method and alternative grid system. The resulting concentration profile is shown together with that calculated previously based on particle trajectory data and an excellent match between the two methods can be seen. However, the hybrid method does produce a smoother and therefore more realistic description of the concentration profile, possibly due to the reliance of the computation on neighbouring grid points and not being restricted by particle trajectories which supply an uneven distribution of data.

Even when using a finer mesh, the processing of this method is much more rapid than the first method solving for individual particle trajectories. Although it is recognised that the interpolation step incorporates errors into the data, figure 5.7 suggests that this is not significant when compared to the irregular profile of the particle trajectory method (dotted line).

5.3.3 Comparison with Analytical Solution

In this section the numerical approaches described above are compared against analytical expressions derived for particles within an acoustic standing wave, although it is recognised that experimental validation would also be of value. Chapter 6 compares the modelled results to experimental results and uses the models to investigate various trends. Some work has been done to verify the analytical solutions (see section 2.3.1), and where the nature of the acoustic field is known there is good agreement with experiment.

Time as a function of particle displacement

To compare the numerical approach developed above to the established analytical solution to acoustic radiation force, an expression is used describing the time taken for a particle to move from y_1 to y_2, both relative to the acoustic node and subjected to acoustic radiation and drag forces. To form this expression, equation (5.14) can be rearranged and integrated with respect to y giving the following equation:

$$t = \frac{C_D}{2kF_{ac}^0}.\left[\ln\left|\tan(ky)\right|\right]_{y_1}^{y_2} \tag{5.20}$$

Figure 5.8(a) shows an example of the radiation force generated by a standing wave where an anti-node is positioned at $y = 0$ (equation (2.8)). Figure 5.8(b) then shows the movement of a particle due to this radiation force as a function of time determined using both equation (5.20) and that calculated numerically from section 5.2.2 removing the buoyancy term for comparative purposes. This shows an excellent comparison where the two curves are almost indistinguishable and suggests that the particle trajectory model produces reliable data.

Concentration profile as a function of time

An analytical solution derived by Higashitiani [72] (alternative derivation supplied by King [64]) describes a normalised form of probability density of particles ψ^* (equivalent to the relative concentration c_M/c_0 used previously) in 1-dimensional space as a function of time:

$$\psi^* = \left[\cos(2\tau)\sinh(4a^{*2}E^*Ft^*/3) + \cosh(4a^{*2}E^*Ft^*/3)\right]^{-1} \tag{5.21}$$

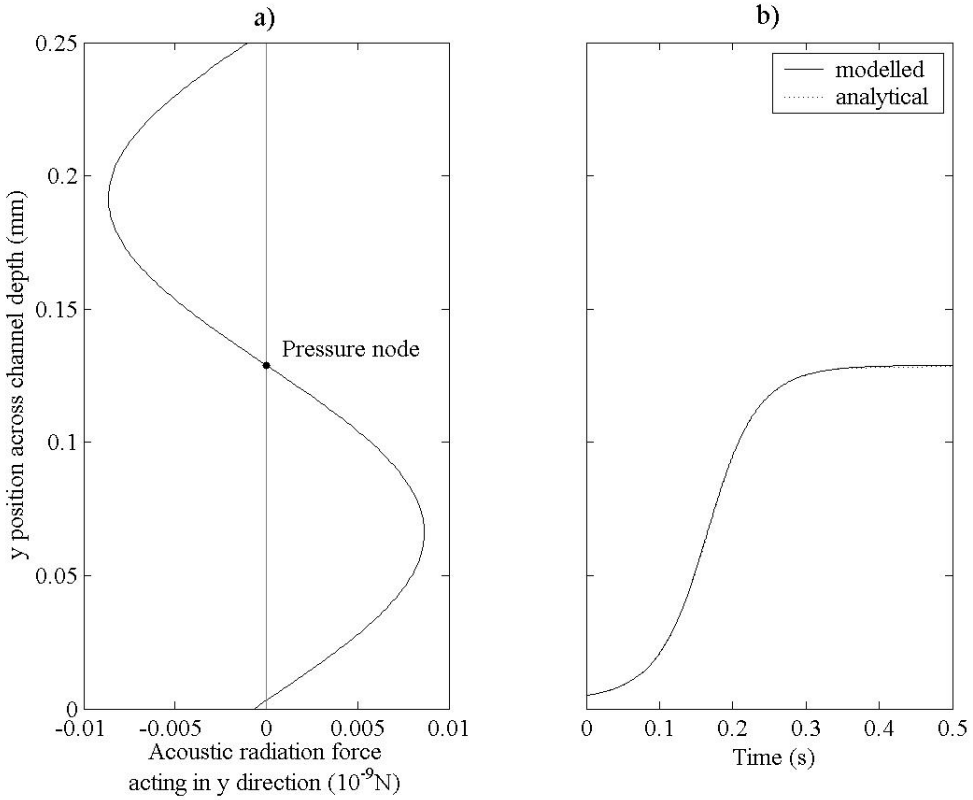

Figure 5.8: Example of a) a half-wavelength acoustic radiation force profile and b) the resulting y position of a particle initially located near an anti-node and plotted as a function of time, determined analytically (equation (5.20)) (dotted line) and modelled (section 5.2.2) (solid line). The channel considered is of height 250μm, width 5mm and arbitrary field length with a fluid flow rate of 0.03ml/s.

where τ, a^*, E^*, F and t^* are dimensionless forms of y position, particle radius, energy density, acoustic contrast and time, respectively.

The derivation is based on particle mass conservation (continuity equation) where particles are subject to both an acoustic radiation force and diffusion. Equation (5.21) is one of two solutions given by Higashitiani depending on whether diffusion is deemed significant or not, i.e. radiation force dominates during initial sound irradiation (equation (5.21)) whereas diffusion dominates sometime later once particles are positioned near the pressure node.

The above is a transient, 1-dimensional expression, but is analogous to the steady-state 2-dimensional system considered in the numerical treatment; for plug flow each step Δx parallel to the acoustic source is equivalent to a time step of $\Delta t = \Delta x/u$ where u is constant throughout the fluid domain. It is therefore possible to compare the modelled concentration profile with that given by equation (5.21) and an example has been given in figure 5.9. An excellent match is presented between the simulated (solid black line) and analytical results (dotted black line obscured by solid line) both labelled plug flow, again almost indistinguishable suggesting that the modelled particle concentration is a reliable approach.

Although not immediately obvious in the figure, there is a small discrepancy between the analytical and numerical methods in the regions near the wall. There is a region of approximately 10μm from the reflector wall ($y = 0.25$mm) where zero concentration is predicted by the numerical approach. However, the analytical solution predicts a small concentration in this region as it does not take into account the presence of the boundary and assumes that particles will move from the pressure antinode within the reflector layer. In contrast, by using a zero concentration boundary condition in the numerical approach, the discontinuity in particle concentration can be more readily approximated (assuming negligible diffusion acting at this discontinuity).

Also shown is the concentration profile as a result of parabolic flow (grey line) which differs significantly with the concentration profile for plug flow. Referring back to figure 5.2, due to the low flow velocity region near the wall in the case of parabolic flow, particles there will achieve a greater y displacement compared to that in plug flow over a given distance x along the channel. This results in a lower concentration towards the walls and a greater degree of clearance as can be seen in the example shown in figure 5.9 up to a position approximately 80μm from the wall. However, the opposite is true towards the centre of the channel where for the lower plug flow velocity greater concentrations can be achieved as particles have more time to converge towards the node.

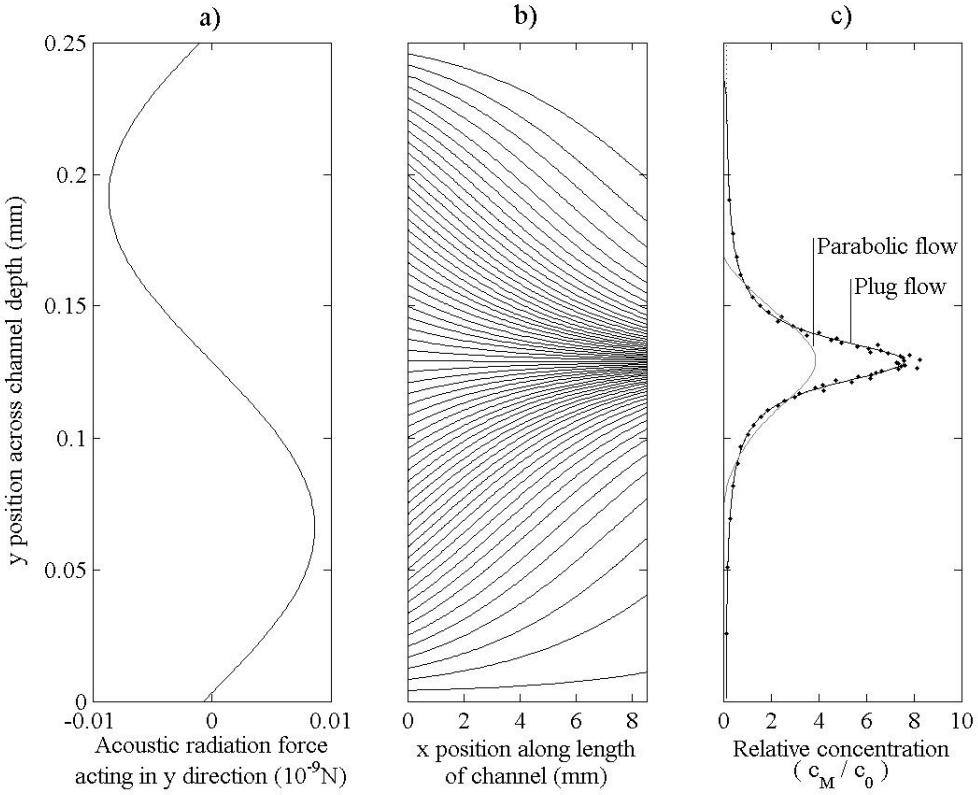

Figure 5.9: Example of a) a half-wavelength acoustic radiation force profile, b) the resulting particle trajectories through the field and along the channel for plug flow conditions and c) concentration in plug flow determined by both modelled (trajectory data (data points) and hybrid method (solid line)) and analytical method (equation (5.21)) (dashed line, mostly obscured) and also compared with concentration in parabolic flow modelled using the hybrid method (grey line). The channel considered is of height 250μm, width 5mm and field length 8.5mm with a fluid flow rate of 0.12ml/s.

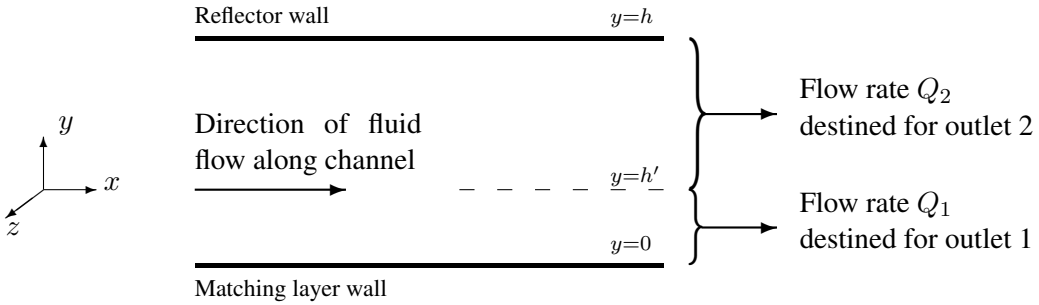

Figure 5.10: Schematic of channel of height h and division of fluid flow between two outlets resulting in flow rates Q_1 and Q_2.

5.3.4 Concentration through Device Outlets

The concentration profile across the channel depth can be used to calculate the subsequent outlet concentrations C_1 and C_2, which indicate the degree of particle separation and are more practical parameters when making comparisons with experimental results. Experimental measurements of particle distribution and concentration profiles could be made by direct observation, but is not possible for the devices discussed in chapter 6 as the side of the fluid chamber in each device is obscured.

For simplicity, it is assumed that the outlet flow rates, Q_1 and Q_2, will ultimately be composed of fluid within the main channel bounded between $0 < y < h'$ and $h' < y < h$ respectively, as described by figure 5.10, but that the position of h' does not vary across the width of the device (z direction).

The particle concentration collected through an outlet is calculated by summing the particle flow rate per unit depth, for example up to the height h', and dividing by the flow rate. For modelled concentration data, discrete intervals in the y direction are considered in the summation such that,

$$C_1 = \frac{\text{particle flow rate}}{\text{outlet flow rate}} = \frac{\sum_{n=1}^{N} c_{n,M}\, u_{n,M}\, \Delta y}{Q_1}, \tag{5.22}$$

where $Q_1 = \int_0^{h'} U_x \, \mathrm{d}y$ per unit depth.

The concentration, C_2, passing through the other outlet can be calculated in a similar manner or by considering conservation of particles and determining the difference between the particle flow

rate calculated above and that at the inlet.

5.4 Conclusions

This chapter demonstrates the development of a numerical tool to determine particle trajectories through an acoustic standing wave and to predict particle concentration, both based on the more significant forces experienced by a particle within the fluid chamber of a resonator, including gravitational (buoyancy), fluid drag and acoustic radiation forces. The model is coupled to the acoustic impedance transfer model described in section 2.5.2 and so predicts the nature of the acoustic field in 1 dimension and associated radiation force. Other forces and phenomena influencing particle motion and not included in the model are discussed and include diffusion, lateral forces and lift forces. Although diffusion is unlikely to have a noticeable influence on particle movement and separation, lateral and lift forces may have a small influence and must be considered when interpreting particle simulations.

Particle trajectories are calculated by summing particle forces and solving a system of equations using MATLAB. This part of the model has been used to demonstrate the influence of a half-wavelength acoustic standing wave on particle trajectories and also the significant effect of the fluid parabolic velocity profile where acoustic pressure anti-nodes coincide with the low fluid velocity regions of the flow profile. Trajectory data can be used to calculate particle concentration spatially, although data is limited by the number of trajectories simulated, the quality of the data is poor and the computation is lengthy considering the size of the resulting data set.

A more efficient approach is demonstrated by considering the conservation of particles and solving using a simple finite difference approach, although care is required to ensure that the method used in stable. As spatial information is required at a steady state condition, a hybrid method is used where particle displacement is considered, although this still computes more rapidly than the approach based on particle trajectories data. The hybrid approach also produces a smoother concentration profile and supplies a larger and an evenly distributed data set. Data describing spatial concentration can also be converted into outlet concentration data where multiple outlets draw fluid from certain regions of the fluid chamber.

The ability of the model to predict particle motion and concentration given a 1-d standing wave field is validated against analytical solutions for simple cases. This gives confidence prior to further use of the particle model for more complex situations, for example, quarter-wave resonant

systems and where a different alignment exists between the acoustic field and parabolic flow profile. Such systems are typical of microfluidics where the wavelength is comparable to the channel depth where the flow profile significantly influences the movement of particles. The particle model is able to simulate this combined effect of the acoustic and fluid flow profiles.

Chapter 6

Experimental Evaluation of Particle Manipulation Devices

6.1 Introduction

This chapter seeks to demonstrate the validity of the modelling approaches described in previous chapters and to use the results of simulation work to explain the behaviour of ultrasonic particle manipulation devices. Two different devices are investigated, the first being the micro-engineered separator device investigated in previous chapters, and the second being a device developed for the capture of cells which uses a quarter-wavelength field.

The following section re-introduces the microfluidic separator described in section 2.5, but presents a fuller description of the parameters used in its simulation and of particular interest for experimental work. Both the measured and simulated performance of the device based on a range of operational conditions are compared and discussed, drawing from previous chapters and simulation work describing the fluid and acoustic fields. The experimental data contained in this section was produced with the kind assistance of Prof. Ding.

Section 6.3 goes on to describe the construction of a quarter-wavelength device developed at Cardiff University which operates to capture cells or spores onto the reflector surface. Simulation and experimental measurements from the system are again compared, but concentrate on describing the influence of geometry on the acoustic system rather than an exhaustive investigation of operational conditions.

In general, this chapter demonstrates the application of the numerical simulations developed in the previous chapter for predicting and explaining behaviour of particles within ultrasonic particle manipulation devices. The other numerical techniques presented in chapters 3 and 4 also contribute in explaining various features observed in the results. The use of complementary simulation tools is thus demonstrated.

6.2 Micro-engineered Particle Separator

The micro-engineered particle separator uses a half-wavelength acoustic field to collect particles along the centre plane of a fluid channel below which clear fluid is drawn off. The relative concentrations of the clear fluid stream and remaining fluid can be measured and is influenced by the operational conditions of the device, such as flow rate and acoustic energy density. These factors are investigated experimentally and are compared against simulated data.

6.2.1 Parametric Description of Device

In order to model the particle separator and simulate particle motion, the properties of the system must be known. This subsection describes briefly the appropriate aspects of the system and parameters, using the input impedance of the device to check the model description.

Transducer

For the transducer layer on the underside of the silicon matching layer, two different transducer types have been used: a bulk PZT material or a thick film printed material, the testing of which is described in Harris et al. [140]. The transducers are illustrated schematically in figure 6.1 which shows the various layers existing in each system. The bulk PZT is modelled according to the equivalent circuit in section 2.5.2 and uses established parameter values for the PZT material. However, the printed structure has electrodes arranged such that it represents two transducers operating back-to-back. When simulating this, the transducer elements seen in the equivalent circuit must be replaced with a pair of similar components placed in parallel. As the properties of the printed transducer element depends heavily on the PZT paste preparation and printing process, parameter values must be estimated experimentally.

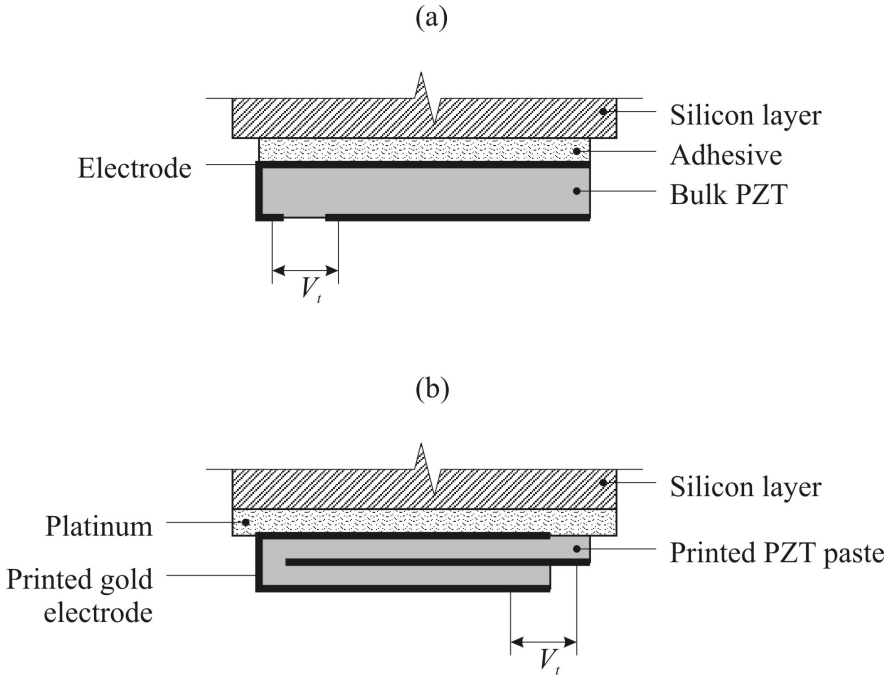

Figure 6.1: Structure of transducer using a) bulk PZT material and b) thick film printed PZT material.

Resonator Layers

The separator device was introduced in section 2.5 describing the basic construction and operation of the system, with the devices tested in this chapter having a fluid layer depth of 175μm and a Pyrex reflector layer thickness of 1525μm.

The properties of the various layers are summarised in table 6.1 for which the quality factor for each material is selected by matching the simulated impedance with the measured impedance of the device, with the fluid channel both air filled and water filled. As the platinum layer has a thickness of only a few microns and is acoustically hard, it has a negligible influence upon the acoustic characteristics of the resonator and is therefore not included in the model as a separate layer.

Electrical Impedance

The transducer and layer data is used as input to the acoustic impedance transfer model coded within MATLAB (section 2.5.2) and describes the 1-d acoustic characteristics of the layered res-

Table 6.1: Properties of particle separator layers.

Layer		Thickness[a] (μm)	Density[b] (kg/m^3)	Speed of sound[b] (m/s)	Quality factor[c]
	Glue[d]	5	1160	2620	50
	Silicon	525	2340[e]	8430[e]	80
Fluid	Air	175	1.293	331.6	50
Fluid	Water	175	1000	1500	50
	Pyrex	1525	2200	5730	1000

[a] Nominal value given, but may be replaced by measured value.
[b] Taken from acoustic material tables [135].
[c] Values determined by matching modelled impedance characteristics with measured data.
[d] Glue layer not applicable to printed PZT device.
[e] Approximate values for anisotropic material used.

onator. The electrical input impedance of the device or voltage across the transducer can be measured over a range of frequencies and can be compared to that calculated by the acoustic model, as demonstrated for example by [2, 5].

The impedance of a bulk PZT device is illustrated in figure 6.2 (measured data taken from Hill et al. [126]) and shows the frequency response of the device. The shape of the impedance plot indicates several resonant frequencies; a large resonance at 2.5MHz due to the transducer resonance, with other frequencies attributed to resonant modes in various layers of the device, examples seen at 3.4MHz and 4.1MHz. When comparing the measured and modelled data there is reasonable agreement between the frequencies at which the more dominant resonant modes occur, especially the higher frequencies 3.4, 4.1 and 4.8MHz. However, the model is less reliable at the lower frequencies and does not predict the resonance occurring at 1.4MHz at all. The magnitude of impedance is predicted with reasonable accuracy at the higher frequencies although is significantly less accurate at frequencies below 3.4MHz. It is noted that there are many smaller features in the measured data which are not predicted by the model, possibly caused by more complex modes in the system attributed, for example, to 3-dimensional modes, misalignment in fabrication or uneven application of the glue layer none of which are considered by the acoustic simulation.

For the printed PZT devices the frequency response is significantly different. Figure 6.3(a) shows measured and modelled impedance data for such a device which generally shows a lower impedance value and a smoother profile than that of a bulk PZT device. Only three resonant frequencies can be discerned, two modes at approximately 3.4MHz and 4.5MHz attributed to the

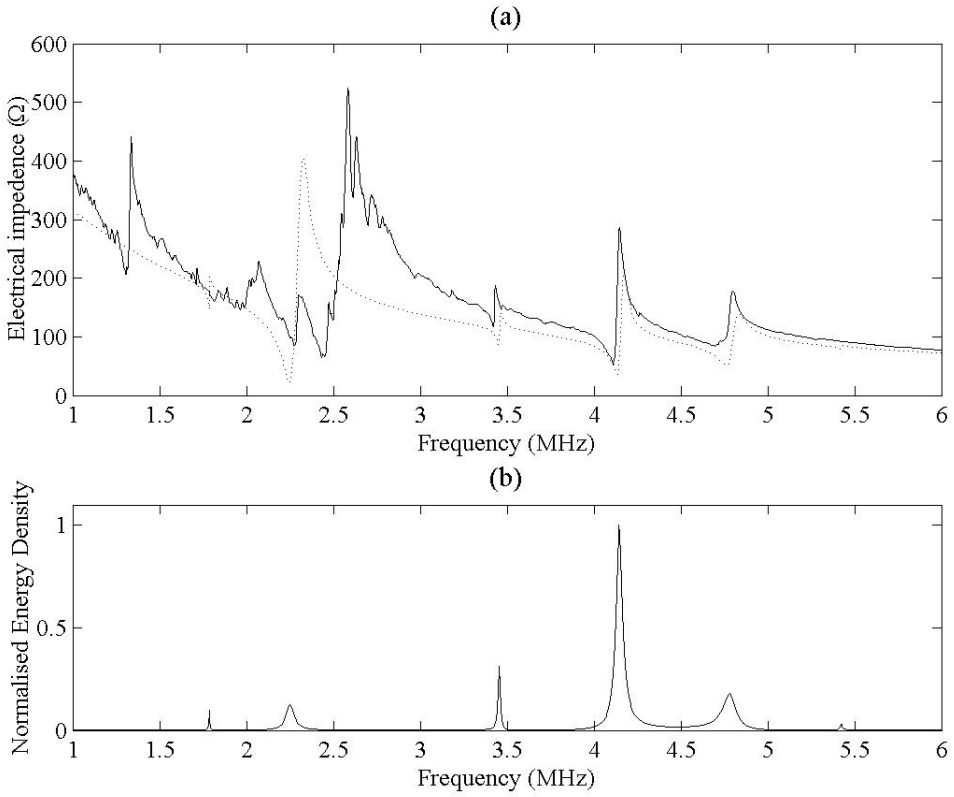

Figure 6.2: Impedance of water filled particle separator using bulk PZT transducer showing (a) measured impedance (solid line) and modelled impedance (dotted line) and (b) modelled fluid layer energy density, $\langle \bar{\epsilon} \rangle$, normalised relative to the peak energy density.

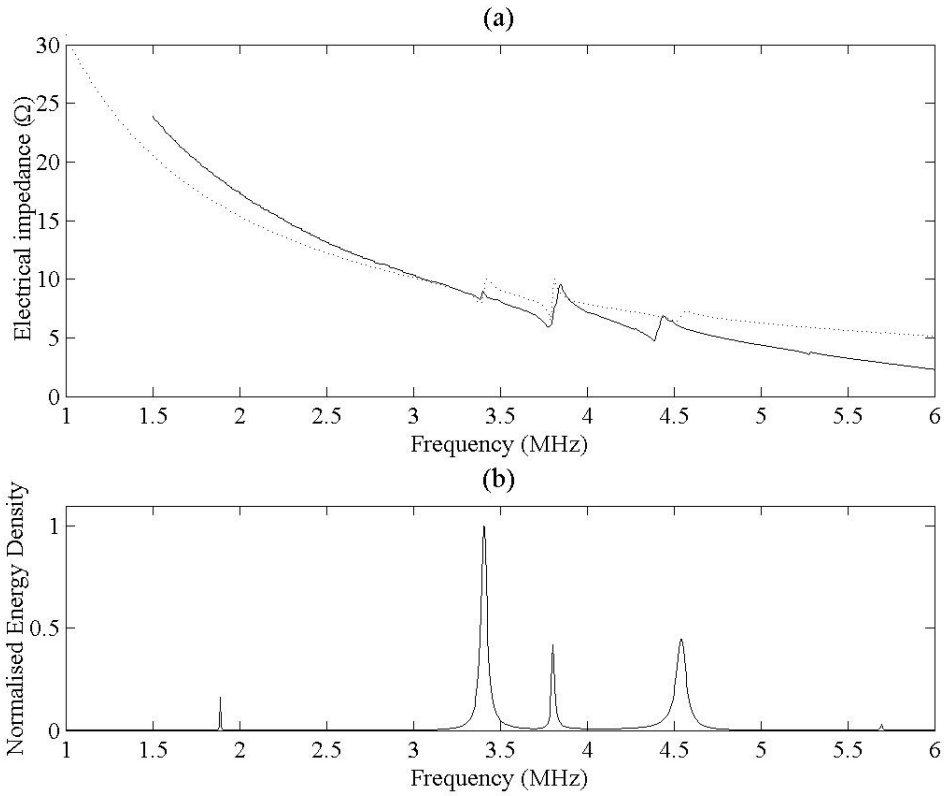

Figure 6.3: Impedance of water filled particle separator using printed PZT transducer showing a) measured impedance (solid line) and modelled impedance (dotted line) and b) modelled fluid layer energy density, $\langle \bar{\epsilon} \rangle$, normalised relative to the peak energy density.

presence of water in the chamber and another due to the transducer/matching layer at 3.7MHz. The association between these frequencies and certain layers is in part confirmed by two things: a) only the 3.7MHz mode is present in experimentally measured and predicted impedance in an air filled device, and b) the acoustic energy in the fluid (water-filled) layer is higher at 3.4 and 4.5MHz frequencies as seen in figure 6.3(b). This also applies to the bulk PZT device where frequencies 3.4 and 4.1MHz are both associated with strong resonance within the fluid layer. In figure 6.3(b) a small peak in acoustic energy can be seen and is likely to correspond to a quarter-wavelength resonance in the fluid layer. This is a low energy resonance, and as no corresponding variation in the impedance can be seen it is difficult to locate based on changes in the electrical characteristics.

The key physical differences between the bulk and printed devices are the transducer structure and material, and the method of adhesion to the silicon. This suggests that the more complex profile

of the bulk PZT data is caused by additional degrees of freedom introduced by the adhesive layer. Further work investigating the efficiency of each transducer type would be of value, although no comparison in efficiency or power is made here. Instead it has simply been ensured that the frequency response can be modelled, an important consideration when simulating the acoustic field within each device.

6.2.2 Experimental Rig

The experimental rig is used to test the ability of the particle separator fabricated using a printed PZT transducer to separate clear fluid from the particle/fluid mixture. Depending on the operating conditions used in experiment, varying degrees of particle separation are observed and are an indication of the true behaviour of particles within the device.

Apparatus

The device is designed to operate in a flow-through mode, therefore for the purposes of experiment a convenient means of connecting pumps and other fluid network elements is facilitated using a manifold. Figure 6.4 shows the separator device mounted on an aluminium manifold which contains ports aligned with the inlet and outlet ducts in the silicon. These ports lead to flexible tube connectors which allows pumps to be easily connected to the appropriate duct. The total dead volume of the system is approximately 1ml.

To control the flow rates through the device ducts, peristaltic pumps are used which are able to deliver low flow rates, but typically issue a pulsed flow. The pumps chosen (Watson Marlow 403U/L) are designed to minimise this fluid pulsing effect. Figure 6.5 illustrates schematically the experimental rig and shows that a pump is connected to each outlet duct, corresponding to flow rates Q_1 and Q_2.

The schematic also shows other parameters used to ensure the correct setting of operating conditions, notably the drive frequency of the transducer f and voltage amplitude V_t across the transducer. These parameters are set using a function generator (TTi TG1304 programmable function generator) feeding to a 50dB amplifier (EIN Model 240L RF power amplifier) then to the transducer. To measure the transducer voltage V_t, an oscilloscope (Hameg) is connected in parallel with the transducer.

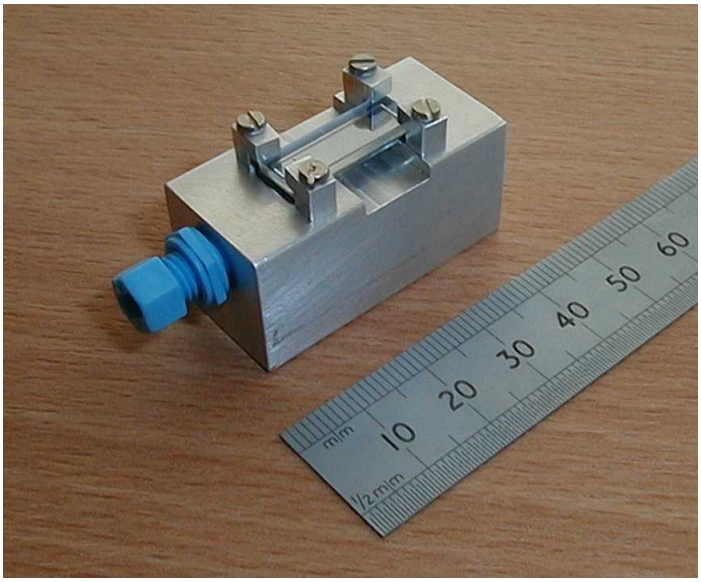

Figure 6.4: Photograph of micro-engineered particle separator mounted on aluminium manifold.

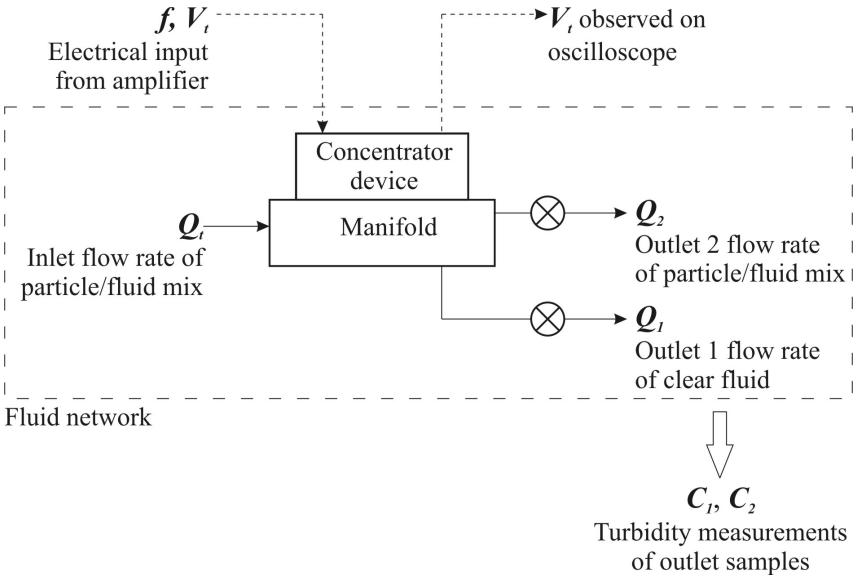

Figure 6.5: Schematic of experimental rig showing flow rates and transducer drive operating parameters.

To prepare the fluid/particle inlet sample, a balance (Mettler) is used to measure a quantity of fluid into which a pipette is used to dispense a particle concentrate. This ensures that the concentration of samples used for each experimental run are consistent. The particles used in experiment are 1μm latex particles (Polysciences Inc.).

The particle concentration of the outlets after each experimental run is measured using a turbidity sensor (Honeywell) giving values C_1 and C_2. To account for particles caught within the fluid network, the inlet concentration C_0 is calculated using weighted values of C_1 and C_2. The turbidity sensor is not connected directly to the fluid network which would facilitate a continuous measurement, but instead measures concentration on fluid samples. This is necessary as the dead volume of the turbidity sensor housing is large, which at the low flow rates used in experiments would allow diffusion and settling of particles to take place, affecting concentration measurements. Such effects are otherwise not a significant problem in the experimental rig as fluid connections and tube diameters are kept to a minimum, ensuring higher flow velocities and minimum sedimentation of particles. Reduced dead volume also reduces experimental time and the time taken for the fluid/particle sample to pass through the fluid network.

Control and Measurement of Parameters

Various parameters are controlled and recorded during the experimental process and include the following:

Input voltage, V_{in}, V_t: The peak-peak voltage input from the signal generator to the amplifier, V_{in}, is selected as an operating condition and relates to the acoustic energy density within the device and therefore the radiation force. The corresponding transducer voltage V_t is occasionally noted, used principally to check the predicted voltage characteristics.

Frequency, f: The frequency of the input signal to the transducer is again controlled via the signal generator. The resonant frequency of the system is determined by first using a combination of measured and simulated impedance data then, more accurately, when connected to the experimental rig by adjusting the frequency until a voltage minimum across the transducer is found (impedance minimum).

Flow rates, Q_t, Q_1, Q_2: For the peristaltic pumps used in the experiments, rotational speed of the pump is selected via a key pad. The flow rate that each pump delivers is proportional to pump speed, therefore, calibration of the pumps provides a simple linear correlation between

flow rate and pump speed, achieved by measuring the time to deliver a known volume of fluid. Calibration is also made for a series of different tube bore diameters, where small diameter tubes deliver small volume flow rates and vice versa. The flow rates are repeatable within measurement error, therefore these calibration results are used throughout the entire experiment. Pumps are connected to the outlet ducts of the device, therefore the pump flow rates correspond to outlet flow rates Q_1 and Q_2 with the sum corresponding to the total flow rate seen within the main channel of the device, $Q_{total} = Q_t = Q_1 + Q_2$.

Concentration, C_0, C_1, C_2: The turbidity sensor is used to provide particle concentration measurements of the inlet C_0 and outlets C_1 and C_2. The turbidity sensor detects a combination of reflected and transmitted light on a fluid sample and relays a voltage signal directly to a pc. Calibration between the data displayed on the pc and particle concentration is required. For latex particles supplied in a diluted form, this is achieved using a haemocytometer to determine particle numbers within a known fluid volume together with a turbidity reading, and making a series of measurements for a range of sample concentrations. Alternatively, for initially dry particles such as yeast, a sample of particles are weighed to which a known quantity of fluid is added and measurements made for further dilution of the sample. Turbidity sensor calibration curves are shown on figure 6.6 where it can be seen that calibration is required for each particle type and size used in experiments. Also, it is noted that the relationship between concentration and the turbidity reading is highly non-linear.

For each data point recorded in the following section, the device is operated using the appropriate voltage and flow rate conditions and at least 5ml of sample is collected from each outlet. This provides enough fluid to enable the turbidity sensor to make a repeatable measurement and is drawn into the sensor using a syringe. Flushing of the sensor is then required to ensure that no particles remain adhered to the sensor surfaces and affecting subsequent measurements.

6.2.3 Particle Concentration Results

In this section the results investigating three parameters, C_0, Q_t and Q_1/Q_t are investigated. Table 6.2 summarises the operating conditions used during each set of experiments, for example, experiment 1 lists the series of C_0 values used in separate experimental runs and also the parameter values, Q_t and Q_1/Q_t maintained at a constant value. For each set of operating conditions chosen the voltage, V_{in}, is also varied in steps of ~ 100mVpkpk, adding another parameter dimension to

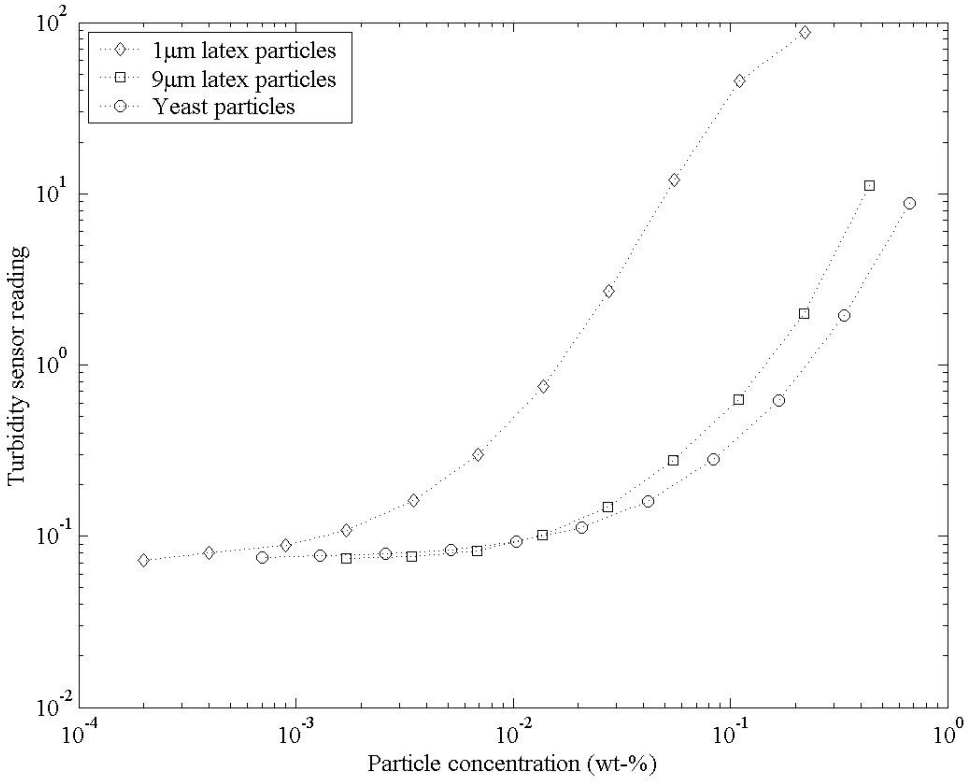

Figure 6.6: Calibration curves for turbidity sensor.

Table 6.2: Operating conditions used for experimental work.

Parameter	Experiment 1	Experiment 2	Experiment 3
C_0 (/ml)	1. 2.2e8 2. 1.5e8 3. 9.5e7	2.2e8	2.2e8
Q_t (ml/s)	0.005	1. 0.005 2. 0.007 3. 0.010	0.005
Q_1/Q_t	0.25	0.25	1. 0.25 2. 0.35 3. 0.45

the experimental work and investigating the majority of operating conditions represented in figure 6.5.

The following subsections present the experimentally measured and corresponding predicted data for each experiment (calculated using the particle model developed in chapter 5), accompanied by a description of the main trends observed in the data. Any explanations are reserved for the following discussion, section 6.2.4.

Experiment 1 - Particle Concentration, C_0

This experiment records the influence of the inlet particle concentration, C_0 using three different concentration values for each run and repeated over a range of voltage levels. Figure 6.7 records data collected for several experimental runs and plots the relative concentration of fluid collected from outlet 1 and outlet 2. The relative concentration gives a simple indication of an increase or decrease in concentration, for example, at V_{in} = 0 the relative concentration is 1 in all cases and informs us that the outlet concentrations are equal to the inlet concentration. At higher voltages, however, the relative concentration of outlet 1 fluid is lower and indicates reduction in concentration, where 0.5 would represent a two-fold reduction.

Looking at the trends shown by the experimental data in figure 6.7, it can be seen that as the voltage increases, fewer particles are drawn through outlet 1, allowing the majority of particles to pass through outlet 2. This trend is expected as an increase in voltage corresponds to increases in acoustic pressure and radiation force experienced by the particles, therefore causing a greater

number of them to reach the acoustic node and be drawn off through outlet 2. The increase of concentration through outlet 2 is limited as Q_2/Q_t is relatively high and the particles are still highly diluted. The theoretical maximum relative concentration through outlet 2 in the case of $Q_1/Q_t = 0.25$ and where all the particles pass through that outlet is 1.33.

Considering the effect of inlet concentration and the data presented by the different curves, the higher particle concentrate shows marginal improvement in separation, i.e. lower outlet 1 concentration and higher outlet 2 concentration. However, a clear difference in trend between C_0 = 1.5e8 and 9.5e7 is not shown, therefore it is reasonable to assume that discrepancies can be attributed to experimental error.

Assuming the data in figure 6.7 to indicate experimental error rather than a distinctive effect of the inlet concentration, figure 6.8 is based on the same data, but plots the mean values and associated error. Also shown in the figure is the predicted concentration (dotted line) which, although it compares well up to V_{in} = 150mVpkpk, predicts more marked separation as voltage increases. In both data sets the degree of separation levels off at the higher voltage values. The discussion section found later in this chapter aims to explain these observations.

Experiment 2 - Total Flow Rate, Q_t

The total flow rate Q_t is investigated and concentration results are shown in figure 6.9 for a range of flow rates. The figure adopts the *mean* experimental errors for clarified and concentrated flow respectively, estimated in the preceding experiment.

The most significant influence that the flow rate has on the results is the reduction of separation at increasingly high flow rates. For example, the concentration through outlet 1 increases as flow rate increases, presumably as fewer particles reach the acoustic node to pass through outlet 2. A corresponding reduction in concentration is seen in the measured results of outlet 2.

It is also noted from these results that the concentration through each outlet (and therefore the degree of separation) levels off at different concentration values at high voltages, and even degrades slightly at 450mVpkpk where a small reduction in separation is recorded (the formation of bubbles due to thermal effects was occasionally observed at these higher voltage levels). In figure 6.10 the predicted concentration values are shown which indicate that, theoretically, the separation levels off to the same value irrespective of the flow rate, the flow rate influencing only the minimum voltage at which that level is reached, differing significantly from the measured data.

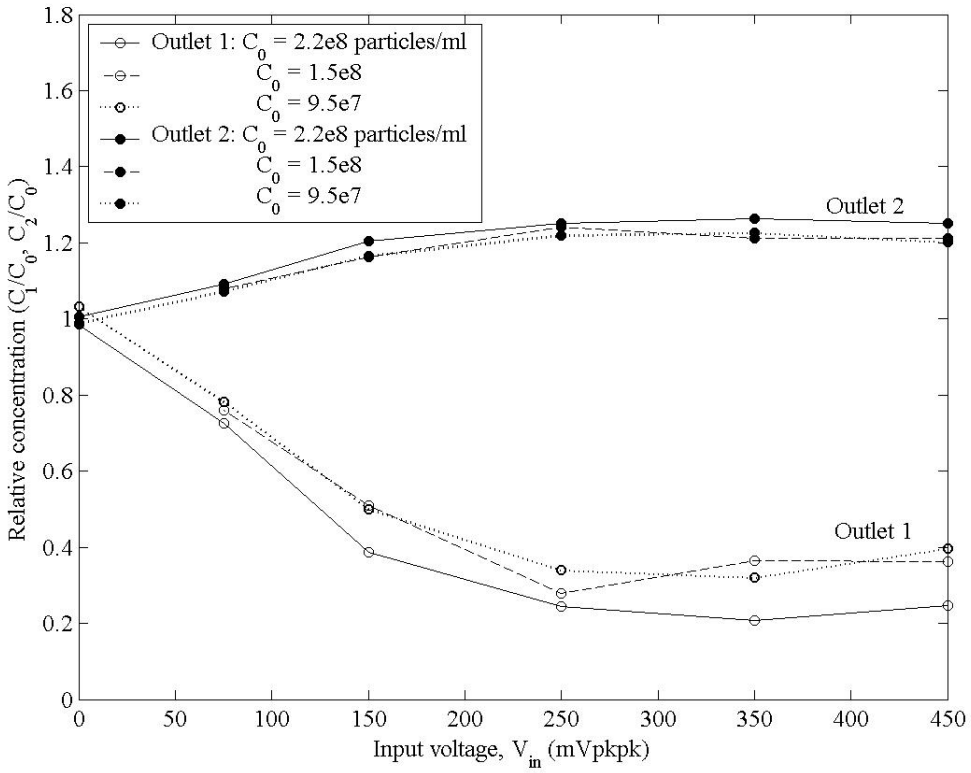

Figure 6.7: Influence of inlet sample particle concentration, C_0, and input voltage, V_{in}, on particle separation. Experiment operated using Q_t = 0.005ml/s and Q_1/Q_t = 0.25.

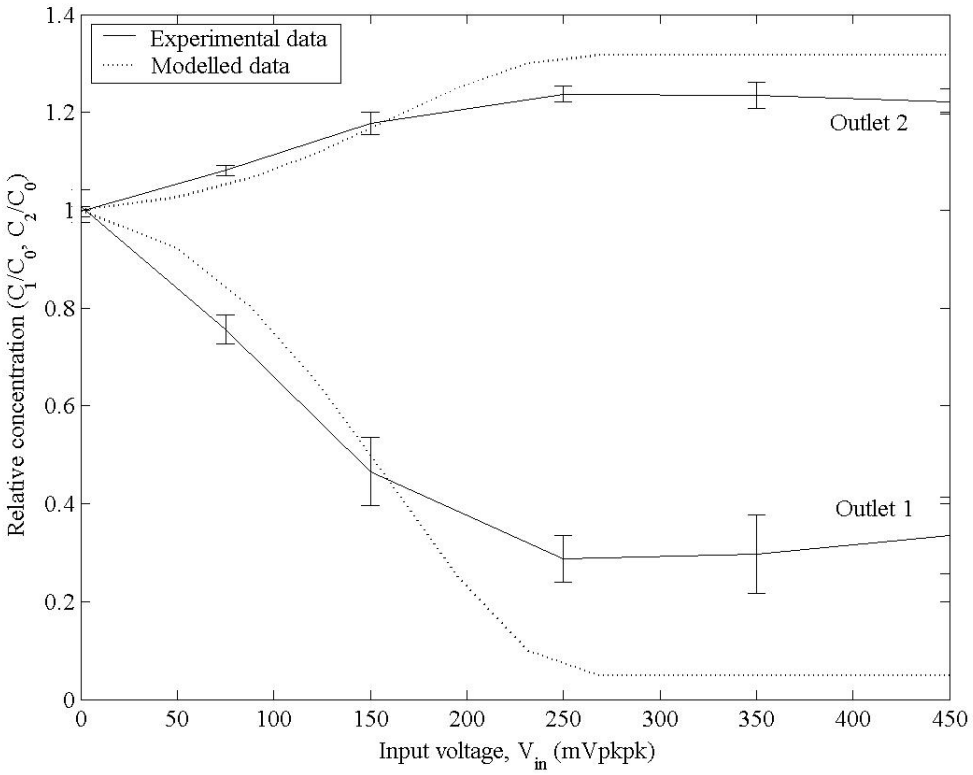

Figure 6.8: Influence of input voltage, V_{in}, on particle separation based on both experimental and predicted data. Experiment operated using Q_t = 0.005ml/s and Q_1/Q_t = 0.25.

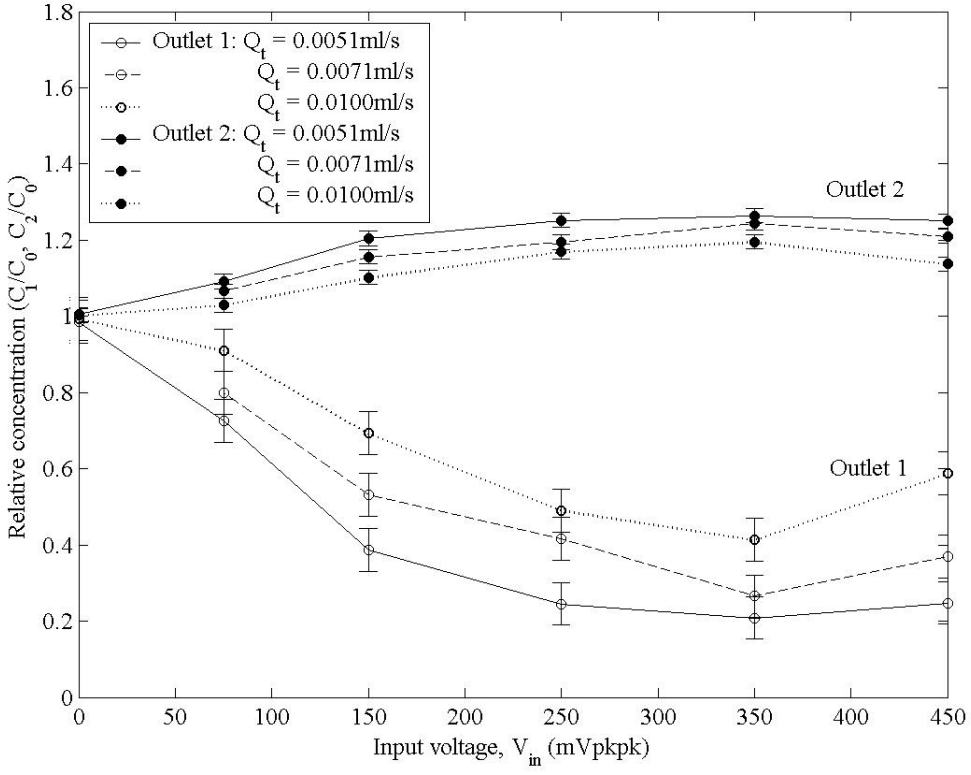

Figure 6.9: Influence of total flow rate, V_t, and input voltage, V_{in}, on particle separation. Experiment operated using C_0 = 2.2e8 particles/ml and Q_1/Q_t = 0.25.

In general, the modelled data does predict increasingly poor separation for an increase in flow rate as for the experimental data. However, the model slightly underestimates the separation up to 170mVpkpk, reflected in both the outlets. Above this voltage the predicted data begins to overestimate the separation, continuing while concentrations values level off at the higher voltages.

Experiment 3 - Outlet Flow Proportions, Q_1/Q_t

The final experiment investigates the influence of the outlet flow proportions. Experimental data recorded for a range of outlet flow rates is shown in figure 6.11 for outlet 1 flow ranging from 25 to 45% of the total flow rate, Q_t, which is held constant. Again, data is recorded for a range of voltages.

It can be seen that as the flow rate through outlet 1, Q_1, increases, the concentration through

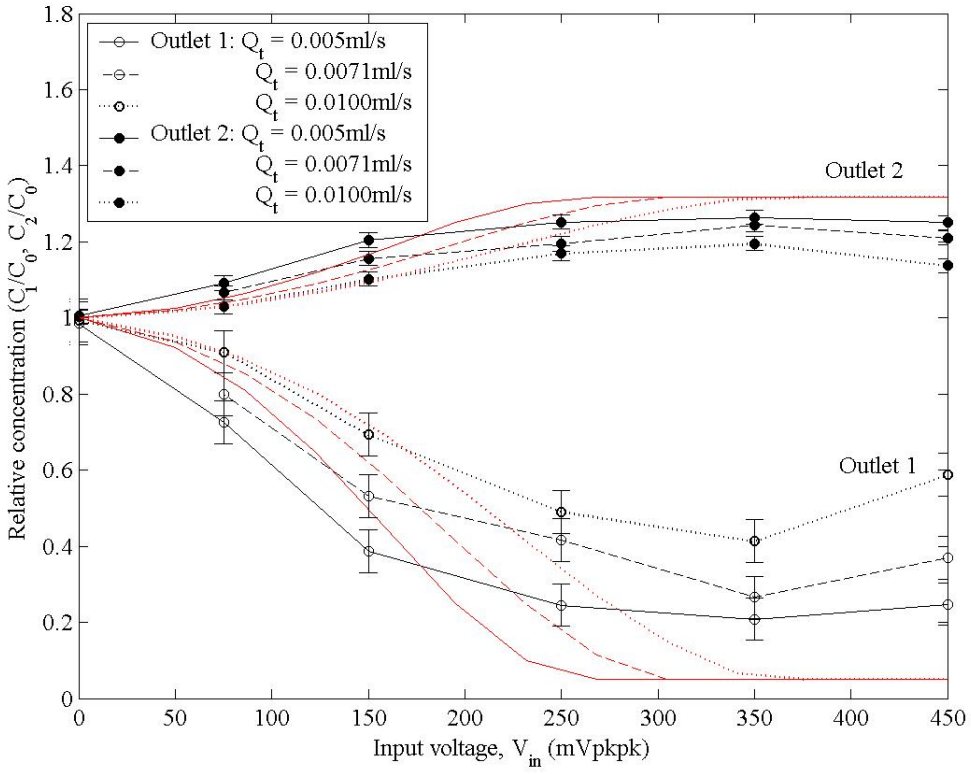

Figure 6.10: Influence of total flow rate, V_t, on particle separation based on both experimental (black) and predicted (red) data. Experiment operated using C_0 = 2.2e8 particles/ml and Q_1/Q_t = 0.25.

that outlet also increases, and even exceeds the concentration through outlet 2 at $Q_1/Q_t = 0.45$. It would appear that as more fluid is drawn through outlet 1, a greater proportion of the particle stream is drawn through the outlet, increasing concentration through outlet 1 and decreasing concentration through outlet 2 and significantly influencing the separation effect.

At high voltages there does not appear to be a small decrease in the separation effect as observed in the previous experiment where at 450mVpkpk outlet 1 concentration increased slightly.

Figure 6.12 compares the experimental data to modelled predictions. As seen in the experimental results, the model predicts that an increase in outlet 1 flow will have a detrimental effect on separation at the lower voltages, although it inaccurately predicts that good separation will be achieved at higher voltages as it assumes that a densely packed particle stream is eventually formed and passes through outlet 2.

With the vast majority of particles passing through outlet 2 (at high voltages), the model suggests that a greater outlet 2 concentration can be achieved by increasing Q_1 and reducing Q_2. This is because the particle stream will be less dilute as it passes through outlet 2 and within a smaller volume of water. A corresponding, although smaller, change is seen in the outlet 1 concentration.

Generally the modelled results differ significantly from the experimental data at the higher voltages where the model does not predict the movement of the particle stream switching from outlet 2 to outlet 1.

6.2.4 Discussion

This section aims to explain the results recorded in the preceding pages and understand the relative importance of the variety of processes which influence particle movement through the separator. The modelled results demonstrate the behaviour of particles under the forces described in section 5.2.1 and also based on assumptions regarding the 1-dimensional nature of the acoustic field and fluid flow profile, not dissimilar to the assumptions adopted for other simulation work discussed in chapter 2. Therefore, disagreement between the experimental and simulated separation results can be attributed to a more complex system of forces and/or significant 2 or 3-d variations with the acoustic and fluid flow fields, some of which have been investigated in detail in chapters 3 and 4 and therefore the discussion also draws from these chapters.

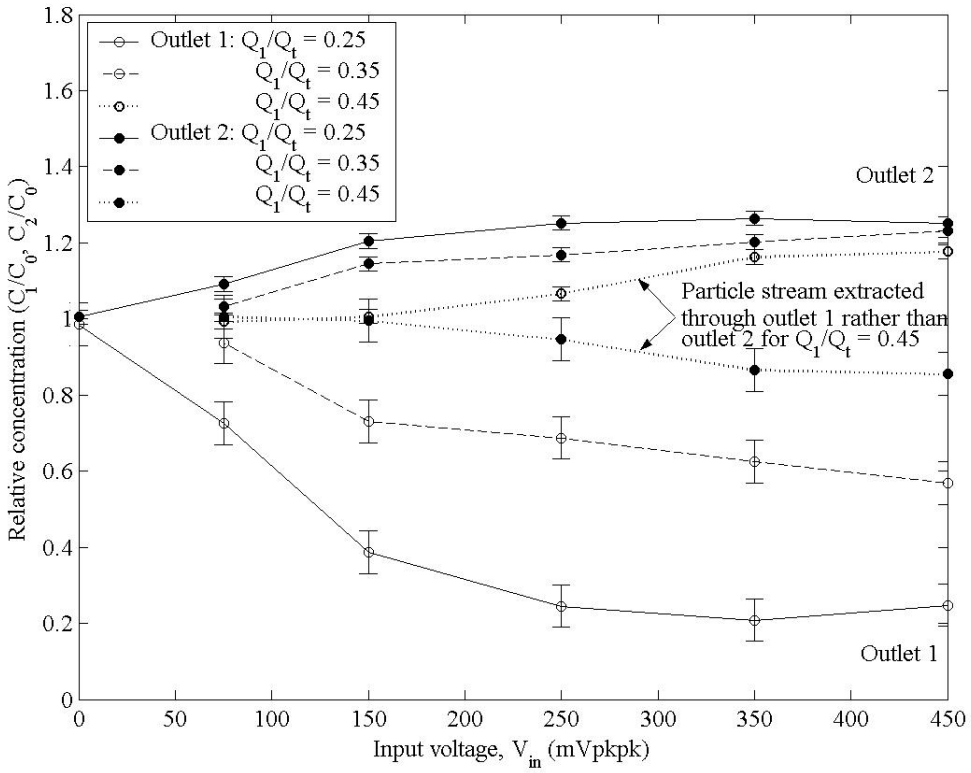

Figure 6.11: Influence of outlet flow proportions on particle separation. Experiment operated using C_0 = 2.2e8 particles/ml and Q_t = 0.005ml/s.

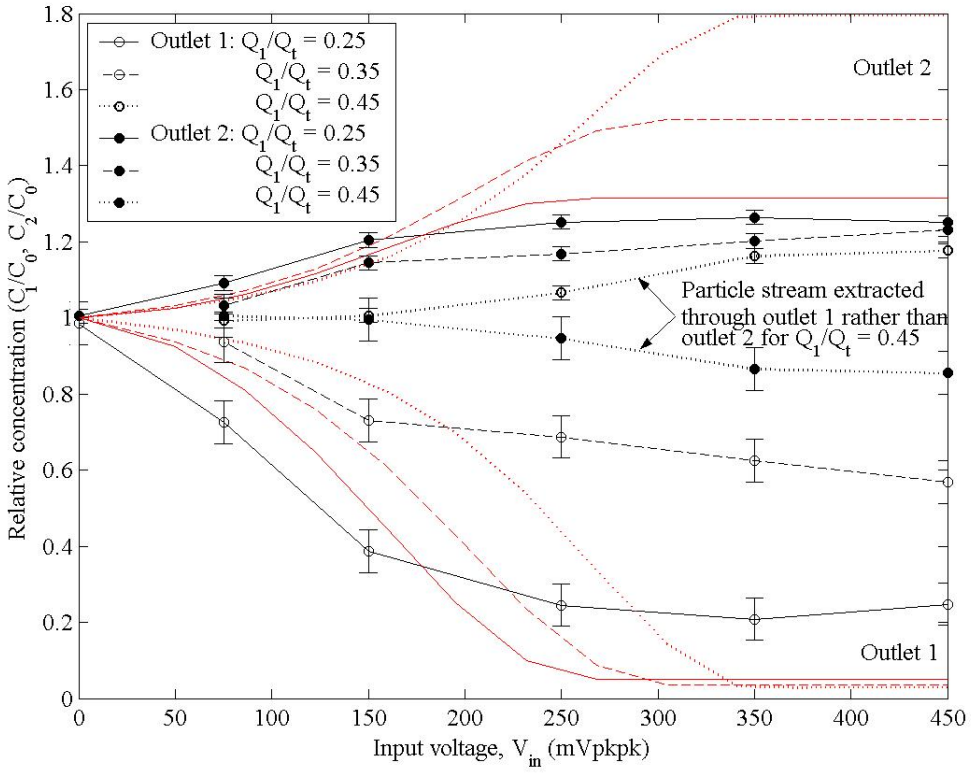

Figure 6.12: Influence of outlet flow proportions on particle separation based on both experimental (black) and predicted (red) data. Experiment operated using C_0 = 2.2e8 particles/ml and Q_t = 0.005ml/s.

Structure of particle stream

The initial set of experiments investigating the influence of concentration C_0 represents the closest comparison between modelled and measured data (figure 6.8) and, indeed, separation of particles is demonstrated. At the lower voltage values experimental error and fluid lift forces explain why the predicted data underestimates the separation slightly, although the particle model incorporating the acoustic impedance transfer model gives a good description of particle movement. However, at increased voltage there is a significant discrepancy between the data sets where the model overestimates the level of separation.

To begin to explain this discrepancy, it is initially assumed that at high voltages a higher radiation force is experienced by the particles and all particles move into a high concentration particle stream. Whilst the prediction assumes that all particles within this stream pass through outlet 2, the experimental results suggest that part of the particle stream passes through outlet 1. For this to be possible, the particle stream cannot consist of particles all accurately aligned along a uniform pressure node plane, but instead be distributed within a band extending a certain distance either side of the pressure node plane.

Two explanations are put forward. Firstly, simulation of the acoustic field covered in chapter 4 suggests that the occurrence of enclosure modes with the fluid layer will prevent a uniform pressure node plane from forming, the vertical position y of the pressure node a function of the lateral position z across the device. The movement of particles towards zero pressure amplitude locations would result in them being distributed at various y positions. Also, the strength of the acoustic field will influence the rate at which a particle moves towards the nodal plane. For example, if a weaker acoustic field exists towards the lateral edges of the fluid chamber, as shown in chapter 4, figure 4.7 for mode 2, the resulting particle stream may be more dispersed within these areas as compared to the centre of the chamber.

The second explanation is that disturbance of the particle stream will cause particles to become more dispersed about the nodal plane. Such disturbance is likely to originate from acoustic streaming which has been observed during subsequent experimental work on the separator. Also, the literature records the occurrence of streaming within similar resonators which influences the movement of 1μm and similar sized particles and, as streaming is related to the acoustic energy losses, streaming velocities will increase as a function of voltage.

Streaming tends to influence the movement of smaller sized particles, as used here, and should

not disturb the movement of larger particles. This is supported by the separation of larger yeast particles as reported by Harris et al. (appendix 5) where almost total clearance is measured, which indicates that for larger particles the particle stream is not significantly dispersed.

Diffusion of the particles may also limit the maximum concentration of the particle stream as predicted by Higashitani [72] where for a long residence time, diffusion becomes more significant relative to the radiation forces. However, the flow rates used in experiment do not result in a sufficiently long residence time to support the significant influence of diffusion upon the maximum concentration of the particle stream. Even without the influence of the acoustic radiation forces, the movement of particles due to diffusion is negligible (see section 5.2.1).

Separation at high voltage levels

At high transducer voltages the radiation forces also should become high and the formation of a concentrated particle stream more likely. However, as the voltage is increased further other forces or phenomena due to the presence of the acoustic field become more significant; for example, the streaming flow velocities and secondary radiation forces (particle interaction) will increase.

Some experimental results indicate that at 450mVpkpk, particle separation becomes less efficient than at 350mVpkpk. It is possible that at the higher voltage particles begin to agglomerate and disturb the flow, the agglomeration being a combined effect of lateral and secondary radiation forces. This would be consistent with some observations, during preliminary tests with larger particles, e.g. yeast.

The formation of bubbles within the fluid chamber has also been observed. This is associated with the heating of the PZT and separator device which causes expansion of gas trapped in the fluid sample. These bubbles are large enough to significantly disturb the flow and increase the flow velocity through the fluid chamber, thus damaging the separation process.

The presence of a highly concentrated particle stream due to a high voltage and located at the nodal plane may influence the acoustic field, as another layer is effectively present in the device. As mentioned in chapter 2, particles of an acoustically soft material may not significantly alter the acoustic impedance and therefore characteristics of the device, similarly for a low concentration of particles. In the experimental results above there is no evidence that the particle stream is tightly packed with a high concentration, which does not suggest that the particle stream formed at high voltages will influence the acoustic field.

Vertical y location of particle stream

The third set of experimental results investigating the influence of relative outlet flow rates provides information regarding the approximate location of the particle stream relative to the position which represents the division of flow between the two outlets. For example, if the position where the flows divide was located at $y = h'$, all fluid passing along the channel within the bounds $0 < y < h'$ will pass through outlet 1 and the remaining fluid within $h' < y < h$ (where h is the height of the channel) will pass through outlet 2. This is illustrated in chapter 5 figure 5.10. It is reasonable to state that as Q_1 increases relative to Q_2, h' moves up towards the reflector layer. Therefore, at a certain flow condition, h' will be located above the acoustic node and the majority of particles will instead pass through outlet 1. This is seen in figure 6.11 where for Q_1/Q_t =0.25 and 0.35 the majority of particles pass through outlet 2, however, this changes for Q_1/Q_t =0.45 where the majority of particles pass through outlet 1.

This switch between outlets has not been predicted by the modelled results, although the following paragraphs explain these observations. As shown in section 3.6, this y position representing the division of the outlet flows is not necessarily uniform across the width of the channel due to the geometry of the outlet region. In the experimental system it is instead likely that the region of fluid drawn through outlet 1 extends further in the y-direction (see figure 3.24) than that assumed in the simulation, which is based on a uniform flow pattern. Therefore, whilst the simulation may predict the extraction of the particle stream through outlet 2 under certain operating conditions, in the experimental system the particle stream may instead be contained within outlet 1 flow, as reflected by the data plotted in figure 6.12. (Other flow effects may explain why a greater degradation in separation than expected is seen with an increase in flow rate Q_t, although no specific explanations can yet be presented.)

Another explanation is that the location of the pressure node has not been accurately predicted and in the experimental system is closer to the silicon matching layer. It is important for the simulation to predict the level of acoustic energy at resonance rather than accurately predict the frequency at which this resonance occurs, therefore the simulation uses the predicted resonant frequency rather than the experimental operating frequency. However, a small error in frequency will influence the predicted acoustic pressure profile and nodal position. Based on simulated data, figure 6.13 illustrates the normalised acoustic pressure profiles at both the experimental operating frequency and the predicted resonant frequency. This figure suggests that the simulation places the node approximately 5μm above the true node location and therefore overestimates the minimum outlet

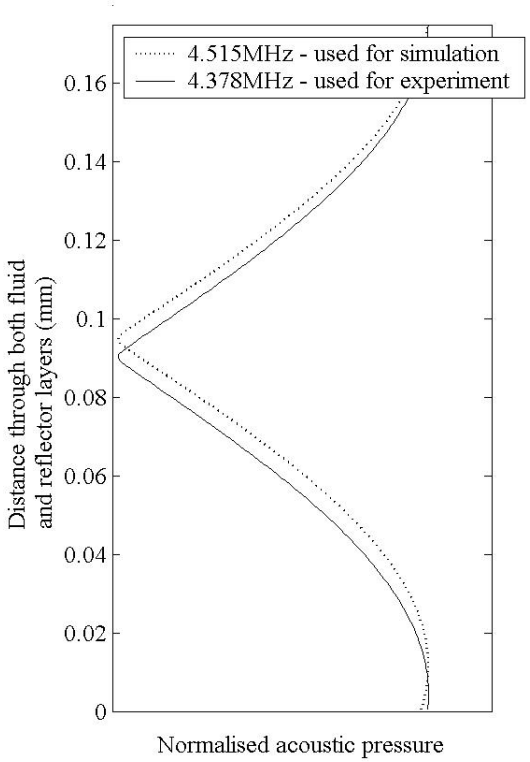

Figure 6.13: 1-d simulation of acoustic pressure profile within fluid chamber at frequencies used for experimental measurements (solid line) and simulated results (dotted line).

1 flow rate (Q_1/Q_t) at which particles will pass through outlet 1. In general, 'alignment' error between the acoustic pressure profile and parabolic flow profile will alter particle trajectories.

What can also be seen in this figure is a pressure anti-node near the silicon layer boundary at $y = 0$ where the pressure amplitude reaches a maximum. This suggests that a small proportion of particles will be forced towards this surface and, if the particles do not adhere to the surface, will be carried to outlet 1 with the clarified flow. This explains why the simulated concentration results do not predict complete clearance (figures 6.8, 6.10 and 6.12).

The position of the pressure anti-node based on the experimental frequency also shown in figure 6.13 is even closer to the silicon surface than for the frequency used in simulation. Therefore, the anti-node cannot be expected to cause a significant increase in concentration within the clarified flow and consequently is not the explanation as to why the experimental results do not show complete clearance. There is more evidence to suggest that streaming is the cause.

Forces experienced by particles

The discussion above has explained a significant number of observations in terms of non-uniformities in the acoustic and fluid flow fields simulated in previous chapters, and other phenomena such as acoustic streaming. As other processes and degrees-of-freedom are present in the experimental system, it is difficult to judge the accuracy of the predicted separation using the particle model and based on the 1-d simulation of the acoustic and fluid flow and associated particle forces. Regarding the acoustic radiation force, the literature discussed in section 2.3.1 is confident about how the acoustic radiation force acting on a particle relates to a known acoustic field, therefore the ability of the model to accurately predict the nature of the acoustic field becomes important.

The predicted and measured device impedance has already been discussed in section 6.2.1. This showed that the acoustic simulation of the device can predict the presence of resonant modes and the general trend of the impedance spectrum, although some error is present in the predicted magnitude of impedance. When simulating the performance of the device at a certain resonance, it is important to use the *predicted* resonant frequency in the simulation in order to more accurately predict the acoustic energy in the fluid layer. However, this does incorporate an error in frequency.

To illustrate this point, figure 6.14 shows the measured and predicted impedance spectra of the printed device and there is an error of at least 100kHz between the two resonant frequencies. For the purposes of experiment the location of the voltage minimum is typically assumed to give a reasonable estimate of the resonant frequency, for which in this case a frequency of 4.378MHz was consistently used. Similarly for the simulation, the location of the predicted voltage minimum was used for simulated concentration results, highlighted in the figure at 4.515MHz and also corresponding to the impedance minimum.

The third graph in the figure describes the predicted acoustic energy density within the system, which is directly related to the magnitude of the acoustic radiation force (equation (2.8)). The peak in this energy is associated with resonance and it is assumed that a similar peak exists for the experimental device at a slightly lower frequency, although this currently cannot be measured. It is assumed that the experimental operating frequency and frequency used for simulation both correspond to similar positions on the respective energy peaks, therefore providing a reasonable estimate of the radiation forces. However, it is noted that the peak appears reasonably sharp and therefore a small change or error in frequency will significantly influence the resulting radiation force.

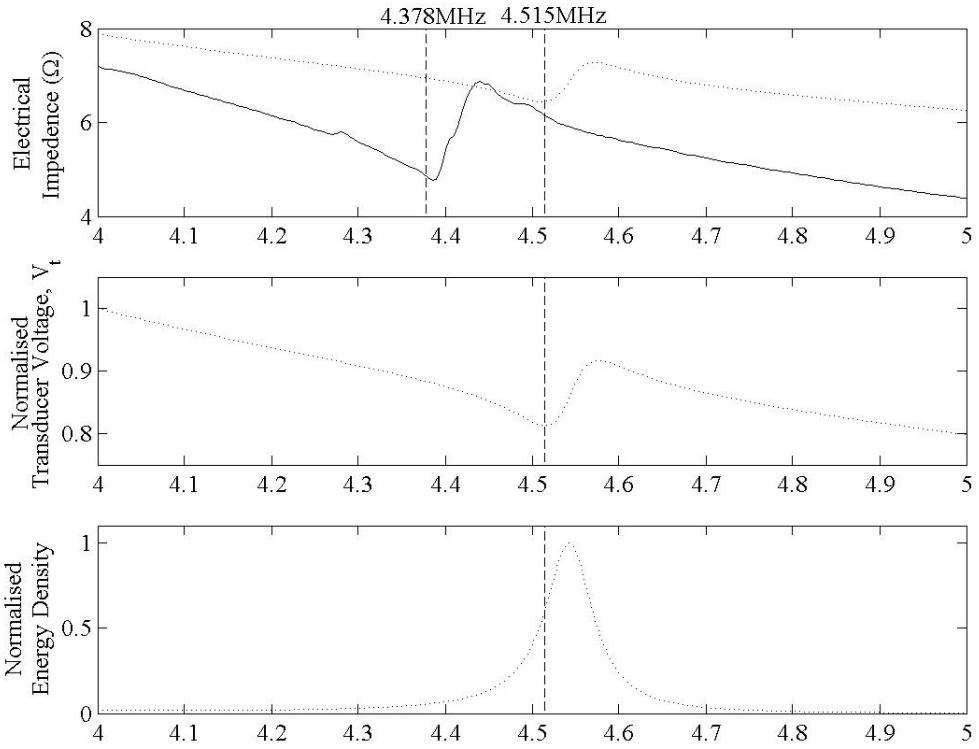

Figure 6.14: Characteristics of impedance, transducer voltage, V_t, and energy density and over region of 4.5MHz resonance and indicating frequency used for simulated results. Transducer voltage and energy density normalised relative to the peak values.

It can also be seen from the figure that the voltage (or impedance) minimum does not necessarily represent the energy maximum and the best frequency for separation. This frequency is located at a slightly higher frequency, typically between the minima and maxima of the voltage or impedance spectra. This suggests that the optimum operating frequency has not been used in the experimental work reported here. It also has implications on micro-processor control of the device and the ability to locate the optimum frequency based on a measurable characteristic of the device, although it is possible that a measure of electrical power could be used.

6.3 Cardiff University Cell Capture Device

This section describes the experimental and modelled results of an ultrasonic device designed ultimately to capture spores, although 1μm latex particles are used to provide data on particle capture. The device is related to the particle separator investigated above in that an acoustic field is used to drive particles to a certain plane within a fluid chamber, although to capture particles a quarter-wavelength resonance is used to move particles to the reflector surface. This section serves to test specific aspects of the particle model based on the experimental data produced, although further investigative work on this device contributed to a substantial paper which can be found in appendix 6 describing more fully the test procedure, experimental trends and the biological aspects of the work. This paper is also included in the list of references (Martin et al. [119]).

6.3.1 Overview of Quarter-wavelength Device and Simulation

Structure

The quarter-wave device was designed, fabricated and tested at Cardiff University and in the thickness direction is of a similar scale to the separator device, but does not rely on micro-engineering techniques in its fabrication. The basic structure of layers is similar although a steel matching layer is used and the fluid layer thickness is defined using a spacer, unlike the micro-engineered separator. A cooling system is also incorporated to draw heat away from the transducer and reduce the risk of damage.

The quarter-wave device structure is illustrated in figure 6.15, the structure consisting of PZT adhered to a steel matching layer, a fluid layer and a glass reflector layer. The construction allows the device to be easily disassembled and permits the removal and replacement of the glass reflector

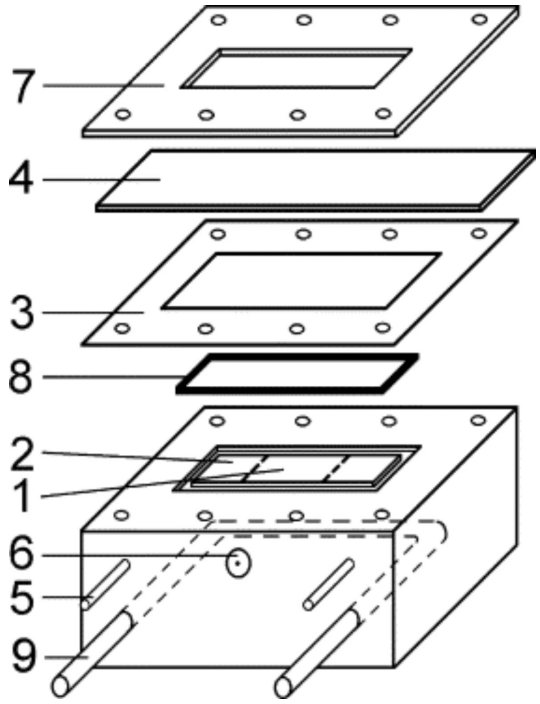

Figure 6.15: Construction of quarter-wave device: (1) transducer's active area, (2) steel layer, (3) spacer for water layer, (4) glass reflector, (5) water inlet (outlet), (6) electrical connection, (7) top brass, (8) elastic gasket and (9) water cooling system. Taken from Martin et al. [118]

layer. This is a useful feature as a series of different reflector thicknesses may be tested without changing the other layers of the device. It is also allows the glass reflector to be prepared with a suitable antibody coating and allows the subsequent microscopic study of the spore/particle capture. The typical acoustic properties of the structural layers are listed in table 6.3, with the parameter values taken from Martin et al. [119].

Operation

The operation of the quarter-wavelength device relies on a half-wavelength resonance being generated in the reflector layer. As the reflector is in resonance the majority of acoustic energy is contained in this layer rather than in the fluid layer. However, in order to move particles using radiation forces, a sufficient level of acoustic energy must be generated within the fluid layer, too. This is most simply achieved by increasing the voltage across the transducer, although this generates excessive heating of the system and thus a cooling system is required.

Table 6.3: Properties of particle separator layers.

Layer	Thickness (μm)	Density (kg/m^3)	Speed of sound (m/s)	Quality factor
Glue	50	2000	2440	25
Steel	1500	7800	5800	500
Water	135	1000	1500	100
Glass	Various	2400	5600	350

The half-wavelength mode in the reflector layer places a pressure node near the reflector/fluid boundary. Particles in the fluid layer will then be drawn towards that node and the reflector surface, thus making it possible to capture particles on the surface. This is useful for sensing applications and environmental monitoring where the sensitivity of a particle or spore sensor can be improved by maximising the number of particles of interest which meet the sensing element. The device is tested with both flow-through and no-flow conditions.

The reflector surface is treated prior to an experiment and is coated with an antibody. During operation of the device spores which move towards the surface then adhere and become captured (referred to as immunocapture). After rinsing, a fluorescent stain is introduced to mark the captured spores. The glass slide (reflector) is then removed from the device and particle capture is then measured under a microscope by counting the number of particles from several sample regions which have adhered to the surface. The spores used in the experiment are *Bacillus globigii* (as a safe alternative to *Bacillus anthracis*), although the data presented in this section are taken from experiments using 1μm fluorescent latex particles. These particles are considered to simulate the behaviour of spores accurately. For the various biological treatments involved in the preparation of the glass surface and spores used please refer to Martin et al. [119].

Device simulation

One of the objectives of the experimental work was to investigate the relationship between the reflector layer thickness and the number of particles captured on the reflector surface. Simulation aims to help explain the observations in terms of the acoustic pressure profile within the fluid layer and its location relative to both the reflector surface and fluid flow profile, as flow-through operation is also considered.

There is a principal difference between the simulation work carried out for the micro-engineered

separator and quarter-wave device. For the separator, the voltage across the transducer was used as an input to the simulation. This then resulted in a predicted pressure profile and amplitude, and therefore radiation force. However, experimental work on the quarter-wave device is used to measure the pressure amplitude within the fluid layer which is then used in the simulation, ensuring that the radiation forces are modelled with reasonable accuracy.

The measurement of pressure amplitude was carried out by those involved in the experimental procedures at Cardiff University. This measurement is typically achieved by observing the levitation of a particle of known mass over a range of voltage settings. The particle will move to a position where gravity and radiation forces balance, therefore, by reducing input voltage the radiation force reduces until the particle is located at the position of maximum radiation force ($\lambda/8$ from the pressure node) and will then fall out of suspension just below a threshold voltage. At this voltage the magnitude of radiation force F_{ac}^{0} is equal to the gravitational force acting on the particle and therefore the acoustic pressure amplitude P_0 can be determined and related to voltage. As the reflector layer thickness is of interest, the pressure amplitude was measured for several reflector thicknesses involved in experimental work and at a set voltage and frequency of 2.82MHz. This data is interpolated providing an estimate of pressure amplitude for a greater range of reflector thicknesses. For reflector dimensions ranging from 0.96mm to 1.05mm thick, the pressure amplitude varies and reaches a maximum for a reflector thickness of 1.01mm. This variation in pressure amplitude is due to the resonant characteristics of the device varying with reflector thickness, therefore it would appear then that the resonant frequency using a 1.01mm reflector is much closer to 2.8MHz than for other reflector thicknesses.

When applying the pressure amplitude data to the simulation, the input parameters are set to a level which predict identical pressure amplitudes. This removes from the simulation its role to predict the resonant frequency and pressure amplitude. However, the model is used to predict the profile of the acoustic field throughout the device, especially within the reflector and fluid layers, and its resulting effect on particle movement and concentration.

6.3.2 Results

Nodal Position

In the investigation, the simulation is first used to determine the relationship between the reflector thickness and acoustic pressure profile. An example of the resulting pressure profile within the

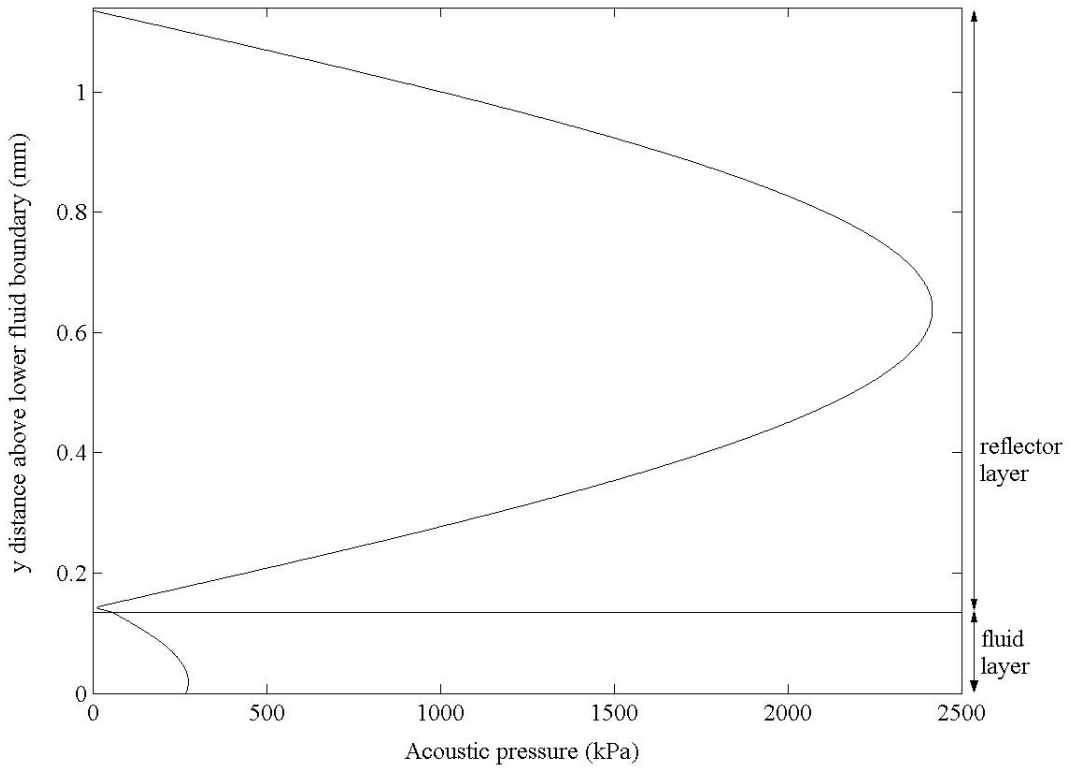

Figure 6.16: Simulated acoustic pressure field within quarter-wave device for 1.00mm thick reflector layer.

fluid and reflector layers is shown in figure 6.16. The pressure profile within the reflector layer indicates the presence of a half-wavelength resonance which is the dominating resonance in the system. As a by-product of this resonance, a node is positioned near the fluid/reflector boundary and, depending on the depth of the fluid, a quarter-wavelength pressure profile is generated in the fluid layer with the anti-node located near the matching layer/fluid boundary ($y = 0$). The pressure amplitude within the fluid layer corresponds to the value measured experimentally.

To investigate the influence of reflector thickness, the pressure profiles based on thicknesses of 0.98, 1.00 and 1.02mm are plotted, the y-axis limits focused on the fluid layer and a small region into the reflector layer. The figure shows that the y position of the pressure node near the reflector surface is strongly influenced by the dimensions of the reflector. With the thinner 0.98mm reflector the node is predicted to exist approximate 30μm within the fluid layer, contrasting with the 1.02mm reflector where the node is positioned 30μm within the reflector layer. By placing the

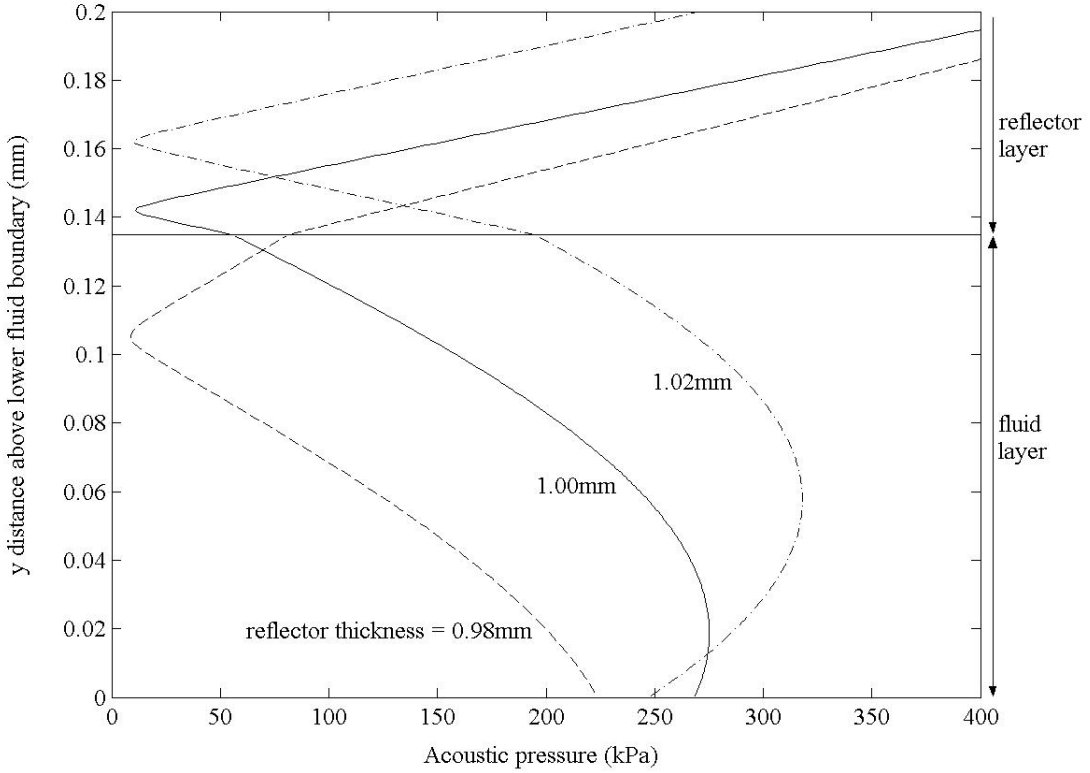

Figure 6.17: Simulated acoustic pressure field for reflector thicknesses of 0.98, 1.00 and 1.02mm.

node within the reflector layer it is expected that particles will move up towards the boundary and become captured, otherwise, if the node is located in the fluid layer particles will not be drawn to the reflector surface and no particle capture would be predicted.

It is also noted that for both the 1.00mm and 1.02mm reflectors an anti-node exists within the fluid layer near the matching layer surface and will result in the movement of a significant number of particles towards the matching layer surface, therefore limiting the maximum number of particles captured on the reflector.

6.3.3 Particle Capture Results

The capture of particles on the reflector layer was measured experimentally at Cardiff University where the influence of reflector thickness on particle capture for a given flow rate and time period was investigated. Figure 6.18 plots the capture results and also shows the predicted particle capture

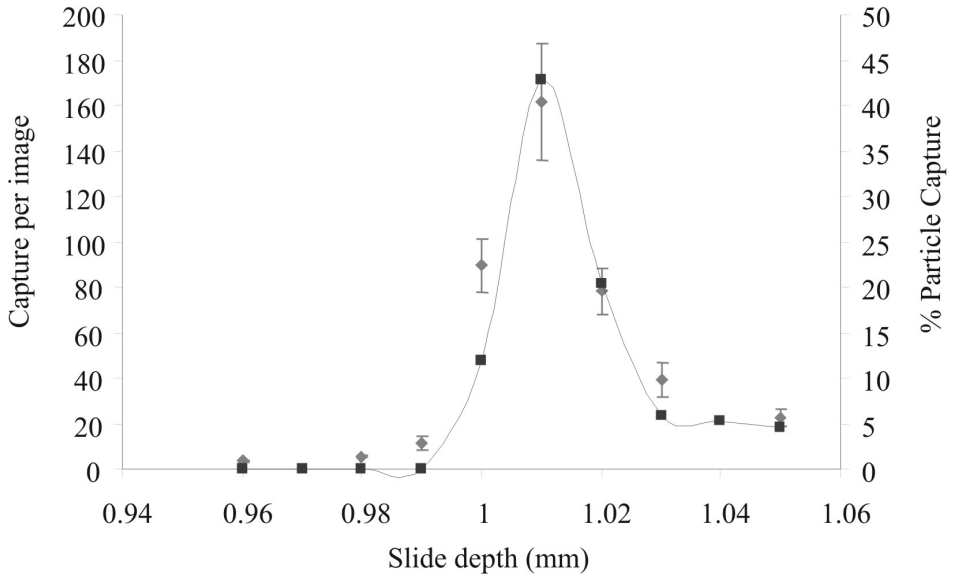

Figure 6.18: Capture of 1μm particles (concentration = 10^7/ml) for glass reflectors of different depths (dark grey points are simulated data, and light grey are experimental data). Each experimental point represents one slide from which fifteen fields of view were counted (P_0 = 460 kPa, assay time = 2 min, Q = 0.2 ml/min). (Figure taken from Martin et al.)

calculated by the particle model and represented as a percentage of particles captured. The two curves are normalised against each other as no correlation has been made between the percentage capture and the particle count measurements. Also, normalising takes into account particles which are only weakly bound to the reflector surface and become dislodged due to fluid flow and rinsing stages, which cannot be predicted by the model.

The experimental and simulated data both display the same trend. At low reflector thicknesses, little or no capture is recorded. However, particle capture rapidly reaches a maximum for a reflector of 1.01mm, presumably as the pressure node moves into the reflector layer. For increasing thickness up to 1.05mm the capture results then reduce again although do not reduce to zero.

The influence of flow rate was also investigated, based on a reflector thickness of 1.01mm and over a period of 2 minutes for each experiment. The percentage capture data produced by the simulation (figure 6.19(b)) are converted to absolute particle capture values by multiplication with the product of flow rate, time and inlet concentration. The results are shown in figure 6.19(a) showing both the experimental and simulated results, and again the data is normalised.

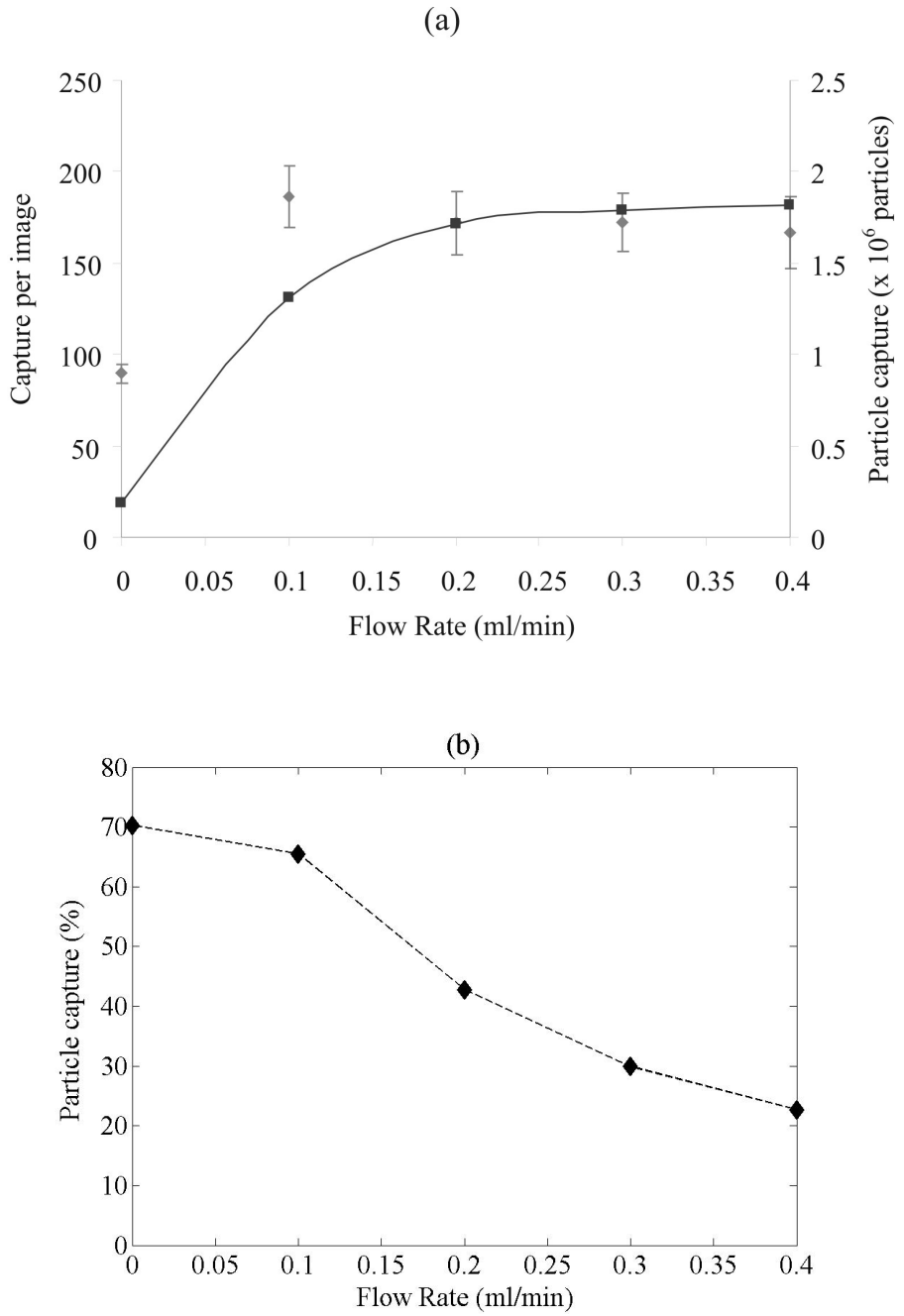

Figure 6.19: Particle capture as a function of flow rate (a) capture per image for 1μm particles (concentration = 10^7/ml) at the reflector surface, f = 2.82 MHz, P_0 = 460 kPa, assay time = 2 min, and a slide thickness of 1.01 mm (simulated data - dark grey points, experimental data - light grey points). The continuous trend is the numerical simulation of capture where maximum capture in millions of cells reaching the reflector is normalised to the highest experimental value of capture per image. Each experimental data point is the mean, $\pm$ standard error of the mean of five replicates (fifteen images per replicate). (Figure taken from Martin et al.) and (b) predicted percentage of particle capture corresponding to predicted data plotted in (a).

The data in figure 6.19(a) indicates that as flow rate increases, the capture increases then levels out. At zero flow the proportion of particles captured is high, but the total number of particles is limited as the fluid is not replenished. As flow rate increases from zero to 0.1ml/min a greater number of particles pass through the fluid chamber, so whilst a high proportion of particles are still being captured, it can be seen that the total capture increases. However, as the flow rate increases beyond 0.1ml/min the proportion of particles captured reduces (figure 6.19(b)), but is compensated by the increase in the number of particles passing through the device and so the total capture reaches a steady value.

6.3.4 Discussion

The influence of the reflector layer thickness on particle capture is consistent with the pressure profile and nodal positions predicted by the model in figure 6.17. The experimental and predicted data together support the notion that capture is expected only when the node is located in the reflector layer, causing particles to move towards this node and up against the reflector surface. Lateral acoustic radiation forces and the formation of particle clumps was only observed when using acoustic pressure values > 500kPa, above that used in the experiments discussed here, or once particles had reached the reflector layer, suggesting that the axial field dominates. Therefore, the 1-d pressure profiles predicted by the model and based on measured pressure amplitudes represent with reasonable accuracy the actual field within the fluid and reflector layers.

The trend in figure 6.18 is also predicted well, although the absolute capture depends on the ability of a particle to adhere to the surface which cannot be predicted by the model, hence the normalisation of the data. This trend demonstrates that an optimum condition exists for capture and depends on the node position, but also on the position of maximum force from the node in relation to the fluid flow profile. Optimum capture has been recorded where the maximum radiation force is found near the surface and in the region of low fluid velocity where particles have a high residence time. For thicker reflector layers, the radiation force near the surface reduces as the $\lambda/8$ section of the field is located within the reflector layer. In general, this work demonstrates the distinct advantage of the particle model in predicting the combined influence of the acoustic and fluid flow fields on particle movement.

The experimental results do record a small level of capture for a reflector of 0.99mm thickness and, although the nodal plane is likely to be positioned within the fluid layer, the increase in concentration at the node makes capture of a particle on the surface more likely, and would be aided

by streaming, for example. This is related to the apparently dispersed particle stream discussed for the separator investigation.

The other experiment investigating the influence of flow rate on particle capture demonstrates that replenishment of the particle suspension does improve particle capture and compensates for the reduced percentage capture seen at higher flow rates. It is anticipated that presence of flow will significantly influence the adhesion of particles to the surface, therefore it is expected that an additional reduction in capture should be observed with the presence of flow and increase at higher flow rates. If the predicted data were normalised against the zero flow capture, it would be seen that the measured capture would be significantly lower than predicted with the presence of flow and with the difference increasing slightly with increased flow rate, supporting the idea that poor adhesion will influence capture.

6.4 Conclusions

This chapter investigates the performance of two different resonators and uses the simulation work of previous chapters to explain observations and trends in measured parameters. The separation performance of the particle separator developed at the University of Southampton and investigated in other chapters is measured, recorded in terms of outlet concentration relative to inlet concentration. Also, experimental particle capture data taken from the quarter-wavelength resonator of Cardiff University is used in conjunction with predicted capture data. The respective predictions of concentration and capture data are made using the particle model developed in chapter 5, with the computational investigations of chapters 3 and 4 providing valuable insight into multi-dimensional nature of the fluid flow and acoustic fields.

Simulation of the separator device relies on accurate descriptions of both the fluid flow and acoustic fields which are both described in 1-d in the particle model. The acoustic field is predicted using the acoustic impedance transfer model which estimates the nature of acoustic field throughout the device based on transducer operating conditions. Comparing the measured and predicted electrical impedance shows that the model predicts the resonance modes, although a small error in frequency may be present and will influence the location of the pressure node. The concentration results predicted by the particle model compared against the measured concentration demonstrate more accurate predictions of concentration and trends at lower transducer voltage levels and, therefore that the fluid drag and radiation forces dominate and dictate the movement

of particles. Lift forces may also have some small influence. Other forces and phenomena significantly influence the movement of particles at higher voltages, most notably due to streaming which has a strong influence on the 1μm particles used in experiment, but less so for larger particles, and will prevent a concentrated particle stream from forming, instead being slightly dispersed. Also, the characteristics of the flow in the outlet region of the device influence separation at certain flow conditions. The effect is consistent with experimental results, and invalidates the assumption that the flow profile is uniform across the width of the device. The presence of lateral forces and non-uniformity of the acoustic field also explains discrepancy between the predicted and measured outlet concentrations.

The performance of the quarter-wave device is investigated, comparing measured and predicted particle capture. In this system issues related to the nature of the fluid flow field through the outlet are avoided and it is known that the acoustic field is reasonably uniform, thus reducing the number of degrees of freedom and sources of error in the particle model. The capability of the particle model to predict particle movement can therefore be tested and describes successfully the influence of reflector thickness on node position and how this influences particle movement to the capture surface. The successful adhesion of particles upon the surface cannot be predicted and data is normalised to compensate for this. However, the particle model can be used to study trends and to explain observations made in experiment.

This chapter demonstrates how the relative importance of various processes and phenomena upon particle manipulation can be established using a range of simulation tools together with experimental work. By using separate simulations for various aspects of the particle manipulation process being studied, their relative effects can be more easily established and the use of excessive computation time and power is avoided.

Chapter 7

Conclusions

7.1 General

This thesis describes the development and use of a range of simulation techniques to characterise various aspects of ultrasonic particle separation and manipulation devices. Work has been guided by the development of a micro-engineered particle separator device, although simulations of a related quarter-wavelength device have also been presented and validated.

A range of ultrasonic devices has been investigated in the literature, aiming to manipulate particles in order to alter particle or cell concentration, enable particle retention or fractionation and generally enhance the processing of fluid samples whilst avoiding further invasive stages. Micro-engineering techniques have also been applied to some of these devices and this is an important progression which extends the applications of particle manipulation devices, particularly for miniaturised fluid analysis systems (or μTAS). Characterisation of micro-engineered devices (potential components of a more complex system) is therefore an important issue and has been undertaken here with an ultrasonic particle manipulator.

A range of modelling approaches has been presented in this thesis, used to characterise the separator device. More detailed particle simulation is based on 1-d descriptions of the fluid and acoustic fields, and can be used to predict the performance of the separator device and similar systems without resorting to highly expensive computational techniques. However, very specific aspects have been simulated using computational packages and this has tested the assumptions of the 1-d model with regard to the uniformity of the acoustic and fluid flow fields. These more computationally expensive techniques have demonstrated the source of various phenomena and, together

with the particle simulation, help interpret separation results.

7.2 Fluid Modelling

Investigations of the fluid flow through the separator device using CFD simulations have revealed regions of the device where the fluid flow cannot be described by classical analytical velocity profiles. Eddy regions (flow separation) exist near geometric features and are associated with regions where particles may become lodged, form aggregates or adhere to the wall. These eddy regions have been simulated and observed experimentally with the CFD model providing a good estimate of the size of these eddies, supporting the use of further simulation work.

CFD simulations have then be used to investigate the flow through alternative duct geometries, and a significant improvement in the flow field can be achieved by producing parallel sided ducts, even though geometry is limited by anisotropic etch fabrication producing angular geometric features. In addition, modification of the geometry is predicted to reduce the pressure drop across the ducts, which may be of advantage when considering low power pumping through more complex analysis systems involving the integration of several processing devices.

Simulation of the flow within the outlet region of the separator device in 3-d has shown that flow patterns are non-uniform across the width of the device and associated with the outlet duct geometries. The characteristics of the flow influence the extraction of the particle stream and significantly influence the separation process which is demonstrated during separation tests.

7.3 Acoustic Modelling

Acoustic simulation work has demonstrated a potential source of lateral variations in the acoustic field. Although axial resonance dominates, significant lateral modes are predicted to exist within the fluid layer at operating frequencies which would cause lateral movement of particles. These lateral modes provide a convincing explanation for the occurrence of striations and the presence of lateral forces within test devices.

At high concentrations and depending on the particles used, lateral forces enhance agglomeration and therefore sedimentation of the suspended particles, seriously affecting the intended particle manipulation process. A brief study has shown that simple geometric and material modifications

influence these lateral modes and provide a means to suppress (or promote) these modes, FEA being a useful tool to test these ideas.

7.4 Particle Modelling

A particle force model has been developed which uses drag force, buoyancy forces and the acoustic radiation force acting on particles, predicted numerically over a range of frequencies, to determine their trajectories through the ultrasonic separator. Particle simulation assumes uniform acoustic and fluid flow patterns in the lateral directions, but despite these simplifications provides a good indication about the deflection of particles and trends observed.

Methods to predict spatial concentration within the device have been investigated and, by modelling the particles as a continuum, a rapid yet detailed solution results. The more common finite difference schemes used to solve the continuum equations are prone to instability when applied to steady state, spatial problems. However, a *hybrid* scheme was adopted which takes particle movement into account and resolves these instability problems successfully. Outlet concentration or wall concentration may be calculated a number of ways, either using particle trajectories or spatial concentration data, and is used to predict performance of the separator.

This model has also been able to predict the effect of moving the acoustic pressure node, to which particles typically move, relative to the fluid channel walls and laminar flow profile. This is important when designing for particle capture (quarter-wavelength devices) where it has been shown that movement of the node due to modification of the reflector layer thickness significantly influences the performance of the device. The model is successful at predicting the optimum reflector thickness and the combined influence of acoustic and fluid flow profiles.

Discrepancies between experimental and modelled separation performance can be discussed in terms of the various phenomena predicted by the more complex 2-d acoustic and fluid flow simulations, demonstrating the combined use of the modelling approaches. Comparison between performance data also highlights other phenomena, not simulated in detail within this thesis, which significantly influence particle manipulation processes. Such effects include streaming flows which influence the movement of micron and sub-micron particles, and it has been demonstrated that such effects warrant more investigation.

In summary, a combination of acoustic, fluid and particle simulation techniques have been used to characterise the various mechanisms which control particle manipulation within ultrasonic devices. These simulations have been used to successfully design and examine aspects of the separator device and experimental work has contributed to the validation of the simulated results. Particle separation has been investigated experimentally showing that separation of particles is occurring, with simulated results comparing well. By considering all the simulation work which has been undertaken, together with experimental separation results, the importance of various phenomena which influence particle movement is revealed. The simulation work contained in this thesis is also applied to a quarter-wave particle concentrator and demonstrates the potential application of these modelling techniques to the development of other ultrasonic particle manipulation devices.

Chapter 8

Future Work

8.1 Development of Models

The undertaking of research inevitably generates more questions. For instance, simulation work within this thesis has identified important features of the fluid flow and acoustic fields which warrant further investigation. This is expanded below:

Fluid flow field: Thorough 2-d studies of the microchannel geometry within the ultrasonic device revealed several eddy regions including eddies within the outlet ducts. The surrounding fluid network would ultimately need to be considered for commercial development of particle manipulation devices (and other microfluidic technologies) and similar flow and geometric studies may reveal similar flow phenomena. It may be necessary to eliminate potential eddy regions and sites where particles and debris may collect in such a fluid network. Before extending the use of the 2-d simulations, it would be sensible to validate the simulations used to predict eddy length by simulating test cases for which established numerical and empirical data exist.

It was shown experimentally that the size of the eddy downstream of the inlet duct varies significantly across the width of the duct due to the flow conditions created by the inlet channel within the aluminium manifold. 3-dimensional CFD studies of the manifold channel leading to the anisotropically etched inlet duct may predict the influence that the manifold geometry has on the fluid flow within the separator. Similarly, the pulsing flow caused by peristaltic pumps, often used where low flow rates are required, can also influence the size of eddies. Transient simulations may help us to understand the effect of these pulsing flows.

3-dimensional simulations of the fluid flow have indicated that the outlet geometry has a significant influence on the flow field, and regions of fluid destined for each outlet, which in turn can have a negative impact on the separation performance. These simulations were not intended to accurately quantify the fluid velocity, for which a finer mesh (and more computation time) would have been required. More refined simulation would be valuable for the redesign of the outlet geometry or, using the current geometry, to thoroughly characterise the flow pattern and improve the accuracy of the particle model, used to predict separation performance.

Acoustic field: Simulation of the acoustic field has so far indicated the significance of enclosure modes giving rise to lateral radiation forces. Lateral forces may be generated by other means, namely near-field effects and structural modes. More extensive FEA simulation and experimental work can be used to determine the significance of these effects, and also be used at the design stage to control the strength of lateral forces. Such work would be applicable to many types of ultrasonic particle manipulator devices; for example, particle trapping devices would benefit from high lateral forces which could be designed into the system.

8.2 Other Phenomena Affecting Device Performance

Chapter 6 compared experimental with predicted separation performance data with many discrepancies explained by the fluid and acoustic simulation work. However, other effects also became apparent, but have not been extensively investigated in this thesis. These other processes demand further investigation:

Streaming: Streaming appears to be an important effect, causing disturbance to the particle stream and being harmful to the separation performance. Ultrasonic manipulation techniques have potential applications for cells and spores down to 1μm in diameter, but it is at these sizes that streaming has a significant influence. The characterisation of streaming flows in high aspect-ratio channels will contribute to the effective control of streaming and, therefore, increase the feasibility of devices designed to manipulate 1μm particles.

Particle agglomerates: At the low particle concentrations considered in this thesis it has been assumed that the presence of particles have a negligible effect upon the fluid and acoustic characteristics. However, the combined action of axial, lateral and inter-particle (secondary)

radiation forces may serve to increase the concentration of particle agglomerates to a value which does have an influence on the fluid and acoustic field. Any changes in the fluid or acoustic field may be deleterious to the operation of the device.

Other particle forces should be investigated, such as the action of Brownian motion which may influence particle capture on a surface. Conversely, van der Waals forces may serve to hold particle agglomerates together and cause particles to adhere to walls within a device. This also relates to the cleaning of microfluidic devices and the ability to successfully remove particles from a system.

Appendices

Journal Publications

1. N.R. Harris, M. Hill, Y. Shen, R.J. Townsend, S. Beeby and N.M. White. A dual frequency, ultrasonic, micro-engineered particle manipulator. *Ultrasonics,* Proceedings of Ultrasonics International 2003 - Edited by P.A. Lewin, W. Sachse. 42(1-9), pp 139-144, 2004.
2. R.J. Townsend, M. Hill, N.R. Harris and N.M. White. Modelling of particle paths passing through an ultrasonic standing wave. *Ultrasonics,* Proceedings of Ultrasonics International 2003 - Edited by P.A. Lewin, W. Sachse. 42(1-9), pp 319-324, 2004.
3. M. Hill, R.J. Townsend, N.R. Harris and N.M. White. Microfabricated acoustic resonators for manipulating particles within a fluid. *Proceedings of the Institute of Acoustics,* 26(2), pp 442-451, 2004.
4. R.J. Townsend, M. Hill, N.R. Harris, N.M. White, S.P. Beeby and R.J.K. Wood. Fluid modelling of microfluidic separator channels. *Sensors and Actuators B: Chemical,* 111-112, pp 455-462, 2005.
5. N.R. Harris, M. Hill, R. Townsend, N.M. White and S.P. Beeby. Performance of a micro-engineered ultrasonic particle manipulator. *Sensors and Actuators B: Chemical,* 111-112, pp 481-486, 2005
6. S.P. Martin, R.J. Townsend, L.A. Kuznetsova, K.A.J. Borthwick, M. Hill, M.B. McDonnell and W.T. Coakley. Spore and micro-particle capture on an immunosensor surface in an ultrasound standing wave system. *Biosensors and Bioelectronics,* 21(5), pp 758-767, 2005.

Conference Publications

1. M. Hill, N.R. Harris, R.J. Townsend, N.M. White and S.P. Beeby. A Microfabricated ultrasonic particle manipulator with frequency selectable nodal planes. Presented at *World Congress on Ultrasonics 2003,* Paris, September 7-10, 2003.
2. R.J. Townsend, M. Hill, N.R. Harris, N.M. White and S.P. Beeby. Numerical Modelling of a microfluidic ultrasonic particle separator. Presented at *Nanotech 2005,* Anaheim, CA, USA. May 2005.
3. R.J. Townsend, M. Hill, N.R. Harris, N.M. White. Investigation of 2-d acoustic resonant modes in a particle separator. Presented at *WCU/UI 2005,* Beijing. August 2005
4. M. Hill, R.J. Townsend, N.R. Harris, N.M. White, S.P. Beeby, M.B. McDonnell. Particle Concentration using a microfabricated ultrasonic resonator. Presented at *WCU/UI 2005,* Beijing. August 2005
5. M. Hill, N.R. Harris, R.J. Townsend, N.M. White, S.P. Beeby, and J. Ding. An ultrasonic MEMS particle separator with thick film piezoelectric actuation. Presented at *2005 IEEE International Ultrasonics Symposium,* Rotterdam. September 2005
6. N.R. Harris, M. Hill, R. Torah, R. Townsend, S. Beeby, N.M. White, J. Ding. A multilayer thick-film PZT actuator for MEMs applications. Presented at *Eurosensors 2005,* Barcelona. September 2005

Available online at www.sciencedirect.com
SCIENCE DIRECT®
Ultrasonics 42 (2004) 139–144
Ultrasonics
www.elsevier.com/locate/ultras

A dual frequency, ultrasonic, microengineered particle manipulator

N. Harris [a,*], M. Hill [b], Y. Shen [b], R.J. Townsend [b], S. Beeby [a], N. White [a]

[a] ECS, Southampton University, Highfield, Mountbatten 3007, Southampton SO17 1BJ, UK
[b] SES, Southampton University, Southampton SO17 1BJ, UK

Abstract

Ultrasonic standing waves can be used to generate forces on particles within a fluid. Recent work has concentrated on developing devices that manipulate the particles so that they are concentrated near the centre of the cavity. It is also possible to design a device that concentrates the particles at the wall of a cavity. This paper describes a device that has the capability of operating in several modes to allow concentration of particles at either the cavity wall or the centre of the cavity, depending on the driving frequency.

Keywords: Ultrasonics; Microfluidics; Particle manipulation

1. Introduction

High frequency acoustic standing waves can be used to separate materials with different acoustic characteristics. The technique can be used to agglomerate particles, to hold particles within a flow, or to manipulate particles with the flow [1].

This paper describes the modelling of such a device and shows how the model has been used to design a chamber that works efficiently at a number of different modal frequencies allowing particles to be concentrated at different points across the cavity depth, depending on the driving frequency.

2. Modelling and construction of the device

The system can be modelled as a multilayered resonant structure as described by Hill et al. [2,3]. The modelling approach has been used successfully in the design of a fluid clarifier (a device which allows a sample of particle-free fluid to be extracted from a flow), shown schematically in Fig. 1. A PZT transducer is attached to a silicon carrier layer in which inlet and outlet ports are etched. The silicon is anodically bonded to a Pyrex wafer into which a fluid filled cavity is etched. This clarifier operates in a half-wave mode, in which the cavity depth is half the acoustic wavelength at resonance, creating a pressure node at which particles gather in the centre of the cavity. The dimensions of the structure were chosen so that the device operated efficiently at a frequency of about 2.4 MHz, with a cavity depth of the order of 240 μm.

The device described in this paper extends this concept, as it allows particles to be positioned at different planes within the cavity, depending on the driving frequency. The device is fabricated in silicon and pyrex, and as such is able to exploit standard silicon processes. In addition, the pyrex allows the cavity itself to be viewed. Driving is achieved via a bonded PZT plate.

The motivation for the work came from two sources:

- experimental observations from Hawkes et al. [4] that for certain combinations of layer geometries, particles can be forced up against the reflector layer, implying a pressure minimum within the fluid lies at the solid boundary—a quarter-wave mode,
- a theoretical prediction [5] that for particular combinations of chamber and reflector layer depths, both half-wave and quarter-wave modes can exist.

The feature of the quarter-wave device mode that is of significant interest is the ability to drive particles to the pyrex boundary. This mode has application in biosensors, where it may be possible to improve the sensitivity of such sensors by concentrating the active element on the sense element. The half wave cavity mode

* Corresponding author. Tel.: +44-2380-593274; fax: +44-2380-592901.
E-mail address: nrh@ecs.soton.ac.uk (N. Harris).

0041-624X/$ - see front matter © 2004 Elsevier B.V. All rights reserved.
doi:10.1016/j.ultras.2004.01.056

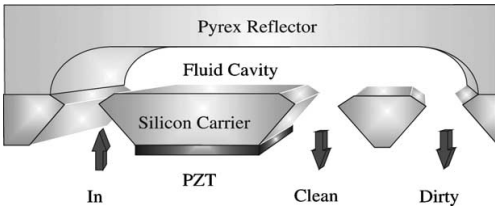

Fig. 1. Cross section of fluid clarifier.

has application in particle separators, and is the mode that can be generated most efficiently.

Theoretical predictions based on the cavity and reflector alone predict that an efficient quarter-wave mode will exist in the cavity if a frequency exists for which the cavity depth is a quarter wavelength and the reflector depth is a half wavelength. This is described in Eq. (1), where c_r, c_f are the sound velocities in the reflector and fluid layers respectively and t_r, t_f are the thicknesses of the reflector and fluid layers. The total thickness of the combined fluid and reflector layer is specified as 1.7 mm, as this is a stock pyrex wafer size.

$$\frac{c_r}{f} = 2t_r, \quad \frac{c_f}{f} = 4t_f \quad \text{and} \quad t_f + t_r = 1.7 \times 10^{-3}\ \text{m} \qquad (1)$$

By substituting $c_r = 5430\ \text{m s}^{-1}$ and $c_f = 1500\ \text{m s}^{-1}$, eliminating f and then solving for the thickness of the fluid layer, it can be shown that the cavity should have a depth of 206 μm.

Hence a quarter wave mode should exist for a cavity depth of about 200 μm with a frequency near 1.8 MHz. This cavity/reflector combination should also produce a half-wave resonance near 3.6 MHz. Simulations were carried out over a range cavity etch depths and Fig. 2 shows the energy density within the fluid layer as a function of frequency and cavity depth.

The expected "quarter wave" mode is the very narrow peak labelled "mode 1" at about 1.8 MHz. However there are two modes (modes 3 and 4), one on each side of the expected "half wave" mode. In addition, there is a mode (mode 2) a little above 2 MHz. The nature of the modes can be explored in more depth if the pressure profiles of these modes are plotted as in Fig. 3. It can be seen that, as expected, mode 1 is approximately a quarter wavelength with a pressure maximum at the silicon boundary and a pressure minimum at or near the reflector boundary. Mode 2 is also a "quarter wave" mode, but in this case the pressure minimum is at, or near, the silicon boundary. Modes 3 and 4 are similar and both are close to a half wavelength with a pressure node near to the centre of the cavity.

As the main aim of this investigation was to demonstrate a device in which particles could be moved either to the centre or a boundary of the cavity, a cavity depth of 175 μm was chosen so that both "quarter wave" modes were predicted to have their pressure minimum at, rather than simply near, the boundaries.

The fabrication technique to be used involves etching the cavity out of a Pyrex plate. The silicon wafer has a thickness of 525 μm.

The device was constructed in a similar manner to the half wave concentrator [6] with the exception that the cavity depth was etched to 175 μm rather than the previous 250 μm. Inlet and outlet ports were etched in the silicon using a standard KOH wet etch. The bulk PZT transducer drive element was bonded onto the silicon using standard Araldite epoxy resin.

In order to allow fluid into and out of the device, a manifold was constructed from aluminium as shown in Fig. 4. The device was held on the top of the manifold with four small screw-on clamps, and the manifold/silicon seal was achieved with a custom silicon O-ring.

3. Verification of the model

In order to verify the model against the fabricated device, an impedance analyser was used. The instrument

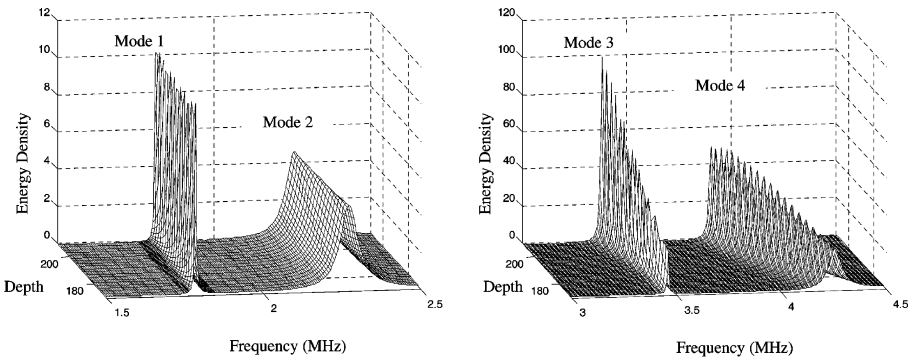

Fig. 2. Energy density (J m^{-3}) in the cavity against depth in microns and frequency in MHz. Note different z-axis scales for the two frequency ranges.

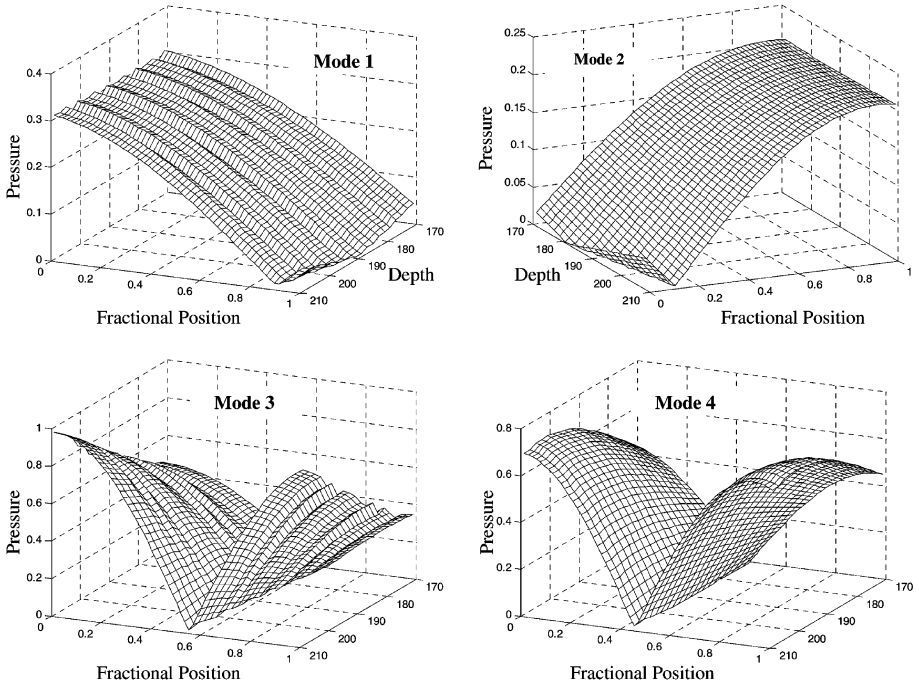

Fig. 3. Modelled pressure distributions across the cavity (fractional distance from the silicon layer) for four cavity modes shown in Fig. 2, plotted against cavity depth in microns.

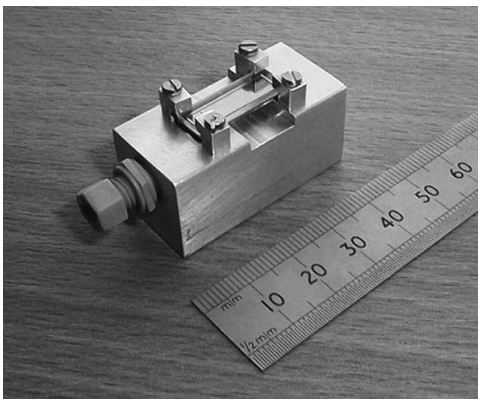

Fig. 4. The micromachined resonator on the aluminium manifold.

used was a Hewlett Packard 4192A frequency analyser, under PC control. Measurements were taken at an excitation voltage of 1 V. The model predictions for impedance are shown in Figs. 5 and 6, together with the corresponding measured results. Fig. 5 shows the results for the chamber filled with air, and Fig. 6 shows the results for the chamber filled with fluid.

In Fig. 5, the dotted line shows the modelled response of effectively the PZT drive element coupled via a glue layer to the silicon layer. As the cavity is filled with air, this is effectively the limit of the model and so no cavity response is expected. Two resonances are expected in this configuration, one at 2.3 MHz and a smaller one at 4.7 MHz. The solid line shows the measured impedance curve. As can be seen there is a large peak at 2.6 MHz and a smaller peak at 4.7 MHz. There are some other artefacts present in the lower frequencies, but the origin of these is unclear at present.

Fig. 6 shows the corresponding results for the device with the cavity full of water. Although the expected cavity modes at 3.5 and 4.1 MHz are clearly visible, those at 1.8 and 2.2 MHz are masked by the transducer/carrier layer resonance and other artefacts.

However, in practical terms, the modes are most easily identified by measuring the voltage drop across the transducer, and so a voltage trace was also taken, using a HP spectrum analyser and is shown in Fig. 7. The right hand axis corresponds to the measured voltage (solid line). The difference in scale is due to the different drive amplitudes in the two cases. Again it is easy to identify the higher frequency modes, but the lower frequency modes are more difficult to spot. It is believed

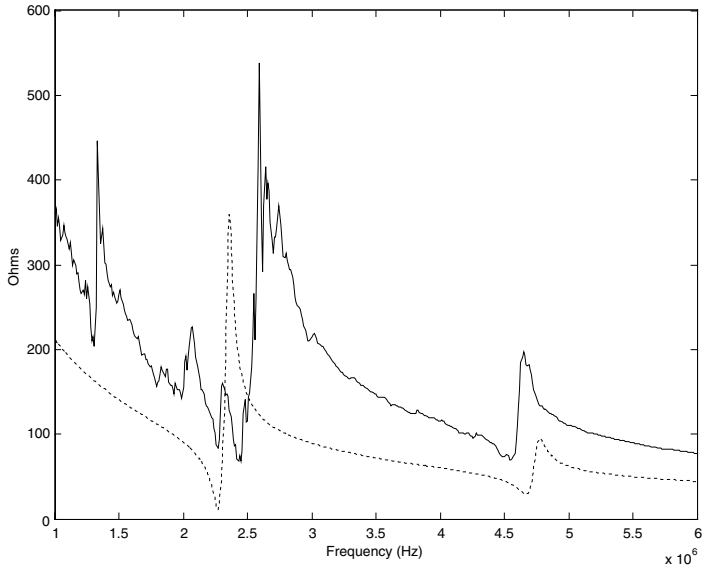

Fig. 5. Modelled (dotted) and measured (solid) impedance plots for the empty device.

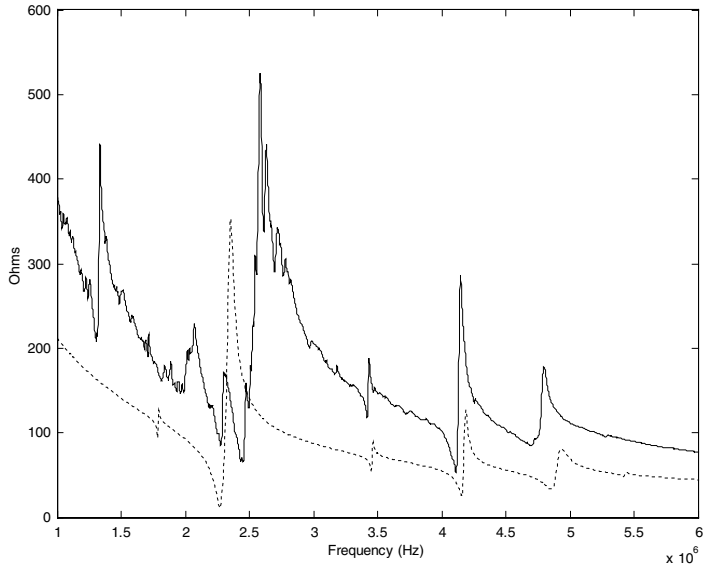

Fig. 6. Modelled (dotted) and measured (solid) impedance plots for the fluid filled device.

that the 2.2 MHz mode is masked by the transducer resonance, but there is some evidence of the 1.8 MHz mode, actually located at 1.714 MHz. Although disappointingly small, this mode proved to be experimentally locatable using an oscilloscope.

4. Experimental results

To verify the operation of the device, an optical microscope was used to measure the position of the particles within the chamber. The principle is that it is

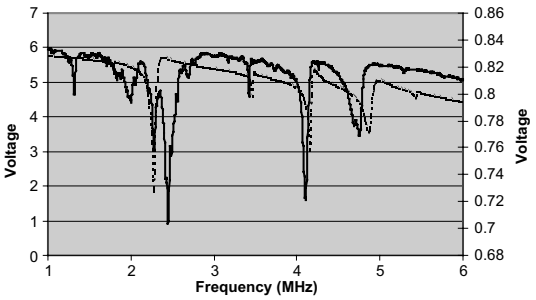

Fig. 7. Modelled (dotted) and measured (solid) voltage plots for the fluid filled device.

possible to focus on particles within a plane if the depth of focus is suitably small. By focussing on the silicon surface, and then the water/Pyrex boundary it is possible to generate a frame of reference.

The device was driven from a Frequency Synthesiser, via a fixed gain RF amplifier (50 dB). The transducer was placed in series with a small resistor (47 Ω) so that the combination acted like a potential divider. This was to allow the variation in voltage across the transducer to be monitored by an oscilloscope to allow voltage nulls to be identified. The frequencies of the expected modes were concentrated on. The chamber was gravity fed with a solution of yeast, and both still pictures and video clips were captured.

The technique of focussing the microscope proved successful, and all four modes could be identified. Modes were identified at 1.71, 2.27, 3.44 and 4.1 MHz, although as expected, mode 1 at 1.712 MHz required extra power to identify. The sequence of images shown in Fig. 8 shows randomly distributed particles being forced to the Pyrex/water boundary against gravity as predicted for mode 1 at 1.712 MHz. Image (a) shows the random distribution of yeast before any power is applied, with the microscope focussed at the Pyrex/water boundary. Image (b) shows the view 5 s after the power is applied, and it can be seen that yeast cells are beginning to move into focus as they are forced against the boundary. Images (c) and (d) show the situations 5 and 10 s on, and many more cells are now in focus. By image

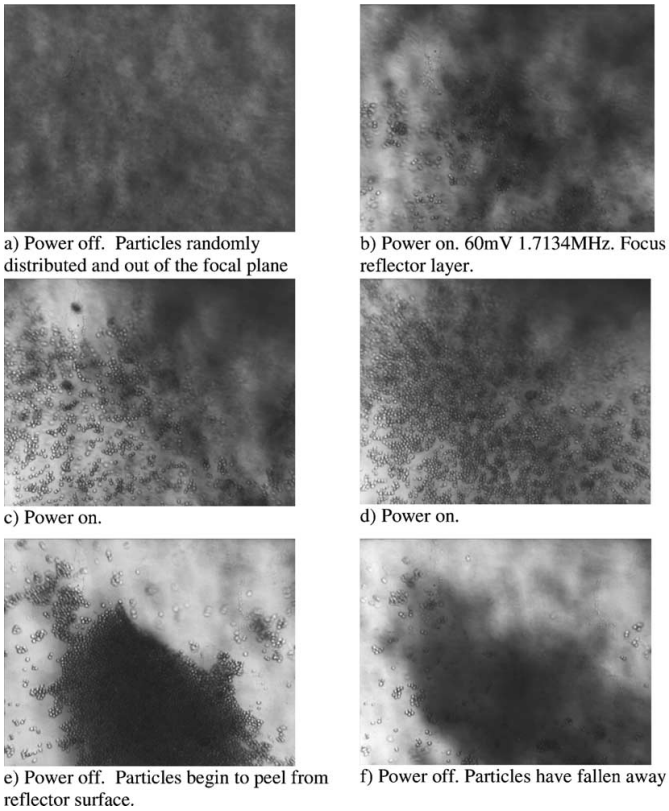

Fig. 8. A sequence of images showing particle movement.

(d) most particles are at the boundary. Particles tend to collect in clumps due to lateral forces, and image (e), taken 20 s later, just after the power has been turned off shows this. Image 6, taken 20 s later, shows the clump of particles peeling away from the Pyrex layer and falling under the influence of gravity towards the silicon layer and thus out of focus.

Similar results were obtained for the other three modes, showing that particles could be forced to either of the cavity boundaries or to the cavity centre.

5. Conclusions

In conclusion, an exercise which aimed to demonstrate a dual mode microfluidic ultrasonic particle manipulator has resulted in the design, fabrication and testing of a device which works at four modes within the frequency range of interest. Although the impedance and voltage responses of the quarter wave modes were less pronounced than expected, it still proved possible to identify these responses experimentally and indeed use them to manipulate yeast particles in the desired manner. The half wave modes were more obvious and also allowed particles to be concentrated in groups within a nodal plane in the centre of the cavity, rather than at a boundary, as in the case of the quarter wave modes.

This work has given very encouraging results and in the future, the model will be used to fine tune the parameters to allow better defined devices to be made.

Acknowledgements

This work has been supported by EPSRC grant number GR/R13333/01, DSTL, and Porvair PLC.

References

[1] M. Gröschl, Ultrasonic separation of suspended particles—Part I: fundamentals, Acustica 84 (1998) 432–447.
[2] M. Hill, R.J.K. Wood, Modelling in the design of a flow-through ultrasonic separator, Ultrasonics 38 (2000) 662–665.
[3] M. Hill, Y. Shen, J.J. Hawkes, Modelling of layered resonators for ultrasonic separation, Ultrasonics 40 (2002) 385–392.
[4] J.J. Hawkes, M. Gröschl, E. Benes, H. Nowotny, W.T. Coakley, Positioning particles within liquids using ultrasound force fields, in: 3rd EAA European Congress on Acoustics, Sevilla, 2002.
[5] M. Hill, The selection of layer thicknesses to control acoustic radiation force profiles in layered resonators, J. Acoust. Soc. Am. 114 (5) (2003) 2654–2661.
[6] N.R. Harris, M. Hill, S.P. Beeby, Y. Shen, N.M. White, J.J. Hawkes, W.T. Coakley, A silicon microfluidic ultrasonic separator, Sensors and Actuators B 95 (2003) 425–434.

Available online at www.sciencedirect.com
SCIENCE DIRECT®
Ultrasonics 42 (2004) 319–324
Ultrasonics
www.elsevier.com/locate/ultras

Modelling of particle paths passing through an ultrasonic standing wave

R.J. Townsend [a], M. Hill [a,*], N.R. Harris [b], N.M. White [b]

[a] School of Engineering Sciences, Electromechanical Research Group, University of Southampton, Southampton SO17 1BJ, UK
[b] Electronics and Computer Science, University of Southampton, Southampton SO17 1BJ, UK

Abstract

Within an ultrasonic standing wave particles experience acoustic radiation forces causing agglomeration at the nodal planes of the wave. The technique can be used to agglomerate, suspend, or manipulate particles within a flow. To control agglomeration rate it is important to balance forces on the particles and, in the case where a fluid/particle mix flows across the applied acoustic field, it is also necessary to optimise fluid flow rate.

To investigate the acoustic and fluid forces in such a system a particle model has been developed, extending an earlier model used to characterise the 1-dimensional field in a layered resonator. In order to simulate fluid drag forces, CFD software has been used to determine the velocity profile of the fluid/particle mix passing through the acoustic device. The profile is then incorporated into a MATLAB model. Based on particle force components, a numerical approach has been used to determine particle paths. Using particle coordinates, both particle concentration across the fluid channel and concentration through multiple outlets are calculated.

Such an approach has been used to analyse the operation of a microfluidic flow-through separator, which uses a half wavelength standing wave across the main channel of the device. This causes particles to converge near the axial plane of the channel, delivering high and low particle concentrated flow through two outlets, respectively. By extending the model to analyse particle separation over a frequency range, it is possible to identify the resonant frequencies of the device and associated separation performance.

This approach will also be used to improve the geometric design of the microengineered fluid channels, where the particle model can determine the limiting fluid flow rate for separation to occur, the value of which is then applied to a CFD model of the device geometry.

Keywords: Radiation force; CFD; Standing waves; Concentration

1. Introduction

Technologies are being studied which exploit acoustic radiation forces on particles within standing waves. Such technologies include particle separation, fractionation and agglomeration, finding applications in areas such as biotechnology [1,2], material processing [3,4] and filter systems.

For particle manipulation techniques, it is important to understand how particle motion is influenced by factors including the acoustic field and fluid motion. By considering the various forces experienced by particles and being able to balance them, it is possible to control their movement and agglomeration rate.

Particle motion can be predicted by considering the principal fluid and acoustic forces, manipulated and solved numerically [5,6] or coded into CFD models [7]. This paper describes a similar approach where particle movement is predicted by summating particle forces and solving the resulting equations numerically. However, the method described aims to include more accurate descriptions of the fluid velocity profile and acoustic radiation force, accounting for the layered nature of ultrasound devices. This approach is generally applicable for ultrasonic devices which exploit acoustic radiation forces, although here an emphasis has been placed on those involving fluid flow through. An ultrasonic separator is used as a specific example, demonstrating the application of the model.

* Corresponding author. Tel.: +44-23-8059-3075; fax: +44-23-8059-3053.
E-mail address: m.hill@soton.ac.uk (M. Hill).

0041-624X/$ - see front matter © 2004 Elsevier B.V. All rights reserved.
doi:10.1016/j.ultras.2004.01.025

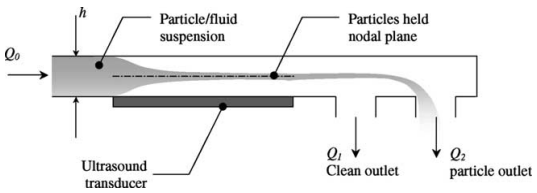

Fig. 1. Schematic of separation device operating in half wavelength mode.

2. Prediction of particle motion and concentration

2.1. Cell parameters

A microfluidic ultrasonic separator is used as an example application in this paper (Fig. 1). At certain frequencies resonance will be induced in the fluid layer. When the transducer is driven at ~3 MHz, a half wavelength mode is excited and a standing wave is produced across the fluid channel, i.e. the height of the fluid microchannel is approximately half the acoustic wavelength, $h = \lambda/2$ As particles of radius R pass through the standing wave they are forced onto the nodal plane and extracted through the second of two outlets with flow rates Q_1 and Q_2, respectively, and where $Q_2 > Q_1$.

In the following text, typical values are applied and include $h = 250$ μm, yeast particle radius $R = 3$ μm and total flow rate $Q_0 = 0.1$ ml/s. Water is used as the working fluid where density $\rho = 1000$ kg/m^3 and dynamic viscosity $\mu = 0.001$ kg/ms.

2.2. Particle forces

To determine the motion of particles through the microchannel and acoustic field, the system of forces on a particle is considered. The dominant forces are discussed:

2.2.1. Acoustic radiation force

Within an acoustic field the time averaged acoustic force on a particle, F_{ac}, in a direction normal to the transducer is given by [8]:

$$\langle F_{ac}(x,y,z)\rangle = -\nabla\langle\phi^{G}(x,y,z)\rangle, \tag{1}$$

with

$$\langle\phi^{G}(x,y,z)\rangle = -V\left[\frac{3(\rho_p-\rho_f)}{2\rho_p+\rho_f}\langle\overline{E}_{kin}\rangle - \left(1-\frac{c_f^2\rho_f}{c_p^2\rho_p}\right)\langle\overline{E}_{pot}\rangle\right], \tag{2}$$

where V is particle volume, ρ_p and ρ_f are the particle and fluid densities, c_p and c_f represent speed of sound for the particle and fluid mediums, $\langle\overline{E}_{kin}\rangle$ and $\langle\overline{E}_{pot}\rangle$ are the time-averaged kinetic and potential energies at a point in the field and ϕ^G is the gradient of radiation force potential.

Using an acoustic impedance transfer model [9,10], the variation in acoustic velocity and pressure through the device can be determined. The acoustic velocity and pressure are then used to derive the kinetic and potential energies, $\overline{E}_{kin}$ and $\overline{E}_{pot}$, respectively, which in turn are used to calculate the variation in F_{ac} across the fluid layer. As the velocity and pressure fields are dependent on acoustic frequency, the radiation force can also be calculated as a function of frequency, therefore its use is not limited to the resonant case.

2.2.2. Fluid drag

For low particle Reynold's number, $Re_p < 0.2$, the drag force F_D on a particle is calculated using Stokes drag, where A is the area of the particle in a plane normal to the flow and the velocity U_0 is the relative velocity between the fluid, $U(x,y)$, and particle, $u(x,y)$:

$$F_D = \frac{1}{2}C_D\rho_f U_0^2 A, \tag{3}$$

where

$$C_D = \frac{24}{Re} \quad \text{and} \quad Re_p = \frac{2R\mu U_0}{\rho_f}.$$

Combining $u(x,y)$ and $U(x,y)$ with Eq. (3) and expressions for C_D and Re_p gives:

$$F_D(x,y) = 6\mu\pi R(U(x,y) - u(x,y)) \tag{4}$$

2.2.3. Buoyancy

The relative densities of the particle and fluid control the buoyancy force on a particle, where F_B is opposite to the gravitational force:

$$F_B = \frac{4}{3}\pi R^3 g(\rho_f - \rho_p). \tag{5}$$

When referenced to the x and y coordinates of the cell, the x and y components of the buoyancy force depend on the orientation of the channel.

2.2.4. Other particle forces

In addition to acoustic radiation and drag forces, particles experience lift [11], van der Waals forces operating in the region of the channel walls [12] and interparticle forces [8]. These forces are generally small compared to the dominant forces already discussed and so, at this stage, have not been included in the modelling reported here.

2.2.5. Summary of forces

The acoustic radiation force F_{ac} operates only in the y direction (ignoring second order effects), whilst drag, F_D and buoyancy F_B can be split into x and y components. They are represented in Fig. 2.

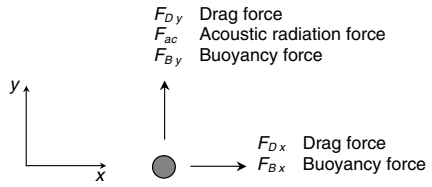

Fig. 2. System of particle forces within fluid suspension and acoustic field.

2.3. Velocity profile through channel

2.3.1. CFD simulations

Accurate characterisation of the laminar flow velocity profile is fundamental to determining the particle drag force, for which a CFD model is used. In order to validate the CFD model a simple case, based on $h = 240$ μm and flow rate $Q_0 = 0.1$ ml/s, has been modelled and compared with classical flow theory.

Due to the low Reynold's number, typically $Re = 20$ using h as the characteristic depth d, the entry length is small (distance before which steady velocity profile develops) and is of the order 0.29 mm, as calculated below:

$$\frac{L_e}{d} \approx 0.06Re. \tag{6}$$

Beyond a distance L_e the flow becomes fully developed, where the fully developed velocity profile U_x between parallel plates is described by a parabolic function [13] and where $\overline{U}$ is the mean fluid velocity:

$$U_x = \frac{6\overline{U}}{h^2}(hy - y^2). \tag{7}$$

The channel has been modelled in CFD software where after a distance equal to L_e flow becomes fully developed. Fig. 3 compares the fully developed velocity profile calculated by theory with that determined by CFD using 12 μm sized elements.

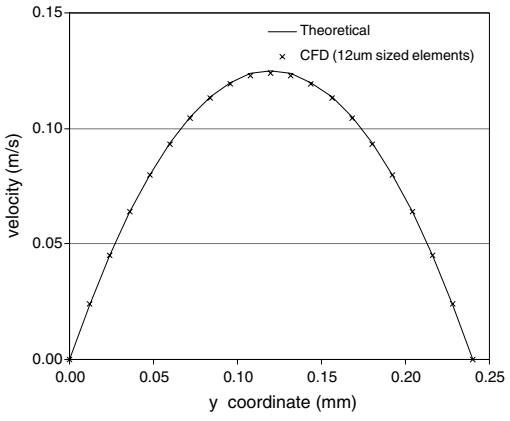

Fig. 3. Theoretical and CFD modelled velocity profile across channel, where $h = 240$ μm and $\overline{U} = 0.083$ m/s ($Q_0 = 0.1$ ml/s).

It can be seen that the CFD derived velocity profile provides a close match with theory, where the element size chosen corresponds to an error <1%. For instances where more complex flow patterns occur within the channel (eddy regions and entry region flow) and which cannot be characterised by classical theory, CFD simulations can be used to describe the velocity field. Once converted into look-up tables, this velocity field data can be integrated into the numerical software model discussed later.

2.3.2. Acoustic streaming

Acoustic streaming occurs when an acoustic wave passes through a fluid medium, where acoustic energy is dissipated into the fluid in the form of momentum and causes steady fluid flow. Of the types of streaming applicable to microchannels, Rayleigh streaming occurs in the fluid bulk producing eddy flows, the size in the order of λ, and also Schlichting streaming, which influences boundary layer flow [14].

Acoustic streaming patterns will influence the velocity profile through the channel. Although not included in the modelling described, the streaming flow field can simply be superimposed onto the laminar flow profile calculated using CFD.

2.4. Numerical solver to determine particle trajectory

To calculate the motion of a particle of mass m, the force terms are summed to give accelerations $\ddot{x}$ and $\ddot{y}$:

$$\ddot{x} = \frac{\sum F_x}{m} = \frac{F_{Dx} + F_{Bx}}{m} \tag{8}$$

$$\ddot{y} = \frac{\sum F_y}{m} = \frac{F_{ac} + F_{Dy} + F_{By}}{m} \tag{9}$$

The option of developing an analytical solution to describe the motion of a particle through a standing wave exists by solving only Eq. (4) and a special case of (1) describing an 'ideal' standing wave, shown below:

$$F_{ac} = 4\pi\langle\bar{\varepsilon}\rangle kR^3\left[\frac{\rho_p + \frac{2}{3}(\rho_p - \rho_f)}{2\rho_p + \rho_f} - \frac{1}{3}\frac{c_f^2\rho_f}{c_p^2\rho_p}\right]\sin(2ky). \tag{10}$$

Additionally, for a near neutrally buoyant particle (e.g. bacteria in water) the buoyancy force tends to zero.

However, when considering resonance within a layered device where the 'ideal' standing wave case is not necessarily applicable, the acoustic force described by Eq. (1) should be used and has been implemented using a numerical approach.

An acoustic description of such a separator device has been modelled numerically by Hill et al. [10] in

MATLAB and uses Eq. (1) to calculate the radiation force. This model has since been developed to include other particle forces and summates these forces as expressed by Eqs. (8) and (9). These equations are then solved using an ODE numerical solver function within MATLAB; this approach ensures that developments to the model, specifically inclusion of other particle forces, can be incorporated easily without requiring potentially complex algebraic manipulation. From the ODE solver, the model provides an output array containing a series of time intervals with associated particle coordinate locations and velocity components. The coordinate locations describe the trajectory of a particle, examples of which are shown in Fig. 4.

The particle trajectories are shown in conjunction with the acoustic radiation force and also illustrate the influence of the laminar flow profile by comparing the particle trajectory with 'plug' flow (uniform fluid velocity). The rate of convergence towards the node is not influenced by the longitudinal flow profile, assuming the effects of lift to be negligible. However, for the parabolic profile the low flow rate at the wall causes the particles to begin converging at a position further upstream as compared to plug flow. This demonstrates the significant influence the flow profile has on the particle trajectory and therefore the implications on design and resulting efficiency of the device.

It can be seen that the acoustic radiation force is not zero at the $y = 0$ channel wall, as would be predicted by Eq. (10), as the method used in the model considers the influence of the layered nature of the device [10]. Further, the nodal plane will not necessarily be located along the centre plane of the channel, but its position can be predicted.

2.5. Particle concentration

By modelling a series of particles at the channel inlet and using the resulting particle coordinates, it is possible to calculate the change in concentration across the channel. The change in concentration is dependent on the change in lateral (x) spacing between each particle. Additionally, the velocity profile influences the concentration; as a stream of particles moves into planes of increased fluid velocity, the longitudinal (y) spacing between particles must increase for particle flow rate to remain constant according to continuity.

Fig. 5 illustrates the convergence of a series of particles towards the nodal plane. At a distance 8.5 mm along the acoustic field the relative concentration of particles across the channel is calculated and plotted.

The asymmetric nature of the acoustic radiation force across the channel is apparent as a small number of particles are forced to the lower wall. This identifies a pressure anti-node which exists within the fluid channel and from which particles are repelled. However, the majority of particles are forced towards the centre of the channel where a peak in particle concentration can be seen.

The concentration through an outlet is calculated by determining particle flow rate between the wall and position at which the flow splits between outlets. Dividing this by the corresponding outlet fluid flow rate results in particle concentration.

2.6. Frequency dependency

As previously discussed, the acoustic radiation force can be modelled as a function of frequency, therefore

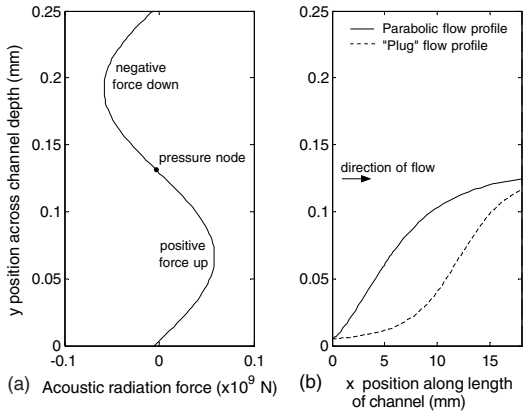

Fig. 4. (a) Acoustic radiation force and (b) trajectory of a particle initially located near channel wall for both parabolic flow and 'plug' flow profiles, where $h = 250$ μm.

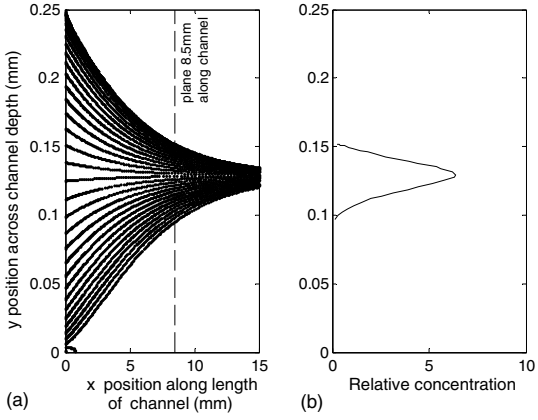

Fig. 5. (a) Convergence of particles towards nodal plane and (b) relative particle concentration across channel at a distance 8.5 mm along channel and acoustic field (relative concentration at inlet = 1) and where $h = 250$ μm.

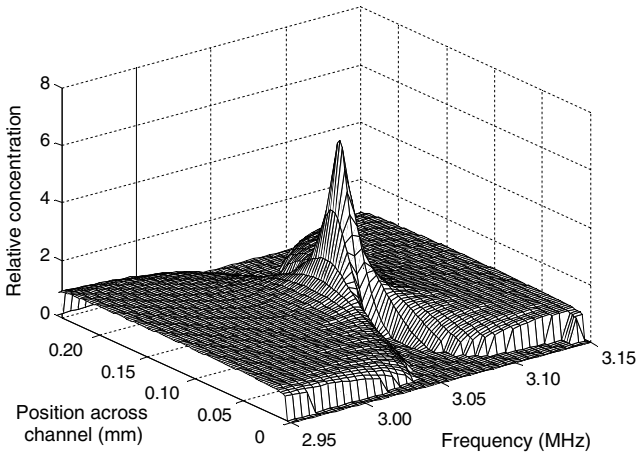

Fig. 6. Concentration across channel as function of frequency taken at a distance 8.5 mm along channel and where $h = 250$ μm.

particle concentration can be plotted against frequency in addition to channel position, y. Fig. 6 shows an example of how the concentration can vary as function of frequency.

The peak seen at a frequency ~3.06 MHz corresponds to a resonant frequency of the device where the radiation force is a maximum. Moving away from this frequency, the radiation force decreases until the particle concentration ceases to change relative to the inlet concentration. Similarly, the relationship between outlet concentration and frequency can be plotted.

2.6.1. Separation test results

A similar device has been tested using the experimental apparatus described by Hawkes and Coakley [6] and concentration through outlet 1 is measured. Fig. 7 shows the concentration measured between frequencies 2.8 and 3 MHz. This is compared to the modelled outlet concentration.

Some discrepancies can be seen where during experiment particles often form into clumps caused by second order acoustic forces [8]. This will influence the measured concentration and is likely to give an inaccurate representation of the true concentration, making the signal appear noisy at higher concentration levels. Any inaccuracy in the measurement of channel depth, h, influences the resonant frequency predicted by the model and will shift the plot along the x-axis. However, the model offers a reasonable prediction of the particle concentration and behavior of particles within the device.

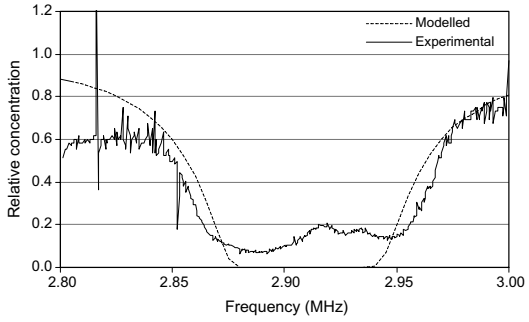

Fig. 7. Concentration through outlet 1 (clean fluid) as a function of frequency, comparing experimental results and modelled performance.

3. Application of model

Generally, the model can be used to predict the influence of various parameters on the agglomeration rate of particles and therefore the influence on separation efficiency or agglomerate concentration, depending on the application of the device. For flow-through applications the model can be used to optimise flow rates and acoustic energy density to maximise the device efficiency, therefore minimising power requirements by the transducer and, for example, avoiding deleterious heating effects.

4. Conclusion

The ability to predict particle concentration levels within an ultrasonic device has been demonstrated, based on a numerical approach to determine particle trajectories. The method has been tested predicting the performance of an ultrasonic separator and can also be used to model macrofluidic as well as microfluidic devices, assuming laminar flow to be applicable. The model can also be adapted to tackle any number of outlets.

It is known that other particle forces and second order acoustic effects, not yet included, influence the motion of particles, but generally these can be incorporated into the model with minimum simplification and manipulation.

Acknowledgements

This work is funded by EPSRC grant GR/R13333/01. The authors gratefully acknowledge the funding and support from Dstl and Porvair Plc. and also Dr. Hawke's assistance with experimental work.

References

[1] W.T. Coakley, J.J. Hawkes, M.A. Sobanski, C.M. Cousins, J. Spengler, Analytical scale ultrasonic standing wave manipulation of cells and microparticles, Ultrasonics 38 (2000) 638–641.
[2] R. Karumanchi, S.N. Doddamane, C. Sampangi, P.W. Todd, Field-assisted extraction of cells, particles and macromolecules, Trends in Biotechnology 20 (2002) 72–78.
[3] Y. Abe, M. Kawaji, T. Watanabe, Study on the bubble motion control by ultrasonic wave, Experimental Thermal and Fluid Science 26 (2002) 817–826.
[4] S. Gupta, D.L. Feke, I. Manaszloczower, Fractionation of mixed particulate solids according to compressibility using ultrasonic standing-wave fields, Chemical Engineering Science 50 (1995) 3275–3284.
[5] D.A. Johnson, D.L. Feke, Methodology for fractionating suspended particles using ultrasonic standing wave and divided flow fields, Separations Technology 5 (1995) 251–258.
[6] J.J. Hawkes, W.T. Coakley, Force field particle filter, combining ultrasound standing waves and laminar flow, Sensors and Actuators B-Chemical 75 (2001) 213–222.
[7] I.L.J. Holwill, The use of ultrasonic standing waves to enhance optical particle sizing equipment, Ultrasonics 38 (2000) 650–653.
[8] M. Gröschl, Ultrasonic separation of suspended particles—Part I: Fundamentals, Acustica 84 (1998) 432–447.
[9] M. Hill, R.J.K. Wood, Modelling in the design of a flow-through ultrasonic separator, Ultrasonics 38 (2000) 662–665.
[10] M. Hill, Y.J. Shen, J.J. Hawkes, Modelling of layered resonators for ultrasonic separation, Ultrasonics 40 (2002) 385–392.
[11] M.T. Lawler, P. Lu, The role of lift in the radial migration of particles in a pipe flow, in: I. Zandi (Ed.), Advances in solid–liquid flow in pipes and its applications, Pergamon Press, New York, 1971, pp. 39–57.
[12] Q. Qi, G.J. Brereton, Mechanisms of removal of micron-sized particles by high-frequency ultrasonic-waves, IEEE Transactions on Ultrasonics Ferroelectrics and Frequency Control 42 (1995) 619–629.
[13] F.M. White, Fluid Mechanics, 4th ed., McGraw-Hill, 1999.
[14] L.K. Zarembo, Acoustic streaming, in: L.D. Rozenburg (Ed.), High Intensity Ultrasonic Fields, Plenum Press, New York, 1971, pp. 137–199.

Proceedings of the Institute of Acoustics

MICROFABRICATED ACOUSTIC RESONATORS FOR MANIPULATING PARTICLES WITHIN A FLUID

Martyn Hill School of Engineering Sciences, University of Southampton, UK
Rosie Townsend School of Engineering Sciences, University of Southampton, UK
Nick Harris School of Electronics and Computer Science, University of Southampton, UK
Neil White School of Electronics and Computer Science, University of Southampton, UK

1 INTRODUCTION

Particles within an acoustic standing wave in a fluid experience forces which tend to move them to the nodal plane of that standing wave. This can be used to agglomerate, filter or fractionate particles[1,2]. An important area for the exploitation of such forces is in microfluidic systems[3] where resonators with critical dimensions of a wavelength or less at ultrasonic frequencies can, in particular, be used to manipulate biological cells[4].

Models of the acoustic energy density and radiation forces within such a resonator predict the ability to move particles to different points within the fluid at different frequencies. This paper describes the use of such models to design multi-layered resonators, and the microfabrication of these resonators from silicon and Pyrex.

It is shown that cells can be moved to planes within the body of the fluid, or to the boundaries of the fluid within a single resonator at different operating frequencies. Experimental results are also presented to demonstrate the ability to use such devices to remove unwanted particles from a microfluidic system and generate a stream of clarified fluid, and these are compared with modelled predictions of separation efficiency.

2 THEORY

2.1 Radiation Forces and Acoustic Modelling

Gor'kov[5], derives the time averaged acoustic radiation force on a spherical particle of radius a, at position x within a one dimensional standing wave as:

$$F(x) = \frac{\partial}{\partial x}\left(\frac{4\pi a^3}{3}\left(\frac{3(\rho_p - \rho_f)}{(2\rho_p + \rho_f)} E_{kin}(x) - \left(1 - \frac{\rho_f c_f^2}{\rho_p c_p^2}\right) E_{pot}(x) \right) \right) \quad (1)$$

where c and ρ are the speed of sound and the mass density of the fluid and the particle, indicated by subscripts f and p respectively. $E_{kin}(x)$ and $E_{pot}(x)$ are the time averaged kinetic and potential energy densities at position x within the fluid. In order to calculate these energy terms, a model of the acoustics of the standing wave field within the fluid is required.

Proceedings of the Institute of Acoustics

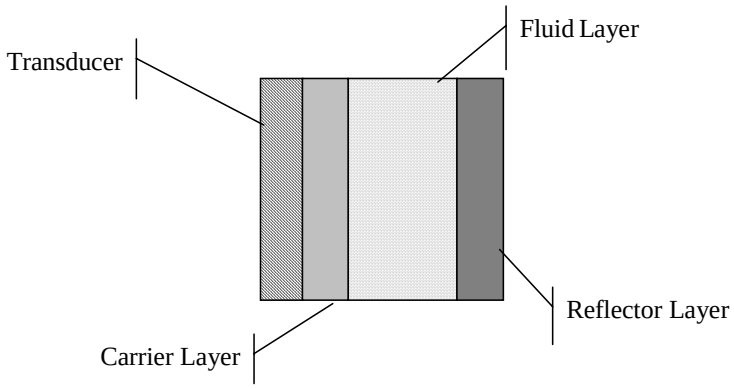

Figure 1. Schematic representation of layered resonator

Figure 1 shows the structure typical of a layered resonator used for manipulating particles within an ultrasonic standing wave in the fluid layer. It is important to model the full device as the boundaries are not perfectly rigid and calculation of the profile of acoustic forces on a particle needs to allow for the characteristics of all the layers, including the transducer. This is done using an equivalent circuit and transfer impedance approach outlined by Hill & Wood[6] and expanded to allow for representation of acoustic parameters[7]. The approach allows acoustic pressure and energy density to be predicted at any point within the acoustic field, along with the radiation forces on a particle within the field

2.2 Flow Modelling

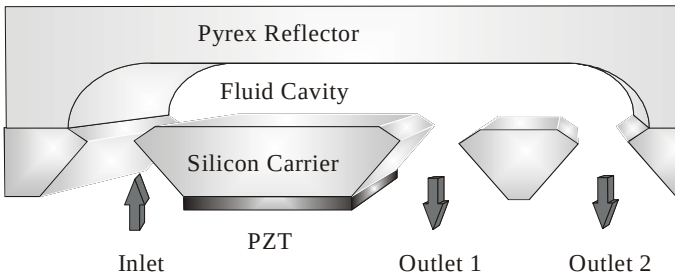

Figure 2. Schematic representation of a microfluidic device.

In many applications of particle manipulation, including filtration and separation, the radiation forces must be balanced against drag forces due to the flow of the surrounding fluid on the particle. A schematic representation of a microfabricated resonator used for particle manipulation is shown in Figure 2. The method used in this work to include the effects of flow is described in greater detail by Townsend et al[8]. For low particle Reynold's number, $Re_p < 0.2$, the drag force on a particle is estimated using Stokes drag calculated using CFD models of the local flow profile in the absence of the particles. Acoustic radiation forces are calculated from the acoustic model described above. These are added to buoyancy and inertial forces and the resulting equations are then solved using an ODE numerical solver function within MATLAB. This approach ensures that developments to the model, specifically inclusion of other particle forces, can be incorporated easily without requiring potentially complex algebraic manipulation. From the ODE solver, the model provides an output array containing a series of time intervals with associated particle coordinate locations and velocity components.

Proceedings of the Institute of Acoustics

By modelling a series of particles at the channel inlet and using the resulting particle coordinates, it is possible to calculate the change in concentration across the channel. The change in concentration is dependent on the change in lateral spacing between each particle. Additionally, the velocity profile influences the concentration; as a stream of particles moves into planes of increased fluid velocity, the longitudinal spacing between particles must increase for particle flow rate to remain constant according to continuity.

The concentration through an outlet is calculated by determining particle flow rate between the wall and position at which the flow splits between outlets. Dividing this by the corresponding outlet fluid flow rate results in particle concentration.

3 CONSTRUCTION OF A MICROFLUIDIC PARTICLE MANIPULATOR

Several microfluidic devices have been fabricated, all using a variation on the design shown in Figure 2 but with different Pyrex and fluid chamber thicknesses. Some have double chamfered ports and some have single chamfers. In order to achieve this, double sided wafer processing was required. The fabrication process used a double sided alignment process and standard wet KOH etching leaving chamfers at the angle of 54.7^{o}. The chamber was then formed by etching a 1.7mm thick Pyrex wafer to the desired depth with a 48% buffered Hydrofluoric acid using a chrome/gold mask (50nm and 500nm thick respectively) and Shipley S1818 resist in order to minimise pinholes. The silicon and Pyrex wafer were then anodically bonded together. The two different port profiles were selected as although the single chamfered port is easier to manufacture, there may be some fluid flow advantages in the double chamfered profile.

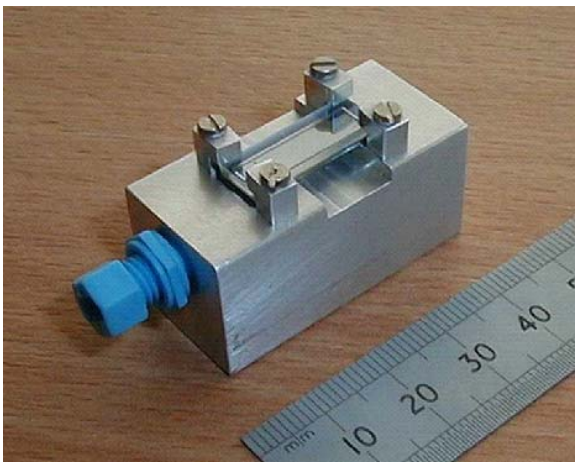

Figure 3. A micromachined resonator on an aluminium manifold

The bulk PZT transducer drive element was bonded onto the silicon using standard Araldite epoxy resin. In order to allow fluid into and out of the device, a manifold was constructed from aluminium as shown in Figure 3. The device was held on the top of the manifold with 4 small screw-on clamps, and the manifold/silicon seal was achieved with a custom silicon O-ring.

4 A PARTICLE MANIPULATOR WITH MULTIPLE MODES

The layered resonator model described above was used to investigate whether a microfluidic resonator could be designed with a number of sub-wavelength modes, each of which would move particles to a different plane within the fluid layer of the resonator. Simulations suggested that a

Proceedings of the Institute of Acoustics

cavity depth of about 200μm would produce 4 modes between 1.5 and 4.5 MHz and the predicted acoustic energy density within the fluid cavity as a function of both frequency and etch depth can be seen in Figure 4.

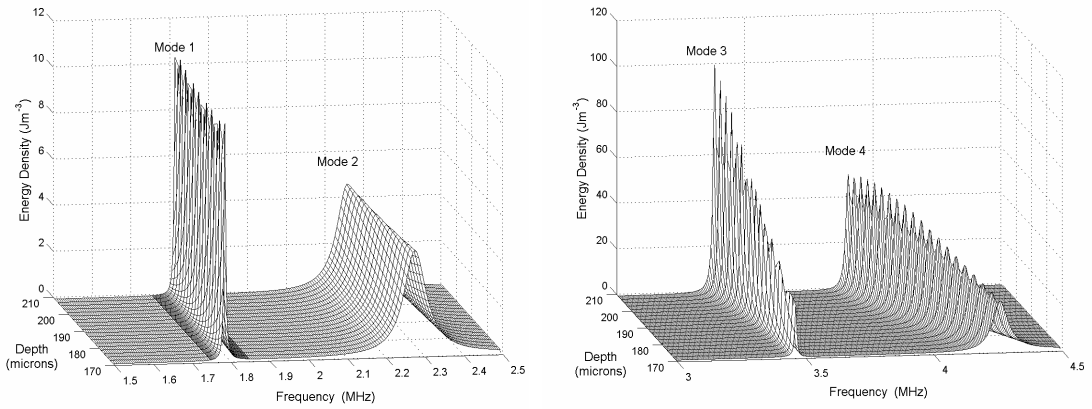

(a) (b)

Figure 4: Energy density against fluid layer depth and frequency between (a) 1.5 & 2.5 MHz and (b) 3 & 4.5 MHz. Note different energy density scale

The simulations can also be used to predict the pressure amplitude across the fluid layer (and its variation with fluid layer depth) as shown in Figure 5

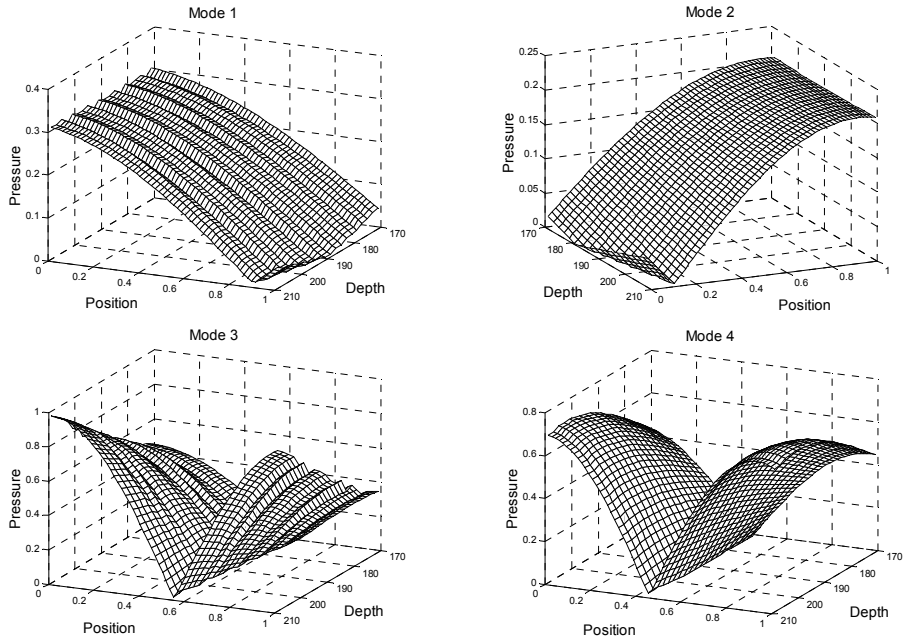

Figure 5: Modelled fluid layer pressure distributions against fractional distance from the carrier layer for the four modes against etched cavity depth (microns).

Modes 3 & 4 are typical half wave (near-rigid boundaries) modes with a pressure minimum near the centre of the cavity. Radiation forces on particles within the fluid will tend to move them to the pressure node at the centre of the cavity. Mode 1 is a quarter wave mode and has a maximum

Proceedings of the Institute of Acoustics

pressure at the carrier layer boundary and a pressure minimum at or near the reflector boundary. This will move particles to the reflector boundary. Mode 2 is also a quarter wave mode, but with its pressure minimum at the carrier layer boundary and a maximum at the reflector. This mode will generate radiation forces that will move particles toward the carrier layer.

The existence of both quarter wave and near half wavelength modes in the same geometry resonator suggests that it should be possible to build a resonator with modes which will move particles to either the centre of the fluid layer or to the fluid boundary, depending on the driving frequency selected.

4.1 Experimental Results for Multiple Mode Chamber

The acoustic model suggests that, between 1.5 and 4.5 MHz, two quarter and two half wavelength modes should be generated for any of the cavity depths modelled between 170 and 210 μm. However a close look at modes 1 & 2 in Figure 5 shows that the model predicts the pressure nodes to be slightly away from the respective boundaries at the higher end of the cavity depth range. Hence a value of 175 μm was chosen for the etch depth.

4.1.1 Impedance Characteristics

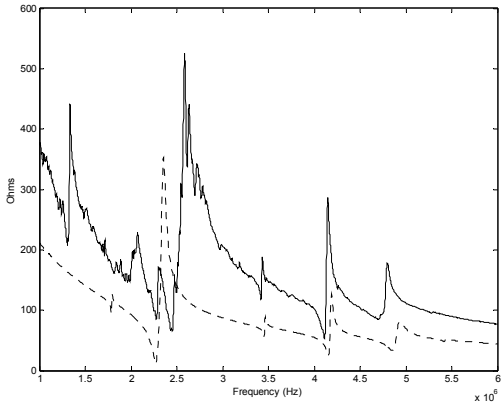

Figure 6: Modelled (dotted) and measured (solid) impedance plots for the fluid filled device

Figure 6 shows the electrical input impedance of the resonator as predicted by the multi-layer model and the measured input impedance. Impedance peaks due to modes 3 & 4 are clearly visible at about 3.5 and 4.1 MHz in both modelled and measured results. However the model is a simplification of the actual resonator, and in particular only considers behaviour in a single dimension, making the measured results more complex than the modelled results at frequencies below about 3 MHz. A small impedance peak in the modelled results at 1.8 MHz corresponds to mode 1, but is not clearly distinguishable in the measured results. The impedance peak associated with mode 2 is completely masked by the large transducer/carrier layer peak visible at about 2.4 MHz in the modelled and 2.7 MHz in the measured results.

4.1.2 Particle Manipulation

An optical microscope, focussed through the Pyrex reflector layer was used to monitor the position of yeast particles within the fluid layer of the resonator. The resonator was driven from a frequency synthesiser, via a fixed gain RF amplifier (50dB). The transducer was placed in series with a 47ohm resistance to allow the variation in voltage across the transducer to be monitored to identify voltage minima. By searching for voltage minima in the region predicted by the model, all four modes were

Proceedings of the Institute of Acoustics

identified. Modes were found at 1.71MHz, 2.27MHz, 3.44MHz and 4.1MHz, although, modes 1 and 2 required very careful adjustment to identify.

The position of the particles within the fluid layer was measured by using the small depth of field of the microscope. For example, in the case of mode 1, the microscope was focussed on the boundary between the fluid and the reflector layers.

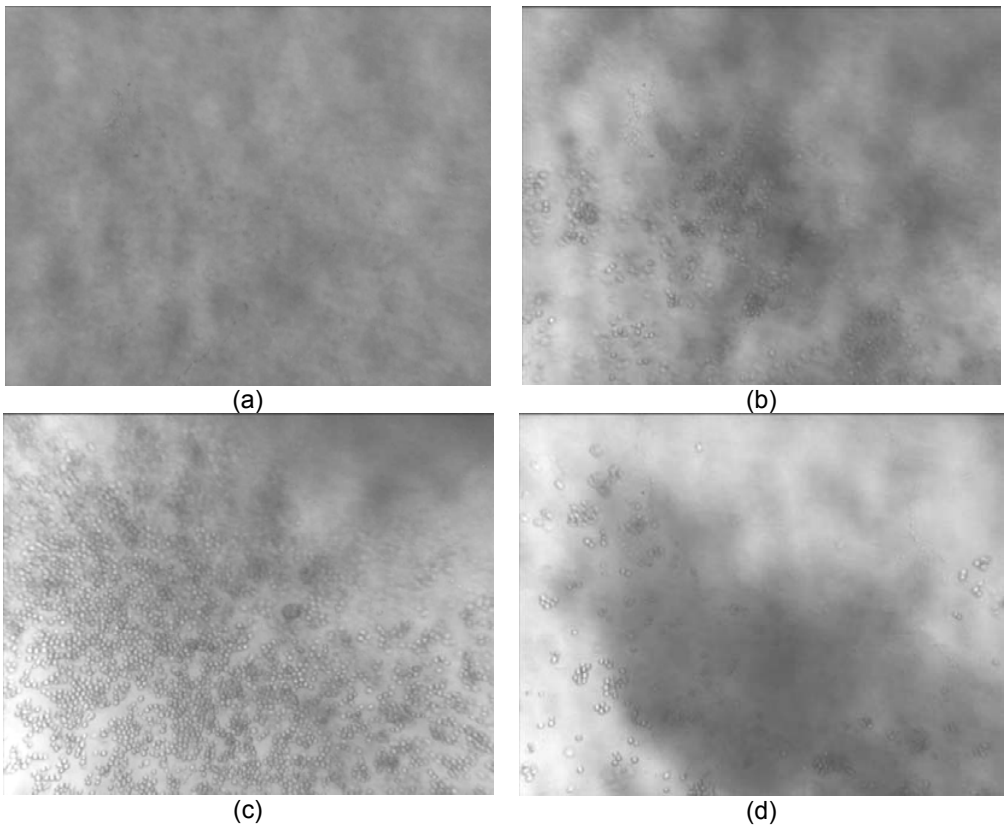

Figure 7: A sequence of images taken as particles move to the reflector boundary driven at the frequency of mode 1.

Figure 7 shows randomly distributed particles being forced to the Pyrex/water boundary against gravity as predicted for Mode 1 at 1.7MHz. Image (a) shows the random distribution of yeast before any power is applied, with the microscope focussed at the Pyrex/water boundary. Image (b) shows the view 5 seconds after the power is applied, and it can be seen that yeast cells are beginning to move into focus as they are forced against the boundary. Image (c) show the situation after 15 seconds and many more cells are now in focus. Particles tend to collect in clumps due to lateral forces, and image (d), taken 40 seconds later, after the power has been turned off shows this. The clump of particles is peeling away from the Pyrex layer and falling under the influence of gravity towards the silicon layer and thus out of focus.

Similar results were obtained for the other three modes, showing that particles could be forced to either of the cavity boundaries or to the cavity centre.

Proceedings of the Institute of Acoustics

5 EXPERIMENTAL EVALUATION OF PARTICLE SEPARATION

5.1 Introduction to Separator Experimental Work

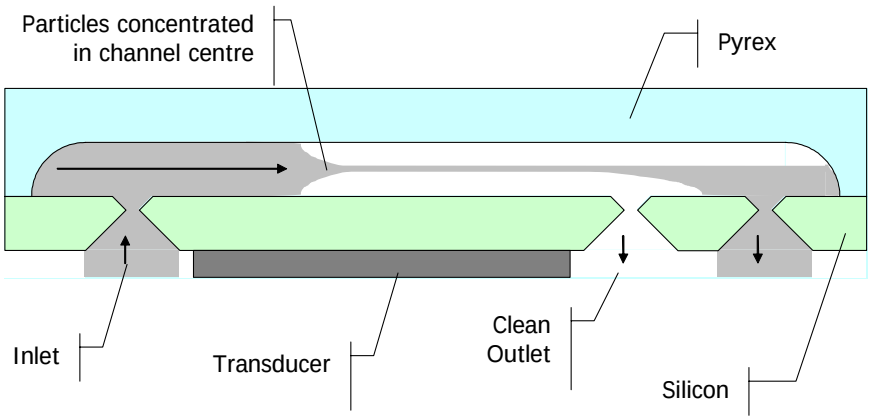

Figure 8. Operation of microfluidic chamber as separator (not to scale)

Experiments were completed on a microfluidic resonator designed for ultrasonic separation, using the principle shown in Figure 8. A fluid/particle mixture enters the fluid channel (between the silicon and Pyrex layers) via the inlet port. The particles are forced to the centre of the fluid layer by radiation forces within the standing wave excited by the PZT transducer. This allows clarified fluid to be drawn from outlet 1, the “clean” outlet, and a concentrated particle fluid mixture to be drawn from outlet 2. Experiments have been conducted using yeast and 1µm latex particles. The frequency applied to the device was approximately 3.4MHz, a half wavelength mode, and such that particles agglomerate near the central plane of the channel. The transducer voltage was varied and test results of outlet concentrations were compared to predictions produced using the numerical approach to predict particle paths. This in turn was used to determine outlet concentrations through the two outlets.

5.2 Apparatus

The experimental set up (Figure 9) consists of two peristaltic pumps, one feeding the inlet of the separator device and one drawing fluid through one of the two outlets. The device is isolated from the pulses produced by the pumps by using a syringe arrangement.

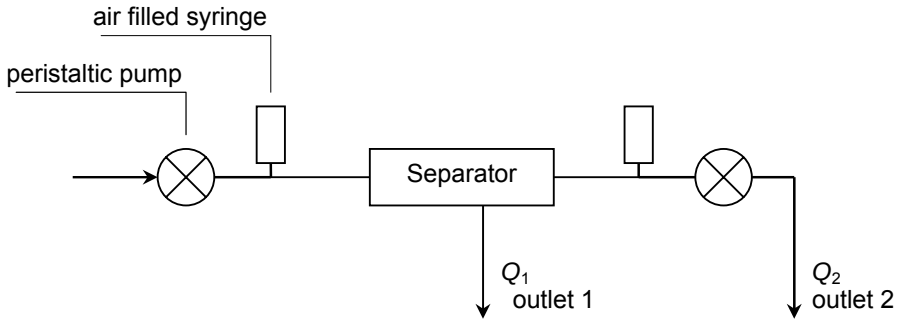

Figure 9. Fluid network used for the testing of the separator.

Proceedings of the Institute of Acoustics

The flow rates through the outlets are chosen such that $Q_1 < Q_2$. Therefore, operating in the half wavelength mode with a particle stream formed along the centre of the separator channel, clear fluid can be extracted through outlet 1 and particle concentrate through outlet 2.

For each test, the fluid through each outlet was collected and concentration measured using a turbidity sensor (Honeywell).

5.3 Results

Experimental and modelled results showing the influence of transducer voltage on both separation of 1 micron latex particles and yeast cells are shown in Figure 10 and Figure 11 respectively. In the experiments for yeast, a total flow rate ($Q_1 + Q_2$) of approximately 0.053ml/s was maintained, 25% of which passed through outlet 1. For 1µm particles these figures were 0.028ml/s and 21% respectively.

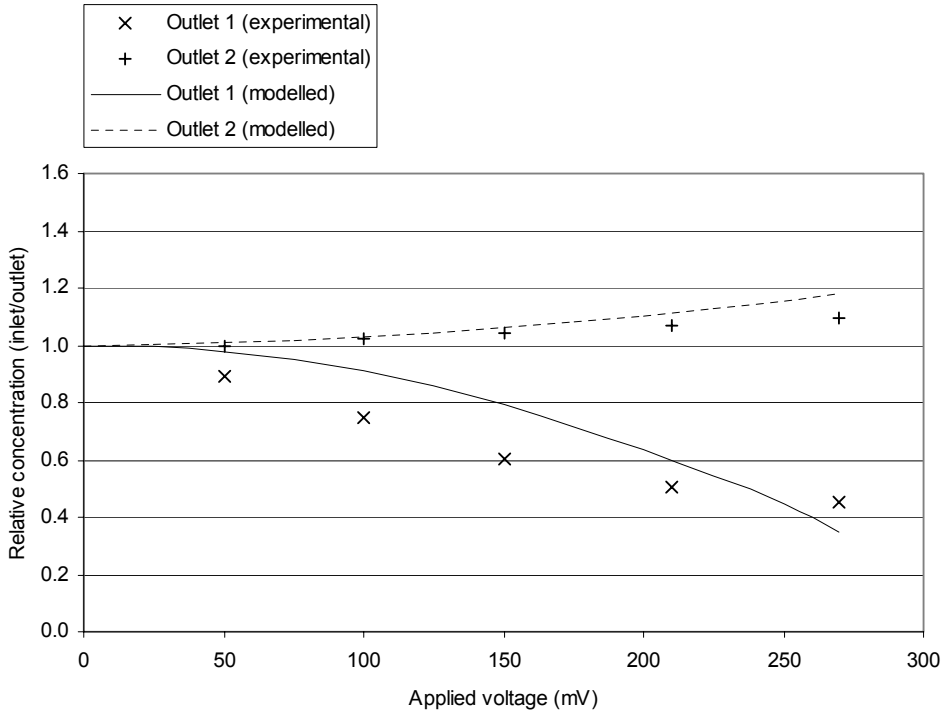

Figure 10. Separation of 1 micron latex particles based on an initial concentration of 0.016% weight. Applied voltage is input voltage to amplifier.

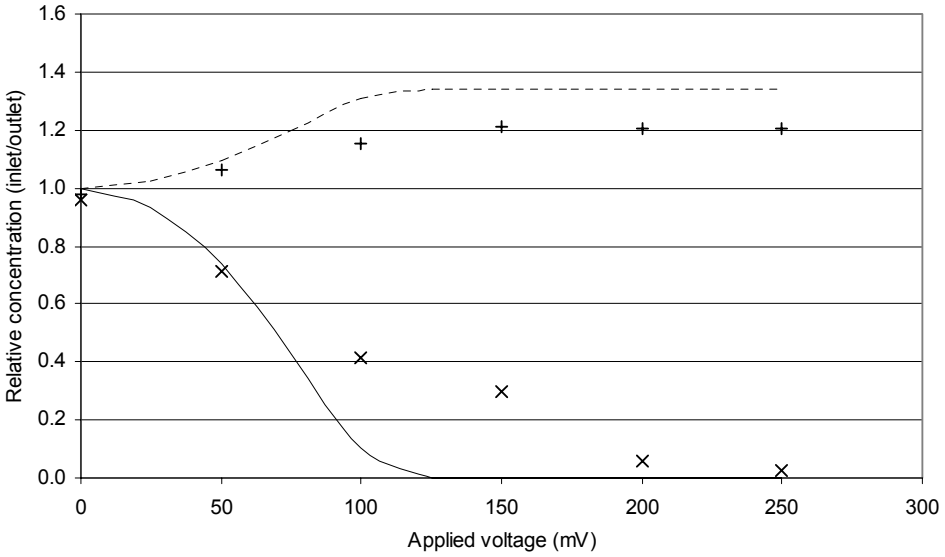

Figure 11. Separation of yeast particles based on an initial concentration of 0.2% weight. Applied voltage is input voltage to amplifier.

Increasing transducer voltage increases the magnitude of the acoustic radiation force acting on suspended particles and in turn the rate at which they agglomerate at the nodal plane. Therefore, and as expected, the results show that increasing voltage causes more particles to pass through outlet 2 and decreases the concentration seen through outlet 1.

The modelled results for the separation of 1 micron particles (Figure 10) compare reasonably well with the experiment results. Generally, the experimental results show slightly lower concentrations than modelled predictions, which can be attributed to the adhesion of particles on the walls within the fluid network surrounding the separator. At higher voltages, particles tend to clump together under higher acoustic forces; potentially disturbing the laminar flow required for successful separation and limiting the possible clearance through outlet 1.

For the separation of yeast (Figure 11), the modelled results are more optimistic than the experimental results. The initial concentration of the yeast was quite high at 0.2% compared to that for the 1µm latex particles where 0.015% was used. This high concentration may impede the motion of the yeast cells towards the nodal plane, indeed clumping was observed to be a greater problem with the yeast than with the latex particles. However, at high voltages separation is successful, producing a high degree of separation. Other preliminary tests (not reported here) have shown that a reduction in the total flow rate can produce clarified flow, the turbidity of which is indistinguishable from water. Further tests are required to investigate the influence of concentration and flow rates on the separation performance.

Although the model does not predict the values of experimental outlet concentration precisely, the significant difference between the two cases is modelled successfully and the modelling approach should provide a useful tool in selecting the operating parameters (voltages and flow rates) required for different particle/fluid combinations.

Proceedings of the Institute of Acoustics

6 CONCLUSIONS

Electro-acoustic modelling, along with flow models can be used to aid the design of microfluidic resonators for acoustic manipulation of particles. Devices have been fabricated successfully using standard microfabrication techniques. A resonator has been constructed which is able to move particles to either boundary of the fluid layer or to the centre of the fluid layer, depending on the driving frequency (and hence the particular mode). Such a device offers the potential to move cells or particles within a microfluidic device in a controlled and predictable manner.

Initial modelling work incorporating numerical predictions of concentration changes in flow-through devices compare well with experimental measurements. However, clumping of particles at high voltages due to lateral radiation forces on the particles reduces separation efficiency. For yeast particles the resonators have been shown to work effectively as a clarifier, but further development is required to improve the performance of the devices in separating smaller particles and in acting as a concentrator.

7 ACKNOWLEDGEMENTS

This work has been carried out with financial support from Dstl and EPSRC under grant number GR/R13333/01, and Porvair PLC.

8 REFERENCES

1. M. Gröschl, Ultrasonic separation of suspended particles - Part I: Fundamentals, Acustica 84, 432-447 (1998).
2. C. J. Schram, in *Advances in Sonochemistry*, edited by T. J. Mason (1991).
3. N. R. Harris, M. Hill, S. P. Beeby, Y. Shen, N. M. White, J. J. Hawkes, and W. T. Coakley, A Silicon Microfluidic Ultrasonic Separator, Sensors and Actuators B 95, 425-434 (2003).
4. W. T. Coakley, Ultrasonic separations in analytical biotechnology, Trends in Biotechnology 15, 506-511 (1997).
5. L. P. Gor'kov, On the forces acting on a small particle in an acoustical field in an ideal fluid, Sov. Phys. Dokl. 6, 773-775 (1962).
6. M. Hill and R. J. K. Wood, Modelling in the design of a flow-through ultrasonic separator, Ultrasonics 38, 662-665 (2000).
7. M. Hill, Y. Shen, and J. J. Hawkes, Modelling of layered resonators for ultrasonic separation., Ultrasonics 40, 385-392 (2002).
8. R. J. Townsend, M. Hill, N. R. Harris, and N. M. White, Modelling of particle paths passing through an ultrasonic standing wave, Ultrasonics (In Press) (2004).

Available online at www.sciencedirect.com
SCIENCE DIRECT®
Sensors and Actuators B 111–112 (2005) 455–462
SENSORS AND ACTUATORS B CHEMICAL
www.elsevier.com/locate/snb

Fluid modelling of microfluidic separator channels

R.J. Townsend [a], M. Hill [a,*], N.R. Harris [b], N.M. White [b], S.P. Beeby [b], R.J.K. Wood [a]

[a] *Mechanical Engineering School of Engineering Science, University of Southampton, Southampton SO17 1BJ, UK*
[b] *ECS, University of Southampton, Southampton SO17 1BJ, UK*

Available online 25 April 2005

Abstract

In a microfluidic ultrasonic separator device, the microchannel geometry is inherently angular due to the anisotropic etch processes used. A CFD model is used to investigate eddy formation induced by this angular geometry. Results are applicable to various microfluidic devices and show that certain etch patterns significantly reduce eddy formation.

Keywords: Microchannels; CFD; Ultrasonic separation; Fluid separation

1. Introduction

There is significant interest in exploiting the phenomenon whereby particles experience a radiation force when within an acoustic standing wave. Various devices using radiation forces have been reported which typically aim to concentrate, fractionate or manipulate particles for sensing purposes [1–4]. Here, a microengineered ultrasonic separator device (Fig. 1) is being developed to manipulate particles suspended within a carrier fluid using either a half or quarter wavelength standing wave to concentrate particles along certain planes within a straight fluid channel [5–7]. Two outlets subsequently draw off either clean fluid or a particle concentrate depending on requirements.

Similar devices have been fabricated from steel and glass [4,8], however for this technique to be realized on a microfluidic scale etched silicon and Pyrex are being used. This has the potential advantages of batch production and easy incorporation into microfluidic systems containing micropumps, etc. which require only very small sample sizes. However, the nature of micro-engineering fabrication techniques restricts the geometric design of the microchannels. The microchannel geometry and fluid operating conditions contribute to the fluid flow field within the device which is significant in terms of the successful operation of the device. This paper concentrates on the geometric design of the cell, and its influence on pressure losses and fluid separation where the fluid becomes separated from the channel walls creating a fluid vortex (fluid separation will subsequently be referred to as eddy flows to avoid confusion with the term 'particle separation' which describes the function of the device). Eddy formation can distort particle trajectories [9] and influences sedimentation formed on the channel walls, in turn strongly influencing the performance of the device. Therefore, a computational fluid dynamics (CFD) model has been used to investigate the effects of microchannel geometry on the fluid flow.

2. Microchannel geometry

2.1. Separator construction and geometry

The micromachined separator device consists of a 525 μm thick silicon wafer and 1700 μm Pyrex wafer, etched and then joined using anodic bonding. Fluid enters and leaves the device via ducts etched into the silicon. The duct geometries currently used in the separator consist of either single or double sided etched ducts that lead to an etched channel within the Pyrex across which the acoustic standing wave is set up. Fig. 2 illustrates the typical wafer geometry incorporating either single or double etched ducts.

* Corresponding author.
E-mail address: m.hill@soton.ac.uk (M. Hill).

0925-4005/$ – see front matter © 2005 Elsevier B.V. All rights reserved.
doi:10.1016/j.snb.2005.03.035

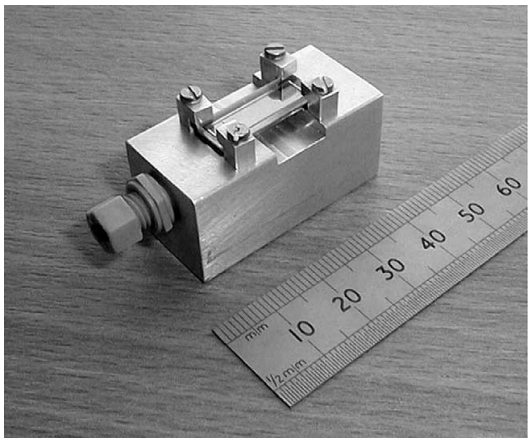

Fig. 1. Microengineered ultrasonic flow-through separator mounted on aluminium manifold.

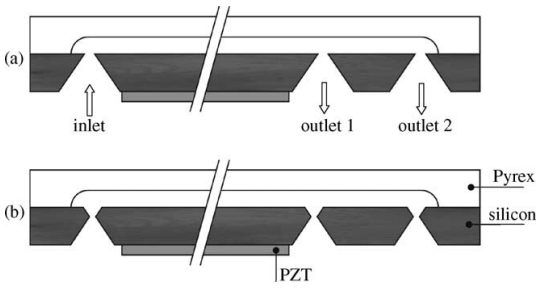

Fig. 2. Schematic of typical cross-section of device structure illustrating both (a) single and (b) double-sided etched duct geometry within the silicon wafer, with both flow direction and materials indicated.

Isotropic and anisotropic etchants are used for the Pyrex and silicon wafers respectively, where the anisotropic etch produces predictable angular geometries where the etch process is effectively halted at the (1 1 1) crystal planes, forming angles of 54.74°. Alternative methods of creating the ducts, such as deep ion etching, exist and although such methods may provide more geometric variations, this study reveals a satisfactory solution based simply on wet etching techniques.

2.2. Influence of geometry on separator performance

Where anisotropically etched geometry is dictated by the orientation of the wafer crystal planes, discontinuities in the wall geometry are created. Such discontinuities cause fluid flow to separate from the channel wall giving rise to eddy flows in which the direction of flow is reversed at the wall [10,11]. Fig. 3 presents an example of a CFD simulation used to predict eddy formation within the inlet region of the device. Fig. 3a illustrates the formation of an eddy downstream of the double-etched duct which is indicated by the reversed flow at the wall. There is also an eddy region at the end of the main channel, contained within the curved isotropic etch profile created in the Pyrex layer. This eddy is associated with the alignment tolerances between the silicon and Pyrex layers which determines the position at which the inlet duct joins the main channel. Fig. 3b describes the variation in pressure through the inlet region and indicates a high pressure loss corresponding with the restriction in the etched duct, which is suggested by the close proximity of the pressure contours.

With regard to eddy flows being present within the ultrasonic separator during operation, the formation of eddies presents a condition where particle movement cannot be predicted. For example, particles are manipulated by the acoustic

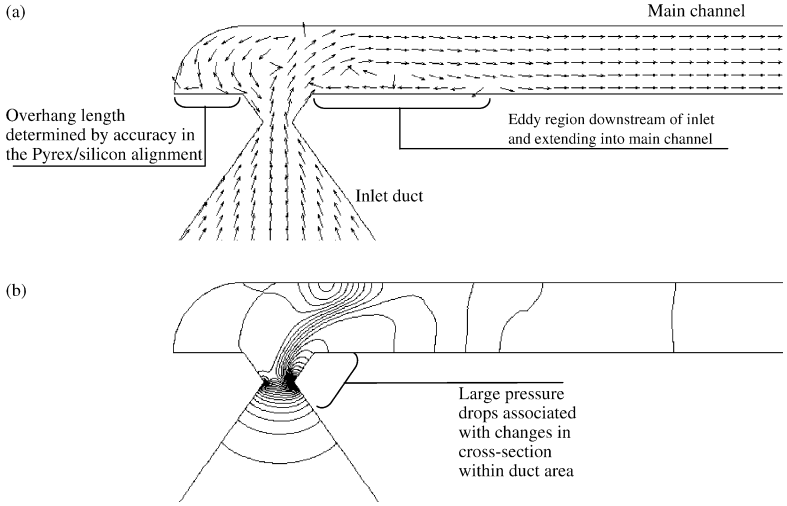

Fig. 3. (a) Vector plot illustrating development of eddy downstream of inlet and (b) associated pressure drop indicated by pressure contours.

field within the main channel, but the presence of an eddy in this region will distort the laminar flow field and also particle trajectories, which in turn influences the separation efficiency of the device. Additionally, the degree to which particles become trapped within eddies is unknown, but presents doubts over the ability to successfully flush clean the device should it be required for subsequent operations.

3. Development of CFD model

In order to study the influence that the microchannel geometry has on the development of eddies, a CFD model is used. This enables a variety of possible geometries to be modelled over a range of flow rates and provides comprehensive visualisation of the flow, an aspect difficult to achieve in the fabricated device.

3.1. Application of CFD to microfluidic simulation

Recent studies exist which aim to identify the scale at which classical flow theory and the Navier–Stokes set of governing equations cease to accurately describe fluid flow systems [12–14]. These studies have been occasionally collated, for example, by Judy et al. [15] and Gad-el-Hak [16]. Judy et al. [15] note that deviations from macroscale flow theory have generally been observed for hydraulic diameters below 100 μm, therefore as the micro-channel dimensions in this work are greater than 100 μm this supports the use of the Navier–Stokes equations in this application. Commercial numerical packages based on the Navier–Stokes equations have been applied to the analysis of fluid flow in microfluidic systems, for example, aspects of fluid flow through injector systems incorporating channels of dimensions 200 μm [17,18] and micromixer channels down to dimensions of 70 μm [19] have been simulated. Therefore, a commercial CFD code, CFX5, has been chosen for the fluid simulation work described in this paper.

The aspect ratio of the fluid channels is typically greater than 20, therefore to reduce the size of the model and therefore computation time, 2D models are used to simulate the fluid flow through various parts of the device. The 2D models are effectively thin 3D slices along the length of the channel bounded either side by symmetry planes. As the concentration of yeast particles used in experiment is low enough to assume negligible effect on the fluid dynamics, the CFD simulations are further simplified by modelling only the fluid flow and exclude the influence of solid phase particles. A mesh dependence study has been completed based on a simulation of the main channel geometry, essentially a model describing flow between parallel plates known as Poiseuille flow. From this study a mesh refinement level has been selected and results in an average error of less than 1% when compared to the classical parabolic velocity profile for laminar flow. In addition, mesh adaption is used for selective mesh refinement during the computation. This refines the mesh in regions exhibiting a high velocity or pressure gradient, which usually occur adjacent to wall boundaries and at geometric discontinuities, associated with the formation of eddy flows.

3.2. Validation of CFD model

An initial batch of microengineered cells has been produced to investigate the ultrasonic separation capabilities of a micro-engineered device and contains devices of the two different duct geometry designs shown in Fig. 2. These devices were also used to validate the CFD model by measuring and comparing the size of the eddy region downstream of the inlet duct. The eddy region in question is illustrated (Fig. 3) and is chosen as it can be observed in the fabricated devices, although it is appreciated that other unobservable eddies exist within the device. The experimental results taken from the fabricated devices were extracted by studying the movement of particles under the influence of the flow field only (it has been assumed that particles have little influence on the fluid dynamics and are neutrally buoyant). This is achieved by pumping a mixture of water and a low concentration of yeast particles through the device at a known flow rate and using a Motic DMB3 digital biological microscope to record images looking down through the device Pyrex layer. An example image is shown in Fig. 4 which illustrates the eddy formation downstream of the inlet duct, discernible from the laminar stream, and corresponds to the geometry and flow pattern shown in Fig. 3 CFD results are collected by modelling the inlet region of both duct designs and using streamline plots to determine the extent of the eddy region from the leading edge of the main channel.

It has been observed that the flow velocity through the inlet duct is not uniform across the width of the device and is

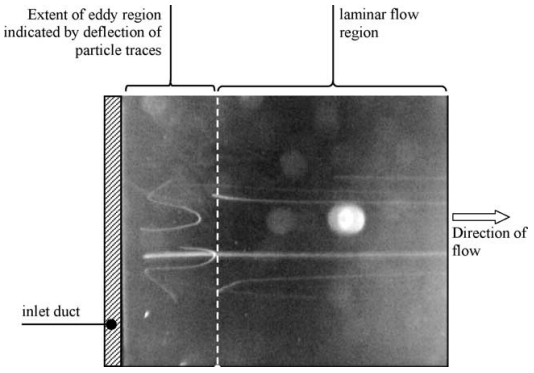

Fig. 4. Image taken whilst looking down through Pyrex layer showing the inlet duct extending across the width of the device. Streamlines created by yeast particles passing along the main channel can be seen. Immediately downstream of the inlet duct some particles are deflected by the eddy region, as can be seen by their convoluted path. To the right of this region particles can be seen following straight streamlines where the laminar flow profile has developed. Video of moving particles gives clearer indication of the extent of the eddy region as compared to still images.

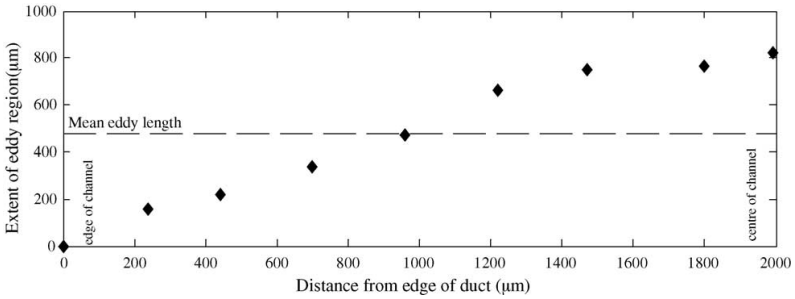

Fig. 5. Variation in eddy size across the width of the main channel and downstream of the double etched inlet duct at a flow rate of 0.3 ml/s.

caused by the manifold geometry beneath the device which issues a narrow jet of fluid towards the centre of the inlet. This causes the size of the associated eddy to vary across the width which is demonstrated in the plot shown in Fig. 5, the data for which is measured experimentally. It can be seen that near the side of the channel the eddy region is small and corresponds to a lower flow velocity, whereas towards the centre of the channel the jet emanating from the manifold creates a larger flow velocity and therefore longer eddy region. At flow rates between 0.1 and 0.3 ml/s the calculated mean eddy size is on average approximately 0.5 times that of the maximum (centre) eddy length and is indicated on the plot. Therefore, to simplify the experimental work, the maximum eddy size only has been measured and adjusted by a factor of 0.5 to take into account the non-uniform flow and to record a mean eddy length.

In Fig. 6, the size of the eddy region is plotted as a function of flow rate and demonstrates that eddy size is strongly related to the fluid flow rate. An initial inspection shows that the CFD results underestimate the length of the eddy region, however they both show that the double-etched geometry produces a slightly smaller eddy region compared to the single etch geometry up to a flow rate of 0.5 ml/s. The difference between experimental and CFD results can be explained by the following: (a) in general the exact conditions at the inlet boundary of the CFD model are unknown although a parabolic profile has been assumed; (b) pulses produced by the peristaltic pumps have been observed to cause fluctuations in the flow rate and therefore variations in the eddy size, although it has not been possible to quantify these variations; (c) as demonstrated in Fig. 5, the flow through the device is not uniform across its width and suggests that a more computationally expensive 3D CFD would be more appropriate; (d) a buildup of particles can reduce the duct size and encourages more significant flow separation and a larger eddy, although the device was flushed frequently during experimental work.

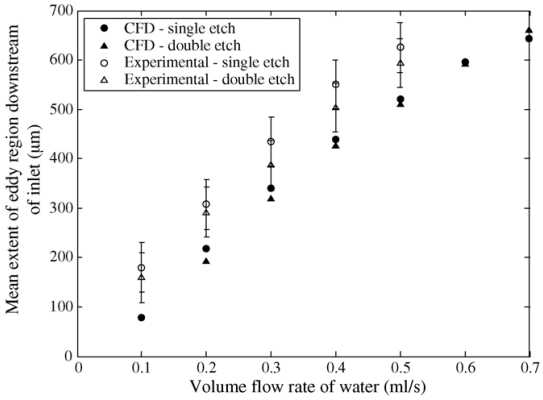

Fig. 6. Extent of eddy region downstream of inlet duct for both single and double etched geometry over a range of flow rates and plotted for both CFD and experimental results. The measurements are based on two sets of experiments and error bars of ±50 μm have been added, reflecting the perceived accuracy of the estimates.

In general this exercise demonstrates that a 2D CFD model provides a valuable method to predict the location and scale of eddy formation within microfluidic channels, in this case for ducts incorporating a minimum dimension of 160 μm. However, by extending the complexity of the simulation to include transient and 3D aspects of the flow, it is anticipated that a more accurate representation of the flow can be generated, should this be required.

4. Geometric study

4.1. Introduction

The geometric study aims to improve the duct design by restricting the onset of eddies and reducing pressure drops. As eddy regions are typically caused by discontinuities found in the duct geometry, an initial visual inspection can be used to identify these features. The visual inspection covers a range of possible geometries created by the anisotropic etch process. This approach serves to reduce the problem to a few geometric designs, which are then each investigated more thoroughly within CFD simulations.

4.2. Qualitative study

Eddy regions occur when the flow becomes separated from the wall. Within a fluid network this occurs in areas where

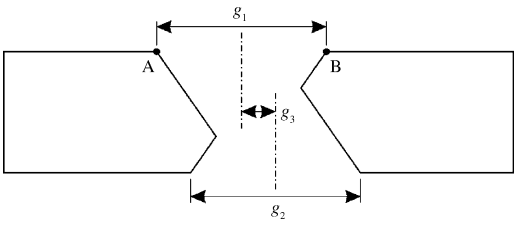

Fig. 7. Parameters describing silicon etched duct geometry; for top and bottom etch masks, g_1 and g_2 describe respective widths, and g_3 the relative offset.

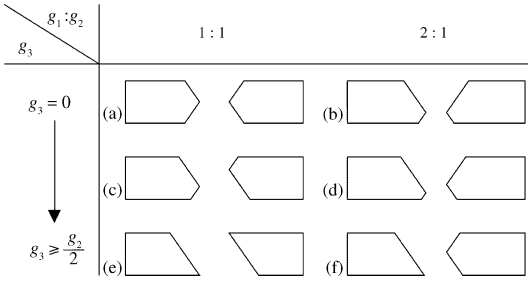

Fig. 8. Basic duct geometry groups.

the cross-section changes such as in diffusive channels and at discontinuities and sharp edges in the wall geometry. For example, an anisotropic etch such as the single-etched duct inherently creates a diffusive duct with an inclusive angle of 109°, recognised to result in significant losses as compared to the optimum angle of 6–7° [11]. Also, the separator device is formed from multiple wafer layers and misalignment between these can introduce sharp edges and sudden expansions or reductions in the fluid channel size. For example, where a single-etched duct acts as a convergent channel (inlet duct in Fig. 2a) as the fluid enters the main channel the fluid is subject to an extreme expansion, although no eddy is necessarily induced in the duct itself.

For the reasons discussed above, the study concentrates on double-etched ducts and in order to efficiently cover a range of possible duct geometries a parametric approach is used. This analysis assumes an anisotropic wet silicon etch such as KOH, where Fig. 7 illustrates the parameters used to describe the resulting etched duct geometry with the direction of flow either way through the duct. Parameters g_1 and g_2 describe the width of the top and bottom etch masks and subsequent etched areas, whereas g_3 describes the distance between the centre points of the top and bottom etch areas, effectively representing their offset and the degree to which the duct is skewed.

For the purposes of the geometric study it has been assumed that the inlet and outlet 2 ducts are positioned at the extreme ends of the main channel, i.e. there are no redundant areas at the ends of the main channel. This is designed to discourage eddy formation either end of the main channel such as that demonstrated in Fig. 3a, near the inlet duct. However, this assumes a fabrication method such that high accuracy is applied both to the alignment of the Pyrex upon the silicon layer and to the isotropic etching of the Pyrex which determines the length of the main channel.

By classifying geometry in terms of the parameters g_1–g_3, Fig. 8 illustrates the basic geometry groups used for the study. Again, fluid flows either way through the duct with the main channel flow passing either from the left or right.

Considering the selection of geometries displayed in Fig. 8, a discontinuity cannot be avoided where fluid passes to the main channel and beyond the silicon layer (point A or B indicated in Fig. 7). However, only the geometry type shown in Fig. 8e is unlikely to encourage eddy formation within the duct area itself; all other geometries contain discontinuities and a divergent element. It is therefore this parallel sided duct geometry which shall be investigated further.

4.3. CFD study

Simple inspection has eliminated geometries which have a significant expansion or contraction. However, more insight is gained from CFD simulations investigating dimensions and the robustness of the flow pattern to small inaccuracies in dimensions and mask alignment. This is achieved by completing a series of simulations of the flow through both the inlet and outlet ducts, investigating the influence of dimensions g_1 (where $g_2 = g_1$) and also the influence of small etch mask inaccuracies which create the geometry illustrated in Fig. 8f. The key observations are as follows and are based on CFD simulations using a flow rate of 0.5 ml/s.

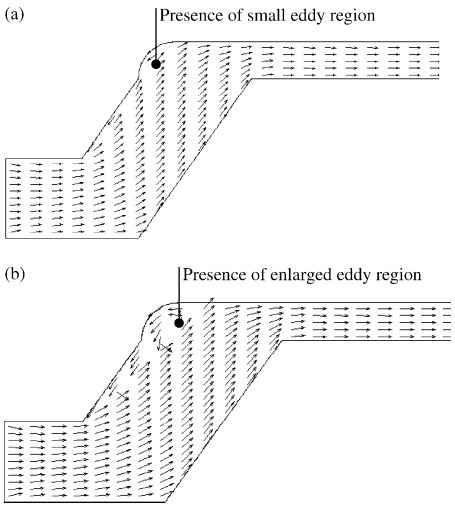

Fig. 9. Vector plots of inlet duct showing the affect of duct width on eddy region size for (a) minimum duct width and (b) an increased duct width of 150 μm.

4.3.1. Duct width

Over a complete series of simulations, an optimum design is observed when subsequent sections of the flow path remain constant or gradually reduce in cross-sectional size, replicating the effect of a convergent duct and ensuring that flow remains adhered to the wall. An example of this is shown in Fig. 9 which demonstrates that as the width of the parallel sided inlet duct is increased and becomes larger than the preceding channel section, an eddy region is created and expands. Note that this is only of significant advantage in the inlet region of the separator device as only the inlet duct leads to the relatively narrow main channel.

4.3.2. Error/offset in masks

Any errors or offset in the double sided alignment process used to align the etch masks on either side of the silicon wafer will potentially introduce a discontinuity. Such discontinuities generally encourage an eddy, the eddy size being related to the magnitude of the error/offset. Fig. 10 depicts the outlet 2 duct shows one example of this where an eddy region forms within the area created by the curved isotropic etch profile within the Pyrex layer and the chamfer within the anisotropically etch silicon duct. However, the flow through outlet 1 is not influenced by the Pyrex etch profile and is less sensitive to double sided alignment inaccuracies. Fig. 11 shows that an eddy only forms within the main channel above the duct at a high degree of alignment inaccuracy where a large chamfer is present in the duct. This is unlikely to occur since the double sided alignment process is typically accurate to $\pm 5\,\mu$m.

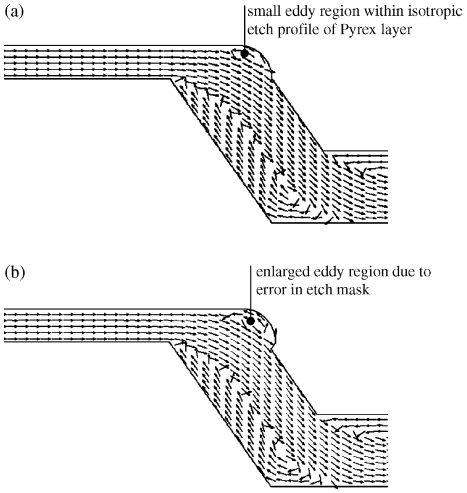

Fig. 10. Vector plots of outlet 2 showing effect of error/offset in etch mask for (a) no offset and (b) top etch increased by 50 μm.

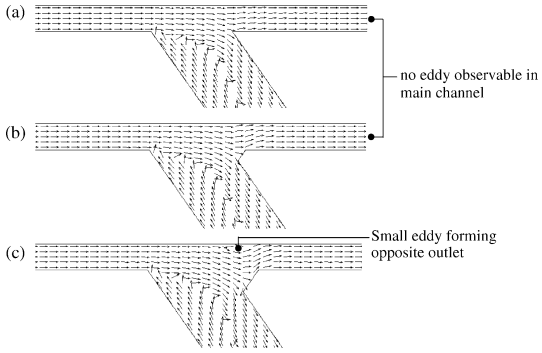

Fig. 11. Vector plots of outlet 1 showing effect of error/offset in etch mask for (a) no offset and (b) top etch increased by 50 μm (c) top etch increased by 100 μm.

5. Device fabrication and test

Parallel ducts have been used within a new batch of devices, where Fig. 12 shows an example of the outlet 2 region and is taken from a cross-sectioned device. The potential chamfering of the duct edges produced by errors in alignment has not occurred. However, the alignment of the

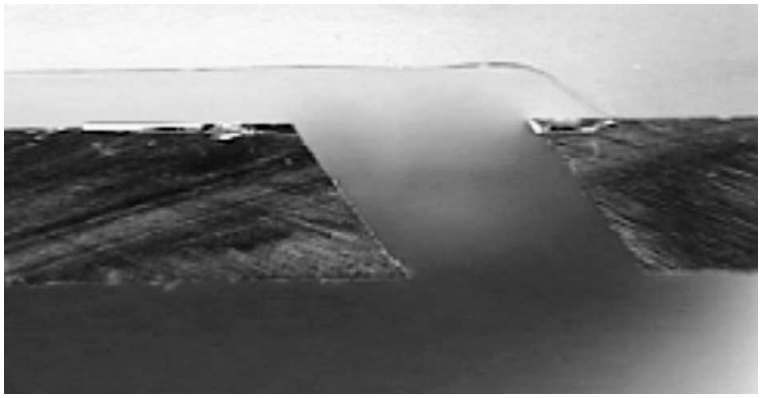

Fig. 12. Cross-section of etched device incorporating revised geometry.

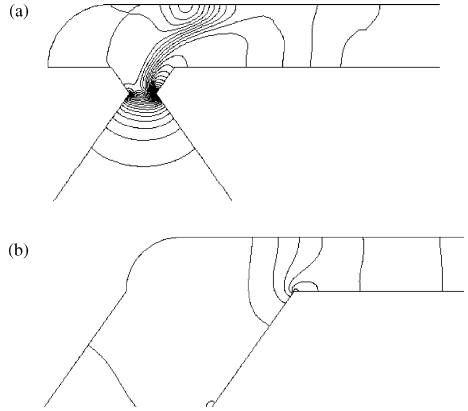

Fig. 13. Pressure distributions within (a) double-etched and (b) parallel sided duct geometry at a flow rate of 0.5 ml/s where contours plotted at ca. 35 Pa intervals.

Pyrex and silicon wafers, which was performed by eye, means that the outlet duct is not aligned exactly with the end of the main channel. The use of an optically aligned anodic bonder would produce more satisfactory results by reducing this overhang.

The device is tested using the same method described in Section 3 and no eddy downstream of the inlet is observed up to flows of 0.6 ml/s, beyond which the flow pattern is difficult to discern. This level of eddy suppression is significant when compared to the results recorded in Fig. 6 for the original, more angular geometry where eddies downstream of the inlet exist at a much lower flow rate of 0.1 ml/s and possibly below this value. The only drawback of the parallel duct is the imposition of a minimum channel width which is based upon the silicon wafer thickness.

Fig. 13 shows the pressure distribution in both the double-etched and parallel sided inlet duct geometry, where the large pressure drops seen within the double-etched geometry are not observed within the new parallel geometry where the pressure contours are much more widely and evenly spaced. It is accepted that eddy formation, and possibly pressure losses, are still likely to be significant within the outlet ducts, although more careful design of the downstream fluid network would be beneficial.

6. Conclusion

The anisotropically etched silicon duct geometries presented in this paper reduce eddy development in the ultrasonic separator and the associated fluid losses. CFD and experimental results demonstrate that this has been most successful in the main channel of the device where highly laminar flow is required for predictable operation of the device in manipulating particles. In one case, problematic eddy formation has been eliminated within a range of flow rates at least six times larger than that of the original geometry. Eddy flows within the ducts, which act as potential capture sites for particles and contaminants, have been investigated and limited by the use of parallel sided ducts. Further work is required to improve aspects of the outlet ducts where the flow field is highly dependent upon the downstream fluid network.

The reduced pressure drops, associated with geometry resulting in the smaller eddy flows, reduce the total pressure drop across the device. This is useful where pumping methods are low power devices and resistance offered by the fluid system needs to be minimised.

Acknowledgements

This work is funded by EPSRC grant GR/R13333/01. The authors gratefully acknowledge the funding and support from Dstl and Porvair plc.

References

[1] C.M. Cousins, P. Holownia, J.S. Hawkes, C.P. Price, P. Keay, W.T. Coakley, Clarification of plasma from whole human blood using ultrasound, Ultrasonics 38 (2000) 654–656.
[2] D.A. Johnson, D.L. Feke, Methodology for fractionating suspended particles using ultrasonic standing wave and divided flow fields, Sep. Technol. 5 (1995) 251–258.
[3] H. Bohm, L.G. Briarty, K.C. Lowe, J.B. Power, E. Benes, M.R. Davey, Quantification of a novel h-shaped ultrasonic resonator for separation of biomaterials under terrestrial gravity and microgravity conditions, Biotechnol. Bioeng. 82 (2003) 74–85.
[4] J.J. Hawkes, W.T. Coakley, Force field particle filter, combining ultrasound standing waves and laminar flow, Sens. Actuators B Chem. 75 (2001) 213–222.
[5] N.R. Harris, M. Hill, S. Beeby, Y. Shen, N.M. White, J.J. Hawkes, W.T. Coakley, A silicon microfluidic ultrasonic separator, Sens. Actuators B Chem. 95 (2003) 425–434.
[6] M. Hill, N. Harris, R. Townsend, N. White, S. Beeby, Separation of particles from a fluid using a microfabricated, ultrasonic device, in: Proceedings of the Fifth World Congress on Ultrasonics, Paris, France, 2003.
[7] M. Hill, Y.J. Shen, J.J. Hawkes, Modelling of layered resonators for ultrasonic separation, Ultrasonics 40 (2002) 385–392.
[8] J.J. Hawkes, W.T. Coakley, M. Groschl, E. Benes, S. Armstrong, P.J. Tasker, H. Nowotny, Single half-wavelength ultrasonic particle filter: predictions of the transfer matrix multilayer resonator model and experimental filtration results, J. Acoustic. Soc. Am. 111 (2002) 1259–1266.
[9] R.J. Townsend, M. Hill, N.R. Harris, N.M. White, Modelling of particle paths passing through an ultrasonic standing wave, Ultrasonics 42 (2004) 319–324.
[10] F.M. White, Fluid Mechanics, McGraw-Hill, 1999.
[11] J.F. Douglas, J.M. Gasiorek, J.A. Swaffield, Fluid Mechanics, Prentice Hall, Harlow, 2000.
[12] J. Pfahler, J. Harley, H. Bau, J. Zemel, Liquid transport in micron and submicron channels, Sens. Actuators A Phys. 22 (1990) 431–434.
[13] X.F. Peng, G.P. Peterson, Convective heat transfer and flow friction for water flow in microchannel structures, Int. J. Heat Mass Transfer 39 (1996) 2599–2608.
[14] G.M. Mala, D.Q. Li, Flow characteristics of water in microtubes, Int. J. Heat Fluid Flow 20 (1999) 142–148.

[15] J. Judy, D. Maynes, B.W. Webb, Characterization of frictional pressure drop for liquid flows through microchannels, Int. J. Heat Mass Transfer 45 (2002) 3477–3489.
[16] M. Gad-el-Hak, The MEMS Handbook, CRC, Boca Raton, 2001.
[17] X.X. Bai, J. Josserand, H. Jensen, J.S. Rossier, H.H. Girault, Finite element simulation of pinched pressure-driven flow injection in microchannels, Anal. Chem. 74 (2002) 6205–6215.
[18] E.B. van Akker, M. Bos, W.E. van der Linden, Convection and diffusion in a micro-flow injection system, Anal. Chim. Acta 373 (1998) 227–239.
[19] S. Ehlers, K. Elgeti, T. Menzel, G. Wiessmeier, Mixing in the offstream of a microchannel system, Chem. Eng. Process. 39 (2000) 291–298.

Biographies

R.J. Townsend graduated in 2000 from the University of Southampton with an MEng in mechanical engineering and is now studying for a PhD within the Electro-mechanical Research Group at Southampton. Her work involves the numerical simulation of particles under the influence of acoustic forces and other aspects of microfluidic device simulation. She is an associate member of the IMechE.

M. Hill is Reader in Electromechanical Systems in the School of Engineering Sciences, Southampton University. He graduated in 1985 from the Institute of Sound and Vibration Research, was appointed lecturer in 1990 and has research interests in acoustics (particularly ultrasonics) and transducers. His work has led to more than 80 publications, he is a chartered engineer, a member of the Institute of Measurement and Control, and a member of the Institute of Acoustics.

N.R. Harris graduated in 1988 from the University of Bath and was awarded a PhD in 1997 from the University of Southampton, on the use of ultrasound for communication purposes. His research interests include thick-film sensors and surface acoustic wave devices, microengineering, and sensor interfacing. He is now a lecturer based in the Electronics and Computer Science Department at Southampton. He is a member of the IEE and a chartered engineer.

N.M. White is a professor of intelligent sensor systems within the School of Electronics and Computer Science at the University of Southampton and also director of the Institute of Transducer Technology. He was awarded a PhD in 1988 for a thesis on the application of thick-film piezoresistors for load cells. Professor N.M. White was appointed as lecturer in 1990, senior lecturer in 1999, reader in 2000 and currently holds a Personal Chair. He has published extensively in the area of thick-film sensors and intelligent instrumentation and is author or co-author of over one hundred scientific publications. He is a fellow of the Institute of Physics, a chartered engineer and a senior member of the IEEE and has served of several committees in various professional bodies.

S.P. Beeby graduated from the University of Portsmouth in 1992 with BEng (Hons) in mechanical engineering. He obtained a PhD from the University of Southampton in 1998. After his PhD he obtained industrial funding for a follow up project to develop a resonant differential pressure sensor. He has since been awarded a prestigious EPSRC Advanced Research fellowship to continue his research into active thick film material development and their combination with micromachined devices. His other research interests include energy harvesting for remote wireless sensor networks and he is the principal investigator at Southampton on an EU funded STREP project entitled 'Vibration Energy Scavenging (VIBES)'. He is also interested in human biometric systems. He has over 90 publications in the field including in learned journals and presented at conferences and colloquia. He is co-author of a recently completed book entitled 'MEMS Mechanical Sensors' published by Artech House. He is a member of the EPSRC peer review College, reviewer for numerous journal publications, a Chartered Engineer and Chartered Physicist and has provided consultancy services to several companies.

R.J.K. Wood has recently been promoted to Professor of Surface Engineering and Tribology in the Materials and Surface Engineering Research Group and is Director of the Institute of Research for Industry within the School of Engineering Sciences at the University of Southampton. He obtained a PhD in erosion-corrosion research from University of Southampton in 1987 and has over 15 years of research experience in the field of tribology and surface engineering. He has spent several years at BP Research but returned to Southampton in 1993 to re-establish surface engineering/tribology research. His group has three postdoctoral research fellows and six research students. Professor R.J.K. Wood has published over 80 papers in tribology research and related areas and has attracted over £2.5M research funding to this area. He has been a member of the EPSRC peer review College since 2000 and a chartered engineer and a member of the Institution of Mechanical Engineers and a member of the Institute of Corrosion since 1992.

Available online at www.sciencedirect.com
SCIENCE DIRECT®
Sensors and Actuators B 111–112 (2005) 481–486
SENSORS AND ACTUATORS B CHEMICAL
www.elsevier.com/locate/snb

Performance of a micro-engineered ultrasonic particle manipulator

N.R. Harris [a,*], M. Hill [b], R. Townsend [b], N.M. White [a], S.P. Beeby [a]

[a] *ECS, University of Southampton, ESD Group, Department of Electronics and Computer Science, Mountbatten Building, Highfield, Southampton SO17 1BJ, UK*
[b] *SES, University of Southampton, Highfield, Southampton SO17 1BJ, UK*

Available online 25 April 2005

Abstract

An ultrasonic microfluidic particle manipulator has been modeled and its experimentally measured separation performance has been compared with the modeled results for 1 μm latex particles, and yeast particles in water.

Keywords: Microfluidic; Ultrasonic; Separator

1. Introduction

High-frequency acoustic standing waves can be used to separate materials with different acoustic characteristics. The technique can be used to agglomerate particles, to hold particles within a flow, or to manipulate particles within the flow [1].

This paper briefly describes the construction and then describes both the acoustic modelling and the particle trajectory modelling of an ultrasonic device that uses this principle to separate particles. The combination of these models allows prediction of the performance of the separator, and these predicted results are compared with experimental performance.

2. Construction and modelling

The device has been constructed in Pyrex and silicon, to make use of standard silicon processes. It consists of a silicon substrate with channels etched through it, and a Pyrex top that has a cavity etched into it, as shown schematically in Fig. 1.

The depth of the cavity is 175 μm, and the unetched thickness of the Pyrex wafer is 1.7 mm. The silicon is 525 μm thick. These dimensions have been chosen as a result of a modelling study [3] and extended in [2].

These studies predicted a half-wave mode at 3.5 MHz and this was confirmed in [2], and this was the mode used for the results described here.

If the PZT transducer is driven at the required resonant frequency of the chamber, the result is an acoustic standing wave generated in the cavity. Particles within the fluid then move towards the pressure nodal plane, driven by acoustic radiation forces. In this case, the device is operated in half-wave mode and so the nodal position is in the centre of the cavity. The device has two outlets, and by selectively adjusting the relative outputs of these two channels, it is possible to arrange to have one flow predominately made up of the cleaner fluid, and the other to contain the majority of the particles. However, to make useful predictions about the separation performance of such a device, it is necessary to incorporate information about how specific particles behave under the influence of the acoustic field. In many ways this interaction between the acoustic field and the hydrodynamic system is the most important part of the system to model, and this model has been used to make predictions of the separation performance of the device as the transducer drive voltage is altered for a given flow rate, for a range of different particles and these predictions are compared with experimental results in this paper.

* Corresponding author.
E-mail address: nrh@ecs.soton.ac.uk (N.R. Harris).

0925-4005/$ – see front matter © 2005 Elsevier B.V. All rights reserved.
doi:10.1016/j.snb.2005.03.036

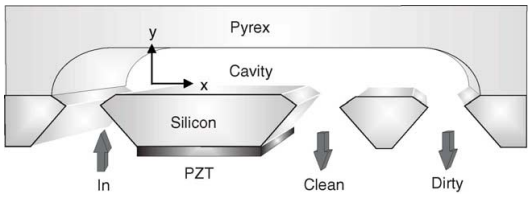

Fig. 1. Schematic of the separator device.

2.1. Predicted performance

As a particle passes along the main channel of the separator, it is subject to acoustic radiation, drag and buoyancy forces. Less significant forces such as those due to lateral acoustic effects, acoustic streaming and interparticle forces [1] are not considered by the following treatment. The dominant forces mentioned are solved numerically within MATLAB, resulting in a description of the particle trajectory as the particle passes through the ultrasonic separator. A series of particle trajectories are used to determine the relative spacing of particles and therefore the concentration as the particles move along the channel. This is a numerical method which enables both frequency dependence and non-uniform flow to be easily considered.

2.1.1. Acoustic radiation force

Within an acoustic field, the time averaged acoustic force on a particle, F_{ac}, in a direction normal to the transducer is given by [1]:

$$\langle F_{ac}(x, y, z)\rangle = -\nabla\langle\phi^{G}(x, y, z)\rangle \tag{1}$$

with

$$\langle\phi^{G}(x, y, z)\rangle = -V\left[\frac{3(\rho_p - \rho_f)}{2\rho_p + \rho_f}\langle\bar{E}_{kin}\rangle - \left(1 - \frac{c_f^2\rho_f}{c_p^2\rho_p}\right)\langle\bar{E}_{pot}\rangle\right] \tag{2}$$

where V is the particle volume, ρ_p and ρ_f the particle and fluid densities, respectively, c_p and c_f the speed of sound for the particle and fluid mediums, respectively, $\langle\bar{E}_{kin}\rangle$ and $\langle\bar{E}_{pot}\rangle$ the time-averaged kinetic and potential energies at a point in the field, respectively and ϕ^G the gradient of radiation force potential. The orientation of the x and y axes are indicated in Fig. 1.

F_{ac} can easily be determined for the resonant case and where the nodal position and level of acoustic energy within the channel is known [1]. However, by using an acoustic impedance transfer model [7,8], the variation in acoustic velocity and pressure through the device can be determined, which allows the kinetic and potential energies, $\langle\bar{E}_{kin}\rangle$ and $\langle\bar{E}_{pot}\rangle$ to be calculated. As the acoustic impedance is determined as a function of frequency, the calculation of F_{ac} is not limited to the resonant condition.

2.1.2. Drag forces

For low particle Reynold's number, $Re_p < 0.2$, the drag force F_D on a particle is calculated using Stokes drag, where A is the area of the particle in a plane normal to the flow and the velocity U_0 the relative velocity between the fluid $U(x, y)$ and particle $u(x, y)$

$$F_D = \tfrac{1}{2}C_D\rho_f U_0^2 A \tag{3}$$

where $C_D = 24/Re$ and $Re_p = 2R\mu U_0/\rho_f$.

Combining $u(x, y)$ and $U(x, y)$ with Eq. (3) and the expressions for C_D and Re_p gives:

$$F_D(x, y) = 6\mu\pi R(U(x, y) - u(x, y)) \tag{4}$$

To determine the drag force, the velocity profile across the depth of the main channel must be known. This can be determined numerically using CFD software but in this case, as laminar flow dominates, a parabolic profile describing flow between parallel plates [9] may be assumed,

$$U_x = \frac{6\bar{U}}{h^2}(hy - y^2) \tag{5}$$

where $\bar{U}$ is the mean fluid velocity and h the depth of the channel.

2.1.3. Buoyancy

The relative densities of the particle and fluid control the buoyancy force on a particle, where F_B opposes gravity:

$$F_B = \tfrac{4}{3}\pi R^3 g(\rho_f - \rho_p) \tag{6}$$

2.2. Particle trajectories

By summing the forces in both x and y directions a system of equations can be formed to give accelerations $\ddot{x}$ and $\ddot{y}$ for a particle of mass m. Note that both buoyancy and drag terms have x and y components, but the acoustic radiation force is assumed to be significant in the y direction only (this allows for the option of inclining the cell)

$$\ddot{x} = \frac{\sum F_x}{m} = \frac{F_{D_x} + F_{B_x}}{m} \tag{7}$$

$$\ddot{y} = \frac{\sum F_y}{m} = \frac{F_{ac} + F_{D_y} + F_{B_y}}{m} \tag{8}$$

This system of equations is solved in MATLAB using an ODE numerical solver function, where F_{ac} is extracted from the acoustic impedance transfer model implemented in MATLAB by Hill and Wood [7]. The ODE solver provides a series of particle coordinate locations and velocity components and therefore the trajectory of a particle, examples of which are shown in Fig. 2a.

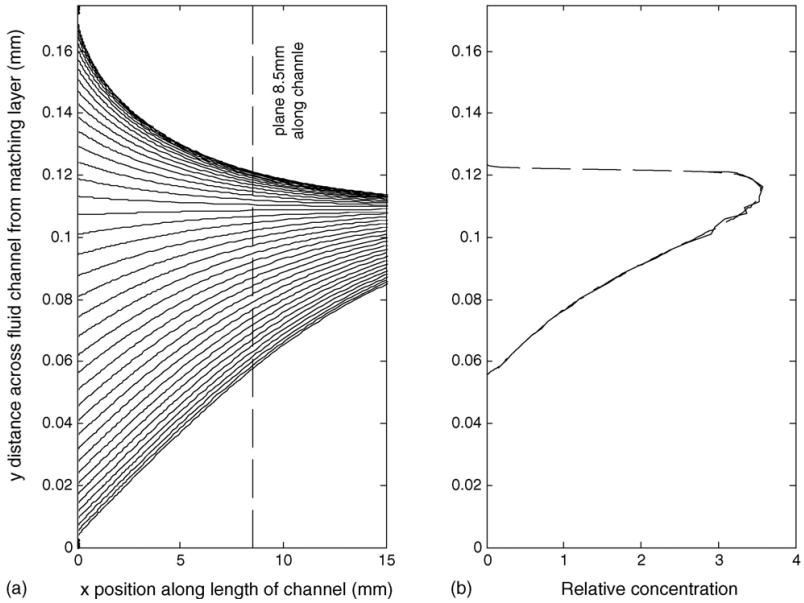

Fig. 2. (a) Convergence of particles towards nodal plane and (b) relative particle concentration across channel at a distance 8.5 mm along channel and acoustic field (relative concentration at inlet = 1) and where $h = 175$ μm.

By modelling a series of particles at the channel inlet and using the resulting particle coordinates, it is possible to calculate the change in concentration across the channel [4]. The change in concentration is dependent on the change in lateral (y) spacing between each particle. Based on the example given in Fig. 2a, at a distance 8.5 mm along the acoustic field (the edge of the acoustic field in a typical device) the particle trajectories illustrated result in the relative concentration distribution plotted in Fig. 2b.

Here, it is again important to consider the influence of the non-uniform flow profile; according to continuity, particle flow rate must remain constant therefore as a stream of particles moves into a plane of increased fluid velocity, the longitudinal (x) spacing between particles must increase thus reducing the concentration seen at that point.

In the ultrasonic separator, two outlets split the flow and depending on the relative flow rates through these outlets the flow can be assumed to divide at a height $y = hN$. The particle flow rate passing through outlet 1, for example, can be calculated using the concentration data described previously within the bounds of $0 < y < hN$. Further, the concentration through the outlet is the particle flow rate divided by the fluid flow rate. A similar method within the bounds $hN < y < h$ can be used for outlet 2 or alternatively, by considering mass (particle) continuity. It is this method that is used to determine the predicted outlet concentration values presented in this paper.

3. Experiment

The experimental set-up consists of two peristaltic pumps, one feeding the inlet of the separator device and one drawing fluid through one of the two outlets. The device is isolated from the pulses produced by the pumps by using air filled syringes to act as dampers as shown in Fig. 3.

The transucer was driven via a fixed gain (50 dB) RF power amplifier by a signal generator at the resonant frequency of the chamber, previously determined to be a nominal 3.5 MHz. Fine adjustment was made by monitoring the transducer voltage with an oscilloscope and adjusting the frequency for a voltage minimum.

The flow rates through the outlets were chosen such that $Q_1 < Q_2$. Therefore, operating in the half-wavelength mode with a particle stream formed along the centre of the separator channel, clear fluid can be extracted through outlet 1 and particle concentrate through outlet 2.

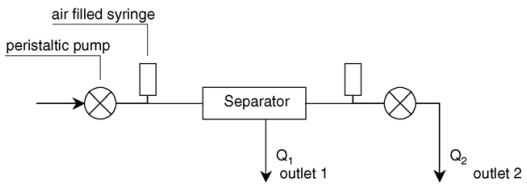

Fig. 3. Schematic of experiment.

3.1. Concentration measurement

For each test, the fluid through each outlet was collected and its concentration measured using a turbidity sensor (Honeywell APMS-10GRCF) [5], previously calibrated for the particles under test.

3.1.1. Sensor calibration

This sensor offers the possibility of a low-cost, flow-through turbidity measuring system. The sensor is manufactured by Honeywell (Part number APMS-10GRCF) [5] and is a microprocessor controlled system that measures turbidity, conductivity and temperature. It was originally designed for use in low cost, high volume applications, and so calibration to assess its suitability for this application was necessary. Readings are output in digital form and can be updated once every 1.3 s. The turbidity measurement is achieved optically by using both a transmissive and a 90° reflective sensor, allowing ratiometric readings. The sensor can be connected to a PC via an RS232 interface board. Custom software was written in Visual Basic to allow ratiometric measurements to be calculated from the raw data, and to be logged.

Measurement values vary with the materials in the fluid, and therefore the device needs to be calibrated for each type of fluid/particle mix. An absolute calibration was carried out using 1 μm latex particles in water, comparing the sensor reading with the actual number of particles in the sample counted using a microscope and haemocytometer. Fig. 4 shows the sensor output against actual particle count for 1 μm latex particles [6].

In addition, a calibration curve for percentage by weight was also established for the yeast particles used. This is shown in Fig. 5.

4. Results

Experimental and modelled results showing the influence of transducer voltage on both separation of 1 μm latex particles and yeast cells are shown in Figs. 6 and 7, respectively.

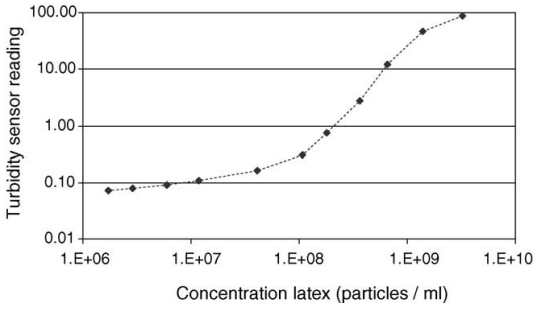

Fig. 4. One micron particle concentration against sensor output.

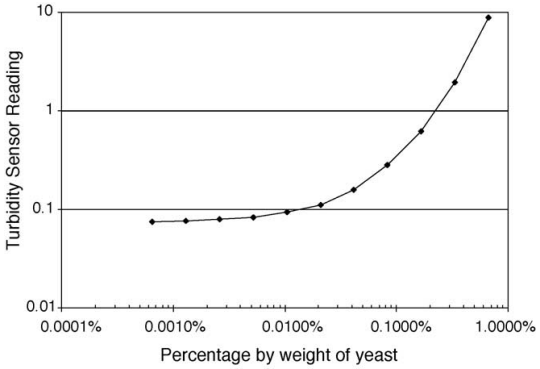

Fig. 5. Percentage of yeast by weight against sensor output.

In the experiments for yeast, a total flow rate ($Q_1 + Q_2$) of approximately 0.053 ml/s was maintained, 25% of which passed through outlet 1. For the 1 μm latex particles, these figures were 0.028 ml/s and 21%, respectively.

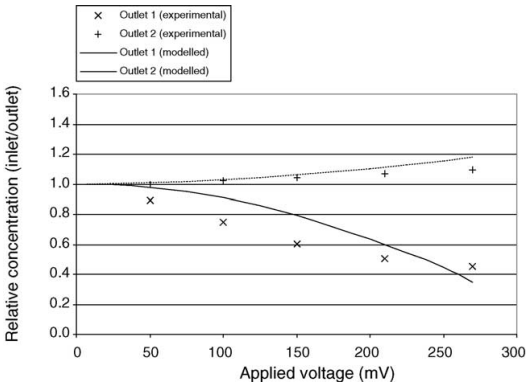

Fig. 6. Separation of 1 μm latex particles based on an initial concentration of 0.016 wt.%. Applied voltage is input voltage to amplifier.

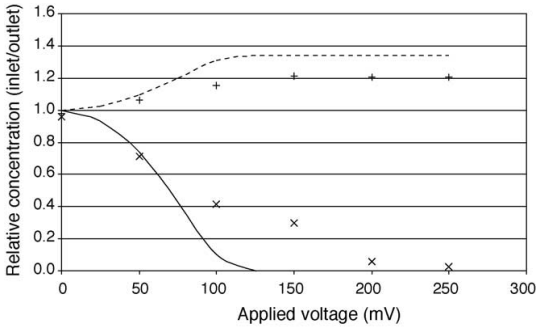

Fig. 7. Separation of yeast particles based on an initial concentration of 0.2 wt.%. Applied voltage is input voltage to amplifier.

Increasing transducer voltage increases the magnitude of the acoustic radiation force acting on suspended particles and in turn the rate at which they agglomerate on the nodal plane. Therefore, and as expected, the results show that increasing voltage causes more particles to pass through outlet 2 and decreases the concentration seen through outlet 1.

The modelled results for the separation of 1 μm particles (Fig. 6) compare well with the experiment results. Generally, the experimental results show slightly lower concentrations than modelled predictions, which can be attributed to the adhesion of particles on the walls within the fluid network surrounding the separator. At higher voltages, particles tend to clump together under higher acoustic forces, potentially disturbing the laminar flow required for successful separation and limiting the possible clearance through outlet 1.

For the separation of yeast, the modelled results are more optimistic than the experimental results. The initial concentration of the yeast was high at 0.2% compared to that for the 1 μm latex particles, where 0.015% was used. This high concentration may impede the motion of the yeast cells towards the nodal plane, indeed clustering was observed to be a greater problem with the yeast than with the latex particles. However, at higher voltages, separation is successful, producing a high degree of clarification. The degree of separation is influenced by flow rate as well as acoustic field strength, and a reduction of overall flow rate allows increased separation to occur. Further tests are required to investigate the influence of concentration and flow rates on the separation performance.

5. Conclusions

Previous work by the authors has investigated the acoustic fields within micro-engineered separators and this has allowed the influence of acoustic radiation forces on stationary particles to be successfully modelled. This work has extended this model to allow the path of particles flowing through the cell to be successfully predicted. The experimental work has verified the principles of the modelling, and this allows the combined model to be used to refine the performance of such separators before committing to production. In addition, the combined model can be used to investigate the feasibility of different configurations of the separator and is able to be easily tailored for specific particles, both in size and material properties. Operating parameters can then be predicted to give the required level of separation.

Acknowledgements

The authors wish to thank both the Engineering and Physical Research Council (EPSRC) and DSTL for their financial support under grant number GR/R13333/01. We also gratefully acknowledge the financial support given by Microfiltrex Ltd.

References

[1] M. Groschl, Ultrasonic separation of suspended particles, part I: fundamentals, Acustica 84 (3) (1998) 432–447.
[2] N.R. Harris, M. Hill, Y. Shen, R.J. Townsend, S. Beeby, N.M. White, A dual frequency, ultrasonic, micro-engineered particle manipulator, Ultrasonics 42 (2004) 139–144.
[3] N.R. Harris, M. Hill, S. Beeby, Y. Shen, N.M. White, J.J. Hawkes, W.T. Coakley, A silicon microfluidic ultrasonic separator, Sens. Actuators B 95 (2003) 425–434.
[4] R.J. Townsend, M. Hill, N.R. Harris, N.M. White, Modelling of particle paths passing through an ultrasonic standing wave, Ultrasonics 42 (2004) 319–324.
[5] Honeywell Sensing and Control Catalogue, Honeywell Inc., Freeport, IL, pp. 27–28.
[6] Polysciences Europe Gmbh, Eppelheim, Germany, www.polysciences.com.
[7] M. Hill, R.J.K. Wood, Modelling in the design of a flow-through ultrasonic separator, Ultrasonics 38 (2000) 662–665.
[8] M. Hill, Y.J. Shen, J.J. Hawkes, Modelling of layered resonators for ultrasonic separation, Ultrasonics 40 (2002) 385–392.
[9] F.M. White, Fluid Mechanics, 4th ed., McGraw-Hill, 1999.

Biographies

Nick Harris is a lecturer based in the Electronics and Computer Science Department at Southampton. He graduated in 1988 from the University of Bath and was awarded a PhD in 1997 from the University of Southampton, on the use of ultrasound for communication purposes. His research interests include thick-film sensors and surface acoustic wave devices, micro-engineering and sensor interfacing. He is a member of the IEE and a chartered engineer.

Rosemary Townsend graduated in 2000 from the University of Southampton with an MEng in mechanical engineering and is now studying for a PhD within the Electro-mechanical Research Group at Southampton. Her work involves the numerical simulation of particles under the influence of acoustic forces and other aspects of microfluidic device simulation. She is an associate member of the IMechE.

Martyn Hill is a reader in electromechanical systems in the School of Engineering Sciences, Southampton University. He graduated in 1985 from the Institute of Sound and Vibration Research, was appointed lecturer in 1990 and has research interests in acoustics (particularly ultrasonics) and transducers. His work has led to more than 80 publications, he is a chartered engineer, a member of the Institute of Measurement and Control, and a member of the Institute of Acoustics.

Steve Beeby graduated from the University of Portsmouth in 1992 with BEng (Hons) in mechanical engineering. He obtained a PhD from the University of Southampton in 1998. After his PhD, he obtained industrial funding for a follow up project to develop a resonant differential pressure sensor. He has since been awarded a EPSRC Advanced Research fellowship to continue his research into active thick film material development and their combination with micromachined devices. His other research interests, include energy harvesting for remote wireless sensor networks. He is also interested in human biometric systems. He has over 90 publications in the field. He is a co-author of a recently completed book entitled ‘MEMS Mechanical Sensors’ published by Artech House. He is a chartered engineer and chartered physicist.

Neil M. White is a professor of intelligent sensor systems within the School of Electronics and Computer Science at the University of Southampton and also director of the Institute of Transducer Technology. He was awarded a PhD in 1988 for a thesis on the application of thick-film piezoresistors for load cells. He has published extensively in the area of thick-film sensors and intelligent instrumentation and is author or co-author of over 100 scientific publications. He is a fellow of the Institute of Physics, a chartered engineer and a senior member of the IEEE and has served of several committees in various professional bodies.

Available online at www.sciencedirect.com
SCIENCE DIRECT®
Biosensors and Bioelectronics 21 (2005) 758–767
BIOSENSORS & BIOELECTRONICS
www.elsevier.com/locate/bios

Spore and micro-particle capture on an immunosensor surface in an ultrasound standing wave system

Stacey P. Martin[a,1], Rosemary J. Townsend[b], Larisa A. Kuznetsova[a], Kathryn A.J. Borthwick[a], Martyn Hill[b], Martin B. McDonnell[c], W. Terence Coakley[a,*]

[a] *School of Biosciences, Cardiff University, Main Building, Park Place, Cardiff CF10 3TL, UK*
[b] *School of Engineering Science, Electromechanical Research Group, University of Southampton, Southampton SO17 1BJ, UK*
[c] *Dstl Porton Down, Salisbury, Wiltshire SP4 0JQ, UK*

Received 22 October 2004; received in revised form 17 December 2004; accepted 20 January 2005
Available online 16 February 2005

Abstract

The capture of *Bacillus subtilis* var. *niger* spores on an antibody-coated surface can be enhanced when that coated surface acts as an acoustic reflector in a quarter wavelength ultrasonic (3 MHz) standing wave resonator (Hawkes, J.J., Long, M.J., Coakley, W.T., McDonnell, M.B., 2004. Ultrasonic deposition of cells on a surface. Biosens. Bioelectron. 19, 1021–1028). Immunocapture in such a resonator has been characterised here for both spores and 1 μm diameter biotinylated fluorescent microparticles. A mean spatial acoustic pressure amplitude of 460 kPa and a frequency of 2.82 MHz gave high capture efficiencies. It was shown that capture was critically dependent on reflector thickness. The time dependence of particle deposition on a reflector in a batch system was broadly consistent with a calculated time of 35 s to bring 95% of particles to the coated surface. A suspension flow rate of 0.1 ml/min and a reflector thickness of 1.01 mm gave optimal capture in a 2 min assay. The enhancement of particle detection compared with the control (no ultrasound) situation was ×70. The system detects a total of five particles in 15 fields of view in a 2 min assay when the suspending phase concentration was 10^4 particles/ml. A general expression for the dependence of minimum concentration detectable on; number of fields examined, sample volume flowing through the chamber and assay time shows that, for a practical combination of these variables, the threshold detection concentration can be two orders of magnitude lower.

Keywords: Ultrasound; Biosensor; *Bacillus subtilis* var. *niger*; BG spores; Immunoassay; Bio-terrorism

1. Introduction

Bacteria-detecting sensors include immunosensors where antibodies in intimate contact with a transducer act as specific capture elements for the cells (Perkins and Squirrell, 2000). Highly sensitive amperometric immunosensors based on antibody immobilization on membranes have been developed for rapid detection of bacteria (Shah et al., 2003). Membrane-filter-based approaches can be limited by blockage problems when monitoring environmental samples. More open systems that rely on molecular capture of bacteria flowing past a sensor surface are limited to sampling that part of the suspension flowing in close proximity to the sensor surface. Hawkes et al. (2004) described a system in which sample flowed through a membrane-free rectangular cross-section channel. An ultrasound transducer and an antibody-coated glass slide, acting as an acoustic reflector, formed the longer sides of the rectangle. The depth of the channel (coupling layer to reflector distance) was less than one half an acoustic wavelength, i.e. less than 0.25 mm at the driving frequency of 3 MHz. Forces associated with the acoustic field drove particles from the flowing suspension onto the reflector surface. Hawkes et al. (2004) reported a 200-fold ultrasound-induced enhancement

* Corresponding author. Tel.: +44 29 20874287; fax: +44 29 20874305.
E-mail address: coakley@cf.ac.uk (W.T. Coakley).
[1] Present address: Smiths Detection, Park Avenue, Bushey, Watford, Herts WD23 2BW, UK.

0956-5663/$ – see front matter © 2005 Elsevier B.V. All rights reserved.
doi:10.1016/j.bios.2005.01.013

of *Bacillus subtilis* spore capture from a 6.6×10^6/ml suspension flowing for 30 min.

Cells in a plane ultrasound standing wave field experience a direct radiation force that moves them towards a pressure node plane. The radiation force (F_r) on a cell of volume V_c, at a distance z from a pressure node is given (Gould and Coakley, 1973) by:

$$F_r = -(0.5\pi P_0^2 V_c \beta_w \lambda^{-1})\phi(\beta, \rho) \sin\left(\frac{4\pi z}{\lambda}\right) \quad (1)$$

where P_0 is the peak acoustic pressure amplitude and λ is the wavelength of sound in the aqueous suspending phase. The 'acoustic contrast factor' $\phi(\beta, \rho)$ is given by:

$$\phi(\beta, \rho) = \frac{(5\rho_c - 2\rho_w)}{(2\rho_c + \rho_w)} - \left(\frac{\beta_c}{\beta_w}\right) \quad (2)$$

where β_c, β_w are the compressibility's and ρ_c, ρ_w are the densities of the cell and suspending phase, respectively. When cells reach the node plane they experience a weaker radiation force acting parallel to the plane that can act to aggregate them (Fig. 1). When an ultrasonic resonator has a depth equal to $\lambda/4$, the thicknesses of other layers in the resonator can be selected so that the only pressure node in the suspension occurs at the surface of the reflector (Hawkes et al., 2002a). Cells should thus be drawn towards that surface.

In addition to the direct radiation force, particles in a chamber can be influenced by several types of acoustically driven flows—streaming—that differ in their origin and spatial scale. Acoustic streaming is non-oscillatory steady fluid motion originating from the spatial non-uniformity of the sound field or from energy dissipation at the liquid–solid interfaces of the container. Spengler et al. (2003) applied a particle image velocimetry technique to measure Rayleigh type streaming within a half wavelength chamber. Kuznetsova and Coakley (2004) applied the technique to both half and quarter wavelength resonant systems. They showed that radiation pressure mostly determined the behaviour of 1 μm particles in quarter wavelength resonators. In half wavelength systems, where streaming vortices developed in the planes parallel to the transducer's radiating surface, radiation pressure had a significant effect on the particle redistribution in the vortices. Interest in acoustic streaming has increased over the last decade as its applications in various processes have been reported. These include acoustic mixing (Suri et al., 2002), enhancement of DNA hybridization rate (Liu et al., 2003) and metal electrodeposition (Jensen et al., 2003).

Bacillus subtilis var. *niger* (also commonly known as *Bacillus globigii*, BG) is used here as a non-pathogenic simulant for *Bacillus anthracis*. A number of different methods have been developed to detect BG spores. These include biochips and microarrays (Stratis-Cullum et al., 2003; McBride et al., 2003; Rowe et al., 1999; Delehanty and Ligler, 2002), surface plasmon resonance (Perkins and Squirrell, 2000) and polymerase chain reaction (PCR; Belgrader et al., 1999). All methods, apart from the PCR, utilise antibodies to identify and capture the spores from suspension.

In the present work, immunocapture of 1 μm diameter latex particles has been examined as a function of acoustic pressure amplitude, slide thickness and flow rate through the chamber. The acoustic pressure in planes parallel to the transducer is simulated. The good agreement between simulations and experimental results for particle capture clarifies the key influence of reflector thickness on enhancement of immunocapture in the resonator. Spore behaviour and immunocapture in the resonator are as for the 1 μm latex particles.

2. Experimental

2.1. Ultrasound chamber

A flow chamber (Fig. 2) consisting of three basic elements, a 3 MHz, 30 mm × 30 mm, PZ 26 ultrasonic transducer (Ferroperm Krisgard, Denmark) glued, by conducting epoxy resin, to a 1.5 mm thick (3/4λ at 3 MHz) steel plate coupling the ultrasound to the sample and a glass microscope slide reflector (Fisher, Loughborough) of nominal thickness 1 mm, which is essentially one half-wavelength (λ/2) at a drive frequency of 2.8 MHz, was prepared. The reflector slide thicknesses were measured by micrometer and grouped into subsets in steps of 0.01 mm, so that the influence of reflector thickness on particle movement could be established. The back transducer electrode was etched (Hawkes and Coakley, 2001) to give a central 20 mm × 10 mm active area. The glass reflector was held in place by a brass top-plate secured with screws, which had a 14 mm × 64 mm window to allow microscopic observation. The depth of the suspending layer (135 ± 10 μm) was measured by microscopy, as the distance between the steel coupling plate and the glass reflector, before each experiment. A gasket (internal dimen-

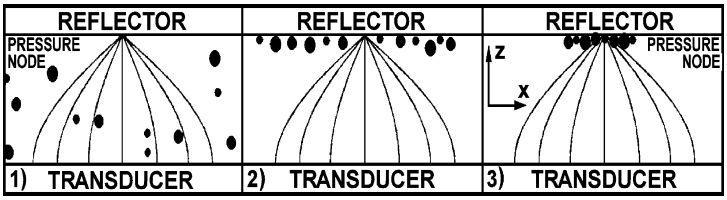

Fig. 1. Effect of the direct acoustic radiation force (RF) on particles in a resonator with λ/4 water path length depth (λ/2 reflector thickness): (1) particle distribution before exposure to sound, (2) axial RF effect and (3) lateral RF effect; *x*: in transducer plane, *z*: normal to plane.

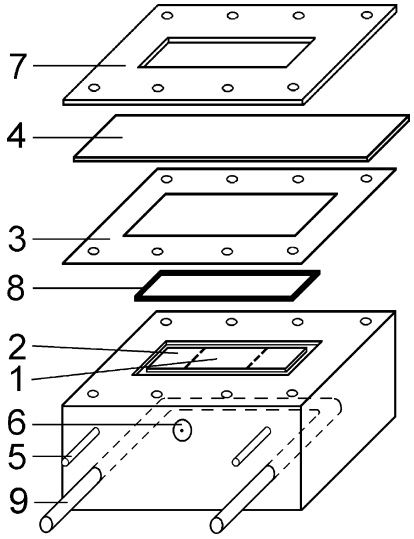

Fig. 2. Resonator design: (1) transducer's active area, (2) steel layer, (3) spacer for water layer, (4) glass reflector, (5) water inlet (outlet), (6) electrical connection, (7) top brass, (8) elastic gasket and (9) water cooling system.

sions 10 mm × 60 mm, prepared from *Sylgard*® 182 silicone elastomer (Farnell, Leeds)) surrounded the chamber cavity and maintained an air- and water-tight seal between the reflector and coupling plate. The 32 mm thick steel base of the chamber included a water-cooling circuit. Generation of the high frequency signal applied to the transducer has previously been described (Spengler et al., 2001).

2.2. Selection of operating frequencies

A one-dimensional transfer matrix model for piezoelectric multilayer resonators (Nowotny and Benes, 1987; Hawkes et al., 2002a,b; Nowotny et al., 1991) relates the piezoelectrically coupled properties of the active piezolayer and the properties of the non-piezoelectric (passive) layers of the resonator system. The model then calculates electrical admittance as a function of frequency (Nowotny and Benes, 1987; Gröschl, 1998; Hawkes et al., 2002a,b). The parameters for the different layers are given in Table 1. The admittance spectrum for a wide frequency range is shown in Fig. 3a. Preliminary experimental observations showed significant particle movement towards the reflector at frequencies close to the minor impedance change (arrowed) at 2.8 MHz. The frequency of this minor change was dependent on the measured thickness of the reflector (2.6 kHz/μm; Fig. 3b) for a given water layer thickness and on the water layer thickness for a given reflector thickness (1.0 kHz/μm; Fig. 3c). The calculated frequency dependence of the acoustic energy density in the water layer also showed maxima at the region of the minor impedance change (Fig. 4). The experimental voltage change detected on the frequency scan of the voltage applied to the transducer at the frequency of the minor admittance change

Table 1
Multilayer model: data for the ceramic and the passive layers

Property	Data for ceramic layer (piezoelectric layer)
Ceramic thickness (mm)	0.67[a]
Ceramic frequency constant (speed of sound/2) (Hz m)[b]	2040[c]
Density (kg/m)	7700[c]
Dielectric constant at F_{min} (ε')	8×10^{-9}[d]
Dielectric constant at F_{max} (ε')	8×10^{-9}[d]
Dielectric loss ($\tan\delta$)	0.003[c]
Coupling factor	0.47[c]
Area of ultrasonic field (mm^2)	200[e]
Equivalent area (mm^2)	200[e]
Quality factor	10[f]

Property	Data for passive layers			
	Epoxy Resin	Stainless steel	Water at 25 °C	Soda lime glass
Thickness (mm)	0.05[f]	1.5[e]	0.135[e]	Various[g]
Frequency constant (Hz m)[b]	1220[h]	2900[a]	750[a]	2800[f]
Density (kg/m)	2000[h]	7800[a]	1000[h,d]	2400[h]
Dielectric constant	1	1	7.08×10^{-10}	1
Dielectric loss	1	1	1.25	1
Quality factor	25[h]	500[h]	100[h]	350[f]

[a] Kaye and Laby (1995).
[b] Half the speed of sound (m/s) in the material.
[c] Ferroperm Piezoceramics (2004).
[d] Hawkes et al. (2002b).
[e] Measured.
[f] Fitted value.
[g] Glass thicknesses modelled were 0.98, 1.00, 1.01, 1.02 and 1.05 mm.
[h] Hill et al. (2002).

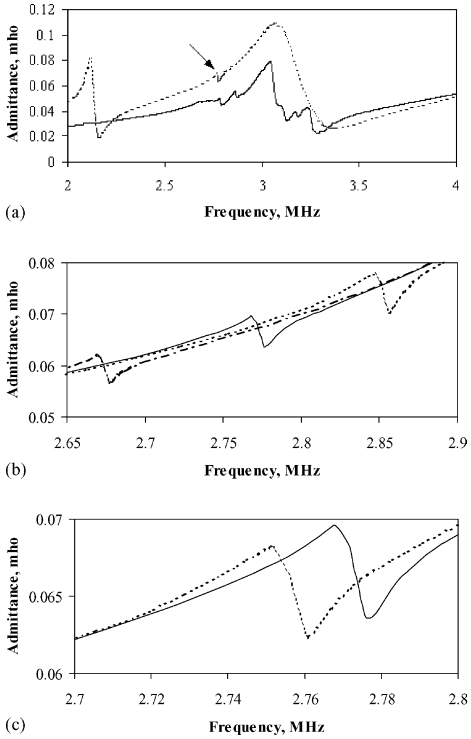

Fig. 3. Transfer matrix multilayer resonator model simulation of the frequency dependence of system admittance for (a) a 1.01 mm glass reflector and 0.135 mm water layer (- - -). A small admittance change at ∼2.8 MHz is arrowed. Measured electrical admittance (—) is also shown; (b) reflectors of 0.98 mm (- - -), 1.01 mm (—) and 1.05 mm (– – –), with a water layer of 0.135 mm; (c) water layers of 0.135 (—) and 0.15 mm (- - -) with a 1.01 mm reflector.

of Fig. 3 was too small to be applied to hunt (Hawkes et al., 2002b) for an optimum operating frequency. Consequently the frequency (f) was maintained at 2.82 MHz throughout the investigation, unless otherwise stated.

The electrical impedance of the chamber was measured using an Agilent Technologies Network Analyser (HP 8753E).

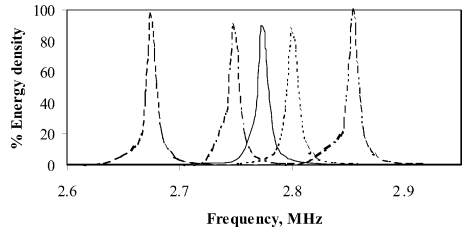

Fig. 4. Energy density in the aqueous layer presented as a percentage of the highest value between 1.5 and 5 MHz for all glass depths modelled. The only variation was found in the region of 2.8 MHz. Glass thicknesses are 0.98 mm (– - - –), 1 mm (- - -), 1.01 mm (—), 1.02 mm (– – –) and 1.05 mm (– –), with a water layer depth of 0.135 mm.

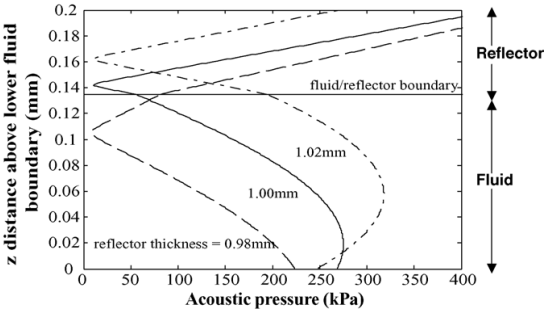

Fig. 5. Simulation of acoustic pressure across a 0.135 mm fluid layer and 70 μm of the reflector for reflector thicknesses of 0.98, 1.00 and 1.02 mm; f = 2.82 MHz.

A transfer impedance model simulation of the acoustic pressures in each layer of the resonator (Hill et al., 2002) is shown for f = 2.82 MHz and for different reflector thicknesses in Fig. 5. The simulation predicts that for a 0.98 mm reflector the pressure node is within the fluid at about 30 μm from the reflector surface. For the 1.00 mm case, the node is just within the reflector, while for the 1.02 mm reflector the node is further into the reflector but for that case particles below the pressure antinode (at about 50 μm from the coupling layer) will be forced downwards toward the lower boundary.

2.3. Calculation of time for latex particles to reach the reflector in a batch (no flow) system

The time t_h taken for a particle of radius r_c to travel, through a suspending phase of viscosity η, from a plane at distance z_1 from the node to another at distance z_2 is (Limaye and Coakley, 1998)

$$t_h = \left(\frac{3\lambda^2\eta r_c}{\pi}\right)\frac{[\ln(\tan(2\pi z/\lambda)]_{z_1}^{z_2}}{[P_0^2 V_c \beta_w \phi(\beta,\rho)]} \quad (3)$$

The values taken here are acoustic pressure P_0 = 460 kPa, λ = 0.516 mm, r_c = 0.5 μm and $\eta = 9\times10^{-4}$ kg/(m s). The density of the latex particle is 1.056 kg/m^3 and $\phi(\beta,\rho)$ = 0.5.

2.4. Numerical calculation of dynamics of particles flowing in a standing wave

It is assumed that a uniform concentration of particles φ enters the acoustic field, carried by a laminar, parabolic, fluid flow. Within the field, the particles are subject to the primary acoustic radiation force (Eq. (1)), a buoyancy force and a Stokes drag force. As the particles move under these forces the concentration at height z varies as (Higashitani et al., 1981):

$$\frac{\partial\varphi(z,t)}{\partial t} = -\frac{\partial(\dot{z}\varphi(z,t))}{\partial z} \quad (4)$$

The acoustic transfer impedance model (Hill et al., 2002), which determines numerically the acoustic radiation force, is

extended and used to solve the above equation numerically to provide a profile of concentrations across the fluid channel. By considering both particle concentration and velocity profile data across the depth of the fluid channel, the particle flow rate (particles/s) through the channel may be calculated. As the number of particles within the system is constant any difference between the particle flow rate at the inlet and a certain distance along the fluid channel can be attributed to the capture of particles at the walls. The capture data presented in later sections is percentage capture on the reflector surface, which in turn can be used to calculate an absolute value of particle capture if the initial particle concentration and total sample volume passing through the device are known.

2.5. Acoustic pressure amplitude measurement

A single 25 μm diameter latex sphere levitated in the standing wave field was observed with a microscope. The transducer voltage was gradually decreased to a threshold value $V_{thr}(x, y)$ below which the particle touched the coupling layer or, in line with the prediction of a pressure antinode in the sample volume for glass thicker than 1.01 mm (Fig. 4), sedimented onto the layer. At that voltage the calculable buoyancy-corrected gravitational force F_b acting on a suspended latex particle of density 1.056 kg/m^3 (measured in a Percoll density gradient (Bazou, personal communication)) equals the radiation force F_r (where for a given voltage, F_r has its maximum value, i.e. when $\sin(4\pi z/\lambda) = 1.0$ for $z = \lambda/8$ in Eq. (1)). Setting $F_b = F_r$, the threshold pressure amplitude $P_{0,thr}$ required, at $f = 2.82$ MHz, to levitate a sphere at a point in the (x, y) plane was then found from Eq. (1) to be 28 kPa.

$V_{thr}(0, 0)$ was calculated from measurements on two or three different single particles levitated in the centre of the active area (where the local peak pressure amplitude had a maximum) for each of a pair of reflectors of equal thicknesses. Since acoustic pressure amplitude is directly proportional to the operating voltage V_{op} applied to the transducer, the acoustic pressure amplitude $P_0(0, 0)$ at that voltage is given, in kPa, by:

$$P_0(0, 0) = 28 V_{op}[\overline{V_{thr}(0, 0)}]^{-1} \quad (5)$$

where $[\overline{V_{thr}(0, 0)}]^{-1}$ is given by the root mean square value of the reciprocals of the 5–6 measurements carried out.

The acoustic pressure amplitude decreased with distance away from the centre of the field but was still quite significant even close to the edge of the field. The pressure $P_0(0, 0)$ and the related P_0^2-dependent radiation force was therefore experienced only by particles in the central part of the field. Since particle collection occurs across the full area of the field it was appropriate to estimate a mean value $P_{0,op}$ for the mean effective pressure amplitude across the field. $V_{thr}(x, 0)$ was measured at a single glass thickness for single particles levitated at 9 points along the longer (x) axis within the acoustically active area. Variation of pressure amplitude in the y direction was similar to that in the x direction. Applying the same averaging factor $\overline{V_{thr}(0, 0)}/\overline{V_{thr}(x, 0)}$ for both x and y situations a mean pressure amplitude $P_{0,op}$ over the chamber area was then calculated as:

$$P_{0,op} = P_0(0, 0)\left[\frac{\overline{V_{thr}(0, 0)}}{\overline{V_{thr}(x, 0)}}\right]^2 \quad (6)$$

The pressure amplitudes given throughout the paper are the values of $P_{0,op}$. The relationship between $P_{0,op}$ and $P_0(0, 0)$ is given by $P_{0,op} = 0.77P_0(0, 0)$. $P_{0,op}$ were calculated to be: 225, 275, 460 and 170 kPa for 0.96, 1.00, 1.01 and 1.03 mm reflector thicknesses, respectively.

2.6. Measurement of acoustic streaming

The observation of particle movement in the direction of sound propagation (z) was carried out with an Olympus BX41M epi-fluorescent microscope. A standard PAL CCD JVC video camera (Victor Company, Japan) was connected via a 0.5 microscope adaptor and the images were recorded onto a standard videotape. The recorded video sequences were transferred to a PC video card in digital format with hardware MJPEG data compression (Pinnacle Miro Video DC30+) to be further processed with PIV software. PIV software analyses time-sequences of the images of convected tracer micro-particles and produces a vector map of the studied area, which exhibits the direction and velocity of the flow. Software FlowManager (Dantec Dynamics, Denmark) was used for the estimation of velocity fields.

2.7. Preparation of slides and test suspension

Standard microscope slides (Fisher; Loughborough, Leicestershire) were immersed in a 2% decon 90 (Decon Laboratories Ltd.; Hove, E. Sussex, UK) solution prepared using warm water, for 20 min, before use. They were then rinsed with warm water and dried in a nitrogen gas stream. The rest of this procedure was carried out in a laminar flow cabinet, to reduce dust particle contamination. The slide surface was modified using 2% 3-aminopropyltriethoxysilane (APTS, from Sigma; Poole, UK) solution in acetone (Fisher) and left for 20 min after which the slides were washed three times with acetone, and the acetone allowed to evaporate. A rectangle (15 mm × 10 mm) was outlined in the centre of the glass slide using an ImmEdge™ Pen (Vector Labs Inc.; Burlingame, CA, USA). When this had dried, 100 μl of a 2% glutaraldehyde solution (VWR; Lutterworth, Derbyshire, UK) in phosphate buffered saline (PBS) was pipetted within the rectangle, left for 1 h, washed several times with PBS and dried using N_2 gas. Following this 100 μl of 1 mg/ml Protein A (Sigma) in PBS was pipetted onto the area within the rectangle and left for 1 h. The slides were then washed with PBS and dried using N_2 gas. They were then incubated with a 0.05% Tween-20 solution prepared in PBS for 20 min to block any unbound glutaraldehyde, and rinsed three times with PBS. After this, 100 μl of 100 μg/ml solution of the anti-

body (anti-biotin from Vector Laboratories or anti-BG spore from Dstl) was pipetted onto the outlined rectangular area and left overnight. The modified slide was then incubated with PBS containing 0.05% Tween-20 and rinsed with normal PBS before being left to dry. The slides were stored in a dry state at 4 °C before use, usually within 7 days.

One micrometer biotinylated fluorospheres (Molecular Probes (Invitrogen); Lieden, Netherlands) were vigorously vortexed before being diluted in PBS. Microscopy showed that no aggregates were present during the experiments unless they were formed, at high acoustic pressures, under the influence of the ultrasonic standing wave. The same procedure was followed for the preparation of the BG spore (Dstl; Porton Down, Wiltshire) suspensions.

2.8. Assay method

The slide was installed into the chamber (Fig. 2). The depth of the sample layer was measured microscopically. A suspension of antigen was drawn through the chamber by a peristaltic pump (Gilson minipuls 3) at various flow rates and the transducer was activated at the selected frequency. On termination of exposure the slide was washed in situ for 2 min with distilled water at a flow rate of 6 ml/min to remove any particles non-specifically bound to the surface. Less than 5% of particles were removed by this procedure suggesting little weak or non-specific adhesion. In the BG spore capture experiments, the chamber was filled with a filtered sterilised solution of Auramine O, which is a fluorescent stain for BG spores, after which the chamber was washed again. The slide was removed from the chamber, 25 μl of Vectorshield was added and a cover slip applied. The slide was then placed on a flat surface at 4 °C until images were taken using an Olympus BX41M microscope with an IMBA filter and a F-view camera. Typically, the number of fluorescent particles within each of 10–15 randomly selected fields of view from the active area of the slide was counted using the AnalySIS software. A mean of the number of particles per field of view (*P*/FV) and its standard error were determined for each slide.

3. Results

3.1. Micro-particle capture dependence on acoustic pressure amplitude

Capture from a fluorescent latex micro-particle suspension of concentration $[M] = 10^7$/ml showed a maximum at a pressure amplitude of 460 kPa. Microscopic observation showed that fewer particles were reaching the glass at lower pressures, in line with the capture results. The reduction in capture at pressures >500 kPa coincided with the formation of particle clumps at the reflector. It may be that the trapping of particles in these clumps reduced the probability of their interaction with reflector-bound antibody. These clumps were washed away from the glass during the in-chamber post-exposure washing phase (i.e. they were not constrained by the presence of the antibody layer).

3.2. Particle behaviour in the chamber with different reflector thicknesses

One micrometer fluorescent particles ($[M] = 10^7$/ml) were observed microscopically in a set of experiments where the water layer thickness ranged from 150 to 170 μm, and the applied voltage was ∼50 V.

3.2.1. Batch mode

For the first 10–15 s of ultrasound application, the particles followed (were markers for) acoustic streaming in the active radiation area circulating within and about the planes parallel to the transducer's radiating surface. After that time they were clearly concentrating in two layers: at the reflector and near the base of the chamber. At 0.96 mm glass the upper layer of particles (80–90% of the population) was at a distance of 30–40 μm from the reflector in line with the prediction (Fig. 5) for thin reflectors. The concentration of a small number of particles near the chamber's base implies the presence of a pressure anti-node in the water phase due probably to its larger than $\lambda/4$ thickness (150 μm). At 1.00 and 1.01 mm glass 60–80% and at 1.11 mm glass about 50% of the particles concentrated in bands and clumps at the reflector. The patterns in the planes near the base and under the reflector were "symmetrical" to z-axis: they had approximately the same x–y coordinates in both planes.

3.2.2. Flow mode

When flow was applied (0.1 ml/min) before or during ultrasound exposure, the particles were smeared over wide areas on the surface of the reflector. High concentration of particles at the reflector's surface was observed in the areas where clumps were formed in batch mode.

3.3. Particle immunocapture

3.3.1. Temporal dependence in batch mode

The prediction that particle clearance would be almost complete after 40 s in a batch system is broadly consistent with optical observations and with the experimental measurements of capture over time (Fig. 6). The microscopic experiments showed that the bulk volume of the chamber's active region was cleared of 1 μm particles after 40 and 60 s for 1.01 and 1.00 mm reflectors, respectively.

3.3.2. Flow rate dependence

Fig. 7 shows that introduction of flow improved capture (*P*/FV) in 2 min by a factor of two compared to the batch result, when the flow rate was 0.1 ml/min and $[M] = 10^7$ /ml. There was no significant change in *P*/FV with increase in flow rate to 0.4 ml/min. The continuous trend in Fig. 7 shows the numerical simulation of capture where maximum number

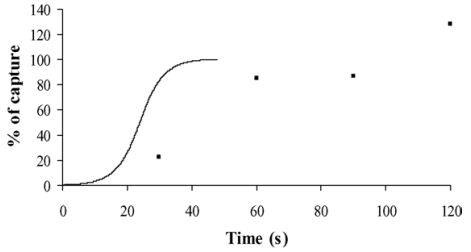

Fig. 6. The distance from the reflector (as a percentage of λ/4) that is cleared of 1 μm particles after a time t (simulation based on Eq. (3); continuous curve) and experimental determination of percentage of particles reaching 1.01 mm reflector (normalised to 100% at the mean of 60, 90 and 120 s capture measurements). [M] = 10^7/ml and Q = 0 ml/min.

of cells reaching the reflector is normalised to the highest experimental value of P/FV.

3.3.3. Particle capture dependence on reflector thickness

Immunocapture was strongly dependent on slide thickness (Fig. 8). The average P/FV was highest for 1.01 mm slides. The continuous trend in Fig. 8 represents the predicted percentage capture for different slide thicknesses normalised against the highest experimental value of P/FV.

3.3.4. Particle capture (experimental) in a flow for different suspension concentrations

A number of 1 μm particle and of BG suspensions were prepared at different values of [M] to determine the ultrasound capture-enhancement factor (Fig. 9). The capture was determined at the different concentrations using the experimental high capture-yield values for acoustic pressure, slide thickness and flow rate. The concentration dependence of spore capture in a batch system is shown in Fig. 9b. Ultra-

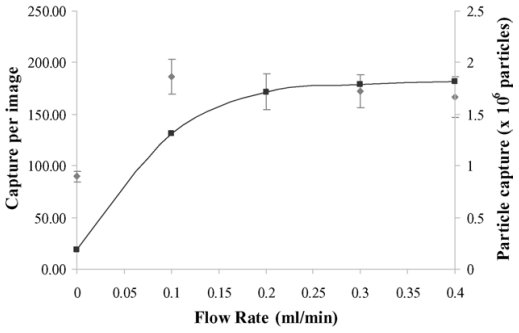

Fig. 7. P/FV for 1 μm particles ([M] = 10^7/ml) at the reflector surface, f = 2.82 MHz, P_0 = 460 kPa, assay time = 2 min, and a slide thickness of 1.01 mm (simulated data—dark grey points, experimental data—light grey points). The continuous trend is the numerical simulation of capture where maximum capture in millions of cells reaching the reflector is normalised to the highest experimental value of P/FV. Each experimental data point is the mean ± standard error of the mean of five replicates (15 images per replicate).

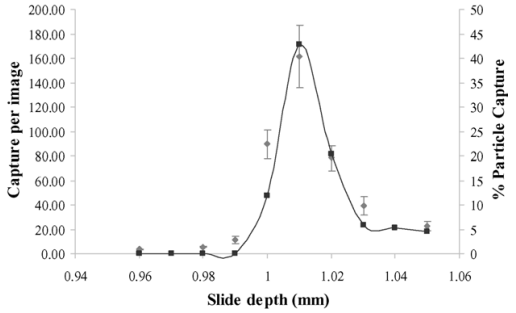

Fig. 8. Capture of 1 μm particles ([M] = 10^7/ml) for glass reflectors of different depths (dark grey points are simulated data, and light grey are experimental data). Each experimental point represents one slide (mean ± S.E.M.) from which 15 fields of view were counted (P_0 = 460 kPa, assay time = 2 min, Q = 0.2 ml/min).

sound enhancement of particle capture was estimated here at the region of most interest, i.e. where P/FV and [M] are low. The decrease in [M] for log(P/FV) = 0 is 100-fold while the increase in P/FV when log([M]) = 6.25 is 50-fold. The

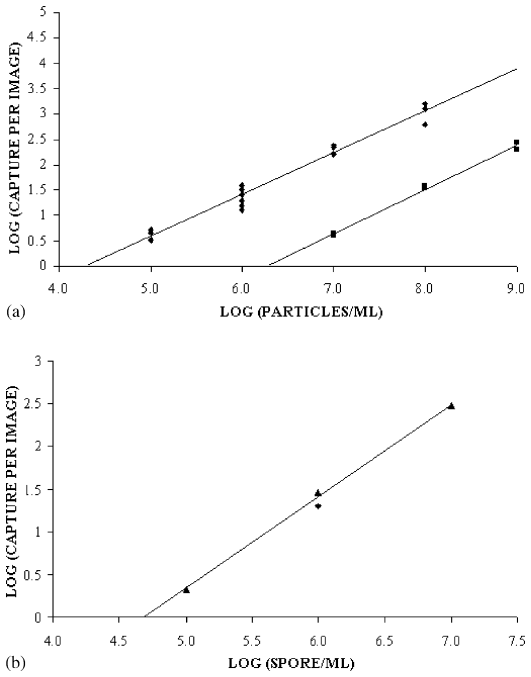

Fig. 9. Capture for P_0 = 460 kPa, assay time = 2 min, and slide thickness = 1.01 mm of: (a) 1 μm biotinylated particles (Q = 0.1 ml/min) with (diamond-shaped points) and without (squares) ultrasound. The slopes of the lines are 0.82 and 0.87 for sonicated and control samples, respectively. (b) BG spores (diamond-shaped) and biotinylated particles (triangles) in a batch system (Q = 0) with ultrasound exposure. The slope of the line is 1.07. Each point is the mean for one slide from which four or 15 images were processed.

enhancement is taken as the 70-fold geometric mean of those values.

4. Discussion

4.1. Resonator impedance, pressure distribution and particle movement

The measured admittance spectrum showed a main peak at 3.05 MHz and some frequencies with lesser changes including a minor change at 2.86 MHz (Fig. 3). The ratio of the measured admittance at 3.05 MHz to that at 2.86 MHz was 1.45. Setting the transducer Q factor in Table 1 to a value of 10 produced comparable 3.05/2.8 MHz admittance ratio in the matrix transfer model admittance spectrum. The frequency at which the admittance peak occurred in the model was most sensitive to the value taken for the glue layer thickness in Table 1. Microscopic observation showed that particle movement towards the reflector was strongest at the frequency of the minor admittance-change (near 2.8 MHz) and was strongly dependent on reflector thickness. The model also showed that the frequency and amplitude of that minor admittance change, and only of that change, were sensitive to glass thickness, speed of sound and the chosen quality factor thus supporting the conclusion that particle behaviour was strongly dependent on the glass layer.

The experimental microscopic observations of particle movement within the chamber and the concentration of particles at or near the glass surface and on the coupling layer were consistent with the simulated (Townsend et al., 2004) dependence of pressure node and antinode position on glass thickness (Fig. 5). The influence of the reflector thickness on pressure node and antinode position arises from the boundary condition that the acoustic pressure at the glass/air interface be zero. The position of the first pressure node within the resonator is then close to the water/glass interface since the nominal thickness of the glass available to us was close to $\lambda/2$ at the operational ultrasound frequency. The simulation provides insight to the experimental results that some particles (those below the pressure antinode) are driven to the coupling layer for the thicker slides (Fig. 10a), and no particle reaches the glass for the lower thicknesses (Figs. 8 and 10b).

Experimental observations showed that almost all particles arriving at the glass were single particles rather than being in clumps or aggregates. The implication that the movement of each particle is not strongly influenced by the concentration of its neighbours is consistent with the result that the slopes of the log–log plots of Fig. 9 are close to 1.0, suggesting linear relationships between capture and initial concentrations of particles and spores.

4.2. Extent of quantitative agreement between experiments, calculation and simulations

The calculated time for micro-particles from a quarter wavelength thick suspension layer, to reach a pressure node

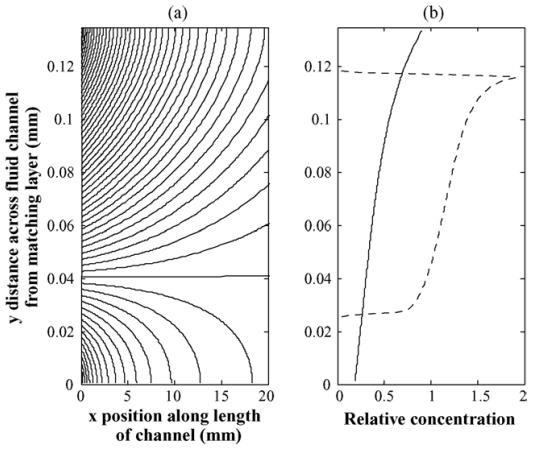

Fig. 10. Simulation of particle movement through the acoustic field for $Q = 0.1$ ml/min, length of field 20 mm, $f = 2.82$ MHz, $P_0 = 460$ kPa showing: (a) particle trajectories through a distance of 20 mm for slide thickness of 1.01 mm, (b) concentration of particles in suspension at a fixed distance (10 mm) along the channel for slide thicknesses 0.98 (broken line) and 1.01 mm (solid line).

at the reflector surface is 45 s (Fig. 6). If one considers, from Fig. 10, that a 1.01 mm reflector will harvest a volume reaching from the glass surface to a depth of 95 μm then that time drops to 35 s. This time is somewhat lower than that assessed (40 s) from microscopic observation of particles under those conditions. The overestimation of clearance by the analytical calculation might be accounted for by approximations in the derivation of the pressure amplitude across the transducer area (Section 2.5). The experimentally estimated time (40 s) to clear a volume of particles in a batch system will be taken below as the mean 'residence' time (t_{res}) of a particle in the acoustic field when almost all particles are captured. We note that, as expected, the analytical result for temporal accumulation of particles at the surface (Eq. (3); Fig. 6) is the same as the simulated value for the case $Q = 0$.

The experimental results for capture in flow have their greatest value when $Q = 0.1$ ml/min (Fig. 7) and that value is about twice the capture value when $Q = 0$. The experimental capture then declines slightly and remain essentially constant afterwards. The presence of a maximum in the number of particles detected, over a fixed assay time t_{assay}, in a flow system can be considered as follows. Few particles will be captured over the later stages of an assay when Q is low because the mean time spent by a particle in the field ($t_{res\text{-}flow}$) is significantly greater than the mean residence time ($t_{res\text{-}batch}$) required to capture most of the particles in a batch system. Capture will increase if Q is increased so that $t_{res\text{-}flow}$ decreases towards and finally reaches $t_{res\text{-}batch}$. Further increase in Q will increase delivery of particles to the test volume, but also decrease the fraction of them reaching the reflector over the assay time so that the total count may no longer grow. The simulation (Fig. 7) shows a larger relative capture increase peaks

at higher Q and then continues to grow slightly compared to the experimental case. The discrepancies decrease on recognising that the experimental $t_{\text{res-batch}}$ is longer than the calculated time (Fig. 6). The optimal efficiency of capture condition $t_{\text{res-flow}} = t_{\text{res-batch}}$ will then occur at lower experimental values of Q. It follows that the optimal flow rate for efficient capture, when the active field volume is V_{act}, is given by:

$$Q_{\text{opt}} = \frac{V_{\text{act}}}{t_{\text{res-batch}}} \quad (7)$$

The trend in experimental capture of particles with increasing glass thickness is well matched to the simulation for that case (Fig. 8). Since the comparison is made by normalising on the largest value of each system it depends only on the profile of the experimentally determined pressure amplitude dependence on glass thickness. It does not depend on the time taken for a particle to reach the glass for any one condition.

4.3. Influence of radiation pressure and streaming on particle movement

The above predictions of particle movement consider radiation force as the controlling acoustic influence. They do not include particle convection by acoustic streaming. While streaming velocities of ~50 μm/s have been measured here (Section 2.6) the extent of agreement between experiment and the radiation force models suggests that any influence they may have on particle arrival at the surface is secondary to that of radiation pressure for 1 μm diameter particles (this situation reverses when particle size is reduced to 200 nm (Kuznetsova et al., submitted for publication)).

4.4. Comparison of spore and latex bead response to acoustic radiation force

Assuming spherical particle forms, the particle properties determining the operating radiation force are its volume, density and compressibility (Eq. (1)). The mode value for the diameter of BG spores is (Hairston et al., 1997) just less than the 1 μm diameter of the fluorescent micro-particles. It is known that spores have low water content and a mechanically strong endospore coat (Driks, 2002). However, values for the density or compressibility of spores are not known to us. Operationally, a comparison of spore and latex capture under the same acoustic conditions suggested that immunocapture was about 60% higher for spores than for latex (Fig. 9b). Direct microscopic observation of the movement towards and collection of spores and of latex particles at the reflector also suggested that spores experienced a slightly greater radiation force. For the present purposes the force on the spore and latex particle will be regarded as comparable.

4.5. Assay sensitivity

The active area of the transducer was 200 mm^2, the depth of the chamber was 0.129 mm so that the volume (V_{act}) of the sample over the transducer was 26 μl when the node was at the reflector surface. The number of particles in 26 μl, when [M] = 10^6/ml, was 26,000. The antibody-coated area was 150 mm^2 while that of a microscopic field of view for the objective magnification employed (×20) was 0.148 mm^2. Consequently the active capture area contained the equivalent of 1010 fields of view. This number of fields of view will be denoted by N_{FV}. The value of P/FV for complete capture would then be 26,000/1010 = 26 in agreement with the best-fit straight line value of 26 for P/FV at [M] = 10^6/ml (Fig. 9). The figure also shows that the particle concentration was 1.9×10^4/ml when log(P/FV) = 0, i.e. P/FV = 1.0, for a 2 min assay. The total count (TC) over the n fields on which the calculation of P/FV was based is given by $n \times (P/\text{FV})$, where n is the number of fields of view interrogated. It is reasonable to assume that repeat values of TC should, when other sources of experimental error are ignored, be randomly distributed according to the Poisson distribution.

The immunocapture assay is an integrating assay when, as in the present case, access to a binding site on the surface is not capture limiting. In principle therefore there is no lower concentration for detection of an appropriately labelled particle provided the assay time is not limited. Limits arise only for specified conditions such as assay time and flow rate. A more appropriate question for assay of pathogens might be 'what threshold concentration ([M]$_{\text{thr}}$) of particles could be present in a sample, under specified flow rate and assay time conditions and yet have a probability <0.05 that no particle be captured in n fields, i.e. what information does a TC = 0 result give? The Poisson Distribution gives e^{-a} as the probability $P_0(a)$ of getting a result TC = 0, in a situation where the expected value of TC is a. Setting $P_0(a) = e^{-a} = 0.05$ gives a value for a that is just less than 3.0.

When V ml of suspension is to be analysed at a flow rate Q_{opt} (Eq. (7)), then the required t_{assay} is set by:

$$t_{\text{assay}} = \frac{V}{Q_{\text{opt}}} = (t_{\text{res-batch}}) \left(\frac{V}{V_{\text{act}}} \right) \quad (8)$$

It follows that, to a reasonable approximation, the probability of failing to capture a single particle in an assayed sample of volume V, when n, from a total of N_{FV}, fields of view are scored at the end of an assay time given by Eq. (8) is <0.05 when the particle concentration exceeds [M]$_{\text{thr}}$ where

$$[M]_{\text{thr}} \sim \left(\frac{N_{\text{FV}}}{n} \right) \left(\frac{3.0}{V} \right) \quad (9)$$

The number 3.0 in Eq. (9) is the value of a, from the discussion of the Poisson distribution above. For a typical case considered here where $N_{\text{FV}} = 1010$, $n = 15$, $V = 1.0$ ml, $V_{\text{act}} = 26$ μl, $t_{\text{res-batch}} = 40$ s (so that $Q = V_{\text{act}}/t_{\text{res-batch}} = 0.039$ ml/min) and the consequent assay time (V/Q) is 25 min then [M]$_{\text{thr}} \sim 200$/ml. The expression above shows how [M]$_{\text{thr}}$ could be reduced by increasing the area of the field interrogated (through increasing n). It also suggests the experimental flexibility available where a higher [M]$_{\text{thr}}$ is tolerable.

5. Conclusions

A pressure amplitude of 460 kPa at a frequency of 2.82 MHz gave high immunocapture efficiencies for both spore and 1 μm diameter biotinylated fluorescent latex microparticle. The fluorescent particles provided good contrast when discriminating specifically captured particles against background. A clear need for precision fabrication or selection of reflector thickness has been established. The time dependence of particle deposition on a reflector in a batch system was broadly consistent with a calculated time of 35 s to bring 95% of particles to the coated surface. A suspension flow rate of 0.1 ml/min gave optimal experimental capture, with a 1.01 mm reflector, in a 2 min assay time. The enhancement of particle detection compared with the control (no ultrasound) situation was ×70. The system detected an average of 1 particle per field of view (*P*/FV) when the suspending phase concentration was 2×10^4 particles/ml in a 2 min assay. That value could drop to a concentration of 200/ml over a 25 min assay with a suspension flow rate of 0.04 ml/min. The sensitivity improves further as the number of microscopic fields assayed per particle size in increased.

Acknowledgements

S.P. Martin and L.A. Kuznetsova were supported by the BBSRC (Research Grant No. 72/E17416) and R.J. Townsend was supported by EPSRC (Research Grant No. GR/R13333/01). The authors are grateful to Dr. Sian Armstrong (School of Engineering, Cardiff University) for the impedance measurements with the Network Analyser.

References

Belgrader, P., Hansford, D., Kovacs, G.T.A., Venkateswaran, K., Mariella Jr., R., Milanovich, F., Nasarabadi, S., Okuzumi, M., Pourahmadi, F., Northrup, M.A., 1999. A minisonicator to rapidly disrupt bacterial spores for DNA analysis. Anal. Chem. 71, 4232–4236.

Delehanty, J.B., Ligler, F.S., 2002. A microarray immunoassay for simultaneous detection of proteins and bacteria. Anal. Chem. 74, 5681–5687.

Driks, A., 2002. Maximum shields: the assembly and function of the bacterial spore coat. Trends Microbiol. 10, 251–254.

Ferroperm Piezoceramics, 2004. Material Program. <http://www.ferroperm-piezo.com.htm> (accessed 20th September 2004).

Gould, R.K., Coakley, W.T., 1973. The effects of acoustic forces on small particles in suspension. In: Bjorno, L. (Ed.), Proceedings of the 1973 Symposium on Finite Amplitude Wave Effects in Fluids, pp. 252–257.

Gröschl, M., 1998. Ultrasonic separation of suspended particles. Part I. Fundamentals. Acustica 84, 432–447.

Hairston, P.P., Ho, J., Quant, F.R., 1997. Design of an instrument for real-time detection of bioaerosols using simultaneous measurement of particle aerodynamic size and intrinsic fluorescence. J. Aerosol. Sci. 28, 471–482.

Hawkes, J.J., Coakley, W.T., 2001. Force field particle filter, combining ultrasound standing wave and laminar flow. Sens. Actuat. B 75, 213–222.

Hawkes, J.J., Gröschl, M., Benes, E., Nowotny, H., Coakley, W.T., 2002a. Positioning particles within liquids using ultrasound force fields. Revista De Acustica 33 (3–4), ISBN 84-87985-06-8, paper PHA-01-007-IP, 6 p.

Hawkes, J.J., Coakley, W.T., Gröschl, M., Benes, E., Armstrong, S., Tasker, P.J., 2002b. Single half-wavelength ultrasonic particle filter: predictions of the transfer matrix multi-layer resonator model and experimental filtration results. J. Acoust. Soc. Am. 111, 1259–1266.

Hawkes, J.J., Long, M.J., Coakley, W.T., McDonnell, M.B., 2004. Ultrasonic deposition of cells on a surface. Biosens. Bioelectron. 19, 1021–1028.

Higashitani, K., Fukushima, M., Matsuno, Y., 1981. Migration of suspended particles in plane stationary ultrasonic field. Chem. Eng. Sci. 36, 1877–1882.

Hill, M., Shen, Y., Hawkes, J.J., 2002. Modelling of layered resonators for ultrasonic separation. Ultrasonics 40, 385–392.

Jensen, J.A.D., Pocwiadowski, P., Perrson, P.O.A., Hultman, L., Møller, P., 2003. Acoustic streaming enhanced electrodeposition of nickel. Chem. Phys. Lett. 368, 732–737.

Kaye, G.W.C., Laby, T.H., 1995. Tables of Physical and Chemical Constants, 16th ed. Longman, Harlow Essex.

Kuznetsova, L.A., Coakley, W.T., 2004. Micro-particle concentration in short path length ultrasonic resonators: roles of radiation pressure and acoustic streaming. J. Acoust. Soc. Am. 116, 1956–1966.

Limaye, M.S., Coakley, W.T., 1998. Clarification of small volume microbial suspensions in an ultrasonic standing wave. J. Appl. Microbiol. 84, 1035–1042.

Liu, R., Lenigk, R., Druyor-Sanchez, R.L., Yang, J., Grodzinski, P., 2003. Hybridization enhancement using cavitation microstreaming. Anal. Chem. 75, 1911–1917.

McBride, M.T., Gammon, S., Pitesky, M., O'Brien, T.W., Smith, T., Aldrich, J., Langlois, R.G., Colston, B., Venkateswaran, K.S., 2003. Multiplexed liquid arrays for simultaneous detection of simulants of biological warfare agents. Anal. Chem. 75, 1924–1930.

Nowotny, H., Benes, E., 1987. General one-dimensional treatment of the layered piezoelectric resonator with 2 electrodes. J. Acoust. Soc. Am. 82, 513–521.

Nowotny, H., Benes, E., Schmid, M., 1991. Layered piezoelectric resonators with an arbitrary number of electrodes (general one-dimensional treatment). J. Acoust. Soc. Am. 90, 1238–1245.

Perkins, E.A., Squirrell, D.J., 2000. Development of instrumentation to allow the detection of microorganisms using light scattering in combination with surface plasmon resonance. Biosens. Bioelectron. 14, 853–859.

Rowe, C.A., Tender, L.M., Feldstein, M.J., Golden, J.P., Scruggs, S.B., MacCraith, B.D., Cras, J.J., Ligler, F.S., 1999. Array Biosensor for simultaneous identification of bacterial, viral and protein analysis. Anal. Chem. 71, 3846–3852.

Shah, J., Chemburu, S., Wilkins, E., Abdel-Hamid, I., 2003. Rapid amperometric immunoassay for *Escherichia coli* based on graphite coated nylon membranes. Electroanalysis 15, 1809–1814.

Spengler, J.F., Jekel, M., Christensen, K.T., Adrian, R.J., Hawkes, J.J., Coakley, W.T., 2001. Observation of yeast cell movement and aggregation in a small scale MHz ultrasonic standing wave field. Bioseparation 9, 329–341.

Spengler, J.F., Coakley, W.T., Christensen, K.T., 2003. Microstreaming effects on particle concentration in an ultrasonic standing wave. AICHE J. 49, 2773–2782.

Stratis-Cullum, D.N., Griffin, G.D., Mobley, J., Vass, A.A., Vo-Dinh, T., 2003. A miniature biochip system for detection of aerosolized *Bacillus globigii* spores. Anal. Chem. 75, 275–280.

Suri, C., Takenaka, K., Kojima, K., Koyama, K.J., 2002. Experimental study of a new liquid mixing method using acoustic streaming. J. Chem. Eng. Jpn. 35, 497–502.

Townsend, R.J., Hill, M., Harris, N.R., White, N.M., 2004. Modelling of particle paths passing through an ultrasonic standing wave. Ultrasonics 42, 319–324.

A MICROFABRICATED ULTRASONIC PARTICLE MANIPULATOR WITH FREQUENCY SELECTABLE NODAL PLANES

M. Hill[+], N.R. Harris[#], R.J. Townsend[+], N.M. White[#], and S.P. Beeby[#]
+School of Engineering Sciences, Southampton University, Southampton, UK
Electronics and Computer Science, Southampton University, Southampton, UK
m.hill@soton.ac.uk

Abstract

Ultrasonic devices designed to manipulate particles rely on an ability to predict the nature of the standing wave within a resonator. The interaction between the properties of the layers within the resonator can generate standing waves that vary significantly from the classic rigid boundary model for half-wavelength resonances.

A simple, two layer, model demonstrates the dependence of standing wave characteristics on the impedance of a reflecting boundary. A multi-layer model that includes a representation of the primary radiation forces on particles is then used to refine the resonator design and allow for interactions with the other layers.

Both models predict that resonators with sub-wavelength critical dimensions can be designed with multiple modes each with pressure nodes at different positions. The models have been used to design a microfabricated resonator with modes that allow particles to be forced to either boundary of the fluid or to the fluid centre, depending on the operating frequency.

Introduction

Ultrasonic standing waves generate small forces on particles within the acoustic field which tend to move those particles to the pressure nodes or antinodes [1, 2] of the field. Design of resonators to manipulate particles demands a model of the acoustic field and the radiation forces generated within it. Several models of the acoustic radiation forces within standing waves have been developed[3-5] and these have typically been used to provide analytical solutions for the force profiles within idealised standing waves.

The electro-acoustic characteristics of more general planar standing waves have been modelled successfully as layered resonators [1, 6-9]. This paper uses two models of standing wave characteristics to examine how the thickness of the reflector and fluid layers can be chosen to determine the position of the pressure nodal plane within the fluid layer.

Theory

A layered resonator, such as those typically used for ultrasonic particle manipulation is shown diagrammatically in Figure 1.

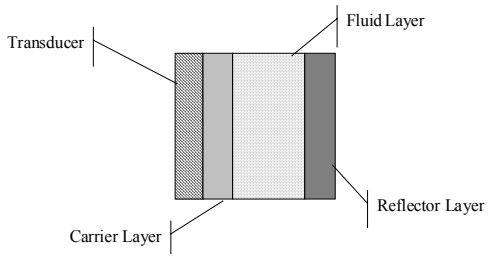

Figure 1: A typical structure for a fluid resonator

The nature of the acoustic standing wave generated within the fluid layer will be a function of the transducer's driving frequency and amplitude, but also of the acoustic impedances presented to each of the layers. To isolate the nature of the standing wave's dependence on the relative impedance of the fluid layer and the reflector layer, consider a simplified resonator in which the left hand boundary of the fluid layer is driven by a constant amplitude sinusoidal displacement. It can be shown that acoustic modes representing energy maxima in the fluid layer will occur when[10]:

$$k_f t_f = \tan^{-1}\left(\frac{r_f\left(r_r^{\,2} + r_0^{\,2}\tan^2\left(k_r t_r\right)\right)}{r_r \tan\left(k_r t_r\right)\left(r_r^{\,2} - r_0^{\,2}\right)}\right) \quad (1)$$

where k is a wave number, t a thickness and r a characteristic acoustic impedance. Subscripts f and r denote the fluid and reflector properties respectively and r_0 is the impedance at the termination of the reflector layer.

Table 1: Material properties used in simulations

Layer	*Material*	*Density* (kgm^{-3})	*Speed of Sound* (ms^{-1})
Fluid	water	1000	1500
Reflector	Pyrex	2200	5430
Reflector Termination	air	1.3	330

For a given set of impedance values, a graph showing solutions to this equation such as that shown in Figure 2 can be generated. The values used in this graph are for an example water filled resonator with a Pyrex reflector and the values used are shown in Table 1. For a particular resonator design the values of t_f/c_f and t_r/c_r may be assumed to be constant, so a "frequency sweep" is represented on the graph by a

straight line passing through zero, of gradient $t_f c_r / t_r c_f$.

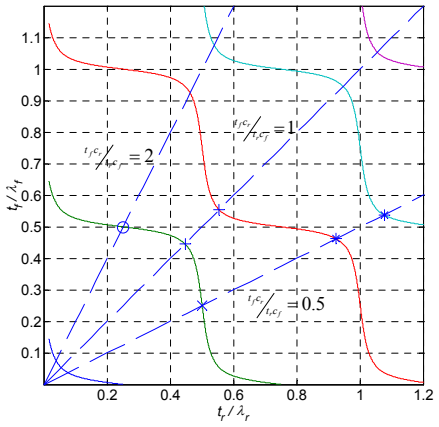

Figure 2: The first four solutions to equation (1).

Three such "frequency sweeps" are shown as dotted lines over the solutions to equation (1). These three represent resonators in which $t_f c_r / t_r c_f$ is equal to 2, 1, and 0.5. In the first case, the resonance marked by a "o" is a half wavelength mode, in which, at the modal frequency, the fluid layer is half the wavelength in thickness and the reflector layer is a quarter wavelength in thickness. The next "frequency sweep" has two resonances marked by a "+". These are near half wavelengths in both fluid and reflector waves and are similar to the coupled resonator case described by Hawkes *et al*. [7, 9].

The final "frequency sweep", for a resonator in which $t_f c_r / t_r c_f = 0.5$, has a resonance marked by an "x". At the frequency of this mode the fluid layer is a quarter wavelength thick and the reflector layer is a half wavelength thick. For this resonator at this frequency the primary acoustic radiation force will move particles within the fluid to the boundary with the reflector, as in contrast to the case with a perfectly rigid boundary, the half wave resonance in the reflector layer causes the pressure node to be up against the solid boundary itself. Also of note for this resonator geometry are the two higher frequency modes marked with a "*". These modes occur at frequencies which are either side of a half wavelength in the fluid layer. The existence of both quarter wave and near half wavelength modes in the same geometry resonator suggests that it should be possible to build a resonator with modes which will move particles to either the centre of the fluid layer or to the fluid/resonator boundary, depending on the driving frequency selected.

Design of an experimental system

In order to demonstrate the existence of a resonator with multiple resonances capable of moving particles to either the centre of the boundary of a fluid a fuller simulation was required which modelled all the layers in the resonator, not just the fluid and reflector layers. The fuller simulation is needed as, just as the fluid and reflector layers interact, so the other layers in the resonator will influence the position and nature of an acoustic mode in the fluid layer.

Numerical multi-layer model predictions

The model used is that described by Hill *et al.* [8, 9]. The structure of the resonator was based on that previously described by Harris *et al.* [11] and consists of a 3 MHz thickness mode PZT transducer glued to a 525 µm thick silicon carrier layer. The carrier layer is anodically bonded to a Pyrex layer into which the fluid cavity has been etched. Hence the material properties are fixed but the cavity thickness (and the associated reflector thickness) becomes the primary design variable. The Pyrex wafer used is 1.7 mm thick, so as the fluid cavity is etched into this, the sum of the fluid and reflector thicknesses will be 1.7 mm. Given the material properties in layer 1 and this constraint on total fluid/reflector thickness, the condition $t_f c_r / t_r c_f = 0.5$ will be met when t_f is about 200 µm and t_r 1500 µm. Such a fluid layer depth would correspond to a quarter wave resonance of about 1.8 MHz. This was used as the basis for a simulation of the variation of energy density within the fluid layer as a function of frequency and etch depth as shown in Figure 3.

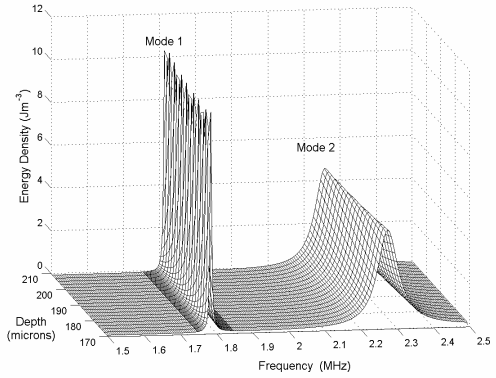

Figure 3: Energy density against fluid layer depth and frequency between 1.5 & 2.5 MHz

The predicted quarter wave mode, marked with an "x" in Figure 2 corresponds to "mode 1" in Figure 3. The predicted near half-wavelength modes marked with "*" symbols in Figure 2 can be seen in Figure 4, which displays the same plot as Figure 3 but over a higher frequency range.

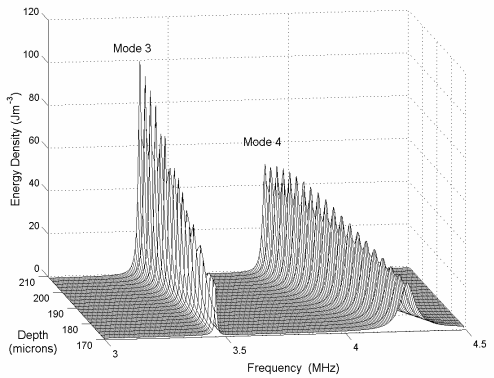

Figure 4: As Figure 3 for frequencies, between 3 & 4.5 MHz. Note different energy density scale.

The energy peak marked as "mode 2" in Figure 3 is not predicted by Figure 2, however. To confirm the nature of modes 1, 3 & 4, and to investigate the nature of mode 2, predictions of the pressure amplitude across the fluid layer (and its variation with fluid layer depth) can be plotted, as in Figure 5

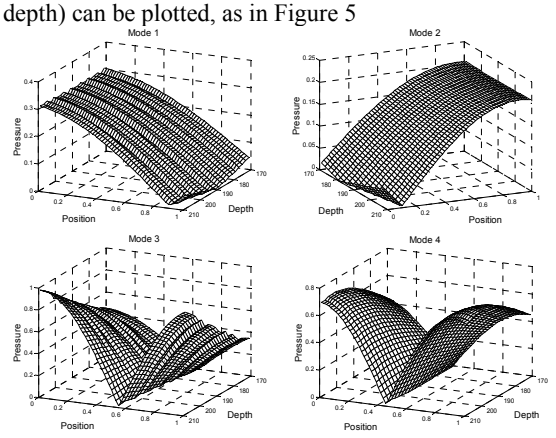

Figure 5: Modelled fluid layer pressure distributions against fractional distance from the carrier layer for the four modes against etched cavity depth (microns).

As expected, mode 1 has a maximum pressure at the carrier layer boundary and a pressure minimum at or near the reflector boundary. Modes 3&4 are similar to typical half wave (rigid-rigid boundary) modes with a pressure minimum near the centre of the cavity. It is now apparent that mode 2 is also a quarter wave mode, but with its pressure minimum at the carrier layer boundary and a maximum at the reflector. This mode appears due to a resonance within the carrier layer and hence was not predicted by the analytical model used to generate Figure 2

Experimental Results

The model described above suggests that, over the frequency range of interest, two quarter and two half wavelength modes should be generated for any of the cavity depths modelled between 170 and 210 μm. However a close look at modes 1 & 2 in Figure 5 shows that the model predicts the pressure nodes to be slightly away from the respective boundaries at the higher end of the cavity depth range. Hence a value of 175 μm was chosen for the etch depth.

Impedance Characteristics

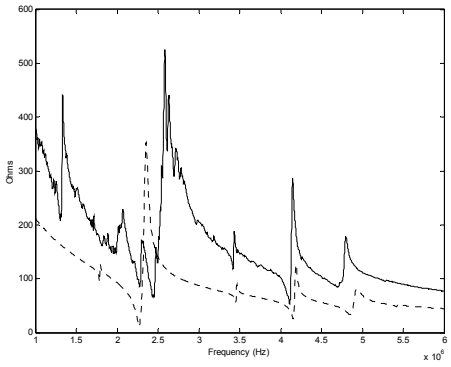

Figure 6: Modelled (dotted) and measured (solid) impedance plots for the fluid filled device

Figure 6 shows the input impedance to the resonator as predicted by the multi-layer model and the measured input impedance. Impedance peaks due to modes 3&4 are clearly visible at about 3.5 and 4.1 MHz in both modelled and measured results. However the model is a simplification of the actual resonator, and in particular only considers behaviour in a single dimension, making the measured results more complex than the modelled results at frequencies below about 3 MHz. A small impedance peak in the modelled results at 1.8 MHz corresponds to mode 1, but is not clearly distinguishable in the measured results. Mode 2 is completely masked by the large transducer/carrier layer peak visible at about 2.4 MHz in the modelled and 2.7 MHz in the measured results.

Particle Manipulation

An optical microscope, focussed through the Pyrex reflector layer was used to monitor the position of yeast particles within the fluid layer of the resonator. The device was driven from a frequency synthesiser, via a fixed gain RF amplifier (50dB). The transducer was placed in series with a 47ohm resistance to allow the variation in voltage across the transducer to be monitored to identify voltage minima. This proved a more sensitive means of identifying modes than the impedance sweep of Figure 6. By searching for voltage minima in the region predicted by the model, all four modes were identified. Modes were found at 1.71MHz, 2.27MHz, 3.44MHz and 4.1MHz,

although, modes 1 and 2 required very careful adjustment to identify.

The position of the particles within the fluid layer was monitored by using the small depth of field of the microscope. For example, in the case of mode 1, the microscope was focussed on the boundary between the fluid and the reflector layers.

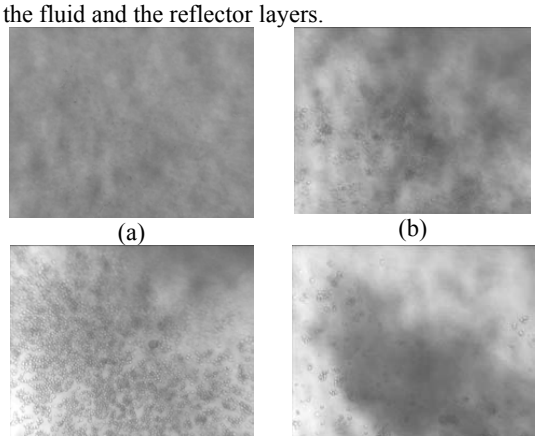

Figure 7: A sequence of images taken as particles move to the reflector boundary driven at the frequency of mode 1.

Figure 7 shows randomly distributed particles being forced to the Pyrex/water boundary against gravity as predicted for Mode 1 at 1.7MHz. Image (a) shows the random distribution of yeast before any power is applied, with the microscope focussed at the Pyrex/water boundary. Image (b) shows the view 5 seconds after the power is applied, and it can be seen that yeast cells are beginning to move into focus as they are forced against the boundary. Image (c) show the situation after 15 seconds and many more cells are now in focus. Particles tend to collect in clumps due to lateral forces, and image (d), taken 40 seconds later, after the power has been turned off shows this. The clump of particles is peeling away from the Pyrex layer and falling under the influence of gravity towards the silicon layer and thus out of focus.

Similar results were obtained for the other three modes, showing that particles could be forced to either of the cavity boundaries or to the cavity centre.

Conclusions

A simple analytical equation which predicts the combination of thicknesses of two layers required to produce an acoustic mode with a specifically positioned pressure node has been used in the initial design of a resonator with both quarter and half wavelength modes. The modelling has been further refined using a simulation of a full resonator system.

A device has been built using microfabrication techniques and has been shown to be able to move particles to either boundary of the fluid layer or to the centre of the fluid layer, depending on the driving frequency (and hence the particular mode).

Although the quarter wave modes were more difficult to identify and drive, such a system offers the potential to move cells or particles within a fluid in a controlled manner.

Acknowledgements

This work has been carried out with financial support from Dstl and EPSRC under grant number GR/R13333/01, and Porvair PLC.

References

[1] M. Gröschl, "Ultrasonic separation of suspended particles - Part I: Fundamentals," *Acustica*, vol. 84, pp. 432-447, 1998.

[2] W. T. Coakley, "Ultrasonic separations in analytical biotechnology," *Trends in Biotechnology*, vol. 15, pp. 506-511, 1997.

[3] L. V. King, "On the acoustic radiation pressure on spheres," *Proc R. Soc. London*, vol. A147, pp. 212-40, 1934.

[4] K. Yosioka and Y. Kawasima, "Acoustic radiation pressure on a compressible sphere," *Acustica*, vol. 5, pp. 167-73, 1955.

[5] S. D. Danilov and M. A. Mironov, "Radiation pressure force acting on a small particle in a sound field.," *Sov. Phys. Acoust.*, vol. 30, pp. 280-3, 1984.

[6] H. Nowotny and E. Benes, "General One-Dimensional Treatment of the Layered Piezoelectric Resonator with 2 Electrodes," *Journal of the Acoustical Society of America*, vol. 82, pp. 513-521, 1987.

[7] J. J. Hawkes, M. Gröschl, H. Nowotny, S. Armstrong, P. Tasker, W. T. Coakley, and E. Benes, "Single half wavelength ultrasonic particle filter: Predictions of the transfer matrix multi-layer resonator model and expreimental filtration results.," *Journal of the Acoustical Society of America*, vol. 111, pp. 1259-1266, 2002.

[8] M. Hill and R. J. K. Wood, "Modelling in the design of a flow-through ultrasonic separator," *Ultrasonics*, vol. 38, pp. 662-665, 2000.

[9] M. Hill, Y. Shen, and J. J. Hawkes, "Modelling of layered resonators for ultrasonic separation.," *Ultrasonics*, vol. 40, pp. 385-92, 2002.

[10] M. Hill, "The selection of layer thicknesses to control acoustic radiation force profiles in layered resonators," *JASA. In press.*.

[11] N. R. Harris, M. Hill, S. P. Beeby, Y. Shen, N. M. White, J. J. Hawkes, and W. T. Coakley, "A Silicon Microfluidic Ultrasonic Separator," *Sensors and Actuators B*, vol. 95, pp. 425-34, 2003.

Numerical Modelling of a Microfluidic Ultrasonic Particle Separator

R. J. Townsend[*], M. Hill[*], N. R. Harris[**], N. M. White[**], S. P. Beeby[**]

[*]School of Engineering Science, University of Southampton,
Southampton, SO17 1BJ, UK, m.hill@soton.ac.uk
[**]School of Electronics and Computer Science, University of Southampton,
Southampton, SO17 1BJ, UK

ABSTRACT

Particle manipulation can be brought about by using the radiation force experienced by particles in an acoustic standing wave. Where the particles are held in a fluid suspension, particle movement may be predicted analytically for basic descriptions of the fluid and acoustic field, although layered resonators have complex resonant characteristics and, in applications approaching microfluidic scale, flow is typically described by a parabolic laminar flow profile. Numerical techniques are used to successfully describe the acoustic field and determine the resulting particle trajectories and concentration in these more complex cases. This is supplemented with more thorough analyses of the acoustic and fluid fields using finite element analysis and computational fluid dynamics, respectively. These approaches are validated against experimental results for a micro-engineered ultrasonic particle separator.

Keywords: numerical model, ultrasonic, radiation force

1 INTRODUCTION

Particles in suspension and within an acoustic standing wave experience a radiation force, the direction and magnitude of which depends on the position within the field, the strength of the field and the physical properties of the particles and suspending fluid. This phenomenon can be used to manipulate or separate particles and so can be used to enhance cell and spore processing [1].

Devices in which a suitable standing wave can be generated can be designed using analytical models, although as the scale of such devices reduces numerical simulation becomes increasingly useful. Where fluid flow is introduced, and where the fluid chamber depth is of the same order as the wavelength, the acoustic and laminar flow fields have a combined effect which significantly influences particle movement, which can more easily be studied numerically.

The reduced scale also demands alternative fabrication routes. Silicon etching is ideal for the batch creation of microfluidic circuits, although geometric variations are limited and influence fluid flow patterns.

Here, a range of numerical simulation techniques is presented based around a micro-scaled ultrasonic particle separator device and used initially to describe the particle movement, the resulting concentration profiles within an ultrasonic field and the subsequent outlet particle concentrations. The fluid and acoustic fields are investigated more thoroughly using computational approaches and demonstrate the ability to study the effect of the etched geometry. In the case of the fluid flow, geometry has been modified to improve the flow characteristics of the device. Fabricated ultrasonic separator devices have been tested experimental and used to validate simulation work.

2 PARTICLE SIMULATIONS

2.1 Acoustic Radiation Force

Particles within an acoustic standing wave experience a time-averaged force as described by Gröschl [2]. The radiation force is related to the acoustic pressure field, an example of which is shown in figure 1, where it can be seen to be twice the spatial frequency of the acoustic pressure field. For solid phase particles, the radiation force causes them to converge towards the pressure node of the standing wave; beneath the pressure node the force acts in the positive *y* direction and above in the negative *y* direction.

The amplitude of the force depends on the acoustic energy density, wave number and properties of the fluid and particle media. The acoustic energy density within the fluid layer of a layered resonator driven by a PZT transducer depends on the transducer voltage and acoustic properties of the various layers.

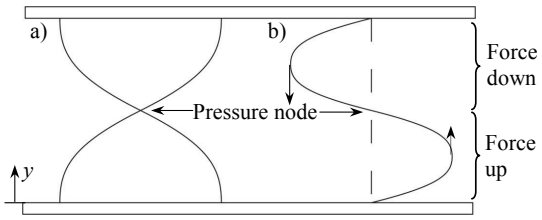

Figure 1: Schematic of a) acoustic pressure profile of a standing wave and b) resulting radiation force profile.

To describe the acoustic field and radiation force more accurately, an acoustic impedance transfer model has been developed which uses an equivalent circuit of the transducer and theoretical acoustic impedance of the resonator. This describes the device response as a function of frequency, predicting the resonant frequencies and the field pattern in 1 dimension through the fluid layer [3]. The acoustic pressure and velocity fields across the fluid chamber are then used to determine the acoustic potential and kinetic energy radiation profiles, respectively, which then relate directly to the radiation force.

This method is implemented in MATLAB and describes the acoustic field and radiation force, such as that shown in figure 1, for a range of frequencies and at discrete points across the fluid chamber. The mode shape and nodal positions are therefore also determined, indicating to which plane particles will converge.

2.2 Particle Trajectories

The movement of particles can be determined by considering the forces acting on a particle and solving Newton's second law numerically. The principal forces acting on a particle within an acoustic field are the acoustic radiation force, Stokes fluid drag force and gravity and are solved using numerical differentiation using a solver contained within MATLAB [4]. Time, coordinate and velocity data are returned by the solver, which, in the case of continuous fluid flow perpendicular to acoustic propagation, describes particle trajectory as the particle moves along the chamber (x-direction) and relative to the nodal plane (y-direction).

This model is coupled to the acoustic impedance transfer model described above which supplies the data describing the radiation force across the chamber.

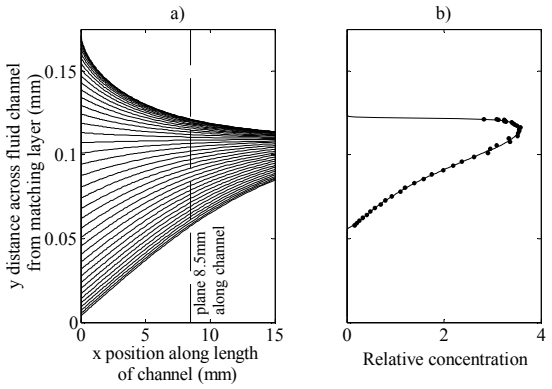

Figure 2: Simulation of particles within an acoustic standing wave showing a) particle trajectories as they are carried by the fluid along the length of the chamber (x-axis) and deflected vertically by the acoustic wave (y-axis) and b) the concentration profile.

To describe the drag force, and so the movement of the particle along the chamber, the fluid velocity profile is assumed to be laminar, therefore similar to flow between parallel plates where the chamber has a high height to width ratio, and varies only as a function of y.

Figure 2a shows an example of the movement of particles passing through an acoustic field where the chamber depth is slightly less than half a wavelength. Similar methods based on particle forces have been used to determine particle movement in acoustic fields [5,6].

2.3 Particle Concentration

Where the concentrated particle stream or cleared fluid is required for subsequent processing, outlets are used to extract the relevant fluid stream. Johnson and Feke [5] and Hawkes and Coakley [6] calculate outlet concentration based on the particle trajectory which marks the split between outlet streams. For applications where particle concentration within the chamber is of importance, it is sometimes more useful to predict the spatial change in concentration, rather than particle trajectories, also from which outlet concentrations can be calculated.

Particle coordinate data, such as that determined by the particle trajectory model, can be used to calculate the change in particle spacing and therefore particle concentration. This requires the simulation of a series of particles, each with different initial positions (figure 2a). In figure 2b, the relative change in concentration based on the adjacent particle trajectories has been plotted (dotted points) and it can be seen that as particles are drawn towards the centre of the chamber the concentration in that region has increased by a factor of 3 upon that at the inlet plane (x=0). It can be seen that the concentration data is slightly noisy and originates from numerical errors in the particle trajectory data.

A more reliable and elegant method is to consider the particles as a continuum described numerically over a grid, reducing computation time by avoiding the need to calculate individual particle trajectories and removing the associated errors. However, care has to be taken in the numerical implementation of this technique in regions where particles do not exist, e.g. either side of the particle stream, and the wall concentration if particles are forced towards the chamber boundary. To avoid these problems whilst still considering particles as a continuum, the method demonstrated here also takes into account particle trajectories and is therefore Lagrangian in nature.

A standard equation of conservation of mass [7] is used where u and v are the x and y components of particle velocity and c is the concentration (analogous to density).

$$\frac{\partial c}{\partial t} = \frac{c\partial u}{\partial x} + \frac{u\partial c}{\partial x} + \frac{c\partial v}{\partial y} + \frac{v\partial c}{\partial y} \quad (1)$$

This is simplified by assuming the following: concentration varies spatially only, reducing the left hand side term to zero; u does not change as a function of x removing the first term of the RHS; there is no particle flux across a particle path, which has the effect of removing the forth RHS term. This reduced equation is then solved by replacing the partial differential terms with simple difference equations and finding successive solutions along the chamber in the x direction. Figure 2b illustrates the concentration calculated using this method (solid line) and is compared against the approach based on particle trajectory data. It can be seen that this latter approach creates a smoother, more convincing profile. Despite providing a more refined dataset, the computation time is reduced.

3 2-DIMENSIONAL FIELD SIMULATIONS

3.1 FEA of Acoustic Field

The above analysis has considered the acoustic field in 1 dimension only. However, striated patterns have been observed in resonators used for particle manipulation, where the acoustic field varies in a direction perpendicular to propagation due to acoustic enclosure modes, creating radiation force components in 3-dimensions.

Finite element analysis (ANSYS) has been used to investigate the 2-d field in two layers of the resonator, the fluid (water) and reflector (Pyrex) layers. Modal analyses predict that in the operating frequency range there are resonance patterns where the acoustic field varies significantly across the width of the chamber (z-direction).

Figure 3 shows the modelled acoustic pressure field at a 2-d resonant frequency of 3.4MHz for fluid and reflector thicknesses of 175µm and 1525µm respectively. Within the fluid chamber there is a series of distinct pressure variations in the z direction. Solid particles converge towards the pressure nodes (zero pressure), which referring to figure 3 suggests that particles will converge towards a series of bands across the width of the fluid chamber, with an average spacing of 0.25mm.

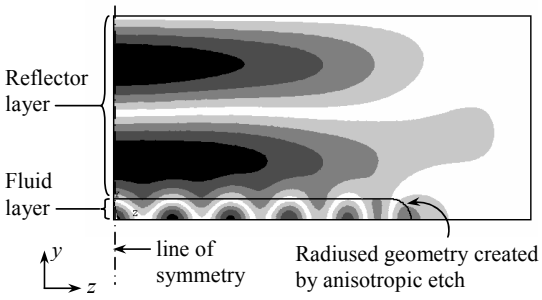

Figure 3: Acoustic finite element analysis of fluid and reflector layers. Contours indicate high magnitude (black) and low magnitude (white) regions of acoustic pressure.

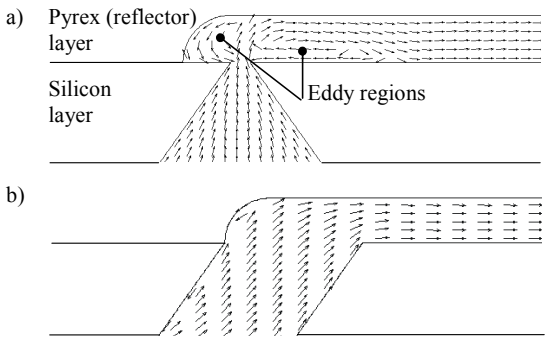

Figure 4: CFD simulation of fluid flow through anisotropic etched ducts leading to main chamber, showing a) eddy regions within a single etch duct design and b) a significant reduction of eddy regions within the revised geometry.

3.2 CFD Analysis of Fluid Flow Field

The fluid flow field is also investigated in 2 dimensions, although in the x-y plane. Dimensions within the fluid chamber and duct are typically 100µm or greater supporting use of the Navier-Stokes equations and macrofluidic methods, as used in commercial computational fluid dynamics packages. The CFD program, CFX, is used to investigate the influence the etched geometry on the fluid flow patterns [8], examples of which are shown in figure 4.

Figure 4a illustrates the predicted flow field through the angular geometry of the silicon KOH etched duct and up into the main chamber contained within an etched Pyrex layer. Eddy regions in the fluid easily form either side of the duct, potential sites for particles to lodge. A parabolic flow profile has been assumed to exist the entire length of the fluid chamber, however the eddy regions invalidate this assumption in the duct regions.

In figure 4b and based on the same flow rate, an alternative etched geometry has been simulated demonstrating that the eddy regions have become insignificant in their size and the flow pattern immediately downstream of the duct quickly tends to a parabolic profile.

4 VALIDATION OF MODELS

A series of ultrasonic particle separators have been fabricated and tested to investigate separation performance within a micro-engineered device. Here the experimental results also serve to validate the simulation techniques described above.

The separator is mounted upon an aluminium manifold which facilitates connection to peristaltic pumps (Watson-Marlow) and the accurate control of flow rates. The separator consists of a series of layers; either a bulk or printed PZT transducer, a silicon wafer which acts as a

matching layer and into which ducts are etched (figure 4), and a Pyrex wafer into which the main fluid channel is etched. The device is designed such that there are several resonant frequencies which cause particles to move towards the centre or edge of the fluid chamber [9].

The acoustic impedance model is used to predict the resonant frequencies of the devices and the associated modes. In experiment, particles are observed to converge towards certain planes within the fluid chamber when the field is switched on, and supports the predictions made regarding the frequencies and field patterns [9].

Work has begun involving the measurement of outlet particle concentration for yeast and latex particles over a range of transducer voltages [10]. Preliminary application of the concentration model compares well with these results and will contribute to further work comparing the performance of the bulk and printed PZT devices.

A study of particle movement, similar to that used in Harris *et al.* [9] is used to compare against the FEA predictions describing the acoustic field and how it varies across the fluid channel. For the case described in figure 3 predicting band spacing of 0.25mm across the width of the chamber, initial experimental results record an average band spacing of 0.21mm, as seen in figure 5 looking down through the Pyrex layer where the white line are created by the build up of yeast particles along low pressure regions. This initial work is encouraging and further simulation work using more precise geometric measurements of the actual device is expected to reduce discrepancy between modelled and experimental results and demonstrate the influence geometry has on the 2-dimensional acoustic field and also particle movement.

Observation of particle movement due to the fluid flow, rather than the acoustic field, makes it possible to determine the extent of the eddy region downstream of the inlet and within the main chamber. The study of eddy regions created by various duct geometries and measured over a range of flow rates validates the CFD results and demonstrates the significant improvement in the flow field based on the geometry illustrated in figure 4b, minimising eddy development within the micro-fabricated device.

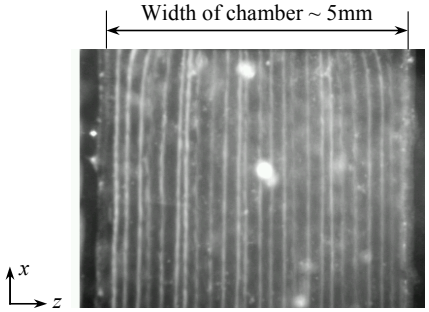

Figure 5: Particle bands formed across the width of the fluid chamber and along it length, caused by variations in the acoustic field. View looking down through Pyrex layer.

5 CONCLUSIONS

A variety of numerical methods have successfully described the behaviour of particles, acoustic field and fluid flow field of a micro-engineered device. The approaches are successful even when limited to a 1-dimension description of the system, although 2-dimensional characteristics can be simulated using alternative, yet commercially available methods with reasonable accuracy at the scale reported. 2-dimensional acoustic and fluid flow field data may be used to expand the more basic 1-dimensional MATLAB numerical model, should a more comprehensive simulation be required.

ACKNOWLEDGEMENTS

This work was funded by EPSRC grant GR/R13333/01. The authors gratefully acknowledge the funding and support from Dstl and Porvair Plc.

REFERENCES

[1] J. J. Hawkes, M. J. Long, W. T. Coakley, and M. B. McDonnell, "Ultrasonic deposition of cells on a surface," Biosensors & Bioelectronics, vol. 19, pp. 1021-1028, 2004.

[2] M. Groschl, "Ultrasonic separation of suspended particles - Part I: Fundamentals," Acustica, vol. 84, pp. 432-447, 1998.

[3] M. Hill, Y. J. Shen, and J. J. Hawkes, "Modelling of layered resonators for ultrasonic separation," Ultrasonics, vol. 40, pp. 385-392, 2002.

[4] R. J. Townsend, M. Hill, N. R. Harris, and N. M. White, "Modelling of particle paths passing through an ultrasonic standing wave," Ultrasonics, vol. 42, pp. 319-324, 2004.

[5] D. A. Johnson and D. L. Feke, "Methodology for fractionating suspended particles using ultrasonic standing wave and divided flow fields," Separations Technology, vol. 5, pp. 251-258, 1995.

[6] J. J. Hawkes and W. T. Coakley, "Force field particle filter, combining ultrasound standing waves and laminar flow," *Sensors and Actuators B-Chemical*, vol. 75, pp. 213-222, 2001.

[7] F. M. White, Vicous fluid flow, 2nd ed. New York: McGraw-Hill, 1991.

[8] R. J. Townsend, M. Hill, N. R. Harris, N. M. White, S. P. Beeby, and R. J. K. Wood, "Fluid modelling of microfluidic separator channels," Sensors and Actuators B: Chemical, In Press.

[9] N. Harris, M. Hill, Y. Shen, R. J. Townsend, S. Beeby, and N. White, "A dual frequency, ultrasonic, microengineered particle manipulator," Ultrasonics, vol. 42, pp. 139-144, 2004.

[10] N. R. Harris, M. Hill, R. J. Townsend, N. M. White, and S. P. Beeby, "Performance of a micro-engineered ultrasonic particle manipulator," Sensors and Actuators A: Physical, In Press.

Investigation of 2-d acoustic resonant modes in a particle separator

R. J. Townsend[a], M. Hill[a], N. R. Harris[b], N. M. White[b]

[a]*School of Engineering Sciences, University of Southampton, SO17 1BJ, UK*
[b]*Electronic and Computer Science, University of Southampton, SO17 1BJ, UK*

Abstract

Particles experience acoustic radiation forces when within an acoustic standing wave, and is a phenomenon which is exploited in particle and cell manipulation devices. When developing such devices, 1-dimensional acoustic characteristics are typically of most importance and determine the primary radiation forces acting on the particles. However, radiation forces have also been observed to act in the lateral direction, perpendicular to the primary radiation force, forming striated patterns. These lateral forces are due to lateral variations in the acoustic field influenced by the geometry and materials used in the resonator. The ability to control them would present an advantage in designing such systems.

The 2-dimensional characteristics of an ultrasonic separator device have been modelled within a finite element analysis (FEA) package. The fluid chamber of the device, within which the standing wave is produced, has a width to height ratio of approximately 30:1 and it is across the height that a half wavelength standing wave is produced to control particle movement. 2-d modal analyses have calculated resonant frequencies which agree well with both the 1-dimensional modelling of the device and experimentally measured frequencies. However, these 2-d analyses also reveal that these modes exhibit distinctive periodic variations in the acoustic pressure field across the width of the fluid chamber. Such variations lead to lateral radiation forces forming particle bands (striations) and are indicative of enclosure modes.

The striation spacings predicted by the FEA simulations for several modes compare well with those measured experimentally for the ultrasonic particle separator device. It is also shown that device geometry and materials control enclosure modes and therefore the strength and characteristics of lateral radiation forces, suggesting the potential use of FEA in designing for the control of enclosure modes in similar particle manipulator devices.

Keywords: lateral radiation force, FEA, particles

1. Introduction

The action of acoustic radiation forces on particles has been exploited in devices designed to manipulate particles. Such devices include particle separators and fractionators in which the nature of the acoustic field significantly influences the performance of the device. Therefore, in order to design ultrasonic devices reliably, the characteristics of the acoustic field must be considered.

These devices typically rely on the presence of a plane standing wave generated using a plate transducer. The resulting acoustic field is usually described 1-dimensionally with the field varying in a direction normal to the transducer plate. Acoustic radiation forces result from these variations, and in a direction normal to the transducer. When the standing wave is generated within a fluid cavity containing a particle suspension, the acoustic radiation forces will typically move particles to the pressure node(s) and form a layer of concentrated particles. However, lateral movement of particles is frequently observed as variations within the acoustic field exist with the particles moving within the nodal plane to areas of high acoustic kinetic energy [1].

The lateral movement of particles can be attributed to lateral variations within the acoustic field which give rise to lateral acoustic radiation forces. The source of these variations is the subject of this paper.

Figure 1 shows the effect of lateral forces on particles within a particle separation device. The images are taken looking down upon the device and in axial (y) direction with the transducer located on the underside of the device and orientated in the xz plane. A half-wavelength standing wave is generated within a fluid layer and forms a pressure node along its centre plane, towards which particles move due to axial radiation forces. Within these images the effect of additional lateral forces can be seen; in (a) with a no fluid flow, particles have moved to positions of high acoustic kinetic energy and have formed a complex 3-dimensional pattern. In (b) fluid flow has been introduced and the fluid drag forces have overcome the acoustic radiation forces acting in the x direction. This reveals the effect of the spatially averaged z component of radiation force and particles can be seen to form a striated pattern.

Depending on the manipulation process, the presence of these lateral forces can be detrimental to performance and may cause particles to form large aggregates which may sediment out of the suspension or block and disrupt the movement of the fluid. However, some recent devices have demonstrated that lateral forces can be used to advantage by influencing the movement and trapping of particles [2,3].

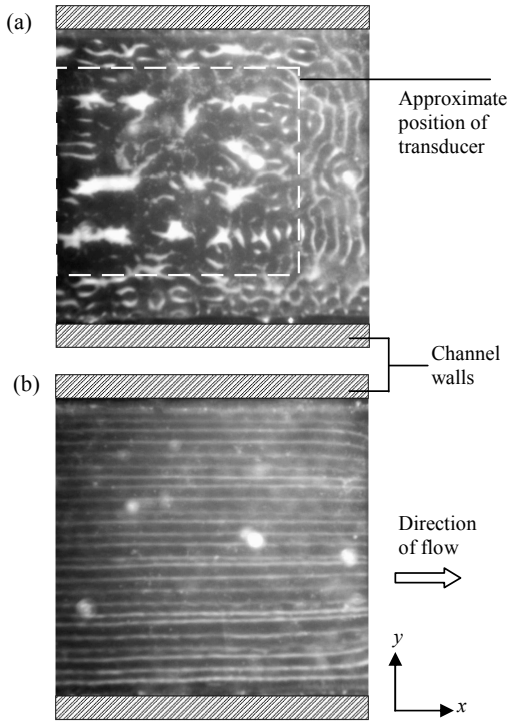

Figure 1: Striated patterns observed using yeast for conditions of a) no-flow and b) continuous flow-through.

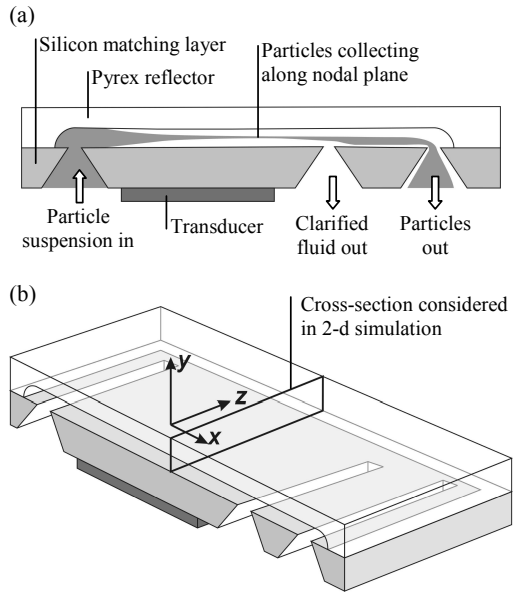

Figure 2: Schematics of particle separator showing a) movement of particles through the device and b) orientation of axial (y) and lateral (z) components

2. Enclosure Modes within Separator Device

The presence of lateral radiation forces are investigated for a micro-engineered particle separator. This device relies on the movement of particles to a nodal plane under the influence of axial (y) radiation forces, then allowing particle clarified flow to be drawn off one side of the particle stream. The device has a layered structure and includes a silicon matching layer, a fluid layer and a Pyrex reflector layer [4]. The layer thickness y dimensions are relatively small compared to the length and width (x and z dimensions), therefore, when driving the device at frequencies which excite a thickness resonance the acoustic characteristics through the y-axis should predominate. Figure 2 illustrates the basic construction and operation of the device, and orientation of the axial y and lateral z axes.

Lateral variations within the device can be caused by structural modes within the chamber walls, near-field effects or enclosure modes. Here, enclosure modes, which may be excited together with the axial modes required for operation, are investigated in isolation. The expression below describes the enclosures modes for a rectangular cavity with either rigid or pressure release boundaries [5]:

$$f = \frac{c}{2}\sqrt{\left\langle \frac{l}{L_x} \right\rangle^2 + \left\langle \frac{m}{L_y} \right\rangle^2 + \left\langle \frac{n}{L_z} \right\rangle^2} \qquad (1)$$

where the various dimensions of the waveguide are given by L_x, L_y and L_z with relative mode orders of l, m and n. The existence of such modes within the separator device will give rise to lateral (z) as well as axial (y) pressure gradients and, therefore, components of acoustic force acting in both these directions. Whilst the mode shape and resonant frequency in a simple rectangular cavity can be determined analytically (equation (1)), the geometry and therefore the mode shapes in layered ultrasonic devices is more complex and a finite element approach is used.

3. Acoustic Simulation

3.1 Fabricated test device

1-dimensional simulation of the through thickness (y) mode shape within the fluid and reflector layers is typically used in the design of the separator. For this 1-d simulation an acoustic impedance transfer model is used which is coded using MATLAB [6,7]. It is also possible to use finite element (FE) analysis to simulate the 1-d case for which the computer package ANSYS is used. The FE model includes elements to describe the fluid and reflector layers with a pressure release boundary applied to the external face of the reflector layer. 'Fluid' elements are used which allow acoustic enclosure modes rather than structural modes

to be simulated. A comparison of the MATLAB model and FE modal analysis is shown in figure 3 and shows a ~λ/2 mode in the fluid layer which will cause suspended particles to move to the nodal plane. The difference between the two curves may be due to the different methods used to describe losses in the respective models. This mode occurs at a frequency of ~3.4MHz in the fabricated test device, therefore both models are thought to present good estimates of the axial field.

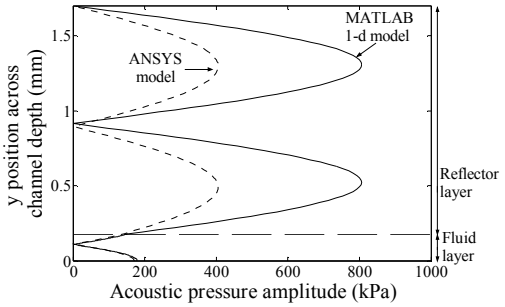

Figure 3: Axial acoustic pressure fields predicted by the FEA and MATLAB models for resonant frequencies of 3.37MHz and 3.46MHz for the respective model, (based on an acoustic particle velocity of 0.002m/s at the fluid plane).

To predict the presence of lateral variations in the acoustic field, the FEA model is extended to describe the fluid and reflector layers in 2-dimensions and a section across the width of the device is simulated (figure 2(b)). The simulation is based on the measured width of the Pyrex layer (external width) of 6.8mm and design width of the fluid cavity of 5mm. The curved side walls created by an isotropic etch process are also included in the model. This model can be compared to experimental observations such as that pictured in figure 1(a) and aims to validate the model and demonstrate the source of the striated patterns.

The mode identified in the previous subsection (~3.4MHz) is investigated as this is one of two modes which may be used during operation of the separator.

4.2 Side-wall Geometry

The boundary conditions applied to a cavity have a bearing on the mode shape and resonant frequency. Applying this to the separator device, it is conceivable that the side wall of the fluid chamber formed by the Pyrex influences the lateral mode shape seen in the fluid layer, but by maintaining the *y* structural characteristics the dominant through-thickness resonance should remain relatively unaffected. The FEA model is used to demonstrate the influence of the side-wall thickness upon the lateral mode whilst maintaining a fluid channel width of 5mm.

4.2 Side-wall Material

Some related devices rely on a separate spacer layer to define the fluid layer depth and use a seal to form the side walls [8,9]. Striations are not readily observed in these devices, but although low magnitude lateral forces may be present within the acoustic field of these devices the axial force is still dominant. The use of an acoustically damping material, e.g. silicone elastomer Sylgard 182, to form the fluid layer side walls may contribute in suppressing lateral modes. This is investigated in the FEA model using elastomer properties to describe the side-wall elements.

4 Results and Discussion

4.1 Analysis of test device

Figure 4(a) shows the results of an FE modal analysis of the reflector and fluid layers where white through to black contours indicate minimum to maximum pressure amplitude of the resonant mode. It can be seen that a standing wave of order approximately m=2 and n=1 is present in the reflector layer, which is predominantly a through thickness resonance resembling the pressure profile in figure 3. The field pattern within the fluid layer is much more complex and is highly non-uniform, showing acoustic 'hot spots' at regular positions across the channel width. These hot spots suggest that particles will move to a series of lateral positions across the fluid chamber with an approximate spacing of 0.25mm. The experimentally observed striations are spaced at approximately 0.21mm apart which is comparable to the modelled results. The small discrepancy between spacings may be due to inaccuracies in the fluid channel dimensions used in the simulation.

Based on the predicted pressure gradients, it is estimated that the lateral gradient of potential energy density (to which radiation force is proportional) may be as much as 85% of the more dominant axial gradient, measured in the central region of the fluid layer near the plane of symmetry. This suggests that radiation forces as a result of enclosure modes will significantly influence the trajectory of a particle and resulting separation performance of the device.

Lateral variations in the fluid layer acoustic field also cause variations in the axial strength of the radiation force which may influence the effectiveness of particle separation. The action of lateral radiation forces will induce particle agglomeration, such as the striations observed, allowing short range inter-particle forces to cause particles to cluster further and

sediment out of suspension, consistent with observations.

4.2 Influence of Side-wall Width

In figure 4 it can be seen that when the thickness of the side-wall is decreased from 0.9mm (a) to 0.2mm (b), the distinctive lateral variations lose definition and the field becomes more uniform across the width. The magnitude of the lateral variations is highly dependent on the impedance presented to the fluid by the side wall and in this case, the lower acoustic impedance offered by the thinner side wall results in a reduction in acoustic pressure at the fluid chamber/side-wall boundary and a more uniform lateral field.

In all three plots of figure 4, the acoustic pressure variations within the fluid layer increase in magnitude from the sidewall boundary towards the centre of the fluid layer (from right to left). Correspondingly, the magnitude of the axial (*y*) acoustic radiation force will increase to a maximum at the centre and therefore a particle will converge towards the nodal plane at a greater rate within the centre of the fluid layer. This is consistent with measurements of acoustic pressure in a similar device [8].

Generally the results suggest that by reducing the side-wall width, particles passing through the fluid layer will move towards a better defined nodal plane across the fluid layer width, rather than moving to acoustic hot spots and forming striations. In addition it may be possible to tune the performance of existing devices by the removal of wall material.

4.3 Influence of Side-wall Material

Figure 4(c) illustrates the mode shape for the through-thickness resonant frequency, but replacing the 0.9mm wide Pyrex side-walls in figure 4(a) with a rectangular cross-section elastomer region. A significant difference between the fluid layer mode shapes of figures 4(a) and 4(c) can be seen with the latter, using the elastomer side-wall, not predicting the presence of acoustic hot spots across the width of the fluid layer and, although the contours suggest a small degree of variability in the acoustic field, it is significantly more uniform. The elastomer region appears to exhibit its own low amplitude enclosure mode as a quadrant pattern can be discerned.

The improved lateral uniformity of the acoustic field could be in part attributed to the properties of the elastomer material being more closely matched to the fluid, significantly altering the impedance boundary conditions of the fluid layer and mode patterns.

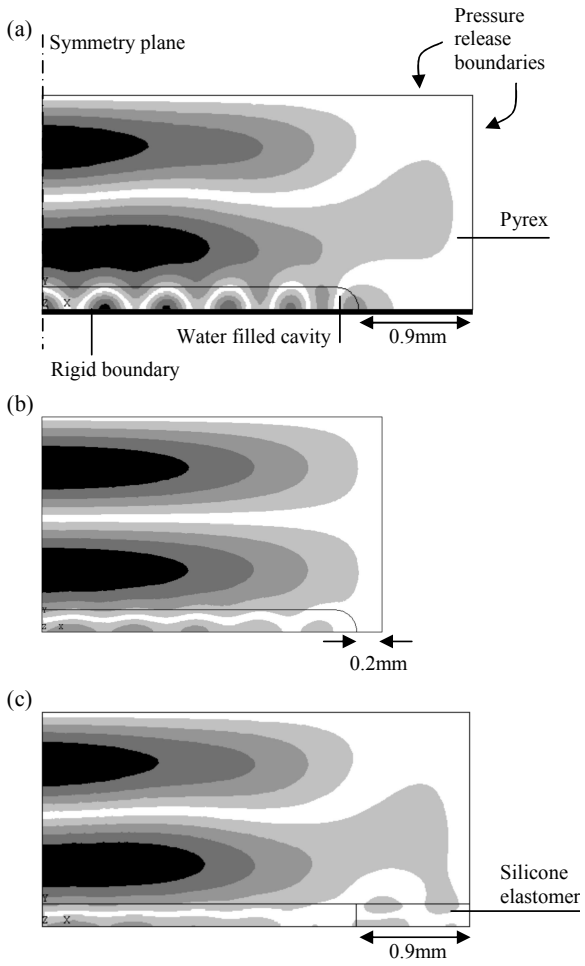

Figure 4: Results of FEA modal analyses using a) the geometry and materials of the fabricated test device and boundary conditions applied to the model, b) reduced side-wall width and c) alternative side-wall material (silicone elastomer).

5. Conclusions

Within particle manipulation devices, lateral variations in the acoustic field can give rise to lateral radiation forces which significantly influence the trajectories of particles and cause particles to agglomerate at certain sites. Although acoustic interference and structural modes can give rise to lateral variations, this paper demonstrates that acoustic enclosure modes are a likely cause within the separator device and should be investigated further.

The model predicts that due to enclosure modes acoustic 'hot spots' exist across the width of the fluid layer, their location corresponding with particle striations observed in experiment. The simulations

also predict that excitation of enclosure modes can give rise to lateral forces which are of the same order of magnitude as the axial forces. FEA is presented as a useful tool to investigate the influence of geometric and material variations upon the acoustic field. Further development of the model will allow near-field and structural modes to be simulated.

Acknowledgements

This work was funded through EPSRC grant GR/R13333/01. The authors also gratefully acknowledge dstl and Porvair Plc. for their support.

References

[1] S. M. Woodside, J. M. Piret, M. Groschl, E. Benes, and B. D. Bowen, "Acoustic force distribution in resonators for ultrasonic particle separation," *AIChE Journal*, vol. 44, pp. 1976-1984, 1998.

[2] T. Lilliehorn, U. Simu, M. Nilsson, M. Almqvist, T. Stepinski, T. Laurell, J. Nilsson, and S. Johansson, "Trapping of microparticles in the near field of an ultrasonic transducer," *Ultrasonics*, vol. 43, pp. 293-303, 2005.

[3] A. Haake, A. Neild, D. H. Kim, J. E. Ihm, Y. Sun, J. Dual, and B. K. Ju, "Manipulation of cells using an ultrasonic pressure field," *Ultrasound in Medicine and Biology*, vol. 31, pp. 857-864, 2005.

[4] N. R. Harris, M. Hill, S. Beeby, Y. Shen, N. M. White, J. J. Hawkes, and W. T. Coakley, "A silicon microfluidic ultrasonic separator," *Sensors and Actuators B-Chemical*, vol. 95, pp. 425-434, 2003.

[5] L. E. Kinsler, A. R. Frey, A. B. Coppens, and J. V. Sanders, *Fundamentals of Acoustics*, 3rd ed. New York: Wiley, 1982.

[6] M. Hill and R. J. K. Wood, "Modelling in the design of a flow-through ultrasonic separator," *Ultrasonics*, vol. 38, pp. 662-665, 2000.

[7] M. Hill, Y. J. Shen, and J. J. Hawkes, "Modelling of layered resonators for ultrasonic separation," *Ultrasonics*, vol. 40, pp. 385-392, 2002.

[8] S. P. Martin, R. J. Townsend, L. A. Kuznetsova, K. A. J. Borthwick, M. Hill, M. B. McDonnell, and W. T. Coakley, "Spore and micro-particle capture on an immunosensor surface in an ultrasound standing wave system," *Biosensors & Bioelectronics*, vol. In Press, Corrected Proof, 2005.

[9] J. J. Hawkes, M. J. Long, W. T. Coakley, and M. B. McDonnell, "Ultrasonic deposition of cells on a surface," *Biosensors & Bioelectronics*, vol. 19, pp. 1021-1028, 2004.

Abstract for WCU/UI 2005

Particle Concentration Using a Microfabricated Ultrasonic Resonator

M. Hill[1], R.J. Townsend[1], N.R. Harris[2], N.M. White[2], S.P. Beeby[2], M.B. McDonnell[3];

School of Engineering Sciences, University of Southampton[1],
School of Electronics and Computer Science, University of Southampton[2],
dstl, Porton Down, Salisbury[3]

Ultrasonic radiation forces have been used by a number of investigators to bring about particle separation. Several strategies have been developed for bringing this about. Some devices rely on particle agglomeration and settling, some use the ultrasonic field to enhance the filtration efficiency of a porous mesh and others rely on laminar flow in conjunction with flow splitters to extract high and low concentration streams from different outlets. The majority of the devices using this latter technique have worked most successfully as clarifiers allowing the extraction of a filtered, particle-free sample. The particle concentration in the remaining fluid is increased, but by a relatively low factor. However there are many applications, biosensing systems for example, in which a flow-through device able to increase particle concentration significantly would be of use.

Recently researchers have shown that ultrasonic resonators can be designed which are able to force particles towards a solid boundary, rather than to the centre of a fluid layer as had typically been the case and devices able to achieve this have been fabricated using bonded silicon and Pyrex microstructures. Such structures offer the possibility of designing a flow-through microfluidic device able to concentrate particles in order to increase the sensitivity of down-stream particle detection systems.

This paper describes the modelling, design and fabrication of such a microfabricated concentrator. The importance of the correct positioning of the standing wave nodal plane is discussed, along with the influence of flow rates and profiles on concentrator performance. It is shown that there are several different modes of operation which can be used within the same resonator structure and the advantages and disadvantages of these are discussed. Test results of a prototype device demonstrate the performance with different particles and at different flow rates are included.

An Ultrasonic MEMS Particle Separator with Thick Film Piezoelectric Actuation

Martyn Hill, Rosemary J. Townsend
School of Engineering Sciences, University of Southampton
Southampton, UK
m.hill@soton.ac.uk

Nicholas R. Harris, Neil M. White, Stephen P. Beeby
Electronics and Computer Science
University of Southampton
Southampton, UK

Jiexiong Ding
School of Mechatronics Eng.
Univ. of Electronic Science and Technology of China
Chengdu, Sichuan, China

***Abstract*—An ultrasonic resonator has been microfabricated from layers of silicon and Pyrex. A fluid channel of approximately 200µm in depth is etched into the Pyrex and allows particles within the fluid to be moved by acoustic radiation forces into the pressure nodal planes of the ultrasonic standing wave. Depending on the required application this can be used to generate a particle-free fluid sample, to concentrate particles prior to analysis, or to move particles to a surface within the resonator to aid analysis. In previously published work this resonator has been driven using a thickness mode bulk piezoceramic. While this has provided reasonable performance, the adhesion of the piezoceramic plate to the silicon has proved both the least repeatable and the least reliable element of the fabrication process. It has also been a factor in the long-term failure of test devices. To overcome these issues, multilayer thick-film printed actuators have been developed to replace the bulk piezoceramic. Thick-film processing offers an effective means of depositing active materials onto substrates, and the technique is compatible with the microfabrication process, allowing multiple actuators to be printed onto a wafer comprising multiple devices. A variety of structures has been tested on ceramic substrates and shown to provide acceptable acoustic outputs when compared with bulk transducers mounted on identical substrates. A two-layer actuator provides a good performance without excessive complexity and this configuration has been used on the resonator. Further acoustic and flow modeling of the device is described, and this has been used both to improve the channel geometry and to select better operating conditions for the system. It is shown that the thick-film actuated device working at the new operating conditions provides significantly improved performance when compared with the bulk piezoceramic device, and in particular is able to offer a five-fold reduction in concentration for 1µm latex particles, which had previously proved difficult to manipulate successfully.**

Keywords – microfluidic; layered resonator; ultrasonic standing wave; radiation forces; µTAS.

I. INTRODUCTION

Miniaturized systems for carrying out chemical and biological analysis, often known as micro total analysis systems (µTAS) or "Lab on a Chip", are currently the subject of significant research interest. An important aspect of many such systems is their ability to handle particles and a variety of techniques has been explored, notably the use of electrophoresis [1]. An alternative technology, well suited to handling particles in the 1-50 µm size range, is the use of ultrasonic standing waves.

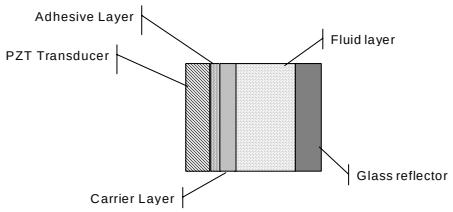

Figure 1. Typical structure of layered resonator

Particles or cells in an acoustic standing wave experience acoustic radiation forces which tend to move them to nodal planes of that standing wave [2]. This can be used to agglomerate [3], filter [4] or fractionate [5] particles. An important area for the exploitation of such forces is in microfluidic systems [6] where resonators with critical dimensions of a wavelength or less at ultrasonic frequencies can, in particular, be used to manipulate biological cells.

This paper describes the use of various modeling techniques to design a multi-layered resonator suitable for use as a microfluidic filter, and its microfabrication from silicon and Pyrex. It also describes the refinement of the initial design by improved flow profiles within the device and the use of novel, thick-film ultrasonic actuation.

II. INITIAL RESONATOR DESIGN AND FABRICATION

A. One Dimensional Acoustic Modeling

Figure 1 shows the typical structure of a layered resonator used to generate the standing waves required for particle manipulation. A simple one dimensional transfer impedance model has been used in the initial stages of the design of microfabricated resonators [7, 8]. While reducing the system to a single dimension ignores many important features of the system, as is discussed below, such models are a useful starting point for selecting materials and geometries.

It was decided to manufacture the resonator from silicon and Pyrex so as to be compatible with other microfluidic devices made using common wet etching techniques. Standard

The authors gratefully acknowledge the help of the Engineering and Physical Sciences Research Council and Dstl in funding this work.

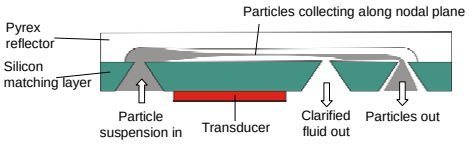

Figure 2. Schematic of particle separator showing movement of particles through the device

silicon wafer of 525 µm thickness was chosen and the impedance transfer model was then used to select appropriate layer thicknesses for the fluid layer and the Pyrex reflector layer. Dimensions were chosen so as to:

- Position the pressure node at the required plane of the channel
- Provide good acoustic energy density
- Be robust to uncertainties in modeling parameters and manufacturing tolerances.

B. Mode of Operation and Fabrication

The one dimensional model described above was used to select layer thicknesses such that the operating frequency was a half wave resonance with a node close to the centre of the fluid layer [6]. It can be shown that combinations of layer thicknesses can be used to place the node at arbitrary positions within the fluid layer [9], even adjacent to the reflector to produce a quarter wave resonance. Such a quarter wave resonance can be used in a similar device to concentrate particles, but this application uses the half wave mode to produce a clarified, particle free sample of fluid, as shown schematically in figure 2.

Initial devices were fabricated with either single or double chamfered ports in the silicon layer. This was achieved using a double sided alignment process and standard wet KOH etching leaving chamfers at the angle of 54.7°. The chamber was then formed by etching a 1.7mm thick Pyrex wafer to the desired depth of 240µm. Ultrasonic actuation was achieved using bulk pzt attached to the silicon layer with adhesive

C. Flow modeling to predict performance

Models were also developed to predict the particle paths through the device, under the influence of both the flow regime and the acoustic field applied [10]. This work has allowed the device separation performance to be predicted under a range of operating conditions

Within the acoustic field, particles are subject to the primary acoustic radiation force, a buoyancy force and a Stokes drag force. As the particles move under these forces the concentration φ at height z varies as:

$$\frac{\partial \varphi(z,t)}{\partial t} = -\frac{\partial\left(\dot{z}\varphi(z,t)\right)}{\partial z}$$

The acoustic transfer impedance model has been extended and used to solve the above equation numerically to provide a profile of concentrations across the fluid and a prediction of separation efficiency.

III. Performance of the Initial Device

The device was tested using the experimental procedure described by Harris et al. [11] and the experimental results compared with model predictions of outlet concentrations. In the experiments for yeast, a total flow rate of approximately 0.053ml/s was maintained, 25% of which passed through outlet 1. For the 1µm latex particles these figures were 0.028ml/s and 21% respectively.

The modeled results for the separation of 1 micron particles (Figure 3, lower graph) compare reasonably well with the experiment results. Generally, the experimental results show slightly lower concentrations than modeled predictions, which can be attributed to the adhesion of particles to the walls within the fluid network surrounding the separator. At higher voltages, particles tend to clump together under higher acoustic forces, potentially disturbing the laminar flow required for successful separation and limiting the possible clearance through outlet 1. For the separation of yeast (upper graph), the modeled results are more optimistic than the experimental results. The initial concentration of the yeast was quite high at 0.2% compared to that for the 1µm latex particles where 0.016% was used. This high concentration may impede the motion of the yeast cells towards the nodal plane, indeed clumping was observed to be a greater problem with the yeast than with the latex particles. However, at high voltages separation is successful, producing a high degree of separation.

IV. Modification and Further Modeling

A. Modification of Fluid Channels

Computational fluid dynamics (CFD) was used to analyze

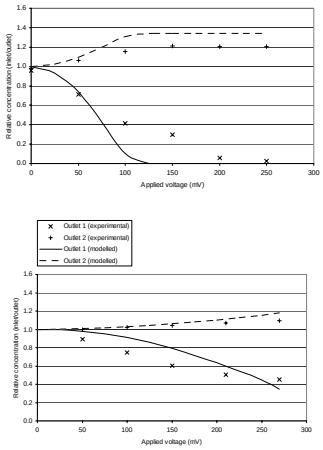

Figure 3. Above: separation of yeast particles based on an initial concentration of 0.2% weight. Below: separation of 1 micron latex particles based on an initial concentration of 0.016% weight. Applied voltage is input voltage to amplifier.

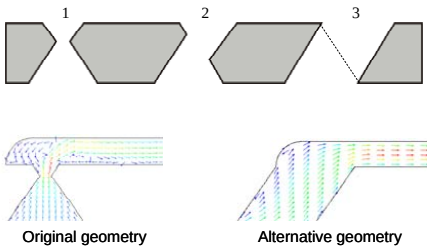

Figure 4. The effect of increasing the offset of upper and lower masks on the inlet channel geometry (above) and the modeled flow for cases 1 & 3 (below).

the flow regime in the device. It was apparent that the performance was being hindered by recirculation zones associated with the overlaps of the Pyrex and the silicon layers. A study was undertaken to establish if improved geometries for inlet and outlet ducts were available [12], while still constrained by etch angles of the anisotropic etches used. The top section of figure 4 shows how this was achieved by offsetting the top and bottom etches, finally resulting in parallel sided ducts as shown in case 3. This resulted in an improved inlet/outlet flow, as predicted by the CFD profiles in the lower part of figure 4.

The validity of the CFD modeling was tested by measuring the extent of the visible eddy zones at different flow rates and comparing them with the predicted zones, for a single sided etch (as shown in figure 2), a double sided etch (geometry 1 in figure 4) and a parallel sided etch (geometry 3 in figure 4). In figure 5 the size of the eddy region is plotted as a function of flow rate. It can be seen that eddy size is strongly related to the fluid flow rate. An initial inspection shows that the CFD results underestimate the length of the eddy region, however they both show that the double-etched geometry produces a slightly smaller eddy region compared to the single etch geometry up to a flow rate of 0.5ml/s. When a parallel sided etch was used an eddy region was no longer visible.

B. Modeling Lateral Acoustic Forces

Finite element analysis of the separator was undertaken

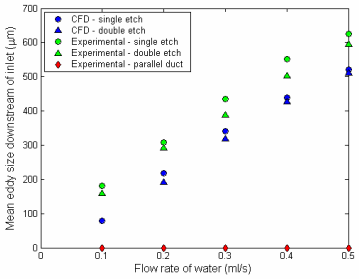

Figure 5. Extent of eddy region downstream of inlet duct for both single etched, double etched and parallel sided geometries over a range of flow rates and plotted for both CFD and experimental results.

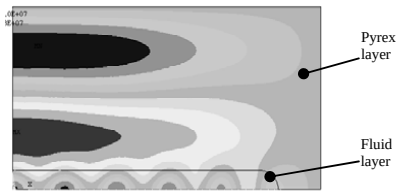

Figure 6. Finite element analysis of the fluid and Pyrex layer showing lateral variations in the acoustic field.

using ANSYS. In experiment lateral forces were seen to form striated patterns in the direction of the fluid flow. Modal analysis has been used to predict the nature of resonance within the separator fluid channel and Pyrex layers. In 1 dimension the results match those of the acoustic impedance transfer model, yet in 2 dimensions variations in the field across the width of the fluid channel are predicted, an example of which is shown in figure 6. The image shows the acoustic pressure field at a half wave resonance (3.4MHz). In the fluid region variations exist in both the x and y directions. Although the dominant force is in the y-direction, the contour plot suggests that particles will also move across the width of the channel in the x-direction as observed experimentally. Modifications of the side wall geometry strongly influence the modeled pattern of pressure variations, allowing the strength of the lateral forces to be reduced relative to the axial forces.

C. Thick Film Piezoelectric Actuation

The device described above uses a bulk pzt actuator glued to the silicon carrier layer. Such a technique is time and labor intensive requiring careful alignment significant effort to create repeatable adhesive layers. Thick-film technology represents a convenient way of depositing active materials, and developments in processing and paste formulation [13] have allowed the technology to be implemented on silicon. It gives several advantages over bonding bulk material in that it is inherently a batch process, so an entire wafer of devices can be printed in one go. It also gives good repeatability as no bonding layer is required.

The thick-film actuating mechanism is manufactured by co-firing several layers of PZT at 890˚C each separated by a gold electrode layer, onto a suitable substrate, in this case silicon.

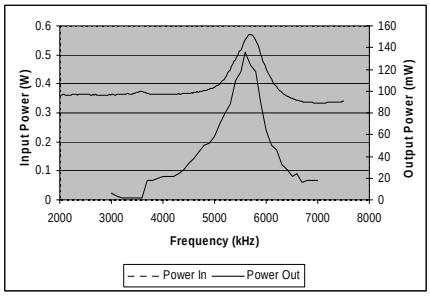

Figure 7. Power measurements for a two layer thick film pzt structure.

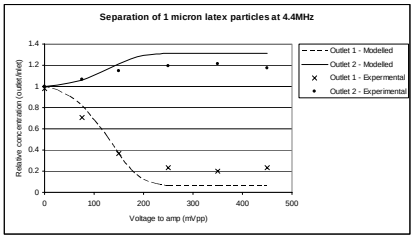

Figure 8. Above: separation of 1 micron latex particles using thick-film actuated device.

Co-firing is a technique whereby multiple layers are printed and dried before being fired once as a complete structure, avoiding the successive degradation of activity caused by repeated firings. In order to develop a suitable actuator, multilayer structures were first printed on 630µm thick 96% alumina tiles. Several devices were constructed consisting of 1, 2 or 3 PZT layers. The selected process and multilayer structure was then applied to a micromachined silicon wafer, 525µm thick for use in the ultrasonic separator. The printed thicknesses of the PZT layers were measured at around 80µm. The firing profile used was a standard thick-film cermet profile, with a peak temperature of 890 °C, held for 15 minutes. The structure requires polarization after firing, and this was achieved by applying a 4MV/m field at 150˚C for 30 minutes across each layer in parallel, before allowing the structure to cool with the field still applied.

The main advantage in producing a multilayered structure is that it enables larger displacements to be generated than would be possible with a single layer having the same total thickness, for a given actuating voltage. In addition, layering the structure allows lower absolute voltages to generate the required polarizing field strength.

The piezoelectric activity of the test actuators was measured using a *Take Control* PM35 piezometer. The activity increased with the number of layers as expected. Direct measurements of the acoustic output power from the test actuators were also made using an acoustic force balance [14]. Power input and output for one of the two layer structures is shown in figure 7. On the basis of these tests a two layer structure was selected as a good compromise between simplicity of manufacture and piezoelectric activity.

V. Performance of the Modified Device

Further fluid modeling suggested that in order to separate 1µm particles successfully a lower flow rate would be required. In experimental tests of the modified device the total flow rate was 5.1µl/min with a flow rate split between the outlets of 75%/25% between outlets 1 and 2

Figure 8 shows modeled and experimental results for outlet concentrations using 1µm particles in the modified separator. Comparing figures 3 and 8 it can be seen the maximum clearance obtained with the thick film device was significantly better than that obtained using the bulk pzt actuation (roughly a five fold reduction in concentration compared with a two fold reduction). This is due, in part, to the use of lower flow rates but at the operating frequencies used the performance of the two actuation methods is comparable. The device does not quite match the predicted performance at higher voltages, but the trends are predicted well by the electro-acoustic & flow modeling.

VI. Conclusions

It has been shown that a microfabricated resonator can be used to manipulate micron scale particles and, in this configuration, substantially reduce the particle concentration in flow through operation. The performance of the separator can be improved by the selection of appropriate flow rates through the modeling techniques described. Further, multilayer thick film pzt actuation provides an efficient and convenient alternative to bulk pzt.

References

[1] T. Vilkner, D. Janasek, and A. Manz, "Micro total analysis systems. Recent developments," *Analytical Chemistry*, vol. 76, pp. 3373-3385, 2004.
[2] M. Gröschl, "Ultrasonic separation of suspended particles - Part I: Fundamentals," *Acustica*, vol. 84, pp. 432-447, 1998.
[3] J. F. Spengler, M. Jekel, K. T. Christensen, R. J. Adrian, J. J. Hawkes, and W. T. Coakley, "Observation of yeast cell movement and aggregation in a small-scale MHz-ultrasonic standing wave field," *Bioseparation*, vol. 9, pp. 329-341, 2000.
[4] J. J. Hawkes and W. T. Coakley, "Force field particle filter, combining ultrasound standing waves and laminar flow," *Sensors and Actuators B-Chemical*, vol. 75, pp. 213-222, 2001.
[5] M. Kumar, D. L. Feke, and J. M. Belovich, "Fractionation of cell mixtures using acoustic and laminar flow fields," *Biotechnology And Bioengineering*, vol. 89, pp. 129-137, 2005.
[6] N. R. Harris, M. Hill, S. P. Beeby, Y. Shen, N. M. White, J. J. Hawkes, and W. T. Coakley, "A Silicon Microfluidic Ultrasonic Separator," *Sensors and Actuators B*, vol. 95, pp. 425-34, 2003.
[7] M. Hill, Y. Shen, and J. J. Hawkes, "Modelling of layered resonators for ultrasonic separation.," *Ultrasonics*, vol. 40, pp. 385-92, 2002.
[8] M. Hill and R. J. K. Wood, "Modelling in the design of a flow-through ultrasonic separator," *Ultrasonics*, vol. 38, pp. 662-665, 2000.
[9] M. Hill, "The selection of layer thicknesses to control acoustic radiation force profiles in layered resonators," *JASA*, vol. 114, pp. 2654-2661, 2003.
[10] R. J. Townsend, M. Hill, N. R. Harris, and N. M. White, "Modelling of particle paths passing through an ultrasonic standing wave," *Ultrasonics*, vol. 42, pp. 319-24, 2004.
[11] N. R. Harris, M. Hill, R. J. Townsend, N. M. White, and S. P. Beeby, "Performance of a Micro-engineered ultrasonic particle manipulator," *Sensors and Actuators A: Physical*, pp. In Press, 2005.
[12] R. J. Townsend, M. Hill, N. R. Harris, N. M. White, S. P. Beeby, and R. J. K. Wood, "Fluid modelling of microfluidic separator channels," *Sensors and Actuators B: Chemical*, pp. (In Press), 2005.
[13] R. N. Torah, S. P. Beeby, and N. M. White, "Improving the piezoelectric properties of thick-film PZT: the influence of paste composition, powder milling process and electrode material," *Sensors And Actuators A-Physical*, vol. 110, pp. 378-384, 2004.
[14] N. R. Harris, M. Hill, R. N. Torah, R. J. Townsend, S. P. Beeby, N. M. White, and J. Ding, "A Multilayer Thick-film PZT Actuator for MEMs Applications," presented at Eurosensors, Barcelona, 2005.

A Multilayer Thick-film PZT Actuator for MEMs Applications

Harris N R*[1], Hill M[2], Torah R[1], Townsend R[2], Beeby S[1], White NM[1], Ding J[3]

[1]School of Electronics and Computer Science, Southampton University,UK
nrh@ecs.soton.ac.uk Tel +44 2380 593274
[2]School of Engineering Sciences, Southampton University,UK
[3]School of Mechatronics Engineering, University of Electronics Science&Technology, Chengdu, China

Abstract: This paper describes a technique for replacing the traditional bonded bulk PZT transducer, commonly used in MEMS devices, with a screen printed equivalent. Previously, the piezoelectric activity available from screen printed PZT has been lower than the bulk material, but recent developments in material composition and device structure have allowed screen printed structures to deliver powers equivalent to bulk devices.

Keywords Ultrasonic, MEMS, thick-film

INTRODUCTION

Work at Southampton has been progressing to develop an alternative to bonded bulk PZT for silicon MEMS actuators. Thick-film deposition represents a convenient way of depositing active materials, and developments in processing [1] and paste formulation [2] have allowed the technology to be migrated to silicon. This work describes an extension of this processing allowing piezoelectric coefficients to be achieved that are comparable to bulk PZT. The motivation for this development was to design a thick-film actuator to drive a microengineered ultrasonic acoustic separator, previously tested using a bulk element, and results are reported for this new device.

DESCRIPTION OF ACTUATOR

The actuating mechanism is manufactured by co-firing several layers of PZT at 890˚C each separated by an electrode layer. Several test devices were constructed, these consisting of either 1, 2 or 3 PZT layers, printed onto a ceramic substrate, and the results from these test samples were used to design a final actuator for use on silicon. In addition, a device using a bulk PZT drive element, glued to the silicon was constructed to allow a comparison.

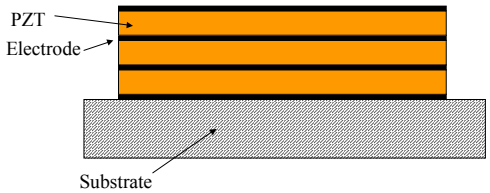

Figure 1 A Multilayer Structure

Figure 1 shows a three layer structure. The PZT paste is formulated within the Research Group [2]. The electrodes are thick-film gold. The structure requires polarisation and this was achieved by applying a 4MV/m field at 150˚C for 30 minutes across each layer in parallel. The main advantage in producing a multilayered structure is that it enables larger displacements to be generated than would be possible with a single layer of the same total thickness, effectively increasing the d_{33} coefficient. This results in lower drive voltages being required.

TEST RESULTS

d_{33} coefficients were measured using a *Take Control* PM35 meter. A layer of waterproof conformal coating was then sprayed on to seal the devices against water ingress.

Impedance Measurements:

The devices were mounted in a frame to allow ease of handling, and mounted face down in a beaker of degassed water. Impedance measurements were taken using a HP 4192A LF impedance analyser. These measurements enabled the transducer

resonance frequency to be identified, and it was noted that this varied with the number of layers in a repeatable manner (Table 1).

Acoustic Power Measurements and Electrical Power Calculations:

An acoustic force balance (Ohmic Instruments UPM-DT-1) was used to measure the acoustic output power of the devices. These were then compared with the calculated power input to the device. This was calculated using the measured impedance, the known input voltage amplitude, and output impedance and gain of the driving amplifier.

Type	d_{33} typical (pC/N)	Resonant frequency	Efficiency %
Bulk	246	3.4MHz	18
1 layer	81	5.7MHz	36
2 layer	178	4.9MHz	43
3 layer	323	3.9MHz	35

Table 1: A comparison of results for different devices

The test devices have shown themselves to be more efficient at converting electrical energy into acoustic energy transmitted into water [5], then an equivalent bulk device (figures 2 and 3), and it was concluded that a two layer device would prove suitable for the separator application.

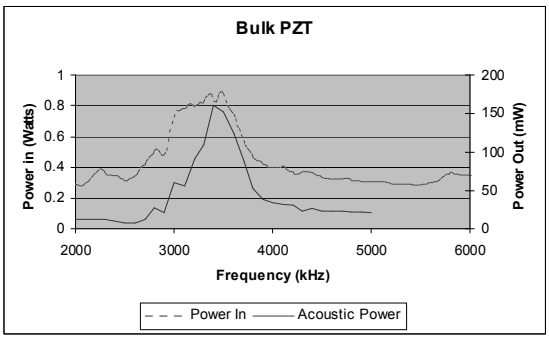

Figure 2 Power measurements for a bulk PZT drive element

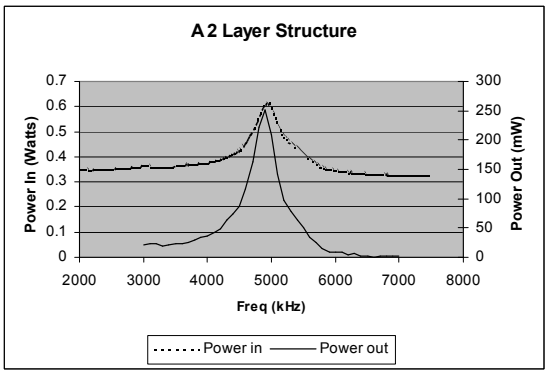

Figure 3 Power measurements for a 2 layer thick-film structure

ULTRASONIC SEPARATOR

The principle of the operation of the separator is given in reference [3] and the model used to predict its operation is given in [4]. The thick-film separator performance was modeled and the results are incorporated in figure 8 for 1 micron latex particles.

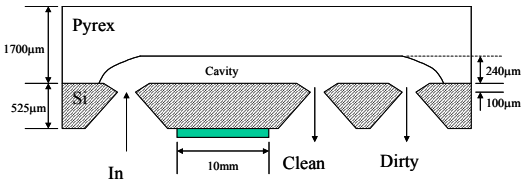

Figure 4 Cross-section of an ultrasonic separator

Figure 4 shows a cross-section of a typical device. In brief, the actuator is used to establish an acoustic standing wave within the cavity, and particles within the fluid are driven to the nodes by radiation forces. In this device we are working with a half-wave cavity.

This concentrates the particles within a layer in the centre of the cavity, and by adjusting the relative flows at the outlets, a ‘clean’ and a ‘dirty’ flow can be extracted.

SEPARATOR CONSTRUCTION

Figure 5 A cross-section of a device

A wafer of devices was fabricated and a two-layer thick-film actuator was deposited on the silicon in place of the bulk PZT. The silicon wafer was a standard 525µm wafer, etched with access ports as indicated in figure 4, and an etched Pyrex wafer was anodically bonded to this wafer to create the device. A 2 layer actuator was printed with gold electrodes, and polarised , as described previously. A sample device was sliced longitudinally and is shown in figure 5. This picture shows (from right to left) the two PZT layers, the silicon carrier layer, the fluid gap and finally the Pyrex backing layer, and gives a good indication of the relative scales of the different layers.

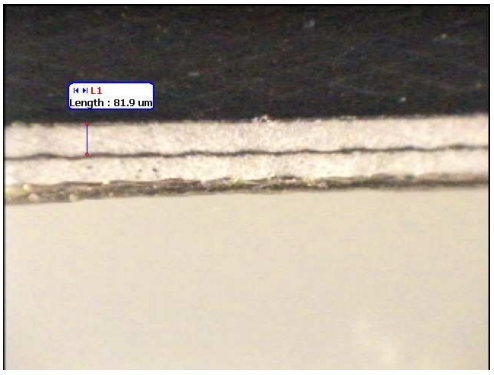

Figure 6 Detail of the PZT layers

Figure 6 shows a more detailed photograph of the thick-film layer. A good uniformity of printing is apparent, with the PZT layer being about 82µm thick. The gold electrode layers are also visible. Impedance measurements indicate that the composite structure has a resonance of about 3.9MHz in air. When filled with water, impedance measurements show that the two predicted half wave modes were present, indicating that the model should give a good indication of the performance of the device. The device was operated at the peak at 4.4MHz.

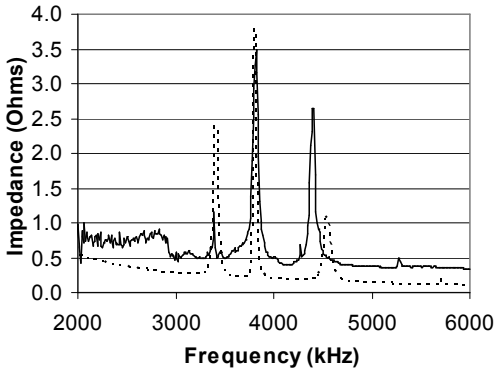

Figure 7 Real part of impedance (solid – measured, dotted - modelled)

SEPARATOR TEST

The experimental procedure was as described in [6], in that turbidity measurements were taken using a Honeywell APMS-10GRCF turbidity sensor, previously calibrated against a haemocytometer for the latex particles used. The total flow rate through the device was 5.1ul/min with a flow rate split between the outlets of 75/25%. The performance of the separator running at 4.4MHz was measured at different drive voltage levels, thus verifying the predictions of the model. Figure 8 shows the measured performance, compared with the predicted performance from the model.

CONCLUSIONS

The successful results show that the thick-film PZT actuator performs well as an acoustic source in this application, and

further that the previously developed model for predicting the performance of bulk PZT driven concentrators has been verified for thick-film PZT actuators. In addition, it can be concluded that thick-film actuators are more efficient than bonded bulk PZT actuators for this application. We therefore conclude that thick-film multilayer actuators are a viable alternative to bonded bulk PZT actuators, with the added advantage of being batch processable on a wafer scale.

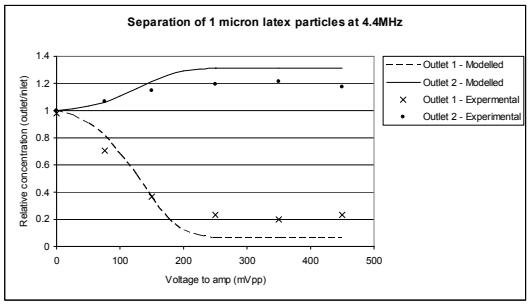

Figure 8 Performance of a thick-film actuated separator

REFERENCES

[1] Maas, R., Koch, M., Harris, N.R., White, N.M., Evans, A. G. R. Thick-film Printing of PZT onto Silicon *Materials Letters* **31** (1997) pp109-112

[2] R.N.Torah,S.P.Beeby,N.M.White Improving the piezoelectric properties of thick-film PZT: the influence of paste composition, powder milling process and electrode material. *Sensors and Actuators A* **110** (2004) pp378-384

[3] Harris NR, Hill M, Townsend R, White NM, Beeby SP, Performance of a Micro-engineered Ultrasonic Particle Manipulator, *Proc Eurosensors XVIII Rome 12-15 September 2004* pp203-204

[4] Townsend RJ, Hill M, Harris NR, White NM, Modelling of Particle Paths passing through an Ultrasonic standing wave *Ultrasonics* 2004 42 pp319-324

[5] Harris NR, Torah RN,White NM, Hill M, Beeby SP, A PZT multilayer actuator for ultrasonic applications, *Proc 15th MicroMechanics Workshop pp17-20, 5-7 September 2004, Leuven, Belgium*

[6] Harris NR, Hill M, Townsend R, White NM,Beeby SP, Performance of a micro-engineered ultrasonic particle manipulator *Sensors and Actuators B2005 in press*

ACKNOWLEDGEMENTS

The authors with to thank the Engineering and Physical Research Council (EPSRC) for their financial support under grant number GR/R13333/01, and acknowledge the Financial support given by DSTL and Porvair Filtration Group. Special thanks are due to Angela Cotton in the Medical Physics department at Southampton General Hospital for the use of the power balance.

References

[1] A. Kundt and O. Lehumann. Longitudinal vibrations and acoustic figures in cylindrical columns of liquids. *Annalen der Physik and Chemie (Pogendorff's Annalen)*, 153:1, 1874.

[2] M. Hill, Y. J. Shen, and J. J. Hawkes. Modelling of layered resonators for ultrasonic separation. *Ultrasonics*, 40(1-8):385–392, 2002.

[3] M. Hill and R. J. K. Wood. Modelling in the design of a flow-through ultrasonic separator. *Ultrasonics*, 38(1-8):662–665, 2000.

[4] J. J. Hawkes and W. T. Coakley. Force field particle filter, combining ultrasound standing waves and laminar flow. *Sensors and Actuators B-Chemical*, 75(3):213–222, 2001.

[5] N. R. Harris, M. Hill, S. Beeby, Y. Shen, N. M. White, J. J. Hawkes, and W. T. Coakley. A silicon microfluidic ultrasonic separator. *Sensors and Actuators B-Chemical*, 95(1-3):425–434, 2003.

[6] J. P. Hulme, S. Mohr, N. J. Goddard, and P. R. Fielden. Rapid prototyping for injection moulded integrated microfluidic devices and diffractive element arrays. *Lab on a Chip*, 2(4):203–206, 2002.

[7] J. Bryzek, K. Petersen, and W. McCulley. Micromachines on the march. *IEEE Spectrum*, 31(5):20–31, 1994.

[8] P. Wilson. Tutorial: silicon micro-machining. *Sensor Review*, 10(4):178–181, 1990.

[9] M. Huff. Tutorial: Mems fabrication. *Sensor Review*, 22(1):18–33, 2002.

[10] D. F. Moore and R. R. A. Syms. Recent developments in micromachined silicon. *Electronics & Communication Engineering Journal*, 11(6):261–270, 1999.

[11] E. Verpoorte and N. F. De Rooij. Microfluidics meets mems. *Proceedings of the IEEE*, 91(6):930–953, 2003.

[12] W. D. Callister. *Materials science and engineering an introduction*. Wiley, New York Chichester, 4th edition, 1997.

[13] Processing tips: How to catch the right etch. *IntelliNews*, 10(2):1–2, Spring 2002.

[14] N. T. Nguyen, S. Schubert, S. Richter, and W. Dotzel. Hybrid-assembled micro dosing system using silicon-based micropump/valve and mass flow sensor. *Sensors and Actuators A - Physical*, 69(1):85–91, 1998.

[15] *Micro valve with a novel electrostatic drive*. http://www.infotech.tu-chemnitz.de/~zfm/eng/research/vwproject.html, Web page accessed on 1 Sept 2003.

[16] J. M. Bustillo, R. T. Howe, and R. S. Muller. Surface micromachining for microelectromechanical systems. *Proceedings of the IEEE*, 86(8):1552–1574, 1998.

[17] M. I. Haller and B. T. KhuriYakub. A surface micromachined electrostatic ultrasonic air transducer. *IEEE Transactions on Ultrasonics Ferroelectrics and Frequency Control*, 43(1):1–6, 1996.

[18] X. C. Jin, I. Ladabaum, F. L. Degertekin, S. Calmes, and B. T. Khuri-Yakub. Fabrication and characterization of surface micromachined capacitive ultrasonic immersion transducers. *Journal of Microelectromechanical Systems*, 8(1):100–114, 1999.

[19] W. P. Eaton and J. H. Smith. Micromachined pressure sensors: Review and recent developments. *Smart Materials & Structures*, 6(5):530–539, 1997.

[20] M. Gad-el Hak. *The MEMS Handbook*. CRC, Boca Raton, 2001.

[21] J. F. Douglas, J. M. Gasiorek, and J. A. Swaffield. *Fluid Mechanics*. Prentice Hall, Harlow, 2nd edition, 2000.

[22] F. M. White. *Fluid Mechanics*. McGraw-Hill International Editions. McGraw-Hill, 4th edition, 1999.

[23] T. Cebeci and P. Bradshaw. *Momentum transfer in boundary layers*. Series in thermal and fluids engineering. Hemisphere Pub. Corp., Washington, 1977.

[24] P. Gravesen, J. Branebjerg, and O. S. Jensen. Microfluidics - a review. *Journal of Micromechanics and Microengineering*, 3(4):168–182, 1993.

[25] G. L. Morini. Laminar liquid flow through silicon microchannels. *Journal of Fluids Engineering-Transactions of the ASME*, 126(3):485–489, 2004.

[26] S. R. Kendall and H. V. Rao. Detection of multiple solutions using a mid-cell back substitution technique applied to computational fluid dynamics. In N. Rhodes, editor, *Computational Fluid Dynamics in Practice*, pages 23–41. Professional Engineering Publishing, Bury St. Edmunds, 2001.

[27] G. Desmet and G. V. Baron. Chromatographic explanation for the side-wall induced band broadening in pressure-driven and shear-driven flows through channels with a high aspect-ratio rectangular cross-section. *Journal of Chromatography A*, 946(1-2):51–58, 2002.

[28] N. T. Nguyen and S. T. Wereley. *Fundamentals and applications of microfluidics*. Artech House, Boston, 2002.

[29] M. Gad-el Hak. The fluid mechanics of microdevices - the freeman scholar lecture. *Journal of Fluids Engineering-Transactions of the ASME*, 121(1):5–33, 1999.

[30] I. Zandi. Hydraulic transport of bulky materials. In I. Zandi, editor, *Advances in solid-liquid flow in pipes and its applications*, pages 1–34. Pergamon Press, New York, 1971.

[31] W. Chang, D. Trebotich, L. P. Lee, and D. Liepmann. Evaluation of various non-newtonian constitutive equations for blood flow in simple microchannels. In *1st Annual International IEEE-EMBS Special Topic Conference on Microtechnologies in Medicine and Biology*, Lyon, France, 2000.

[32] R. J. K. Wood, M. Hill, N. R. Harris, and P. G. Dargie. An investigation into the feasibility of flow-through ultrasonic separation. Technical Report 98/EC215, Mechanical Engineering Consultacy Service, University of Southampton, July 1998.

[33] C. M. Cousins, P. Holownia, J. J. Hawkes, C. P. Price, P. Keay, and W. T. Coakley. Clarification of plasma from whole human blood using ultrasound. *Ultrasonics*, 38(1-8):654–656, 2000.

[34] G. W. Govier and K. Aziz. *The flow of complex mixtures in pipes*. Van Nostrand, Princeton, 1972.

[35] J. Pfahler, J. Harley, H. Bau, and J. Zemel. Liquid transport in micron and submicron channels. *Sensors and Actuators A - Physical*, 22(1-3):431–434, 1990.

[36] G. M. Mala and D. Q. Li. Flow characteristics of water in microtubes. *International Journal of Heat and Fluid Flow*, 20(2):142–148, 1999.

[37] X. F. Peng and G. P. Peterson. Convective heat transfer and flow friction for water flow in microchannel structures. *International Journal of Heat and Mass Transfer*, 39(12):2599–2608, 1996.

[38] J. Judy, D. Maynes, and B. W. Webb. Characterization of frictional pressure drop for liquid flows through microchannels. *International Journal of Heat and Mass Transfer*, 45(17):3477–3489, 2002.

[39] I. Papautsky, J. Brazzle, T. Ameel, and A. B. Frazier. Laminar fluid behavior in microchannels using micropolar fluid theory. *Sensors and Actuators A - Physical*, 73(1-2):101–108, 1999.

[40] E. B. van Akker, M. Bos, and W. E. van der Linden. Convection and diffusion in a microflow injection system. *Analytica Chimica Acta*, 373(2-3):227–239, 1998.

[41] F. G. Tseng, I. D. Yang, K. H. Lin, K. T. Ma, M. C. Lu, Y. T. Tseng, and C. C. Chieng. Fluid filling into micro-fabricated reservoirs. *Sensors and Actuators A - Physical*, 97-8:131–138, 2002.

[42] Y. H. Zhang, X. J. Gu, R. W. Barber, and D. R. Emerson. An analysis of induced pressure fields in electroosmotic flows through microchannels. *Journal of Colloid and Interface Science*, 275(2):670–678, 2004.

[43] S. Ehlers, K. Elgeti, T. Menzel, and G. Wiessmeier. Mixing in the offstream of a microchannel system. *Chemical Engineering and Processing*, 39(4):291–298, 2000.

[44] X. X. Bai, J. Josserand, H. Jensen, J. S. Rossier, and H. H. Girault. Finite element simulation of pinched pressure-driven flow injection in microchannels. *Analytical Chemistry*, 74(24):6205–6215, 2002.

[45] M. Koch, A. G. R. Evans, and A. Brunnschweiler. Coupled FEM simulation for the characterization of the fluid flow within a micromachined cantilever valve. *Journal of Micromechanics and Microengineering*, 6(1):112–114, 1996.

[46] *ANSYS / Multiphysics TM*, volume 2002. http://www.ansys.com/ansys/multiphysics.htm, Web page accessed on 2 Sept 2002.

[47] M. Koch, A. G. R. Evans, and A. Brunnschweiler. Characterization of micromachined cantilever valves. *Journal of Micromechanics and Microengineering*, 7(3):221–223, 1997.

[48] M. Koch, N. Harris, A. G. R. Evans, N. M. White, and A. Brunnschweiler. A novel micromachined pump based on thick-film piezoelectric actuation. *Sensors and Actuators A - Physical*, 70(1-2):98–103, 1998.

[49] B. Husband, M. Bu, V. Apostolopoulos, T. Melvin, and A. G. R. Evans. Novel actuation of an integrated peristaltic micropump. *Microelectronic Engineering*, 73-74:858–863, 2004.

[50] N. T. Nguyen, X. Y. Huang, and T. K. Chuan. Mems-micropumps: A review. *Journal of Fluids Engineering-Transactions of the ASME*, 124(2):384–392, 2002.

[51] R. Hart, M. Hudson, A. Newsome, and J. Ratcliffe. Microfluidics & microfiltration. Multidisciplinary report, University of Southampton, 2nd March 2001.

[52] N. T. Nguyen. Micromachined flow sensors - a review. *Flow Measurement and Instrumentation*, 8(1):7–16, 1997.

[53] M. Koch, H. Witt, A. G. R. Evans, and A. Brunnschweiler. Improved characterization technique for micromixers. *Journal of Micromechanics and Microengineering*, 9(2):156–158, 1999.

[54] M. Koch, D. Chatelain, A. G. R. Evans, and A. Brunnschweiler. Two simple micromixers based on silicon. *Journal of Micromechanics and Microengineering*, 8(2):123–126, 1998.

[55] M. Krishnan, S. N. Brahmasandra, D. T. Burke, C. H. Mastrangelo, and M. A. Burns. A novel strategy for the design of multiple reaction systems for genetic analysis. *Sensors and Actuators A - Physical*, 95(2-3):250–258, 2002.

[56] M. Q. Bu, M. Tracy, G. Ensell, J. S. Wilkinson, and A. G. R. Evans. Design and theoretical evaluation of a novel microfluidic device to be used for pcr. *Journal of Micromechanics and Microengineering*, 13(4):S125–S130, 2003.

[57] A. Mehra, X. Zhang, A. A. Ayon, I. A. Waitz, M. A. Schmidt, and C. M. Spadaccini. A six-wafer combustion system for a silicon micro gas turbine engine. *Journal of Microelectromechanical Systems*, 9(4):517–527, 2000.

[58] L. G. Frechette, S. A. Jacobson, K. S. Breuer, F. F. Ehrich, R. Ghodssi, R. Khanna, C. W. Wong, X. Zhang, M. A. Schmidt, and A. H. Epstein. High-speed microfabricated silicon turbomachinery and fluid film bearings. *Journal of Microelectromechanical Systems*, 14(1):141–152, 2005.

[59] A. Manz, N. Graber, and H. M. Widmer. Miniaturized total chemical-analysis systems - a novel concept for chemical sensing. *Sensors and Actuators B-Chemical*, 1(1-6):244–248, 1990.

[60] D. R. Reyes, D. Iossifidis, P. A. Auroux, and A. Manz. Micro total analysis systems. 1. introduction, theory, and technology. *Analytical Chemistry*, 74(12):2623–2636, 2002.

[61] P. A. Auroux, D. Iossifidis, D. R. Reyes, and A. Manz. Micro total analysis systems. 2. analytical standard operations and applications. *Analytical Chemistry*, 74(12):2637–2652, 2002.

[62] C. G. J. Schabmueller, M. Koch, A. G. R. Evans, and A. Brunnschweiler. Design and fabrication of a microfluidic circuitboard. *Journal of Micromechanics and Microengineering*, 9(2):176–179, 1999.

[63] Z. A. Gol'dberg. Acoustic radiation pressure. In L.D. Rozenburg, editor, *High Intensity Ultrasonic Fields*, pages 75–133. Plenum Press, New York, 1971.

[64] L. V. King. On the acoustic radiation pressure on spheres. *Proceedings of the Royal Society of London*, A147:214–240, 1934.

[65] K. Yosioka and Y. Kawasima. Acoustic radiation pressure on a compressible sphere. *Acustica*, 5:167–173, 1955.

[66] M. Gröschl. Ultrasonic separation of suspended particles - Part I: Fundamentals. *Acustica*, 84(3):432–447, 1998.

[67] L. P. Gor'kov. On the forces acting on a small particle in an acoustical field in an ideal fluid. *Soviet Physics: Doklady*, 6(9):773–775, 1962.

[68] K. Yasuda. Measurement of microscopic spatial distribution of acoustic radiation force using microspheres and electrostatic force. *Japanese Journal of Applied Physics Part 1-Regular Papers Short Notes & Review Papers*, 38(5B):3316–3319, 1999.

[69] T. L. Tolt and D. L. Feke. Separation of dispersed phases from liquids in acoustically driven chambers. *Chemical Engineering Science*, 48(3):527–540, 1993.

[70] A. A. Doinikov. Acoustic radiation pressure exerted by a spherical wave on a bubble in a viscous liquid. *Wave Motion*, 24(3):275–279, 1996.

[71] T. G. Leighton. Bubble population phenomena in acoustic cavitation. *Ultrasonics Sonochemistry*, 2(2):S123–S136, 1995.

[72] K. Higashitani, M. Fukushima, and Y. Matsuno. Migration of suspended particles in plane stationary ultrasonic-field. *Chemical Engineering Science*, 36(12):1877–1882, 1981.

[73] A. Hancock, M. F. Insana, and J. S. Allen. Microparticle column geometry in acoustic stationary fields. *Journal of the Acoustical Society of America*, 113(1):652–659, 2003.

[74] K. Yasuda and T. Kamakura. Acoustic radiation force on micrometer-size particles. *Applied Physics Letters*, 71(13):1771–1773, 1997.

[75] M. A. H. Weiser, R. E. Apfel, and E. A. Neppiras. Interparticle forces on red-cells in a standing wave field. *Acustica*, 56(2):114–119, 1984.

[76] E. Benes, M. Gröschl, H. Nowotny, F. Trampler, T. Keijzer, H. Böhm, S. Radel, L. Gherardini, J.J. Hawkes, R. König, and Ch. Delouvroy. Ultrasonic separation of suspended particles. In *2001 Ultrasonics Symposium, Oct 6-10 2001*, volume 1 of *Proceedings of the IEEE Ultrasonics Symposium*, pages 649–659, Atlanta, GA, 2001.

[77] T. Tuziuti, T. Kozuka, and H. Mitome. Measurement of distribution of acoustic radiation force perpendicular to sound beam axis. *Japanese Journal of Applied Physics Part 1-Regular Papers Short Notes & Review Papers*, 38(5B):3297–3301, 1999.

[78] C. J. Schram. Manipulation of particles in an acoustic field. In T. J. Mason, editor, *Sonochemistry*, pages 293–322. Royal Society of Chemistry, Cambridge, 1990.

[79] G. Whitworth and W. T. Coakley. Particle column formation in a stationary ultrasonic-field. *Journal of the Acoustical Society of America*, 91(1):79–85, 1992.

[80] S. M. Woodside, B. D. Bowen, and J. M. Piret. Measurement of ultrasonic forces for particle-liquid separations. *AIChE Journal*, 43(7):1727–1736, 1997.

[81] S. M. Woodside, J. M. Piret, M. Groschl, E. Benes, and B. D. Bowen. Acoustic force distribution in resonators for ultrasonic particle separation. *AIChE Journal*, 44(9):1976–1984, 1998.

[82] T. Lilliehorn, U. Simu, M. Nilsson, M. Almqvist, T. Stepinski, T. Laurell, J. Nilsson, and S. Johansson. Trapping of microparticles in the near field of an ultrasonic transducer. *Ultrasonics*, 43(5):293–303, 2005.

[83] J. Lighthill. *Waves in fluids*. C.U.P., Cambridge, 1978.

[84] N. Riley. Steady streaming. *Annual Review of Fluid Mechanics*, 33:43–65, 2001.

[85] W. L. M Nyborg. Acoustic streaming. In W. P. Mason, editor, *Physical Acoustics*, volume II - Part B. Academic Press, New York, 1965.

[86] J. Spengler and M. Jekel. Ultrasound conditioning of suspensions - studies of streaming influence on particle aggregation on a lab- and pilot-plant scale. *Ultrasonics*, 38(1-8):624–628, 2000.

[87] L. A. Kuznetsova and W. T. Coakley. Microparticle concentration in short path length uftrasonic resonators: Roles of radiation pressure and acoustic streaming. *Journal of the Acoustical Society of America*, 116(4):1956–1966, 2004.

[88] J. F. Spengler, W. T. Coakley, and K. T. Christensen. Microstreaming effects on particle concentration in an ultrasonic standing wave. *AIChE Journal*, 49(11):2773–2782, 2003.

[89] L. K. Zarembo. Acoustic streaming. In L.D. Rozenburg, editor, *High Intensity Ultrasonic Fields*, pages 137–199. Plenum Press, New York, 1971.

[90] J. W. S. Rayleigh. *The theory of sound*, volume 2. Dover, New York, 1945.

[91] M. F. Hamilton, Y. A. Ilinskii, and E. A. Zabolotskaya. Acoustic streaming generated by standing waves in two- dimensional channels of arbitrary width. *Journal of the Acoustical Society of America*, 113(1):153–160, 2003.

[92] S. D. Danilov and M. A. Mironov. Mean force on a small sphere in a sound field in a viscous fluid. *Journal of the Acoustical Society of America*, 107(1):143–153, 2000.

[93] A. A. Doinikov. Acoustic radiation pressure on a rigid sphere in a viscous- fluid. *Proceedings of the Royal Society of London Series a- Mathematical and Physical Sciences*, 447(1931):447–466, 1994.

[94] P. A. Belter, E. L. Cussler, and W. Hu. *Bioseparations: downstream processing for biotechnology*. Wiley, New York, 1988.

[95] L. Svarovsky. Efficiency of separation of particles from fluids. In L. Svarovsky, editor, *Solid-liquid separation*, pages 43–73. Butterworths, London, 3rd edition, 1990.

[96] H. G. W. Pierson. The selection of solid-liquid separation equipment. In L. Svarovsky, editor, *Solid-liquid separation*, pages 614–627. Butterworths, London, 3rd edition, 1990.

[97] R. J. Gochin. Flotation. In L. Svarovsky, editor, *Solid-Liquid Separation*, pages 591–613. Butterworths, London, 3rd edition, 1990.

[98] R. S. M. S. Karumanchi, S. N. Doddamane, C. Sampangi, and P. W. Todd. Field-assisted extraction of cells, particles and macromolecules. *Trends in Biotechnology*, 20(2):72–78, 2002.

[99] P. Gascoyne, J. Satayavivad, and M. Ruchirawat. Microfluidic approaches to malaria detection. *Acta Tropica*, 89(3):357–369, 2004.

[100] *Biosep acoustic cell retention (AppliSens)*. http://www.applisens.com/biosep.html, Web page accessed on 9 June 2005.

[101] *Sonosep*$^{\mathrm{TM}}$ *Technologies Inc.* http://www.sonosep.com/, Web page accessed on 8 June 2005.

[102] V. M. Gorenflo, L. Smith, B. Dedinsky, B. Persson, and J. M. Piret. Scale-up and optimization of an acoustic filter for 200 l/day perfusion of a cho cell culture. *Biotechnology and Bioengineering*, 80(4):438–444, 2002.

[103] H. Böhm, L. G. Briarty, K. C. Lowe, J. B. Power, E. Benes, and M. R. Davey. Quantification of a novel h-shaped ultrasonic resonator for separation of biomaterials under terrestrial gravity and microgravity conditions. *Biotechnology and Bioengineering*, 82(1):74–85, 2003.

[104] E. Benes, M. Gröschl, H. Nowotny, H. Böhm, S. Radel, J. B. Hauser, J. B. Power, K. C. Lowe, L. G. Briarty, and M. R. Davey. The ultrasonic h-shape separator harvesting of the alga spirulina platensis under zero-gravity conditions. In *5th World Congress on Ultrasonics*, Paris, France, 2003.

[105] S. Gupta, D. L. Feke, and I. Manaszloczower. Fractionation of mixed particulate solids according to compressibility using ultrasonic standing-wave fields. *Chemical Engineering Science*, 50(20):3275–3284, 1995.

[106] F. Petersson, A. Nilsson, C. Holm, H. Jonsson, and T. Laurell. Separation of lipids from blood utilizing ultrasonic standing waves in microfluidic channels. *Analyst*, 129(10):938–943, 2004.

[107] D. A. Johnson and D. L. Feke. Methodology for fractionating suspended particles using ultrasonic standing wave and divided flow fields. *Separations Technology*, 5(4):251–258, 1995.

[108] Z. Mandralis, W. Bolek, W. Burger, E. Benes, and D. L. Feke. Enhanced synchronized ultrasonic and flow-field fractionation of suspensions. *Ultrasonics*, 32(2):113–121, 1994.

[109] P. W. S. Pui, F. Trampler, S. A. Sonderhoff, M. Groeschl, D. G. Kilburn, and J. M. Piret. Batch and semicontinuous aggregation and sedimentation of hybridoma cells by acoustic-resonance fields. *Biotechnology Progress*, 11(2):146–152, 1995.

[110] T. Gaida, O. DoblhoffDier, K. Strutzenberger, H. Katinger, W. Burger, M. Groschl, B. Handl, and E. Benes. Selective retention of viable cells in ultrasonic resonance field devices. *Biotechnology Progress*, 12(1):73–76, 1996.

[111] W. T. Coakley, J. J. Hawkes, M. A. Sobanski, C. M. Cousins, and J. Spengler. Analytical scale ultrasonic standing wave manipulation of cells and microparticles. *Ultrasonics*, 38(1-8):638–641, 2000.

[112] J. F. Spengler and W. T. Coakley. Ultrasonic trap to monitor morphology and stability of developing microparticle aggregates. *Langmuir*, 19(9):3635–3642, 2003.

[113] J. Morgan, J. F. Spengler, L. Kuznetsova, W. T. Coakley, J. Xu, and W. M. Purcell. Manipulation of in vitro toxicant sensors in an ultrasonic standing wave. *Toxicology in Vitro*, 18(1):115–120, 2004.

[114] S. Gupta and D. L. Feke. Acoustically driven collection of suspended particles within porous media. *Ultrasonics*, 35(2):131–139, 1997.

[115] S. Gupta and D. L. Feke. Filtration of particulate suspensions in acoustically driven porous media. *AIChE Journal*, 44(5):1005–1014, 1998.

[116] Z. W. Wang, P. Grabenstetter, D. L. Feke, and J. M. Belovich. Retention and viability characteristics of mammalian cells in an acoustically driven polymer mesh. *Biotechnology Progress*, 20(1):384–387, 2004.

[117] Y. Abe, M. Kawaji, and T. Watanabe. Study on the bubble motion control by ultrasonic wave. *Experimental Thermal and Fluid Science*, 26(6-7):817–826, 2002.

[118] J. J. Hawkes, M. J. Long, W. T. Coakley, and M. B. McDonnell. Ultrasonic deposition of cells on a surface. *Biosensors & Bioelectronics*, 19(9):1021–1028, 2004.

[119] Stacey P. Martin, Rosemary J. Townsend, Larisa A. Kuznetsova, Kathryn A.J. Borthwick, Martyn Hill, Martin B. McDonnell, and W. Terence Coakley. Spore and micro-particle capture on an immunosensor surface in an ultrasound standing wave system. *Biosensors and Bioelectronics*, 21(5):758–767, 2005.

[120] C. Suri, K. Takenaka, H. Yanagida, Y. Kojima, and K. Koyama. Chaotic mixing generated by acoustic streaming. *Ultrasonics*, 40(1-8):393–396, 2002.

[121] G. G. Yaralioglu, I. O. Wygant, T. C. Marentis, and B. T. Khuri-Yakub. Ultrasonic mixing in microfluidic channels using integrated transducers. *Analytical Chemistry*, 76(13):3694–3698, 2004.

[122] K. R. Nightingale and G. E. Trahey. A finite element model for simulating acoustic streaming in cystic breast lesions with experimental validation. *IEEE Transactions on Ultrasonics Ferroelectrics and Frequency Control*, 47(1):201–215, 2000.

[123] H. Nowotny and E. Benes. General one-dimensional treatment of the layered piezoelectric resonator with 2 electrodes. *Journal of the Acoustical Society of America*, 82(2):513–521, 1987.

[124] H. Nowotny, E. Benes, and M. Schmid. Layered piezoelectric resonators with an arbitrary number of electrodes (general one-dimensional treatment). *Journal of the Acoustical Society of America*, 90(3):1238–1245, 1991.

[125] J. J. Hawkes, W. T. Coakley, M. Groschl, E. Benes, S. Armstrong, P. J. Tasker, and H. Nowotny. Single half-wavelength ultrasonic particle filter: Predictions of the transfer matrix multilayer resonator model and experimental filtration results. *Journal of the Acoustical Society of America*, 111(3):1259–1266, 2002.

[126] M. Hill, N. Harris, R. Townsend, N. White, and S. Beeby. Separation of particles from a fluid using a microfabricated, ultrasonic device. In *5th World Congress on Ultrasonics*, Paris, France, 2003.

[127] P. Wu, R. Kazys, and T. Stepinski. Analysis of the numerically implemented angular spectrum approach based on the evaluation of two-dimensional acoustic fields .1. errors due to the discrete fourier transform and discretization. *Journal of the Acoustical Society of America*, 99(3):1339–1348, 1996.

[128] P. Wu, R. Kazys, and T. Stepinski. Analysis of the numerically implemented angular spectrum approach based on the evaluation of two-dimensional acoustic fields .2. characteristics as a function of angular range. *Journal of the Acoustical Society of America*, 99(3):1349–1359, 1996.

[129] E. R. F. de Sarabia, J. A. Gallego-Juarez, G. Rodriguez-Corral, L. Elvira-Segura, and I. Gonzalez-Gomez. Application of high-power ultrasound to enhance fluid/solid particle separation processes. *Ultrasonics*, 38(1-8):642–646, 2000.

[130] R. J. Wakeman and A. J. L. Bailey. Sonothickening: Continuous in-line concentration/clarification of fine particle suspensions by power ultrasound. *Chemical Engineering Research & Design*, 78(A4):651–661, 2000.

[131] F. Durst, D. Milojevic, and B. Schonung. Eulerian and lagrangian predictions of particulate 2-phase flows - a numerical study. *Applied Mathematical Modelling*, 8(2):101–115, 1984.

[132] I. L. J. Holwill. The use of ultrasonic standing waves to enhance optical particle sizing equipment. *Ultrasonics*, 38(1-8):650–653, 2000.

[133] L. E. Kinsler, A. R. Frey, A. B. Coppens, and J. V. Sanders. *Fundamentals of Acoustics*. Wiley, New York, 3rd edition, 1982.

[134] *CFX-5 Help*. AEA Technology CFX 5.4.1 online documentation.

[135] *Onda Coporation acoustic material tables*. http://www.ondacorp.com/tecref_acoustictable.html, Web page accessed on 11 April 2005.

[136] A. Einstein. *Investigations on the theory of the Brownian movement*. Dover, London, 1956.

[137] P. G. Saffman. The lift on a small sphere in a slow shear flow. *Journal of Fluid Mechanics*, 31:624, 1968.

[138] F. M. White. *Viscous fluid flow*. Mechanical Engineering. McGraw-Hill, New York, 2nd edition, 1991.

[139] W. T. Ames. *Numerical methods for particle differential equations*. Academic Press, New York, 2nd edition, 1977.

[140] N. R. Harris, M. Hill, N. M. White, and S. P. Beeby. Acoustic power output measurements for thick-film pzt transducers. *Electronics Letters*, 40(10):636–637, 2004.